Advanced Operating Strategies for Non-Isothermal Fixed-Bed Reactors Exemplified for CO_2 Methanation

Dissertation
zur Erlangung des akademischen Grades

Doktoringenieur
(Dr. - Ing.)

von **Jens Bremer, M.Sc.**
geboren am 14.11.1987 in Schwerin

genehmigt durch die Fakultät für Verfahrens- und Systemtechnik
der Otto-von-Guericke-Universität Magdeburg

Promotionskommission:
Prof. Dr.-Ing. habil. Evangelos Tsotsas (Vorsitz)
Prof. Dr.-Ing. habil. Kai Sundmacher (Gutachter)
Prof. Dr.-Ing. Jorg Thöming (Gutachter)
Prof. Tapio Salmi (Gutachter)

eingereicht am: 28. August 2020
Promotionskolloquium am: 16. November 2020

> *What we know is a drop, what we don't know is an ocean.*
>
> — **Isaac Newton**

Abstract

Fixed-bed reactors can effectively perform chemical reactions with high space-time-yields and are, therefore, an essential part of many processes in the chemical industry. With the increasing integration of volatile renewable energies, these processes, and thus also the installed reactors, will operate at different loads more often. Using the example of the exothermic CO_2 methanation, as part of a power-to-gas process, this work takes up two key questions on load-flexible reactor operation:

1. Which operating points are attainable by fixed-bed reactors?
2. How does a fixed-bed reactor need to be operated to reach and maintain a new operating point / load?

To be able to answer both questions, classical aspects of reaction engineering, such as the performance and durability of the catalyst, are addressed first. Although industrial catalysts for CO_2 methanation show high activities and very high selectivities, temperatures above 550 °C can lead to strong degradations of the active component - primarily by sintering. Insufficient heat management of the fixed-bed reactor can easily lead to a hot reaction zone (hot-spot) with temperatures above this limit. Due to complex physicochemical effects, even higher temperatures can be reached during the transition between two operating points (e.g., in the case of ”wrong-way” behavior). Hence, the exact description and prediction of the reactors temperature profile under both static and dynamic conditions are one of the key aspects of this work.

With regard to the first question, the steady state of the fixed-bed reactor is fundamentally investigated at the beginning of this work. Thereby, aspects such as uniqueness, multiplicity, and stability of the respective operating point are of particular interest. The literature on ideal reactors with zero or total back-mixing already provides numerous quantitative and qualitative descriptions of these characteristics. For the case of a real, non-isothermal fixed-bed reactor with finite back-mixing, the literature also provides numerous qualitative statements, but significant gaps still exist in the quantitative description. To close this gap, this work develops novel mathematical criteria based on CSTR cascade analogy. They can be used to shown that low back-mixing is far more relevant for the reactor’s operating range than currently reported in the literature.

To further support the derived criteria, this work also presents a detailed dynamic reactor model. This model is then used to compare different reactor concepts with regard to

fixed-bed temperature and reactor conversion at relevant, steady-state operating points. Here it can be shown that reactor operation at unstable operating points allows high conversions even at low bed temperatures. Simulation studies also show that the required stabilizing control is technically feasible and thus makes the usually neglected unstable operating points accessible.

In order to answer the second question, the probably most difficult load change case is examined: the cold start of the reactor. Using the dynamic reactor model within an optimal control problem shows that certain coolant temperature trajectories exist and allow for fast and safe reactor start-up. An exceeding of the maximum reactor temperature can be avoided with this sophisticated operating strategy.

The last chapter presents a pilot plant specifically designed to underpin the theoretical and computational results with experiments. The industrial-scale single-tube reactor in this plant is equipped with an exceptional temperature sensor that enables precise measurements of the reactor's temperature field in real time. Several pilot plant runs are used to validate and calibrate the developed dynamic reactor model. The simultaneous determination of kinetic and heat transport parameters of a reactor of this size has not been found in the literature so far and provides a variety of new findings. Although a slight recalibration of the model is necessary, it proves to be well suited for rigorous dynamic studies. Furthermore, it can be shown that the predictions from the developed criteria are consistent with the results of the experiments.

The models and methods developed in this work show that the conventional fixed-bed reactor can be operated in a much wider range than usually assumed. The derived criteria help to re-evaluate questions about safe reactor operation and might replace old, often conservative criteria. Furthermore, the criteria may be relevant to develop new reactor concepts and designs. Theory, modeling, and experiments turned out to be highly relevant for the further development of flexible fixed-bed reactors, which makes this work an essential contribution to the current state of knowledge.

Zusammenfassung

Festbettreaktoren können chemische Reaktionen mit hoher Raum-Zeit-Ausbeute effizient umsetzen und sind damit ein essentieller Bestandteil vieler Prozesse der chemischen Industrie. Durch die zunehmende Einbindung unstetiger erneuerbarer Energien müssen diese Prozesse, und damit auch die darin befindlichen Reaktoren, zunehmend bei verschiedenen Lasten betrieben werden. Am Beispiel der exothermen CO_2 Methanisierung, als Teil eines Power-to-Gas Prozesses, greift diese Arbeit zwei Kernfragen zum lastflexiblen Reaktorbetrieb auf:

1. Welche Betriebspunkte kann ein Festbettreaktor erreichen?
2. Wie muss ein Festbettreaktor betrieben werden, um einen neuen Betriebspunkt zu erreichen und zu halten?

Um beide Fragen beantworten zu können, werden zunächst klassische Aspekte der Reaktionstechnik, wie die Leistungsfähigkeit und Belastbarkeit des Katalysators, berücksichtigt. Die für die CO_2 Methanisierung großtechnisch relevanten Katalysatoren weisen zwar eine gute Aktivität und sehr gute Selektivität auf, jedoch können Temperaturen oberhalb von 550 °C zu starken Degradationserscheinungen führen – vor allem durch das Sintern der Aktivkomponente. Bei unzureichendem Wärmemanagement existieren breite Reaktorbetriebsbereiche, in denen das katalytische Festbett eine heiße Reaktionszone (Hotspot) mit Temperaturen oberhalb dieser Grenze ausbildet. Aufgrund der komplexen physikochemischen Effekte im Reaktor können beim Übergang zwischen zwei Betriebspunkten zeitweise sogar noch höhere Temperaturen erreicht werden (z.B. im Falle eines ”wrong-way” Verhaltens). Daher ist die genaue Beschreibung und Vorhersage des Temperaturfeldes im Reaktor sowohl unter statischen als auch unter dynamischen Bedingungen ein zentrales Thema dieser Arbeit.

Mit Blick auf die erste Frage wird zu Beginn dieser Arbeit der statische Zustand des Festbettreaktors fundamental untersucht. Dabei geht es vor allem um Aspekte wie Eindeutigkeit, Vielfachheit und Stabilität des jeweiligen Betriebspunkts. Die in der Literatur weit verbreiteten idealen Modellvorstellungen mit keiner oder totaler Rückvermischung liefern bereits zahlreiche quantitative und qualitative Ansätze zur Beschreibung dieser Charakteristiken. Für den Fall eines realen, nicht-isothermen Festbettreaktors mit endlicher Rückvermischung liefert die Literatur zwar ebenfalls unzählige qualitative Aussagen, jedoch existieren bislang großen Lücken in der quantitativen Beschreibung.

Um die Lücke zu schließen, entwickelt diese Arbeit neuartige mathematische Kriterien basierend auf der CSTR-Kaskadenanalogie. Darüber hinaus kann gezeigt werden, dass selbst niedrige Rückvermischungsraten weit relevanter für die Gesamtheit der möglichen Reaktorzustände sind, als zurzeit in der Literatur berichtet.

Um die abgeleiteten Kriterien zu untermauern, präsentiert diese Arbeit ebenfalls ein detailliertes dynamisches Reaktormodell. Damit werden verschiedene Reaktorkonzepte hinsichtlich Festbetttemperatur und Reaktorumsatz an relevanten, stationären Betriebspunkten verglichen. Hierbei kann gezeigt werden, dass ein Reaktorbetrieb im Bereich der instabilen Zustände hohe Umsätze bei geringen Reaktortemperaturen ermöglicht. Simulationsstudien zeigen außerdem, dass die dafür notwendige stabilisierende Reglung technisch machbar ist und damit die bislang ungenutzten Betriebspunkte zugänglich macht.

Zur Beantwortung der zweiten Frage wird der wohl schwierigste Lastwechselfall untersucht: der Kaltstart des Reaktors. Unter Nutzung des dynamischen Reaktormodells innerhalb einer Optimalsteuerungsaufgabe wird gezeigt, dass bestimmte Kühlmitteltemperaturtrajektorien existieren, welche einen schnellen und sicheren Reaktorstart ermöglichen. Eine Überschreitung der maximalen Reaktortemperatur kann mit dieser ausgeklügelten Betriebsstrategie vermieden werden.

Um die computergestützten Ergebnisse dieser Arbeit mit experimentellen Ergebnissen zu untermauern, präsentiert das letzte Kapitel eine speziell entwickelte Pilotanlage. Mit Hilfe dieser Anlage und der darin befindlichen Messtechnik kann das Temperaturfeld eines industrieskaligen Einzelrohrreaktors hochgenau und in Echtzeit untersucht werden. Mit den experimentellen Daten wird das zuvor entwickelte dynamische Reaktormodell validiert und anschließend justiert. Die dabei erstmals gleichzeitige Bestimmung von Kinetik- und Wärmetransportparametern im Festbett eines Reaktors dieser Größe ist bislang nicht in der Literatur zu finden und liefert eine Vielzahl neuer Erkenntnisse. Obwohl eine leichte Nachjustierung des Modells erforderlich ist, erweist es sich als gut geeignet für rigorose dynamische Studien und untermauert damit die Relevanz der Ergebnisse. Darüber hinaus kann gezeigt werden, dass die Aussagen aus den entwickelten Kriterien mit den Ergebnissen der Experimente übereinstimmen.

Die in dieser Arbeit entwickelten Modelle und Methoden zeigen, dass der klassische Festbettreaktor in einem sehr viel breiteren Bereich betrieben werden kann, als bisher angenommen wurde. Die abgeleiteten Kriterien können übliche Fragestellungen zum Betrieb und Design eines Festbettreaktors neu bewerten und damit alte, meist sehr konservative Kriterien ablösen. Theorie, Modellierung und Experimente erwiesen sich als höchst relevant für die Weiterentwicklung flexibler Festbettreaktoren, was diese Arbeit zu einem essentiellen Beitrag zum bisherigen Stand des Wissens macht.

Preface

Several journal articles were published in the course of the present dissertation. In order to assign the contribution of each individual article, the following list shall be considered:

- The first part of the theoretical background (Section 3.1) presents a simplified modeling approach and derives fundamental criteria to evaluate the operating range of non-isothermal fixed-bed reactors. To large extents, this section and the corresponding appendices are based on Bremer and Sundmacher [BS21].
- The second part of the theoretical background (Section 3.2) presents a detailed reactor model that is used throughout the whole dissertation. This section and the corresponding appendices are partly taken from [BS19]. In addition, the investigation on reactor operating ranges (Chapter 4) is also primarily based on Bremer and Sundmacher [BS19].
- The study on the optimal reactor start-up (Chapter 5) is adapted from Bremer et al. [BRS17]. The problem formulation as well as the results are taken from this journal article, whereas introduction and summary of this chapter are reorganized to allow for a reasonable placement within the dissertation.

Journal articles used for this dissertation:

[BRS17] J. Bremer, K. H. G. Rätze, and K. Sundmacher. „CO_2 methanation: Optimal start-up control of a fixed-bed reactor for power-to-gas applications“. In: *AIChE Journal* 63.1 (2017), pp. 23–31 (cit. on pp. ix, 13, 19, 27, 79).

[BS19] J. Bremer and K. Sundmacher. „Operation range extension via hot-spot control for catalytic CO_2 methanation reactors“. In: *Reaction Chemistry & Engineering* 4 (2019), pp. 1019–1037 (cit. on pp. ix, 13, 49, 63).

[BS21] J. Bremer and K. Sundmacher. „Novel multiplicity and stability criteria for non-isothermal fixed-bed reactors“. In: *Frontiers in Energy Research* 8 (2021), p. 549298 (cit. on p. ix).

Contents

Abstract v

Zusammenfassung vii

Preface ix

1 Introduction 1
- 1.1 State of the Art . . . 4
- 1.2 Scope of this work . . . 14

2 Carbon Dioxide Methanation 17
- 2.1 Thermodynamics and Reaction Kinetics . . . 20
- 2.2 Methanation Process Concepts . . . 24

3 Theoretical Background 29
- 3.1 Fundamentals of Reactor Modeling . . . 31
  - 3.1.1 State-Space Multiplicity . . . 33
  - 3.1.2 CSTR Analogy . . . 40
  - 3.1.3 CSTR Cascade Analogy . . . 43
  - 3.1.4 Novel Stability, Uniqueness, and Multiplicity Criteria . . . 51
- 3.2 Detailed Dynamic Fixed-Bed Reactor Model . . . 55
  - 3.2.1 Reaction Kinetics . . . 56
  - 3.2.2 Mass and Heat Transport Assumptions . . . 58
  - 3.2.3 Computational Aspects . . . 60

4 Reactor Operating Ranges 63
- 4.1 Steady-State Operation . . . 63
- 4.2 Stabilized Operation . . . 68
  - 4.2.1 Stability Analysis . . . 73
  - 4.2.2 Technical Aspects . . . 75
- 4.3 Chapter Summary . . . 77

5 Optimal Reactor Start-Up 79
- 5.1 Dynamic Optimization . . . 79

5.1.1 Solution Strategy 81
5.2 Results 82
5.3 Chapter Summary 85

6 Experimental Validation 87
6.1 The FOReCAST Pilot Plant 87
6.1.1 Reactor 89
6.1.2 Catalyst 90
6.1.3 Distributed Temperature Sensing (DTS) 93
6.1.4 Thermal Oil Heat Transfer Unit 95
6.2 Model Calibration 96
6.2.1 Plant Operation and Testing Procedure 97
6.2.2 The Uncalibrated Model 98
6.2.3 Model Calibration and Parameter Identification 101
6.3 Dynamic Experiments and Criteria Validation 107
6.4 Chapter Summary 111

7 Conclusions and Outlook 113
7.1 Concluding Remarks 113
7.2 Outlook 115

A Appendix 119
A.1 CSTR Analogy 119
A.1.1 Mass balance 119
A.1.2 Energy balance 121
A.2 CSTR Cascade Analogy 124
A.3 Components of Detailed Reactor Model 127
A.3.1 Fixed-Bed Transport Correlations 127
A.3.2 Coolant Transport Correlations 129
A.3.3 Reaction Rate Expressions 130
A.4 Reference Case of Detailed Reactor Model 133
A.5 Experiments 139
A.6 Numerical Diffusion within the FVM 143

Bibliography 145

List of Symbols 163

List of Figures 167

List of Tables 171

1

Introduction

Avoiding the further use of limited fossil resources and reducing the additional accumulation of atmospheric CO_2 is probably the most challenging transnational task of the 21st century. Renewable energy will successively transform our understanding of energy supply and transportation. Especially in Germany, this transformation is strongly motivated by the government and broadly supported throughout the population. Although Germany only contributes approx. 1.7 % (2019) to the world's CO_2 emissions, it intends to become a role model and technological leader in the field of sustainable and decarbonized energy systems. In 2018, Germany already generated 226 TWh renewable electricity (37 % of gross electricity generation) [VDI19]. In order to achieve the reduction of CO_2 emissions by 95 % (compared to 1990) until 2050, Bard et al. [Bar+18] proposed a massive expansion of Germany's renewable power generation. Accordingly, 1337 TWh renewable electricity need to be generated on national territory and 1430 TWh abroad. Thus, from production to consumption, the dominant share of used energy will have been in the form of electricity at least once. Therefore, wind, solar, and biomass are assumed to be the ruling energy sources. Due to legitimate concerns about the availability of fuel crops, environmental damage, biodiversity loss, and competition with food crops, the energy generation from biomass will remain at the same level as it is today [Bro+18]. In such scenarios, the conversion of electricity into other energy carriers and chemicals, *Power-to-X* (PtX) technologies will become an indispensable element for Germany's future energy system to couple the electricity sector with all other sectors (heat, transport, and chemistry). Whereas today's electricity demand for PtX (mainly Power-to-Hydrogen) is approximately 0.5 TWh [VDI19], Bard et al. [Bar+18] predicted a demand of 1419 TWh in 2050 mainly covered by wind and solar energy outside of Germany. In total, the electricity demand will increase by a factor of four to five and, thus, transform electricity into the future primary energy carrier.

Even if Germany and other nations miss their CO_2 emission targets, PtX will most likely still become a key technology for future energy systems. The right choice of the "X" is, however, subject of ongoing research [SB15; Tre+15; Bon+18; URS19; MMZ19; GR19], since it depends on a variety of different aspects (e.g., infrastructure, energy density, efficiency, economics). For the conversion of *Power-to-Gas* (PtG), possible products are hydrogen, methane, and syngas. They can be used or discharged by power plants, heating systems, vehicles, and the chemical industry. Furthermore, methanol and liquid fuel production are usually considered as *Power-to-Liquid* (PtL). Due to their high energy density, these products are favored for long-distance transportation (e.g.,

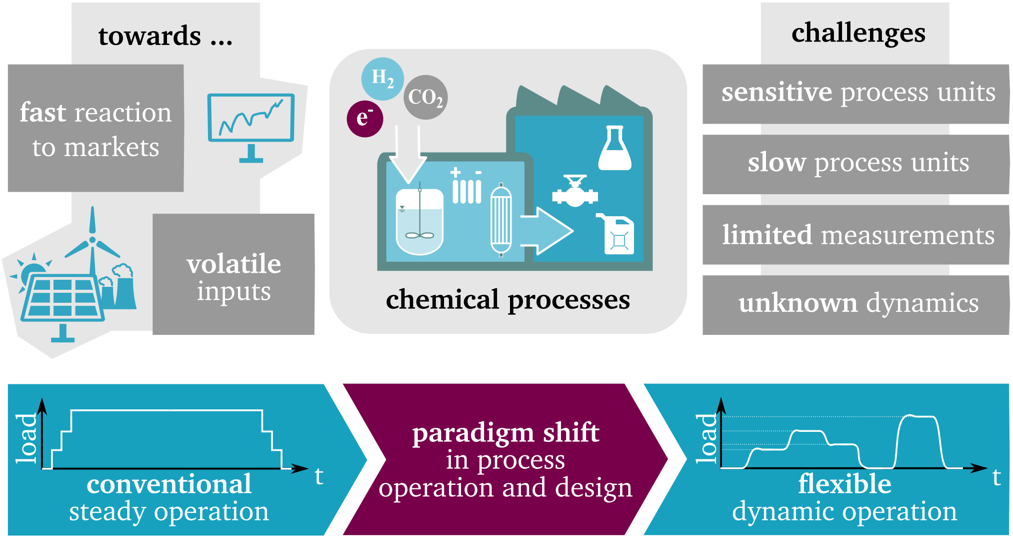
towards ...
fast reaction to markets
volatile inputs
H_2
CO_2
e^-
chemical processes
challenges
sensitive process units
slow process units
limited measurements
unknown dynamics
load
t
conventional steady operation
paradigm shift in process operation and design
load
t
flexible dynamic operation

Fig. 1.1.: Towards more flexible processes in chemical engineering.

aviation). Similar to syngas and hydrogen, methanol is also widely used in the chemical industry as a platform chemical.

As key elements of such future supply chains, PtX processes will be affected in particular by the discontinuous availability of renewable electricity, but also by new market environments (e.g., the European Union Emissions Trading System). In fact, the trend towards a more flexible production to react to markets as well as volatile inputs in particular demands unsteady process operation. In this regard, large, centralized chemical production sites, as they currently dominate the fossil fuel-based chemical industry, might not be the economically most efficient solution anymore. Instead, smaller, intelligent, and decentralized production units with an increased potential for fast interaction with volatile demands and supplies are gaining more relevance [WA17; BK19]. This paradigm shift, as illustrated in Fig. 1.1, is already in progress since the term flexibility has gained a foothold in the marketing departments of many global players in the chemical industry.

However, the term flexibility is used very differently. One way of looking at a flexible process is the ability to switch feedstocks, utilities, or products as needed. The other way considers feedstocks, utilities, or products to be fixed but processable within a broad load range. The latter load flexibility is particularly relevant when volatile inputs from renewable energies are involved [The19; FF20]. In such scenarios, the process benefits from a broad load range and fast transitions from one load to another (e.g., via start-up and shut-down). Bruns et al. [Bru+20] presents further types of process flexibility as well as their relevance for chemical engineering in recent years. The present work examines such aspects with regard to non-isothermal fixed-bed reactors for catalytic methanation in the context of PtG.

Catalytic reactors are key components of many chemical processes, and also of central importance for PtX. The involved catalysts are crucial for the efficiency and economy of the overall system. Unfortunately, the catalyst is also the most sensitive component and must, therefore, be treated with special care regarding safety, durability, and performance. These objectives are often mutually exclusive and have, thus, been of interest in reaction engineering for many decades [Ert+08; ER00; Eig08]. For instance, dealing with exothermic reactions often requires to inhibit distinct temperature excursions and, thus, results in lower productivities. Switching to alternative reactor designs, tailored for the specific application, has been one option to bypass certain contradicting objectives. Therefore, typical designs that have been developed are, e.g., fluidized-bed reactors, wall-coated reactors, membrane reactors, slurry reactors, or microstructured reactors. More advanced designs correspond to so-called integrated or multi-functional reactor concepts [HS97; AR88; KFE00]. They attempt to realize an optimal reaction route by incorporating optimal fluxes for heat and mass directly at the reaction site. Still, most of these concepts and designs are optimized for steady or batch-wise operation, but not for the operation at different loads and with frequent start-ups and shut-downs.

New reactor designs and operating strategies come to the fore when an unsteady operation is taken into consideration [BSM08; Mat89]. Kalz et al. [Kal+17] recently highlighted in detail the conceptional importance of future catalytic systems under dynamic reaction conditions and concluded that this research direction is still under-represented in the literature, especially for the synthesis of chemical energy carriers. Earlier studies in this area mainly focus on the catalytic material, surface, and structure under dynamic conditions. Nevertheless, the dynamic behavior of reactive systems has already been investigated back in the late 60s [HL67; Gil68; Ari69]. Even with limited computational capabilities, these investigations, often based on first principle models, built an impressive fundamental knowledge about the dynamics of reactive systems and proposed possible dynamic interaction concepts that can lead to higher reactor performance. However, the relative share of these concepts in commercial applications remains low due to the increased technical requirements [SK95]. The ongoing paradigm shift mentioned above, however, is again fueling the need for dynamic reactor operation. Furthermore, modern high-performance catalysts, each tailored for specific reactions, became more active and selective, but also more sensitive, e.g., in terms of temperature resistance. Thus, the interest in detailed predictions on the reactor dynamics has become more important than ever before [van17].

In summary, the complex interplay between climate change, market environments, and technology demands modern engineering disciplines to reevaluate past achievements and adapt them to today's challenges. The present work intends to follow this idea by taking up the example of catalytic methanation from a reaction engineering point of view. The non-isothermal fixed-bed reactor serves as showcase example for applying advanced operating strategies as possible technological milestone towards more flexible production chains.

1.1 State of the Art

In the late 50s, the dynamic reactor behavior became an essential characteristic to understand and improve chemical conversion systems. Possible instabilities and sensitivities, resulting from various physicochemical effects, were known to reduce productivity or even damage the entire reactor (e.g., due to runaways). In response to this, Aris and Amundson [AA58b] elaborated a pioneering series of articles and provided fundamental knowledge about reactor stability, state-space multiplicity, and control of homogeneously catalyzed continuously stirred tank reactors (CSTRs). Based on first principles models and control theory, the authors showed how unstable states could be stabilized and analyzed oscillations as well as limit cycles. In addition to these findings, Horn and Lin [HL67] proposed to operate reactors in particular under forced-periodic conditions, showing that this approach can lead to significant performance improvements (e.g., higher conversion). The *forced-periodic operation* proved to be advantageous for mathematical analyzes regarding the dynamic reactor behavior. Analytical expressions for optimization and control purposes have been derived, based on variational methods [SB80]. Later, many other authors took up *forced-periodic operation* by applying flow direction switches to maintain a slowly moving reaction front [AR88; Mat89; SK95], periodical input and environment manipulations [Sil98], as well as *frequency response analyzes* [Pet01; MMP08]. This concept has also been demonstrated experimentally for the propane oxidation and other reactions, particularly for the autothermal operation of reactions that feature a low exothermicity [EN88; NKE94b]. Silveston and Hudgins [SH13] and Bunimovich et al. [BSM08] give comprehensive overviews and more details on further applications.

The leading works of Padberg and Wicke [PW67], Eigenberger [Eig72a], and Gilles [Gil77] have shown that instabilities and state-space multiplicity can also be obtained from applications with fixed-bed reactors (FBRs). In comparison to prior CSTR investigations, the spatial distribution of the heterogeneous reactive site in a FBR leads to more complex phenomena (e.g., hot-zone formations and moving reaction fronts). For instance, Padberg and Wicke [PW67] found the oxidation of CO on a Pt-Al_2O_3 carrier catalyst to be very suitable to investigate instabilities of catalytic tubular reactors under adiabatic conditions at relatively low temperatures. Ignition and extinction characteristics were investigated and stability criteria were developed closely related to the CSTR findings of Aris and Amundson [AA58b]. Eigenberger [Eig72a] found that conductive heat transport along the solid catalyst phase is the key to understand existing multiple steady states. In addition, Gilles [Gil77] considered poisoning as one source of durability reduction, as well as relaxation oscillations for a class of endothermic reactions. He also concluded that the interaction between heat transfer and reaction essentially determines the reactor dynamics. Similarly interested in reactor durability, Weng et al. [WEB75] studied poisoning kinetics of thiophene on a nickel catalyst for the exothermic benzene hydrogenation. Their aim was to predict the propagation of activity zones induced by poisoning. Although a power law with first order in catalyst activity and thiophene concentration was identified to predict the activity rate change accurately, the activity zone propagation turned out to require an extended semi-empirical two-site deactivation model. As Gilles [Gil77] already confirmed the importance of mathematical modeling for dynamic investigations, Heinemann and Poore [HP81] used numerical bifurcation techniques for a systematic study of the state-space multiplicity, stability, and oscillatory dynamics of non-adiabatic tubular reactors. The authors illustrated the co-existence of up to seven steady states and periodic solutions.

More relevant for PtX applications, an early investigation on the dynamics of methanation reactors was provided by Lunde [Lun74]. Although the main objective at that time was neither related to energy efficiency nor energy storage, there was a vast interest in this technology as an oxygen support system for space exploration. Thereby, hydrogen from electrolysis and carbon dioxide from the astronaut's metabolism are used to produce water, which is then fed back to the electrolysis. This ensures the oxygen to circulate within the space station instead of being dumped into space. For such applications, the reactor performance was of essential interest also under load changes (e.g., due to higher or lower metabolic activities). The authors proposed to control the reactor with a counter-current coolant gas and also included model-based analyses to predict certain critical extinction scenarios better.

Further investigations on model-based control and reactor automation were elaborated by van Doesburg and Jong [vJ76a] for planning start-ups, shut-downs, and changes in operating conditions caused by changes in feeding or by the need to vary product quality. Here, the methanation of carbon oxides over a Ni/Al_2O_3 catalyst was considered as a purification step in the process sequence for hydrogen and ammonia synthesis by steam reforming or partial oxidation of hydrocarbons. They concluded that a very simple quasi-homogeneous plug-flow model could be used to predict the transient behavior of their pilot methanator. In an extensional work, van Doesburg and Jong [vJ76b] also pointed out inhibitory effects by CO contents during the transient operation of CO_2 methanation. Dissinger et al. [DJS80] investigated an entire process for the methanation of coal syngas in order to substitute dwindling US natural gas reserves. A model-based approach was used to regulate the reactor feed temperature by diverting some gas around interstage heat-exchangers. Advanced controller selection and tuning were found to be necessary, especially since conventional controller tuning gave controller settings that caused numerical problems with integration stability and efficiency.

Shortly after that, another interesting dynamic phenomenon, the so-called *wrong-way behaviour*, was studied in more detail. Wrong-way behavior occurs when the reactor feed temperature is suddenly decreased, leading to a subsequent packed bed temperature rise. This nonintuitive dynamic feature is caused by the difference in the propagation speed of concentration and temperature disturbances. Problems arise when the transient temperature rise damages the catalyst, initiates inactive side reactions or leads to a runaway. Mehta et al. [MSL81] made use of a pseudo-homogenous plug-flow reactor model and identified the dimensionless adiabatic temperature rise, activation energy, heat transfer capacity, coolant temperature, the magnitude of temperature drop, and the length of the reactor to be the most important to quantify wrong-way behavior. Furthermore, a simple expression for predicting the maximum temperature rise was derived. Although their relatively simple model was capable of describing general trends, it failed when steady-state multiplicity existed so that wrong-way behavior may lead to an ignition or extinction of the reactor. Considering more details on heat transport in axial direction as well as on interfacial transport resistances between catalyst particle and fluid were seen as possible remedies to overcome this issue, which was further discussed in subsequent studies [PCL88; CL89].

As one further source of reactor runaway, Bilous and Amundson [BA56] pointed out that in some cases, the temperature profile is very sensitive to the involved operational and physicochemical parameters and introduced the term *parametric sensitivity*. Following this, Morbidelli and Varma [MV82] aimed for an easily applicable exact reactor runaway criterion for all positive-order exothermic reactions. Therefore, the authors considered the Arrhenius temperature dependence of the reaction rate for all values of the inlet temperature. The authors also stressed the fact that parametric sensitivity has to be seen as a steady-state characteristic and not as a dynamic feature. Under certain conditions, however, parametric sensitivity can significantly affect dynamic operation by preventing it from approaching specific operating points.

With advancing computational capabilities, the aforementioned complex dynamic behaviors increasingly became the focus of model-based *reactor control* approaches. This way, one hoped to bypass the occurrence of critical temperature excursions. A comprehensive review until 1986 on reactor dynamics and control was given by Jørgensen [Jør86]. The author pointed out that catalytic FBRs are predestined for control purposes due to their sensitivities regarding possible disturbances, strong nonlinearities, non-minimum phase characteristics, and dead-times. In the author's view, seven steps are essential to achieve adequate reactor control:

1. Investigation of process statics and dynamics.
2. Selection of model representation.
3. Selection of identification and control strategy.
4. Selection of number and location of sensors.
5. Process identification either off- or on-line.
6. Control design for stabilization, disturbance rejection and set-point tracking.
7. Optimizing control design.

By reviewing the literature on all these seven steps, he concluded that, back then, investigations were mainly carried out with lab-scale FBRs, where the Reynolds number is often significantly lower than in industrial practice. However, he found the dynamic behavior of these reactors qualitatively well understood. In order to solve the remaining modeling issues for large-scale systems, more attention needed to be paid to heat transfer and other nonlinear effects. As a consequence, linear control approaches were found to be dominant in the literature at that time. To extent the local validity of linear control approaches, the author identified that sequences of step changes covering a relatively large operating range are most promising for practical application via robust control and adaptive control concepts. More conceptional discussions on batch and tubular reactor control, along with its relation to safety engineering were elaborated by Eigenberger and Schuler [ES89]. The key message of their work is that an appropriate control can permit reliable operation at unstable operating points, while even global stability does not necessarily rule out a runaway reaction (e.g., if a strongly exothermic reaction has a pronounced sensitivity with respect to uncertain parameters). Therefore, they concluded that instability is, in general, not a problem for safe operation, as long as the unstable system reacts so slowly that it can be easily stabilized by quick transient adjustments. Similar to Jørgensen [Jør86], Eigenberger and Schuler [ES89] also highlighted that until that time, reaction engineering was concentrated on research about the stability of a number of idealized systems. Consequently, these results were quite meaningful for basic modeling but had little relevance to practical problems. This conflict between science and practice further escalated in the mid-1990s, when Stankiewicz and Kuczynski [SK95] pointed out that despite the large number of studies on dynamics and control of chemical converters, the relative share of commercial applications was still very limited due to increased technical requirements.

Proceeding technical advancements and more precise measurements enabled a more accurate description of the nonlinear physicochemical effects, as well as the resulting complex dynamic behavior of catalytic reactors. Sheintuch [She97], who discussed sources of oscillatory behavior, transitions to chaotic solutions and *spatiotemporal patterns* in reactors of various geometries, gave a very comprehensive overview of this growing scientific field of heterogeneous catalysis. As one key example, he pointed to the increasing participation of surface science in catalytic studies (e.g., via surface potential measurements, surface IR-absorption, ellipsometry and X-ray diffraction), which gave many more insights about the inhomogeneous catalyst state (porosity, adsorbate concentration, active sites) varying across its entire support material. Consequently, the discrete distribution of reaction sites within the entire reactor will influence the dynamic behavior. In his explanations, Sheintuch [She97] referred to bistability or oscillatory features that can arise in each crystallite (or pellet). These effects might be communicated over several scales by heat transfer through the support, by diffusion through the gas phase as well as through their support (spillover). Since this explanation could be confirmed experimentally by spatiotemporal patterns [Jar+01], the importance of this multi-scale perspective on reactor dynamics became indispensable from thereon. Besides, Sheintuch [She97] predicted that future research will attempt to derive more detailed kinetic models tailored for specific reactions and that further efforts should be made towards suggesting practical applications of temporal oscillations or spatiotemporal patterns.

Further investigations on *spatiotemporal patterns* where conducted by Marwaha and Luss [ML03] focusing on hot-spot evolution and dynamics in packet-bed reactors during atmospheric oxidation of carbon monoxide on the top surface of a shallow packed bed, consisting of a few layers of spherical catalytic pellets (Pd/Al_2O_3). They observed a very intricate periodic motion in which the hot zone repeatedly split and coalesced, as illustrated in Fig. 1.2. Although the velocity of the fronts was found to be rather low (in the order of mm/min), they hypothesized that in commercial FBRs with much larger diameters, several distinct hot regions might co-exist and interact. In turn, this certainly affects the yield, deactivates the catalyst, and may also pose severe safety hazards. Moreover, it was highlighted that accurate reactor

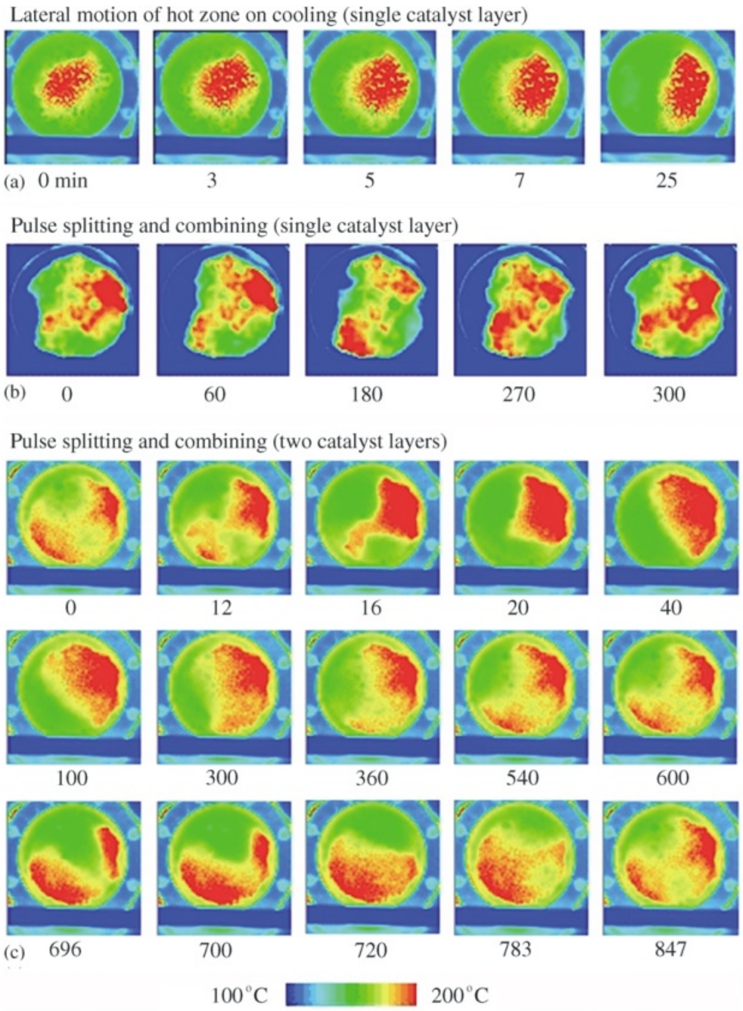
Lateral motion of hot zone on cooling (single catalyst layer)
(a) 0 min
3
5
7
25
Pulse splitting and combining (single catalyst layer)
(b) 0
60
180
270
300
Pulse splitting and combining (two catalyst layers)
0
12
16
20
40
100
300
360
540
600
(c) 696
700
720
783
847
100°C
200°C

Fig. 1.2.: Several motions of hot zones on catalyst particles for (a) single-layer case when the vessel was cooled from 110 °C to 107 °C, (b) single-layer case at vessel temperature of 105 °C and (c) for two-layer case at vessel temperature of 93 °C. The total flow rate was 1200 cm^3/min, reprinted from [ML03], Copyright (2020), with permission from Elsevier.

models for the observed phenomena were still missing since the required reliable kinetic models were not always available or hard to obtain. Comprehensive reviews on further experimental and theoretical studies of the formation of spatiotemporal temperature patterns on catalytic surfaces were elaborated by Luss and Sheintuch [LS05] and Viswanathan et al. [VSL08]. Both emphasized the practical relevance of moving reaction fronts. The authors also outlined that with micro-kinetic oscillatory reactions, one can predict the formation of a plethora of intricate spatiotemporal temperature patterns and temperature front motions. These motions turned out to be sensitive to the reactor operating conditions and properties such as diameter and initial conditions. Hence, the conventional understanding of a hot-spot as something with homogeneous expansion within a packed bed was increasingly converted to an arrangement of three-dimensional structures, often very small, and difficult to detect in large reactors. Tedious 3-D simulations, as provided by Nekhamkina and Sheintuch [NS12], were seen to be indispensable to understand further the size, shape, and dynamic features of hot zones. Their investigations, for instance, stressed previously developed criteria for adiabatic reactors, claiming the emergence of transversal patterns when

$$(\Delta T_{\mathrm{ad}}/\Delta T_{\mathrm{max}})/(\mathrm{Pe}^{\mathrm{m}}/\mathrm{Pe}^{\mathrm{e}}) > 1,$$

where ΔT_{ad} and ΔT_{max} are adiabatic and maximal temperature rise and Pe^{m} and Pe^{e} are mass and energy Péclet numbers, respectively. Based on detailed calculations, they argued that transversal patterns are highly unlikely to emerge in practical adiabatic and cooled FBRs with a single exothermic reaction, as in practice $\mathrm{Pe}^{\mathrm{m}}/\mathrm{Pe}^{\mathrm{e}} > 1$. However, this conclusion may not hold for micro-kinetic models and for two or more competing reactions. Furthermore, they suggested that a 1-D model may be sufficient to analyze a single reaction in an adiabatic reactor, and a 2-D axisymmetric model is sufficient for a cooled reactor of simple geometry.

In conclusion to this section, transient reactor operation has been of interest for quite some time and has led to a profound understanding. However, by the end of the 20th century, only little practical relevance has been achieved in this field. The reason for this dilemma seemed to be two-sided: On the one hand, there was no significant need for transient reactor operation, as feedstocks were continuously available, and high throughputs were of priority. On the other hand, the transient reactor behavior was often only qualitatively accessible due to limited computational resources or missing accurate descriptions of reaction kinetics and transport phenomena. Both aspects of this dilemma have dramatically changed within the last two decades. For instance, computational resources are now capable of performing even tedious calculations with strong and well-elaborated nonlinear reactor characteristics over several scales - from the active site up to the gas and catalyst phase. Additionally, the need to operate reactors dynamically and flexible is increasing every year as the value and availability of feedstocks is becoming increasingly volatile (e.g., due to the utilization of renewable energies). The following section focuses less on the dynamic fundamentals; instead, it depicts some studies relevant for this work, which make use of known dynamics to design and operate reactors under transient scenarios.

Towards Flexible Reactor Operation

The early studies from above helped significantly to understand basic dynamic reactor features. Nevertheless, reactor flexibility was not yet sufficiently addressed. The continuous development in reactor control and multi-scale, nonlinear modeling over the last two decades has shown many new incentives to take this criterion also into account. In order to explain this development in greater detail, the following explanations will proceed with special focus on chemical energy conversion systems and other closely related applications.

Ahead of its time, the pioneering work of Wright and Edgar [WE94] introduced advanced nonlinear control concepts to the field of catalytic FBRs applied to the water-gas shift (WGS) reaction. This was mainly achieved due to significant computational improvements that allowed to switch from linear model predictive control (LMPC) [ER91] to nonlinear model predictive control (NMPC). Although the computational burden was still very high to solve a very simplified reactor model with two 33 MHz and one 16 MHz central processing units, a relatively low sampling rate and a master-slave configuration with a low-level, fast sampling linear controller was effectively used for set-point tracking and reactor start-up. Furthermore, the performance of NMPC for set-point tracking of this nonlinear process was shown to be superior to conventional adaptive control, since parameter estimates varied as rapidly as the state, making successful parameter adjustment extremely difficult. Apart from that, NMPC allowed for input and state constraints simultaneously, which is often vital for practical applications and flexible reactor operation in a broad operating range.

More focused on detailed dynamic nonlinear modeling of WGS reactors, Adams II and Barton [AB09] developed one of the first dynamic, heterogeneous, two-dimensional models for high and low-temperature shifts and at scales ranging from industrial (for power plant applications) to small (such as automotive fuel cell applications). Excellent agreement between model and dynamic experimental data from an IGCC - TIGAS polygeneration plant has been obtained. In particular, their model was capable of predicting hot-spot developments during start-up or transitions between steady states and they observed that under these scenarios, the peak catalyst core temperatures could reach as much as 100 K above the maximum expected steady-state value - an evidence of the importance of dynamic considerations. Confirming the findings of older studies, they also found the rate equations to have the biggest impact on the overall modeling results.

Besides the WGS reaction, methanation also became of interest for dynamic investigations due to its key role for chemical energy conversion. Güttel [Güt13] studied dynamic responses of CO methanation based on a simplified reactor model under isothermal conditions. The reactor was perturbed by step changes in the inlet compositions of H_2 and CO, as well as by periodic changes with different cycling times. In contrast to the previously mentioned studies on periodic operation, an improvement of the time-averaged reaction rate could not have been observed. Nevertheless, a self-stabilizing feature was found with respect to inlet cycling, as the outlet amplitude was damped due to axial mass dispersion. This feature was found to be very valuable for safe and robust reactor operation under dynamic conditions, which is directly associated with the load flexibility. However, the author pointed out that unsteady state reaction kinetics, still missing in the literature, are of major importance to reproduce the reactor dynamics more accurately. A more detailed, cooled, low-temperature methanation reactor model with mass and heat recycle was used for hot-spot control by Li et al. [LYZ13]. The authors analyzed this reactor with a recycle loop in order to obtain further insights about process stability, response rapidity, and controllability. One major outcome was that the associated thermal feedback results in more sensitive system stability, while mass feedback may weaken this effect. Furthermore, an integral controller term turned out to be mandatory to ensure sufficient control precision without permanent system deviation.

In the context of demand-oriented use of renewable energy with combined power and synthetic natural gas (SNG) production, Rönsch et al. [Rön+14] clearly emphasized the importance of flexible plant operation. The most challenging unit was related to the temperature-sensitive adiabatic methanation unit fed with synthesis gas. Problems arise if the reactor is operated below 300 °C (due to CO induced nickel carbonyl formation) and above 600 °C (due to sintering and gum formation). Therefore, the authors adapted the recycle approach from Li et al. [LYZ13] to control the temperature and to evaluate load flexibility potentials for methanation. A dynamic plant model consisting of three simplified, CSTR-type reactors was used to investigate transient plant load changes under different recycle ratios. They concluded that the recycle strategy (ideally realized via adaptive control) is capable of reducing a potential catalyst overheating due to load changes, which consequently increases the load flexibility. However, additional auxiliary units are required and may become economically challenging for practical applications. Instead of feeding synthesis gas for methanation, Jürgensen et al. [Jür+15] considered biogas (mainly CH_4 and CO_2) from anaerobic digestion and hydrogen from renewable energy systems as feed composition. As the feed is enriched with CH_4, the diluted reactive gas avoids an excessive heat generation. Such a biogas upgrading strategy with cooled reactors was found to be feasible for SNG production at gas grid standards using a single reactor setup. The authors also concluded that further work has to be concentrated on the start-up and shut-down of the entire process chain to facilitate surplus electricity from renewable energy systems effectively.

Another option to reduce thermal sensitivities is given by three-phase methanation reactors. Lefebvre et al. [Lef+15] evaluated the performance of a slurry bubble column reactor under steady-state and dynamic scenarios. Also, focusing on the load flexibility of these reactor types, load changes were performed via inlet gas velocity step changes. The authors stated that the reactor time constant depends only on the final gas velocity, while the reactor temperature profile remained isothermal during all operations. However, further investigations are needed for upscaled systems.

A very comprehensive overview of the flexible operation of FBRs was elaborated by Iglesias González et al. [IES16]. They proposed the catalytic FBR for the hydrogenation of CO_2 to gaseous hydrocarbons on a large scale under flexible load conditions. Among the variety of possible syntheses, methanol, dimethyl ether (DME), and methanation synthesis were identified as relatively simple reaction routes under flexible conditions due to the high and robust selectivity of the desired product with limited sensitivity towards temperature variations and catalyst stability. In order to control such often strongly exothermic synthesis steps under variable loads, the recycle concept and a non-adiabatic reactor was found to be the most attractive technical solution. Furthermore, characteristic time scales of physicochemical processes on the reactor and the catalyst level (see Fig. 1.3) were analyzed to show their effect on the dynamic response of the system.

However, auxiliary units attached to the reactor were not considered on the dynamic response. With this, the authors concluded that flexible operation would lead to an increase in reactor size (higher investment cost) and/or in the power demand for the recycle compressor (higher operational cost). Another drawback may correspond to an

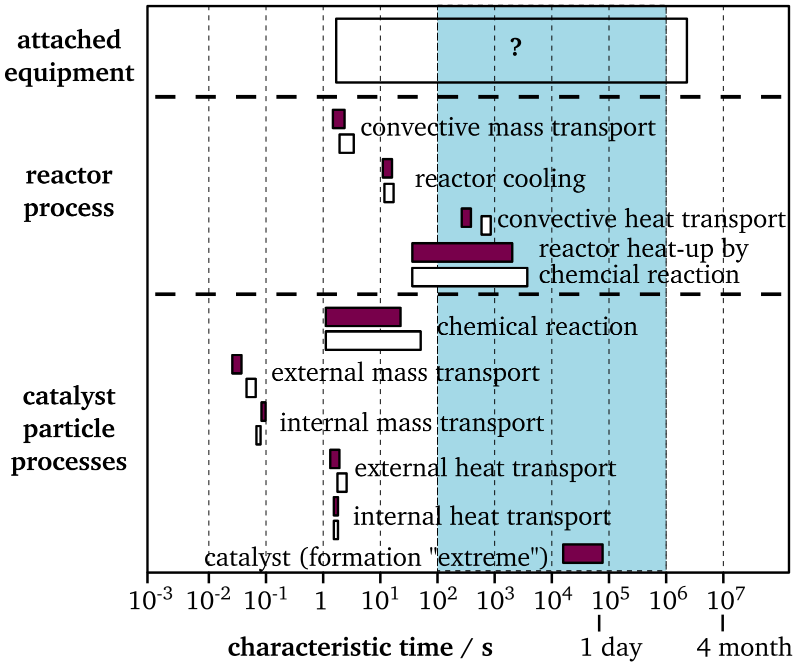

Fig. 1.3.: Characteristic times for maximum (purple, 100 %) and minimum reactor load (white, 70 %) at the catalyst bed for z=0 and z=L calculated for exemplary reactor dimensions, large blue area: expected characteristic times for variation in inlet conditions (assumption), adapted from [IES16].

accumulation of impurities, which might be expected from catalyst deactivating sulfur components when an upstream anaerobic digestion is involved [SWH18]. Nevertheless, such a configuration would pay off if the investment costs for chemical buffers exceed the additional costs for enhanced flexibility. Consequently, future economic investigations are proposed to obtain more substantial data on this aspect. Building up on the recycle reactor concept, Matthischke et al. [Mat+16] underpinned this approach with experimental results and additionally found that the reactor behavior is independent of the load change velocity in the investigated range. In extension to this, a model-based investigation compared adiabatic and cooled recycle reactor arrangements and claimed the latter to be less flexible due to an increased sensitivity to load changes [MRG18].

Apart from the recycle reactor approach, Bremer et al. [BRS17] (author of this work) reconsidered the concept of optimal coolant control as another, yet computationally demanding, option to ensure moderate temperatures of the fixed catalytic bed for stoichiometric feed ratios of hydrogen and carbon dioxide. The authors assumed that there exists a certain transient control strategy that allows manipulating the reaction zone such that hot-spot formation is mitigated. Based on a rigorous, dynamic, two-dimensional reactor model for methanation in combination with a computationally demanding dynamic optimization, a control trajectory was found that fulfilled the desired needs. In a continuing work, Bremer and Sundmacher [BS19] deducted that the used control approach stabilized the reactive zone so that operating points became accessible within unstable operating regimes. This finding, in particular, is one major aspect of the underlying dissertation. Another aspect points to the computationally demanding calculations as one bottleneck of such investigations. Therefore, Bremer et al. [Bre+17] additionally proposed proper orthogonal decomposition and discrete empirical interpolation (POD-DEIM) as one possible mathematical tool for complexity reduction of rigorous reactor models. In this study, the authors investigated reactor load changes as well as entire start-up simulations concerning their potential for model complexity reduction. Since this problem class is known to be mathematically well structured due to the spatial and temporal PDE discretization, the proposed method was able to reduce the computational effort by at least one order of magnitude. This speed-up is, in particular, promising for online applications, as the afore-mentioned NMPC strategies, but also to assist further time-consuming dynamic studies.

Also focusing on detailed, multi-scale, model-based analyses for CO_2 methanation, Try et al. [Try+17] analyzed conventional dynamic features like wrong-way behavior, traveling hot-spots, state-space multiplicity, and over/undershooting. The authors also emphasized the importance of thermal inertia/heat capacity for dynamic considerations.

Long-term dynamic investigations also have been the objective of ongoing research. Sun and Simakov [SS17] analyzed the deactivation of a Ni/Al_2O_3 catalyst for CO_2

methanation due to coking caused by CH_4 cracking at elevated temperatures. Therefore, a reactor model with additional deactivation kinetics for the catalyst was used to predict the catalytic activity over time. They found a substantial performance decline of over 80 % after 10,000 h time on stream (TOS). Significantly faster deactivation times of approximately 3000 min TOS for nickel-based methanation catalysts are reported by the experimental investigations of Schüler et al. [SWH18]. The authors fed an operating reactor with 5 ppm H_2S and observed poisoning effects indirectly by capturing moving temperature fronts of constant velocity with thermography. With this, a model for catalyst poisoning was correlated to the hydrogen uptake capacity at room temperature.

1.2 Scope of this work

In summary, chemical reactors certainly have earned a place among the most complex technical systems known in engineering. The simultaneous interplay of different physicochemical effects on various scales has stimulated the interest of research and industry for many decades. As a result, chemical reactors are fundamentally well understood, which is sufficient for common applications in the chemical industry. However, the increasing relevance for dynamic and flexible reactor operation is seen as a new driving force for reevaluating more advanced reactor designs and operating strategies. The present work shall support this progress by revising the current state of knowledge, making use of modern numerical and experimental tools, as well as delivering practical relevance for transient reactor operation. These aspects are addressed from different viewpoints in the following five chapters.

Chapter 2 reflects the technological perspective, providing more details on PtX with particular focus on the exothermic carbon dioxide methanation. Thermodynamics and reaction kinetics are discussed in order to identify fundamental and catalytic limits for advanced reactor operation. For long-term operation, the occurrence of possible side reactions as well as catalyst degradation is evaluated according to the literature. Furthermore, state-of-the-art process concepts for methanation are evaluated and compared with respect to future requirements. As a result, heat management turns out to be the prime objective for the following steady and dynamic reactor operating concepts.

Chapter 3 considers the fundamental perspective on conventional but also unconventional operating ranges of non-isothermal fixed-bed reactors. By analyzing all relevant reactor scales and phases, mass and energy-based sensitivities are identified as key characteristics for stability, multiplicity, and uniqueness. So far, the quantification of these characteristics is primarily accessible for ideal reactor concepts with zero or infinite back-mixing. Based on a CSTR cascade modeling approach, this chapter derives novel criteria for stability and multiplicity applicable to real reactors with finite back-mixing.

Furthermore, the connection to other reactor features such as runaway and parametric sensitivity is demonstrated and exemplified for realistic conditions. The new criteria indicate that thermo-kinetic multiplicities induced by back-mixing remain relevant even for high Bodenstein numbers. In consequence, generally accepted back-mixing criteria (e.g., Mears' criterion) appear insufficient for real non-isothermal reactors. The criteria derived in this chapter are applicable to any exothermic reaction and reactors at any scale. Ignoring uniqueness and multiplicity would disregard a broad operating range and thus a substantial potential for reactor flexibility. In addition, Chapter 3 also presents a detailed dynamic fixed-bed reactor model. This model considers an industrial-scale tubular reactor geometry surrounded by a cooling channel, detailed heat transport correlations, as well as a quasi-stationary particle model.

Chapter 4 serves as a reactor simulation study that performs rigorous numerical investigations based on the dynamic model proposed in Chapter 3. In comparison to the results obtained from the CSTR cascade model, these studies are much closer to reality by incorporating further details at catalyst and reactor level. Therefore, the identified reactor concepts from Chapter 2 are analyzed with respect to the expected operating range, including the occurrence of state-space multiplicity. Stabilizing control is found as a very promising yet unexploited heat management approach, which allows for moderating the reactive zone (hot-spot) via adaptive coolant temperature variations. This way, unconventional operating points in regions of steady-state multiplicity are attainable and enable reduced catalyst temperatures ($< 500\,^{\circ}\mathrm{C}$) while maintaining elevated reactor performance. When considering these additional operating points, a broader and more flexible operation of industrial reactors becomes feasible. Systematic sensitivity studies regarding relevant reactor and operating parameters indicate that a robust technical implementation of these operating points is possible.

Chapter 5 outlines how advanced control concepts enable the identification of realistic reactor operating policies that ensure fast and safe transitions between different reactor loads. While focusing on the transition from a reactor off-state to an operating point that is in line with thermal restrictions, it is shown that the observed unconventional operating points from Chapter 4 are attainable without hazardous temperature excursions. The applied methodology for optimal control is found to be computationally demanding, but in combination with a moving horizon strategy, the problem becomes feasible. In accordance with the previous literature review, the results confirmed that reactors are predestined for control purposes as they offer improved performance in closed-loop settings. Hence, advanced control concepts appear to be an essential link for making future reactors more flexible.

Chapter 6 reflects the experimental perspective and showcases a novel pilot plant concept which has been developed in the course of this work. The essential unit of the experimental setup is a reactor whose design is developed entirely based on the preliminary numerical results. Furthermore, the setup offers novel opportunities for studying the temperature field in real-time, and a unique heat transfer unit enables fast interactions with the reactor via coolant temperature changes. Steady-state experiments are conducted to capture significant reactor states which are used for model validation and adjustment. Finally, the adjusted model is used to compare the experimental and computational dynamic reactor behavior with respect to cool-down perturbation experiments. Although a slight readjustment of the model is necessary, the model proves to be well suited for rigorous dynamic studies, and thus underpins the relevance of the results from Chapters 4 and 5. Furthermore, the novel criteria for stability and multiplicity developed in Chapter 3 are evaluated for selected experimental conditions. The criteria predict reasonable relations between mass and energy-based sensitivities, which is confirmed due to observed non-intuitive temperature excursions after cool-down perturbation.

2

Carbon Dioxide Methanation

Chapter 1 introduced various PtX concepts that are currently under investigation. Among the manifold of selection criteria for each PtX pathway, flexibility is the major aspect addressed in this work. Generally speaking, the simpler the process route, the more flexible it can be used. Under this aspect, the hydrogen production path with only one process step (electrolysis) can be a very flexible option for realizing PtX [Leh+14; Göt+16]. However, hydrogen has the lowest energy density ($1\,\mathrm{kWh}_{\mathrm{LHV}} \mathrel{\widehat{=}} 0.3\,\mathrm{Nm}^3_{\mathrm{H2}} \mathrel{\widehat{=}} 0.1\,\mathrm{Nm}^3_{\mathrm{CH4}} \mathrel{\widehat{=}} 0.2\,\mathrm{NL}_{\mathrm{MeOH}}$), which needs to be compensated with energy-intensive compression (e.g., up to 700 bar for fuel cell vehicles) or liquefaction (liquid at temperatures below 21.15 K). Furthermore, the infrastructure for large-scale hydrogen storage, distribution, and usage is currently unavailable and requires significant investments [Sto+13; BS16]. For this reason, hydrogen might be further converted into chemicals that have existing or low-cost supply chains. However, this additional conversion step essentially determines the overall PtX process flexibility and, thus, the necessity for hydrogen buffers. If hydrogen storage is no limiting factor (e.g., due to available underground caverns), then there is no particular need for a flexible subsequent conversion step. Without underground hydrogen storage, buffer tanks filled with highly pressurized hydrogen (usually up to 300 bar) would be a possible but costly alternative [Göt+16]. Avoiding or minimizing the hydrogen storage capacity is certainly recommended for mid and small-size PtX plants but requires subsequent conversion steps to be sufficiently flexible.

Methanol production from hydrogen also suffers from the obstacle of an unavailable infrastructure, but its liquid form is very beneficial for storage, distribution, and usage. Nevertheless, the additional step from hydrogen to methanol requires several high-pressure reactor stages (typically 50-100 bar), recycles, and further upstream, as well as downstream processes (e.g., distillation) [MMZ19; URS19]. This makes methanol production rather challenging to operate in a flexible manner. There are attempts towards methanol conversion within one single reactor stage [BU14; Tid+13], but considering the required high process pressures of up to 950 bar and the corresponding heat generation, an industrial relevance for flexible methanol production is still questionable. Further difficulties for flexible production might also arise, due to activity changes of industrial methanol catalysts under varying gas loads and compositions [Muh+94; Sei+18]. Similarly, PtL fuel production from hydrogen also involves several process steps (e.g., reverse water gas shift or Fischer-Tropsch), which restrict an overall flexible fuel production and, thus, require upstream hydrogen buffers.

Methane synthesis from hydrogen via catalytic *CO_2 methanation* is favorable due to already existing infrastructures for natural gas storage and supply. For instance, Germany has already a total capacity of about 200 TWh by pore and cavern storages and a fully developed natural gas grid [VDI19], which can be directly used for synthetic methane (SNG). Furthermore, SNG can be used already for gas power plants, vehicles, and heating. However, CO_2 methanation processes are yet barely implemented on a commercial scale. Only CO methanation with hydrogen is already in use since 1910 for feed gas cleaning for ammonia synthesis and later for fuel cell applications as well as coal gasification. Comprehensive reviews on CO and CO_2 methanation are elaborated by Kopyscinski et al. [KSB10], Götz et al. [Göt+16], and Rönsch et al. [Rön+16b]. Due to growing interests in PtX technologies for energy storage over the last decade, CO_2 methanation became increasingly important in science and industry. Corresponding PtX process routes with CO_2 methanation are illustrated in Fig. 2.1.

Fig. 2.1 (a) shows the probably most often considered process assembly for Power-to-Methane (PtM). Renewable electricity is initially converted into hydrogen (via electrolysis) and afterwards chemically bonded to carbon (via catalytic CO_2 methanation). The obtained methane is then fed into the natural gas network for distribution. The required carbon dioxide might be taken from biogas production, the atmosphere [Kei09; Goe+12; DA20], or CO_2-intensive industries (e.g., cement industry) [Göt+16]. Fig. 2.1 also highlights process parts that are capable of flexible operation. The conventional assembly in Fig. 2.1 (a) prefers to operate CO_2 methanation in a continuous manner, which requires intermediate storage tanks for hydrogen and water to buffer volatile hydrogen production. Considering, that CO_2 methanation processes are often equipped with several reactor stages and intercoolers [ERS15; URS19], this process design would undoubtedly be the most reasonable. However, by integrating CO_2 methanation into the flexible process part (Fig. 2.1 (b)), one could replace hydrogen and water storages with one storage for carbon dioxide. This is very beneficial because the production of one standard cubic meter methane requires four standard cubic meter hydrogen and only one standard cubic meter carbon dioxide. Thus, storing carbon dioxide allows for more compact process designs, as well as lower investment and operating costs. Another process route that might be interesting for decentralized applications is shown in Fig. 2.1 (c). Here the natural gas grid is replaced with a separate storage tank for methane. When discharging, carbon dioxide is captured from the exhaust of a power station fueled with oxygen and methane. With this *carbon cycle*, energy is ideally charged and discharged neither with carbon dioxide emissions nor with external carbon dioxide supply. Although this concept enables grid-independent electricity storage, it requires several storage tanks for water, oxygen, carbon dioxide, and methane. Besides, a further hydrogen storage tank is required, if the methanation process is not sufficiently flexible.

Although flexible methanation offers several advantages, research activities in this direction just started to evolve within the last six years. First investigations mainly

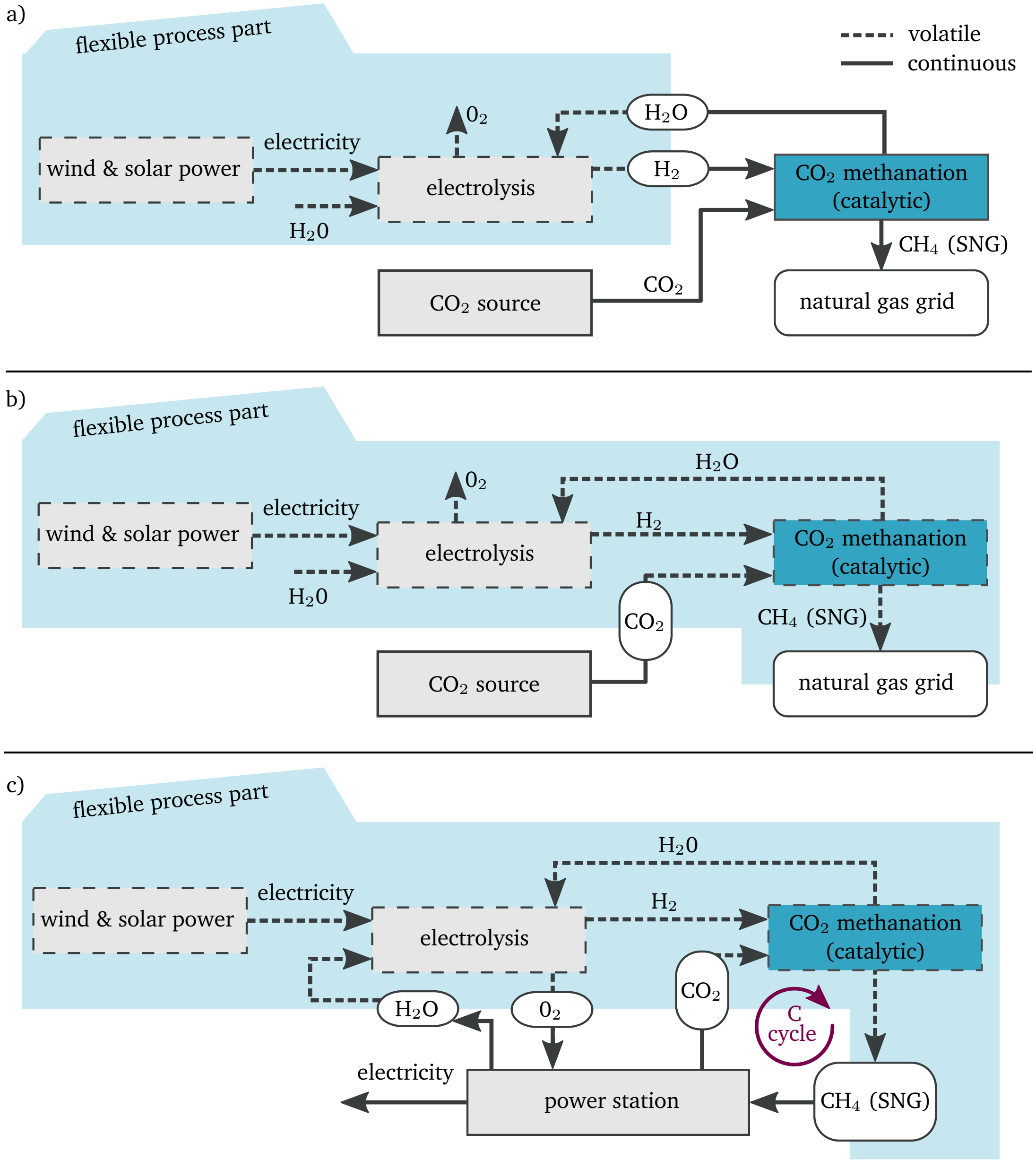
a)
flexible process part
volatile
continuous
wind & solar power
electricity
O_2
electrolysis
H_2O
H_2O
H_2
CO_2 methanation (catalytic)
CH_4 (SNG)
CO_2 source
CO_2
natural gas grid
b)
flexible process part
wind & solar power
electricity
O_2
H_2O
electrolysis
H_2
H_2O
CO_2 methanation (catalytic)
CO_2
CH_4 (SNG)
CO_2 source
natural gas grid
c)
flexible process part
wind & solar power
electricity
H_2O
electrolysis
H_2
CO_2 methanation (catalytic)
CO_2
H_2O
O_2
C cycle
electricity
power station
CH_4 (SNG)

Fig. 2.1.: Methane-based PtX process routes with flexible (dashed) and continuous (solid) processes and fluxes, storage tanks for intermediates with capacities > 1 d.

cover load changes and start-up behavior [Mat+16; BRS17; Bre+17; Fac+18; MRG18; KWT18] but also periodic operations [Güt13; Kre+19]. The major challenge for CO_2 methanation is related to the high exothermicity of the reaction, which is typically solved with several reactor stages, recycles, and intercoolers [Leh+14; Göt+16]. Similar to methanol synthesis, such complex processes are not favorable for flexible operation. Under usual technical pressures, however, methane synthesis from hydrogen and carbon dioxide is thermodynamically more favorable than methanol synthesis (see Section 2.1), which offers more possibilities to design simpler and more flexible processes (e.g., by process designs with fewer reactor stages or less separation effort). More details on thermodynamic aspects are addressed in the following section.

2.1 Thermodynamics and Reaction Kinetics

The main reaction for CO_2 methanation was firstly mentioned by Sabatier and Senderens [SS02] in 1902 and reads:

$$\mathrm{CO_2} + 4\,\mathrm{H_2} \rightleftharpoons \mathrm{CH_4} + 2\,\mathrm{H_2O}, \qquad \Delta_R \tilde{H}^0 = -164.9\,\mathrm{kJ\,mol^{-1}}. \tag{2.1}$$

This reaction is one of several possibilities to activate the carbon dioxide. Further reactions are, for instance, CO_2 dissociation, dry reforming, reverse water-gas shift (RWGS), and methanol synthesis. However, under these reactions, CO_2 methanation is thermodynamically the most favored, as it exhibits the lowest Gibbs free energy of reaction in a temperature range from ambient to 900 K ($\Delta_R \tilde{G}^0 = -142$ kJ mol^{-1}) [Wen18]. As depicted in Eq. (2.1), CO_2 methanation also features a strong exothermicity, such that lower temperatures shift the chemical equilibrium to the product side. This fact is supported by Fig. 2.2, which shows the result of chemical equilibrium calculations assuming stoichiometric feed over a wide temperature range and for technical relevant pressures (thermochemistry data taken from [LM97; Hay17]).

At temperatures above 800 K, the conversion of CO_2 significantly decreases, and CO formation becomes thermodynamically favored. Due to the reduction of the total number of moles in Eq. (2.1), higher pressures are able to compensate for the conversion drop to

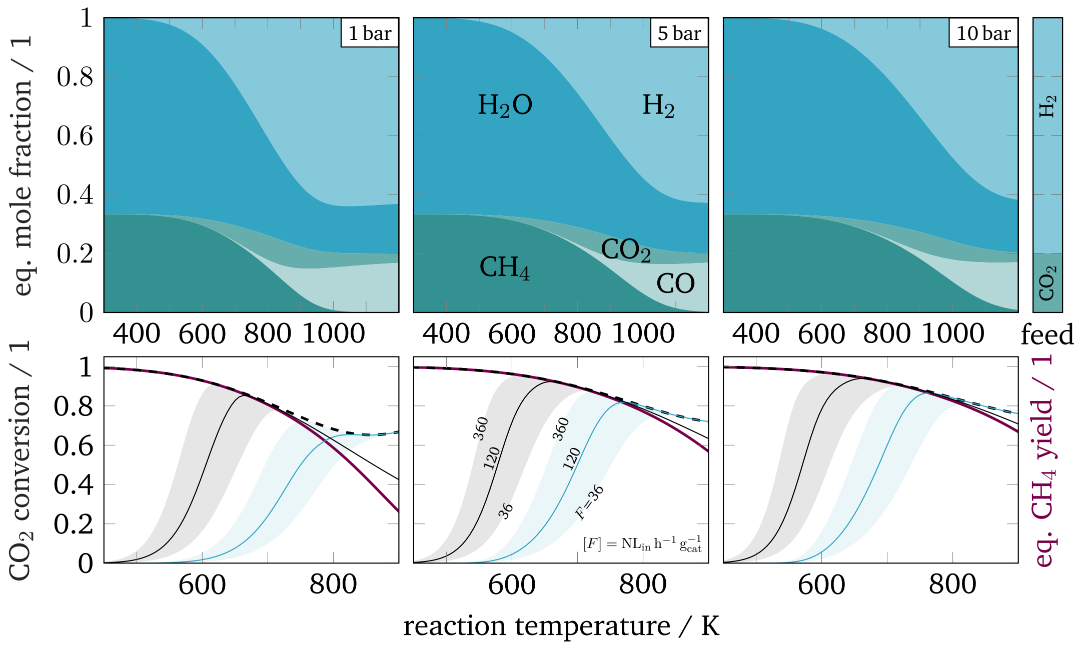

Fig. 2.2.: Mole fractions at chemical equilibrium (top row) and kinetic conversion (bottom row) over temperature for pure, stoichiometric feed ($H_2/CO_2 = 4$) at different pressures and flows, computed via Gibbs-free-energy minimization, kinetic model according to Koschany et al. [KSH16] (——) and Xu and Froment [XF89] (——), equilibrium CO_2 conversion (- - - -), equilibrium CH_4 yield (——).

some extent. Thus, reaction temperatures above 800 K should be avoided if high product gas purities are desired. Although lower temperatures would thermodynamically support almost complete conversion, the reaction at these low temperatures remains kinetically limited for most known catalysts. Among the relevant catalyst materials (nickel, ruthenium, iron, cobalt), nickel is highly active and the most selective catalyst [Hwa+12; Rön+16b]. Furthermore, nickel is very appealing for industrial applications due to its comparatively low price. Consequently, this work mainly relies on a recently published kinetic expression for $\mathrm{Ni/Al(O_x)}$ by Koschany et al. [KSH16], but also considers older, more often referred to expressions proposed by Xu and Froment [XF89]. The latter exhibit a significantly lower activity for carbon dioxide methanation, since it was performed with a steam methane reforming (SMR) catalyst, whereas Koschany et al. [KSH16] refer to a state-of-the-art methanation catalyst. This performance difference is clearly shown in the bottom row of Fig. 2.2. Here, carbon dioxide conversion $X_{\mathrm{CO_2}}$ and methane yield $Y_{\mathrm{CH_4}}$ are considered as

$$X_{\mathrm{CO_2}} = \frac{\dot{n}_{\mathrm{CO_2,feed}} - \dot{n}_{\mathrm{CO_2}}}{\dot{n}_{\mathrm{CO_2,feed}}}, \qquad Y_{\mathrm{CH_4}} = \frac{\dot{n}_{\mathrm{CH_4}} - \dot{n}_{\mathrm{CH_4,feed}}}{\dot{n}_{\mathrm{CO_2,feed}}},$$

where the molar flows $\dot{n}_{\mathrm{CO_2}}$ and $\dot{n}_{\mathrm{CH_4}}$ are result of kinetic as well as equilibrium calculations. As seen in Fig. 2.2 the kinetic model from Koschany et al. [KSH16] differs significantly at temperatures above 700 K and shows higher methane yields due to the exclusion of carbon monoxide. Xu and Froment [XF89], in contrast, considered the CO methanation and RWGS reaction (Eqs. (2.2) and (2.3)) to account for carbon monoxide. This was certainly motivated by the lower activity, which achieves sufficient conversion only at higher temperatures where CO formation becomes relevant.

$$\mathrm{CO} + 3\,\mathrm{H_2} \rightleftharpoons \mathrm{CH_4} + \mathrm{H_2O}, \qquad \Delta_R\tilde{H}^0 = -206.3\ \mathrm{kJ\,mol^{-1}}, \tag{2.2}$$

$$\mathrm{CO_2} + \mathrm{H_2} \rightleftharpoons \mathrm{CO} + \mathrm{H_2O}, \qquad \Delta_R\tilde{H}^0 = 41.1\ \mathrm{kJ\,mol^{-1}}. \tag{2.3}$$

Although both reactions certainly occur, they are not favored at elevated pressures and mean bed temperatures below 800 K. Further details about the rate equations are given in Section 3.2.1. A more detailed analysis on thermodynamic limitations is comprehensively illustrated by Gao et al. [Gao+12], who also showed possible amounts of solid carbon under $\mathrm{CO_2}$ excess. More detailed calculations on that are presented by Kiewidt [Kie17], who identified considerable amounts of solid carbon at feed ratios $\mathrm{H_2/CO_2} < 3.2$.

Another scenario, where solid carbon formation could become an issue, is related to biogas upgrading [Jür+15]. After removing small amounts of impurities (e.g., nitrogen, water, oxygen, ammonia, and hydrogen sulfide) biogas typically consists of 50 - 70 vol% of methane and 30 - 50 vol% of carbon dioxide [Moh+12]. To save efforts for costly $\mathrm{CO_2}$ separation, this mixture is enriched with hydrogen (ensuring $\mathrm{H_2/CO_2} = 4$) and then fed to a $\mathrm{CO_2}$ methanation reactor to convert the excess carbon dioxide. Similarly, but with lower carbon dioxide concentrations, such procedures are certainly conceivable for gas cleaning in the oil and gas industry, as it is already done with carbon monoxide impurities. Fig. 2.3 illustrates these cases: biogas with high carbon dioxide content (top), biogas with low carbon dioxide content (center), gas cleaning with very low carbon dioxide content (bottom).

Fig. 2.3 indicates that at high temperatures (> 600 K) the risk of carbon formation increases with growing methane content. Higher pressures or water injections can minimize the risk, but also increase the process complexity and necessary separation efforts. At lower temperatures (< 600 K) carbon formation is less likely but demands for a highly active catalyst and appropriate heat management.

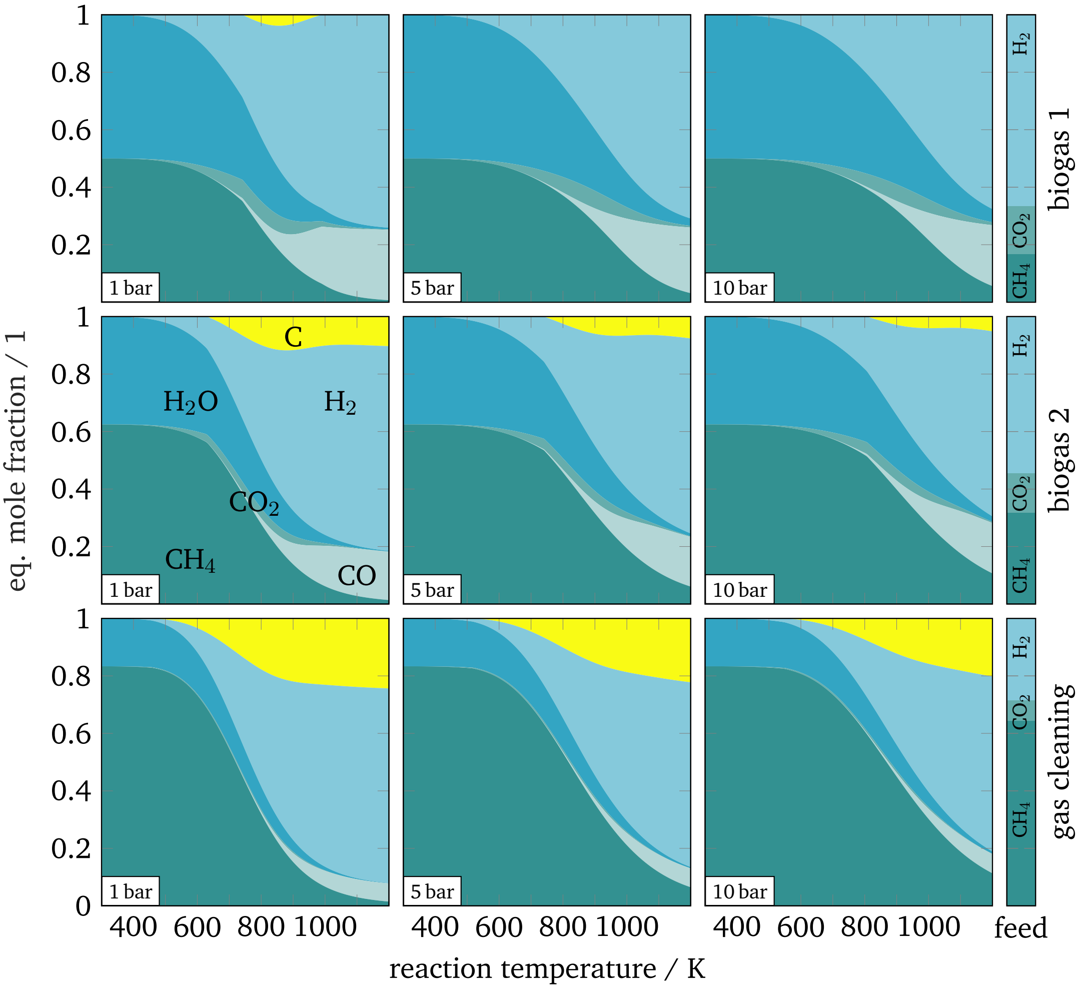

Fig. 2.3.: Mole fractions at chemical equilibrium over temperature at different pressures, CO_2/CH_4 feed ratios: 0.5 (top), 0.3 (center), 0.1 (bottom), H_2/CO_2 feed ratio: 4 (all), computed via Gibbs-free-energy minimization.

In order to assess the temperature increase due to the exothermicity of the reaction, the adiabatic temperature rise (ATR) is considered as an appropriate worst-case estimate. The ATR is defined as

$$\Delta T_{\mathrm{ad}} = \frac{c_{\mathrm{CO_2}}\,(-\Delta_R \tilde{H})}{\rho_{\mathrm{gas}}\, c_{p,\mathrm{gas}}} = \frac{w_{\mathrm{CO_2}}\,(-\Delta_R \tilde{H})}{M_{\mathrm{CO_2}}\, c_{p,\mathrm{gas}}}, \tag{2.4}$$

and exemplary evaluated for standard, stoichiometric feed conditions

$$\Delta T^0_{\mathrm{ad}} = \frac{0.845\,(-164900\,\mathrm{J\,mol^{-1}})}{0.044\,\mathrm{kg\,mol^{-1}}\,2950\,\mathrm{J\,kg^{-1}\,K^{-1}}} = 1073.5\,\mathrm{K}.$$

Looking at Eq. (2.4) reveals that the ATR is pressure-independent, since $\Delta_R \tilde{H}$ and $c_{p,\mathrm{gas}}$ depend exclusively on temperature under ideal gas conditions. Although a higher pressure leads to more reactants and thus more heat generation, the gas heat capacity increases simultaneously and compensates for a further temperature rise. The temperature dependence of the ATR is rather negligible as illustrated in Fig. 2.4 for pure stoichiometric as well as for diluted feeds.

Combining these high temperatures with sensitive heterogeneous catalysts requires improved heat management concepts for technical implementations. In addition to possible carbon formation [Jür+15] or rupture of tube materials [Bri+05], commercial low-active nickel catalysts deactivate significantly at temperatures above 900 K due to thermal degradation (sintering) of the active nickel sites [Bar01; Zha+13; NWS13]. Sintering of the active metal sites leads to a loss of surface area and, thus, a reduction of catalyst activity. An increase in catalytic activity, usually achieved by higher nickel contents, already leads to thermal degradation at temperatures of 773 K. [Hwa+12; Aba+16; Rön+16b].

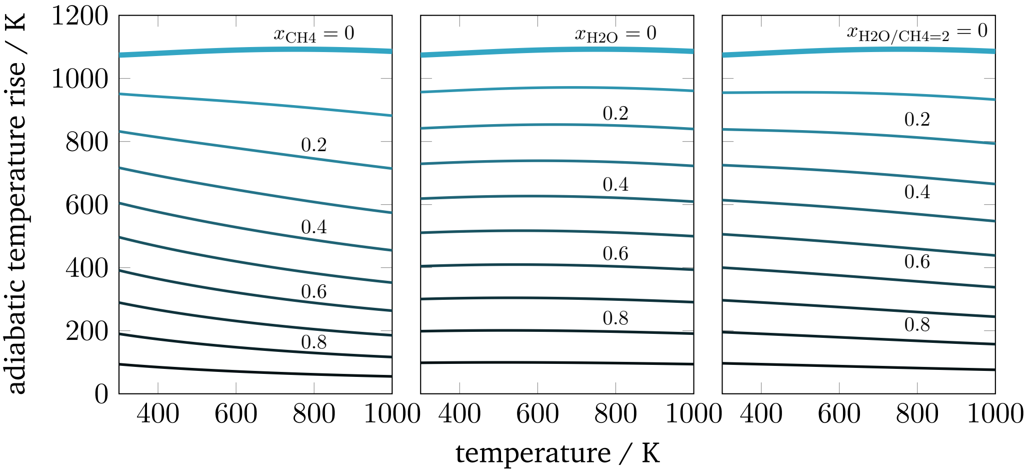

Fig. 2.4.: Adiabatic temperature rise of CO_2 methanation for various temperatures and for stoichiometric feed ($H_2/CO_2 = 4$) diluted with different methane (left), water (center), and product gas (right) fractions.

Besides sintering and coke deposition, further catalyst deactivation mechanisms in fixed-bed reactors are poisoning by sulfur components and nickel carbonyl formation in the presence of carbon monoxide (at temperatures below 500 K) [Mia+16; Rön+16b]. In case of CO_2 methanation, the relevant temperatures for carbonyl and CO formation (see Fig. 2.2) do not overlap, which means that carbonyl formation is rather unlikely for CO_2 methanation. Carbonyl formation might become relevant if CO_2 dissociates at the metal-support interface to adsorbed CO*, following the dissociative mechanism as discussed by [Mia+16]. However, no clear evidence for carbonyl formation at CO_2 methanation conditions could have been found in the literature yet.

To sum up this section, the reactor temperature is the most relevant design parameter for CO_2 methanation reactor and process development. The next section will, therefore, give a brief overview on state-of-the-art CO_2 methanation process concepts.

2.2 Methanation Process Concepts

Today, the few commercial CO_2 methanation plants are mainly used for small- and mid-scale SNG production in the context of PtM [Rön+16b]. Thema et al. [TBS19] evaluated a total amount of 153 PtG projects (active and inactive) in 22 countries from 1993 to 2020. Therein, 30 projects involve catalytic CO_2 methanation and utilize in total 39.05 MW electricity (corresponding to the upstream electrolysis). Thus, the average methanation plant operates at an electrical power between 1-2 MW. The largest installed plants are able to utilize up to 6 MW electricity ($\sim$1440 $Nm^3\,h^{-1}$ hydrogen) at the present (E-gas-plant, Werlte, Germany) and up to 10 MW ($\sim$2400 $Nm^3\,h^{-1}$ hydrogen) in the near future (MeGa-stoRE Com 1, Denmark). A PtM plant size of 10 MW corresponds to a SNG production of 480 $Nm^3\,h^{-1}$ (assuming full hydrogen conversion), which is significantly lower than the SNG production capacity of 100’000-700’000 $Nm^3\,h^{-1}$ in commercial CO methanation plants as build in China, for instance (with gasified coal as feed) [Rön+16b]. Considering that the technical realization for steady CO methanation is almost directly applicable for steady CO_2 methanation, PtM scale-up is in principle not limited by the methanation unit.

One of the leading large-scale CO (or syngas) methanation technologies is the Topsøe Recycle Energy-efficient Methanation Process (TREMP) from Haldor Topsøe. As illustrated in Fig. 2.5, the TREMP consists of three adiabatic fixed-bed reactor stages with intercoolers after each stage and recycle after the first stage. The most productive first stage provides approximately 80 % of the overall process conversion. However, this high load also results in high temperatures, which require resilient and, thus, low-active catalysts (low nickel loading). The last two stages are mainly used to convert the remaining reactants further. Due to less heat generation and lower temperatures, the last reactor stage can be filled with high-active catalysts (high nickel loading). A detailed analysis of this methanation technology goes back to Höhlein et al. [HMR81],

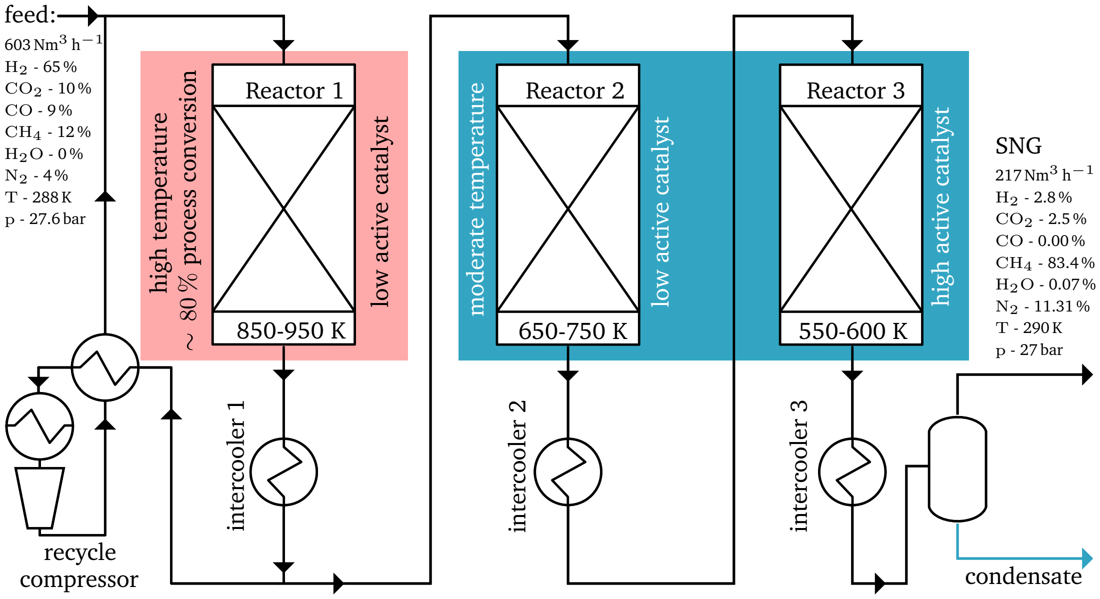
feed:
603 Nm³ h⁻¹
H₂ - 65 %
CO₂ - 10 %
CO - 9 %
CH₄ - 12 %
H₂O - 0 %
N₂ - 4 %
T - 288 K
p - 27.6 bar
high temperature
~ 80 % process conversion
Reactor 1
850-950 K
low active catalyst
moderate temperature
Reactor 2
650-750 K
low active catalyst
Reactor 3
550-600 K
high active catalyst
SNG
217 Nm³ h⁻¹
H₂ - 2.8 %
CO₂ - 2.5 %
CO - 0.00 %
CH₄ - 83.4 %
H₂O - 0.07 %
N₂ - 11.31 %
T - 290 K
p - 27 bar
intercooler 1
intercooler 2
intercooler 3
recycle
compressor
condensate

Fig. 2.5.: Commercial SNG TREMP^{TM} technology flow-sheet, adapted from [HMR81; Höh+85; Bad+11]

who worked with a syngas feed of 603 $Nm^3\,h^{-1}$ and a recycle flow of 914 $Nm^3\,h^{-1}$. This system was designed for long-distance nuclear energy transport. The nickel catalysts used at that time are state-of-the-art and still available in Haldor Topsøe's product portfolio. The intercooling stages are used to co-generate superheated steam, which is essential for the process efficiency and profitability ($\Delta_R H^0 / \mathrm{HHV}_{\mathrm{CH4}} \approx 0.17$). Other large-scale methanation technologies (e.g., Lurgi methanation, Vestas, HICOM, RPM) differ mainly in the number of reactor stages, intercoolers, water separation units and the positions for feed injection [Kop10; KK18].

Switching the reactor concept from adiabatic to polytropic (e.g., by cooled multi-tubular bundle reactors) leads to fewer reactor stages, and thus lower catalyst volumes. This is reflected by the reaction pathways in Fig. 2.6. Nevertheless, polytropic reactors are more difficult to construct and maintain (e.g., in case of catalyst replacements), which is in particular difficult for process scale-up. Hence, the performance benefit must outweigh the increased complexity of the reactor. In the context of gas-to-liquids (GtL), Fischer-Tropsch synthesis is an example of the successful use of multi-tubular reactors on a large scale [WNT12]. However, for large-scale CO or syngas methanation, only a few applications with cooled reactors have been reported (e.g., Linde SNG process) [KSB10].

Polytropic reactors without gas recycling are preferably used for small- and mid-scale methanation. For instance, the mentioned 6 MW PtM plant (E-gas-plant, Werlte, Germany) uses multi-tubular reactors cooled with molten salt [BS16]. Gruber et al. [Gru+18] reported a highly efficient PtM setup with 10 kW electrolyzer and two water/steam-cooled multi-tubular reactors in series with intermediate and down-stream water separation. Due to the significant heat generation of undiluted reactants, however,

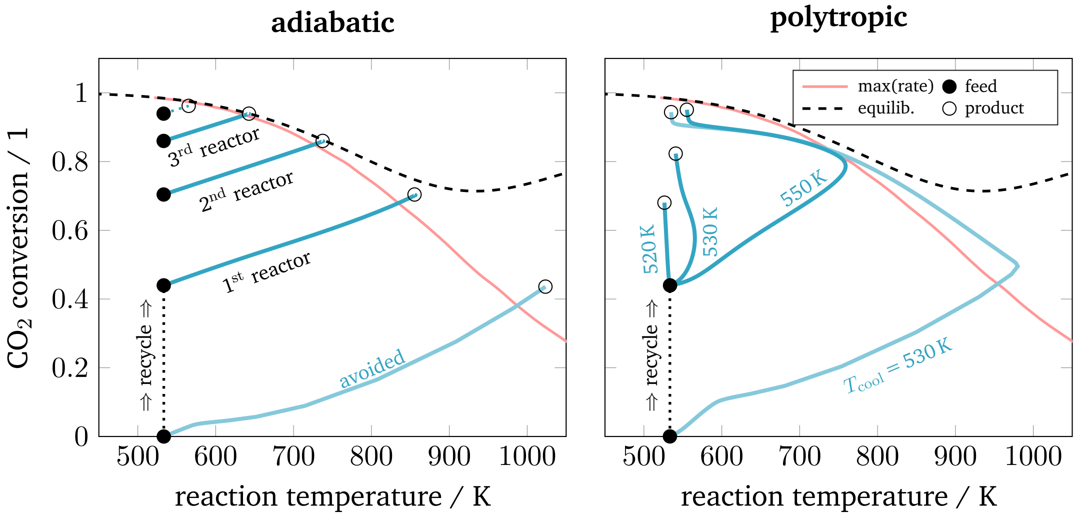

Fig. 2.6.: State-space diagram of exemplary reaction pathways in adiabatic and polytropic reactors, reactor length: 2 m, pressure: 5 bar, reaction: CO_2 methanation according to Koschany et al. [KSH16] with undiluted, stoichiometric feeds.

distinct hot-spots are typically observed in polytropic reactors (see Fig. 2.6). These hot-spots are crucial for the reactor performance (e.g., conversion, selectivity, catalyst lifetime, space-time yield - see Section 2.1). Hence, the required heat management is one primary objective of ongoing research for small- and mid-scale methanation applications and becomes increasingly important for flexible reactor operation [Rön+16a; Göt+16].

A common approach for improved heat management is to develop reactor concepts with intensified heat transfer. This is achieved by increasing the ratio between heat removal and reactive heat generation. Therefore increasing cooling surfaces or heat conductivities within the fixed-bed is one option and refers to micro-reactors, honeycomb reactors, monolithic reactors, plate reactors or catalytic wall reactors [Sch15; Sud+10; Tro+04; Bro+07; BMP17; Bia+13; Kie17]. In contrast, fluidized-bed reactors and multi-phase reactors aim at better heat dissipation by catalyst mixing in gaseous or liquid phases. In terms of heat management, these *intensified reactor* concepts (see Fig. 2.7 left) have been proven to be superior to industrial-scale tube bundle reactors. However, this advantage comes at a cost, i.e., lower throughputs and higher investment

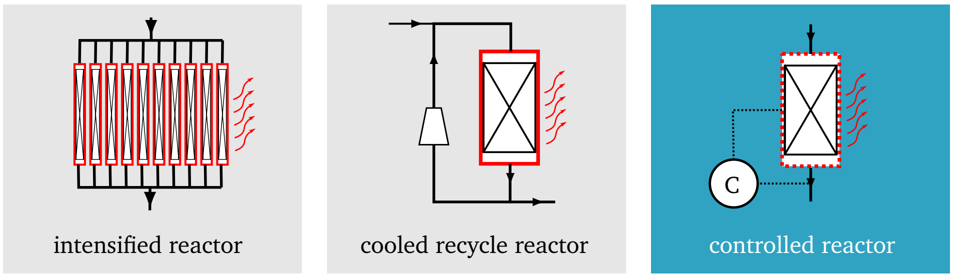
intensified reactor

cooled recycle reactor

controlled reactor

Fig. 2.7.: Polytropic reactor concepts for improved heat management, the main concept examined in this work is highlighted in blue.

costs. Matthischke et al. [Mat+16] proposed a more convenient approach for heat management during dynamic operation. They used the *recycle reactor* concept (see Fig. 2.7 center) in their experimental setup to effectively reduce the heat generation while increasing the reactor's flexibility for load changes. Nevertheless, disadvantages can appear due to thermal and material feedback, which might lead to instabilities during load transitions. Apart from that, lower space-time-yields and additional auxiliary units also lead to economic drawbacks. A *controlled reactor* concept (see Fig. 2.7 right) based on optimal transient coolant control during start-up was recently proposed by the author in [BRS17] and represents an elementary part of the present work.

Besides the classification in Fig. 2.7, there are many more studies on heat management, often assuming steady-state conditions. Kiewidt and Thöming [KT15] proposed a model-based Semenov number optimization approach to compute optimal axial temperature profiles while maintaining the catalyst temperature limitation. Further optimization studies in this context, with special focus on the steady operation of an entire methanation plant model, were provided by El Sibai et al. [ERS17].

In terms of the reactor flexibility, large-scale, adiabatic reactors are known to exhibit a significantly slower behavior with regard to load changes, start-ups, and shut-downs, which is mainly due to their large reactor volume and the corresponding high heat capacity. For instance, the TREMP technology in Fig. 2.5 with $600\,\mathrm{Nm^3\,h^{-1}}$ feed flow rates and reactor volumes of $0.1 - 0.3\,\mathrm{m^3}$ requires 1.5 days for heat up under non-reactive conditions. Nevertheless, load changes within 1 - 2 hours in a broad range of 30 - 100 % and standby times (the time between feed interruption and successful restart without additional heating) of 1 hour could have been achieved. A detailed technical report about this plant is available in [Höh+85]. Recently, Rönsch et al. [ROD17] simulated an adiabatic reactor for methanation of similar dimensions and observed standby times of 4 hours. In dynamic scenarios, polytropic reactors usually respond much faster, which results from the much smaller single-tube reactor volume ($0.001 - 0.003\,\mathrm{m^3}$). This way, start-up times around 10 min are possible [BRS17]. Concerning load changes, polytropic reactors are also reported to feature bandwidths between 20 - 100 % [Gru+18].

In summary, the following conclusions can be drawn:

- Processes for CO_2 methanation are mainly assigned to PtM applications.
- For several decades steady CO methanation with adiabatic reactors has been used successfully and has technological requirements similar to those of steady CO_2 methanation.
- The commercial SNG production capacity of CO_2 methanation plants is currently three orders of magnitude smaller than that of CO methanation plants.

- Polytropic reactors show faster dynamics and offer higher degrees of freedom, which allows for defined interactions (via cooling) along the entire reaction pathway. Therefore these reactors are better suited for flexible operation than adiabatic reactors.

Although investigations on reactor dynamics, control, and flexibility exist already for decades, only few research is dedicated to improving the reactor design or operation for these criteria. This is currently changing by an increasing need for small- and mid-scale reactor concepts ready for flexible operation. The present work can be placed precisely in this field of research and is intended to motivate further investigations to re-evaluate traditional criteria for process design and synthesis about this new objective. For instance, an increasing need for flexible reactors might create new incentives to favor polytropic reactors over adiabatic reactors, even at larger-scales.

Theoretical Background

3

This chapter outlines the required fundamentals for advanced reactor operation. Before, it is necessary to explain some terms that recur throughout this work. Thereby the terms *flexibility*, *operating point*, *operating range*, and *operating parameter* are particularly relevant.

Despite the frequent use of the term *flexibility* in the literature, there are only a few concise definitions available yet. A systematic description of various flexibility types in chemical engineering is presented in a recent survey by [Bru+20]. A more mathematical approach to assess flexibility goes back to the early work of Grossmann and Morari [GM83], which was again taken up in a more recent survey for quantifying resiliency and flexibility of chemical processes by Grossmann et al. [GCG14]. Accordingly, *flexibility* is seen as a steady-state feature, measuring the capability of feasible operation in various steady states. In contrast, *resiliency* considers the dynamic capability to easily recover from process disturbances in a fast and smooth manner. Both together address the guaranteed feasibility of process operation over a range of conditions.

The present work is aligned with the perspective of Grossmann et al. [GCG14]. Consequently, a stationary reactor state is further considered as *operating point*, and the *operating range* is interpreted as the set of all attainable operating points. For fixed-bed reactors, both terms are typically associated with performance values such as conversion, yield, selectivity, or the maximum bed temperature. Furthermore, operating points result from a particular set of *operating parameters*, which refer to the reactor design (e.g., length, diameter) and its operating condition (e.g., inlet temperature, flow rate).

According to this terminology, the identification of all possible operating points is the key to understand the flexibility of chemical reactors. This very aspect is the core of the underlying work. As outlined in Chapter 1, chemical reactors exhibit numerous stable but also unstable operating points. Despite the pervasive opinion to avoid unstable operating points in practical applications, this work refers to the pioneering work of Eigenberger and Schuler [ES89], who stated that

> *... instability is not a problem insofar as safe operation is concerned if the unstable system reacts so slowly that it can easily be stabilized by a quick adjustment.*

Consequently, access to unstable operating points in a reactive system is not per se prohibited, but rather subject to possible stabilization strategies. To find and to evaluate the reactor performance at these unstable states, this chapter motivates the exploration of regions with steady-state multiplicity.

Although the existence of unstable states is widely discussed for various applications [HP81; JR82; WE95; BW14], so far, very little attention has been given to the question of how to make use or even operate at these states within industrial-scale reactors. Nevertheless, enabling chemical reactors to operate within unstable regimes would significantly widen its conventional operating range, and thus lead to increased flexibility.

To make use of the unstable operating points a concept for transient interaction is vital. So far, two major concepts have been established in the literature: *forced-periodic operation* and *stabilizing control*.

- *Forced-periodic operation* goes back to Horn and Lin [HL67] and covers flow direction switches, e.g., simulated moving beds chromatographic reactors [PGC96] or reactor switches [NKE94a; SK95; MB96], as well as periodical input and environment manipulation [Sil98; MMP08]. Further comprehensive overviews are given by Hudgins et al. [Hud+13] and Bunimovich et al. [BSM08]. Even for methanation this approach was recently considered [Güt13; KWT18].
- *Stabilizing control* for chemical reactors was already mentioned in the pioneering work of Aris and Amundson [AA58a]. The authors introduced and analyzed in depth the influence of proportional temperature control to the stability of exothermic continuously stirred tank reactors (CSTR). Building upon this, Viel et al. [VJB97] further elaborated control schemes for global CSTR stabilization including possible input constrains. Other studies focused on reactor control aspects such as robustness, uncertainties, Kalman filters, state observer, and optimal control [DPY92; AA06; Bak+09; Mor+10; Bak+12].

Forced-periodic operation is not the objective of this work as it is continuously stressing process units and actuators which often leads to serious doubts in its technical feasibility and scale-up potential [SK95]. Instead, process control is an essential and already implemented component of many technical applications, such that the realization of stabilizing control potentially requires little effort in comparison to its achievable process improvements.

To date, detailed elaborations in this direction are still insufficiently represented in the literature. In order to fill this gap, the present chapter will initially discuss the fundamental aspects and properties of catalytic reactors. With the help of a simplified reactor model, operating ranges (including state-space multiplicity) are investigated in depth. Afterwards, a detailed tubular reactor model for catalytic methanation is introduced, which will be the basis for subsequent simulation, control, and optimization studies.

3.1 Fundamentals of Reactor Modeling

Modeling chemical fixed-bed reactors requires to incorporate a variety of physicochemical interactions and is often motivated by models from first-principles. Solving these models can lead to a challenging computational task due to the complex coupling of mass, energy, and momentum transport. However, putting all available details into consideration is not always necessary. Simplifying assumptions are essential to guarantee sufficiently fast and accurate computation. In this work, for instance, the momentum balance is neglected in order to exclude less relevant effects with low time constants, which easily lead to higher numerical stiffness of the dynamic system, and thus much higher computational effort [GA13]. Instead, pressure and gas velocities are considered based on correlations derived specifically for fixed-bed reactors.

Considering the law of conversation for mass and energy, an arbitrary control volume of various shape and size inside the reactor is governed by the following fundamental set of balance equations (Eulerian specification):

$$\text{total mass} \qquad \frac{\partial \rho}{\partial t} = -\nabla \cdot \left(\rho \vec{v}\right), \tag{3.1}$$

$$\text{component mass} \qquad \rho \frac{\partial w_\alpha}{\partial t} = -\rho \vec{v}\, \nabla \cdot w_\alpha - \nabla \cdot \vec{j}_\alpha + M_\alpha \sum_\beta \nu_{\alpha,\beta}\, \tilde{\mathrm{r}}_\beta, \tag{3.2}$$

$$\text{energy} \qquad \rho c_p \frac{\partial T}{\partial t} = -\rho c_p \vec{v} \cdot \nabla T - \nabla \cdot \vec{q} - \sum_\beta \left(\Delta_R \tilde{H}_\beta\right) \tilde{\mathrm{r}}_\beta. \tag{3.3}$$

Further assumptions behind Eq. (3.3) are: no kinetic and potential energies, constant pressure, no body forces, no energy contribution by shear stress, no heat radiation. Eqs. (3.2) and (3.3) are sufficient to consistently describe an arbitrary reactor, if all relevant components α are included. If Eq. (3.1) is considered, Eq. (3.2) applies only to α-1 components.

In addition to physical assumptions, the considered control volume boundary also determines the relevant balance components of Eqs. (3.1) to (3.3). This differentiation meets the two *ideal reactor* concepts for continuously operated reactors:

- the ideal continuous stirred tank reactor (CSTR),
- the ideal plug flow tubular reactor (PFTR).

The CSTR concept often considers a control volume around the entire reactor volume (integral balance). In contrast, the control volume for the ideal PFTR typically refers to an infinitesimally small volume segment within the reactor volume (differential balance). The PFTR allows to describe in detail spatial distributions of the reactor's state variables (e.g., temperature and mass fraction), but also requires higher numerical efforts. Both ideal reactors also represent the two limiting cases for back-mixing / axial dispersion, which is typically measured by the axial Bodenstein number for mass and energy according to

$$\mathrm{Bo}^{\mathrm{m}} = \frac{v_z\, L}{\mathcal{D}_z}, \quad \mathrm{Bo}^{\mathrm{e}} = \frac{v_z\, \rho_{\mathrm{gas}}\, c_{p,\mathrm{gas}}\, L}{\lambda_z}, \tag{3.4}$$

which are essential for later discussions. In case of an ideal CSTR the reactive volume is fully mixed ($\mathcal{D}_z = \lambda_z \to \infty$, $\mathrm{Bo}^{\mathrm{m}} = \mathrm{Bo}^{\mathrm{e}} \to 0$), whereas in case of the ideal PFTR no back-mixing / dispersion exists ($\mathcal{D}_z = \lambda_z \to 0$, $\mathrm{Bo}^{\mathrm{m}} = \mathrm{Bo}^{\mathrm{e}} \to \infty$). [Lev99; SMW19]

Real reactors, as considered in this work, are allocated right in between these two limiting cases. The corresponding modeling approaches are

- the CSTR cascade (tanks-in-series model, cell model),
- the tubular reactor model with axial dispersion (dispersion model).

In order to represent real reactors more accurately, the control volume may also differentiate between bulk gas phase and catalyst phase. Two model concepts are commonly applied:

- the pseudo-homogeneous model (no phase distinction),
- the heterogeneous model (phase distinction with interfacial and intraparticle mass and energy transport).

Depending on the considered model, the energy dispersion coefficient in Eq. (3.4) is considered differently. The pseudo-homogeneous model lumps solid and gas phase, which requires an effective energy dispersion term ($\lambda_z = \lambda_z^{\mathrm{eff}}$). On the contrary, the heterogeneous model allows for the distinction between gas and solid-phase dispersion and, thus, accounts for two separate energy-based Bodenstein numbers ($\mathrm{Bo}^{\mathrm{eg}}, \mathrm{Bo}^{\mathrm{ec}}$). For real fixed-bed reactors, the mass-based Bodenstein number is reported to be three to ten times higher than the energy-based Bodenstein number [Pus+81; BS10]. Thus, energy back-mixing is the dominating axial dispersion mechanism within fixed-bed reactors [Mea76]. Note that some studies define the here stated Bodenstein number as Péclet number. In this work, these numbers are distinguished by their characteristic length, which is the reactor length L for the Bodenstein number and the particle diameter d_{p} for the Péclet number.

Both model concepts offer different levels of sophistication, e.g., one-, two-, or three-dimensional spatial resolution, stationary or dynamic, with or without axial dispersion. How sophisticated a model needs to be is often rated by criteria (e.g., Mears' criterion), which incorporate dominating transport phenomena and reactor design. A comprehensive overview is provided by Pérez-Ramírez [Pér00]. Besides these criteria, distinct model or transport components may be examined separately. This decoupling approach is well-established to identify and analyze, for instance, different sources of state-space multiplicity. In this context, Nibbelke et al. [NHM98] emphasized that the identification of multiplicity sources is inevitable for a correct interpretation of numerical and also experimental results. This observation is crucial for the construction of adequate reactor models as well as for optimal reactor operation and control. Further explanations on state-space multiplicity are part of the following section.

3.1.1 State-Space Multiplicity

There are numerous sources for state-space multiplicity for which three scales are in particular of interest: the scale of the active site, the catalyst pellet (including pores), and the reactor [She87]. Fig. 3.1 illustrates all three scales and the corresponding multiplicity sources (A to E) that have been most discussed in the literature.

Although, the term *feedback* was used in several studies to reason multiple steady states [PW67; Eig83], none was found that conclusively explains what is meant by feedback. Therefore, some clarifications are necessary at this point.

Feedback, as illustrated in Fig. 3.1, typically relates to mass and energy fluxes (components on the right hand side of Eqs. (3.2) and (3.3)) within a reactor control volume ∂V. These fluxes have the natural drive to equalize temperature and concentration differences caused, for instance, by reactive sources and sinks. All fluxes are determined by corresponding transport resistances and linked in a network connecting scales and phases. Depending on inlet and surrounding conditions of the control volume, some resistances are rate-determining for the overall mass and energy transport. According to conservation laws, at steady state all fluxes, sources, and sinks are in equilibrium, meaning that Eqs. (3.1) to (3.3) equal zero. A change of inlet and surrounding conditions disturbs the entire network, and a new flux equilibrium emerges. At reactor scale, there exists a unique flux equilibrium if all individual fluxes are unique and if inlet and surrounding of the control volume are not influenced by the control volume itself. If the control volume influences its inlet and/or surrounding (e.g., due to back-mixing), multiple flux equilibria, and, thus, multiple steady states are possible. This interaction

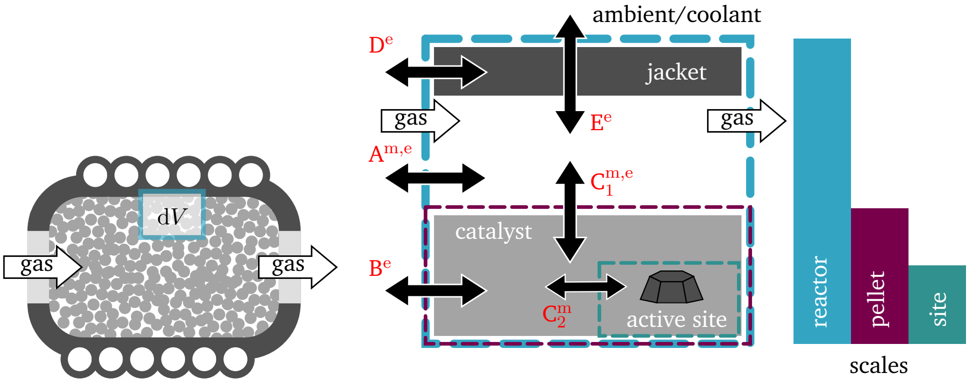

Fig. 3.1.: Flux network and sources A to E for multiplicity within fixed-bed reactors, double arrows indicate mass (^{m}) and/or energy (^{e}) fluxes to be part of the respective source.

is typically denoted as feedback at reactor scale. Similarly, these feedbacks may also occur at catalyst and site scale due to the interaction with neighboring scales.

In order to explain the feedback mechanism more comprehensively, the following simplifying example is considered: It is assumed that under exothermic conditions the reaction energy in an arbitrary control volume, as illustrated in Fig. 3.1, is solely transported from the active site to the ambient/coolant, such that the flux network boils down to the following flux chain:

$$\xmapsto{\dot{q}_{\text{react}}} T_{\text{site}} \xrightarrow{\dot{q}_1} T_{\text{cat}} \xrightarrow{\dot{q}_2} T_{\text{gas}} \xrightarrow{\dot{q}_3} T_{\text{jac}} \xrightarrow{\dot{q}_4} T_{\text{amb/cool}}.$$

Further assuming that the flux between jacket and coolant is rate-determining leads to isothermal conditions within reactor interior:

$$\xmapsto{\dot{q}_{\text{react}}} \underbrace{T_{\text{site}} = T_{\text{cat}} = T_{\text{gas}} = T_{\text{jac}}}_{T_{\text{react}}} \xrightarrow{\dot{q}_4} \underbrace{T_{\text{amb/cool}}}_{T_{\text{op}}},$$

such that only one heat resistance and the reactive source remain as rate-determining candidates. Flow parity holds at steady state:

$$\begin{aligned} \dot{q}_{\text{react}}\, A_{\text{react}} &= \dot{q}_4\, A_4 = \mathrm{k}\,(\mathrm{T}_{\text{react}} - \mathrm{T}_{\text{op}}), \\ \dot{Q}_{\text{react}} &= \dot{Q}_4. \end{aligned}$$

In general, an exothermic reactive source $\dot{Q}_{\text{react}}$ increases exponentially with reaction temperature according to the Arrhenius relation and depletes as soon as reactants are consumed or chemical equilibrium is reached. For this reason, the reactive source typically shows an S-shaped nonlinear temperature trend as illustrated in Fig. 3.2 a). On the contrary, the coolant energy flow $\dot{Q}_4$ increases linearly with reaction temperature. Despite each individual flow exhibits a unique solution with respect to one reaction temperature, their coupling might result in multiple flow equilibria (also denoted as multiple steady states or operating points). Such operating points (OP) are qualitatively shown in Fig. 3.2 b) for the case of threefold flow equilibrium. The fact that reaction temperature and operating temperature differ significantly in OP_2 and OP_3, however, requires an internal back-mixing which is induced only by the transport resistance between jacket and coolant. Ultimately, this back-mixing is meant by *feedback*. It is important to note that without back-mixing, the rate-determining energy transport would be solely on the reaction side, such that all states remain unique, as illustrated in Fig. 3.2 a).

Fig. 3.2 b) shows that the higher the difference between T_{react} and T_{op} the more feedback must be involved. In order to tune feedback intensity and corresponding operating points (OP), it is necessary to influence the functional trend of $\dot{Q}_{\text{react}}$ and $\dot{Q}_4$. Therefore a change of the operating temperature T_{op}, heat transfer coefficient k,

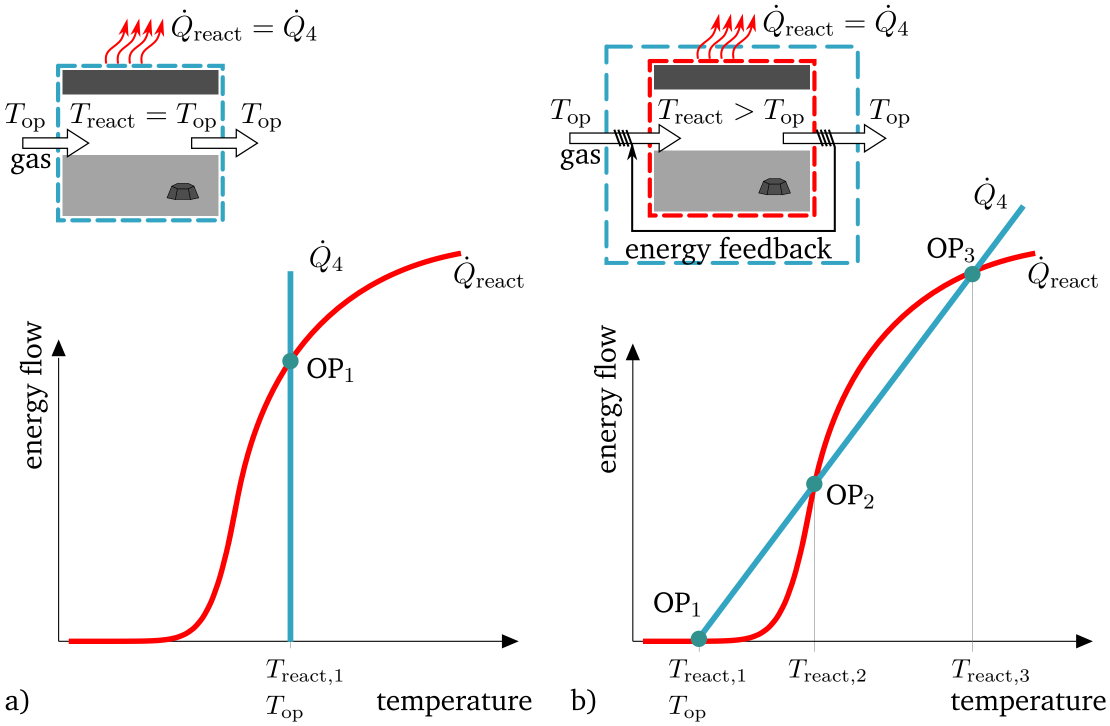
$\dot{Q}_{\text{react}} = \dot{Q}_4$
T_{op}
gas
$T_{\text{react}} = T_{\text{op}}$
T_{op}
$\dot{Q}_4$
$\dot{Q}_{\text{react}}$
OP_1
energy flow
$T_{\text{react},1}$
T_{op}
temperature
a)
$\dot{Q}_{\text{react}} = \dot{Q}_4$
T_{op}
gas
$T_{\text{react}} > T_{\text{op}}$
T_{op}
energy feedback
$\dot{Q}_4$
OP_3
$\dot{Q}_{\text{react}}$
energy flow
OP_2
OP_1
$T_{\text{react},1}$
T_{op}
$T_{\text{react},2}$
$T_{\text{react},3}$
temperature
b)

Fig. 3.2.: Qualitative energy flows under exothermic conditions without a) and with b) coolant transport resistance, OP - operating point.

residence time, or reaction setting (e.g., activation energy, rate coefficient, multiple reactions) is possible. In addition to the threefold flow equilibrium in Fig. 3.2 b), these slope changes can lead to three additional scenarios (see Fig. 3.3).

The analysis of multiple steady states is closely related with stability. As one of the first, svan Heerden [sva53] stated that each OP is stable if the following relation holds:

$$\frac{d\dot{Q}_{\text{react}}}{dT} \leq \frac{d\dot{Q}_4}{dT}.$$

This shows that there must be always an odd number of OPs, among which every unstable OP is surrounded by stable OPs.

The explanations from above are not limited to exothermic reactions or energy transport. When steady-state multiplicities in fixed-bed reactors are observed (either numerically or experimentally), they often result from several sources simultaneously. In order to assign the observed multiplicity to the correct source, careful evaluation of each source is required. Therefore, Sheintuch [She87] divided multiplicity sources from Fig. 3.1 into three classes:

- purely kinetic (C_2^{m}),
- isothermal (A^{m}, C_1^{m}),
- thermo-kinetic (A^{e}, B^{e}, C_1^{e}, D^{e}, E^{e}).

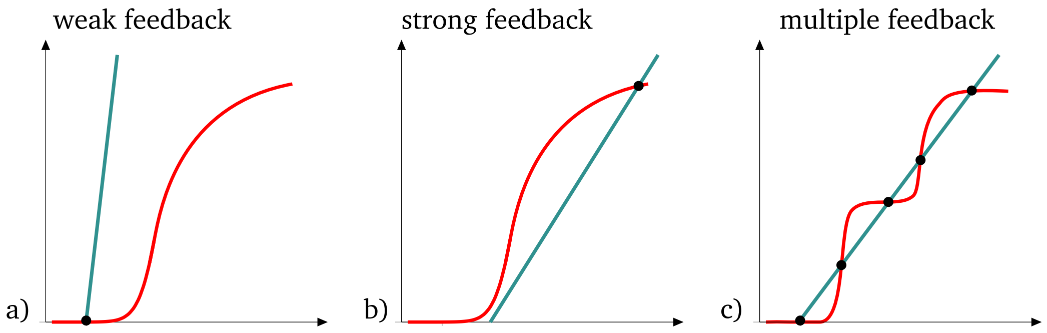

Fig. 3.3.: Feedback scenarios according to Fig. 3.2, a) high heat transfer coefficient or low residence time, b) low heat transfer coefficient or high residence time, c) multiple reactions/reaction networks.

Purely kinetic sources belong to mass transport at the active site induced by nonlinear kinetics (e.g., adsorption vs. reaction) [NHM98], concurrent reactions / reaction networks [BL83; EE93; NHM98; Moh+01], or catalyst deactivation [Gil77; Eig83]. *Isothermal* sources arise from mass transport at catalyst (diffusion) [MSV86; LMV87] or reactor scale (convection, dispersion). *Thermo-kinetic* sources are mainly caused by nonisothermicities, which influence the nonlinear reaction rate coefficients according to the Arrhenius relation [Eig72a; HP82; WE95].

Furthermore, multiplicities are also able to propagate through different scales and along with spatial directions. As a result, a large amount of multiple steady states (in theory up to infinity) at reactor scale can be produced by only a few (typically three) multiple steady states at pellet or site scale [NHM98; LMV87; AR91]. Due to the variety of different sources and their ability to propagate through scales, literature (going back to the early 60s) reports very differently or even controversially about total number, relevant sources, and necessary conditions of multiple steady states in fixed-bed reactors. This aspect is demonstrated by a brief literature survey in Tab. 3.1.

As shown in Tab. 3.1, the investigation of steady-state multiplicity is mainly performed via cell models and dispersion models. Both model types have been used to outline the two theoretical limiting cases: a reactor without state-space multiplicity and with an infinite number of multiple steady states. The dominating opinion is that the ideal PFTR is free of any state-space multiplicity due to the absence of transport in countercurrent direction (feedback). However, some studies opposed that the ideal PFTR is rather characterized by an infinite number of steady states [LA62; WE95; NHM98]. These studies refer to the fact that the continuum description of an ideal PFTR corresponds to a series of infinite CSTRs. Assuming that the ignition can occur at any CSTR within the series gives rise to an ignition possible at any position along the reactor axis. This thought experiment allows for discontinuous solutions in packed-beds, which is often correlated to multiple steady states of single particles [AR91] or active sites [NHM98]. Although the confusing concept of infinite solutions was discussed very controversially, it was certainly the main driver behind many investigations. Thereby, two objectives

Tab. 3.1.: Review on multiplicity sources within fixed-bed reactor models and experiments.

active source Fig. 3.1	**class**	**# MSS**	$\mathbf{Bo^{m},Bo^{e}}$ Eq. (3.4)	**model type**	**reference**
none	none	1 (stable)	$\to \infty^{m,e}$	id. PFTR	[SA63; SHV76] [Var80; JR82]
none	none	∞	$\to \infty^{m,e}$	id. PFTR	[LA62; WE95; NHM98]
pseudo-homogeneous models (lumped gas and solid phase)					
A^{e}, B^{e}, E^{e}	tk	1^{exp},2^{exp}	100^{e}	DM	[KV80]
$A^{m,e}$, B^{e}, E^{e}	tk	1,2 (stable)	40-1900^{m}, 3-160^{e}	DM	[Pus+81]
$A^{m,e}$, B^{e}, E^{e}	tk	1,3,5,7	1-$5^{m,e}$	DM	[HP81; HP82]
$A^{m,e}$, B^{e}, E^{e}	tk	1,3,5	1-320^{m}, 1-100^{e}	DM	[JR82]
$A^{m,e}$, B^{e}	tk	1^{exp},2^{exp},3	300^{m}, $8^{e,exp}$, 30^{e}	DM	[WL84]
A^{e}, B^{e}, E^{e}	tk	1,3	10-10000^{e}	DM	[PBL89]
A^{m}, C_2^{m}	k,i	∞	$1 - \infty^{m}$	CM,DM	[NHM98]
C_2^{m}	k,i	1,3,5	∞^{m}	CM,DM	[NHM98]
$A^{m,e}$, B^{e}	tk	1,2,3	$6^{m,e}$	DM	[Doc18; Dra+08]
heterogeneous models					
$A^{m,e}$	tk	∞	100-$300^{mg,eg}$	DM	[LA63]
B^{e}, E^{e}	tk	1,3,5	280^{ec}	DM	[Eig72a; Eig72b]
$A^{m,e}$, $C_1^{m,e}$	tk	∞	9.5-43^{mg},40-172^{eg}	CM,DM	[Sin+76]
C_1^{m}	i	1,3	∞^{mg}	DM	[MSV86; LMV87]
A^{m}, C_1^{m}	i	1,3,5,7,9	$0<Bo^{mg}<\infty$	DM	[LMV87]
A^{m}, C_1^{m}	i	1,3	0^{mg}	DM	[LMV87]
A^{m}, C_1^{m}	i	∞	0^{mg}	CM	[AR91]
$A^{m,e}$, B^{e}	tk	1,3,∞	$40^{mg,eg}$, $>40^{eg}$	CM	[WE95]
C_1^{m}	i	∞	∞^{mg}	DM	[TR96]
A^{m}, C_1^{m}	i	∞	1-10^{mg}	DM	[TR97]
B^{e}, C_2^{m}	tk,k	∞	similar to [Eig72a]	CM,DM	[NHM98]
$C_1^{m,e}$	tk	1,3	$\infty^{mg,eg}$	DM	[DBW99]
B^{e}, $C_1^{m,e}$	tk	1,3,5,11	$\infty^{mg,eg}$, 50-3000^{ec}	DM	[AWB07]
$A^{m,e}$, B^{e}, E^{e}	tk	1,3,5	0-560^{eg}, 0-5600^{ec} 0-1680^{mg}	DM	[BS10]
purely experimental studies - (comprehensive reviews given by [PW67; WL84; HL85; AS90])					
		2^{exp} (stable)			[PH84; AS90]
		4^{exp} (stable)			[HL85]

m - mass, e - energy, g - gas, c - catalyst, ^{exp} - experimental, k - kinetic, i - isothermal,
tk - thermo-kinetic, CM - cell model, DM - dispersion model, MSS - multiple steady states

became the most relevant for technical applications: Firstly, the ability to operate at various states promises performance improvements. Secondly, state-space uniqueness is of great value for safety reasons (e.g., to avoid runaways).

Apart from ideal reactors, many studies in Tab. 3.1 also focus on real reactors considering finite Bodenstein numbers Bo within dispersion models or finite numbers n of representative CSTRs within cell models. As shown by Levenspiel [Lev99], both concepts are interchangeable due to the relation

$$\frac{1}{n} = \frac{2}{\mathrm{Bo}} - \frac{2}{\mathrm{Bo}^2}\left(1 - \exp\left(-\mathrm{Bo}\right)\right) \quad \text{and} \quad n = \frac{\mathrm{Bo}}{2} \quad (\text{if } \mathrm{Bo} > 100). \tag{3.5}$$

Besides the different model concepts, various assumptions are made in order to uncover the influence of specific sources of steady-state multiplicity. Therefore, the studies in Tab. 3.1 differ in many aspects of the model constitution (e.g., heterogeneous vs. homogeneous, isothermal vs. non-isothermal, first-order reaction vs. LHHW-type reaction, with vs. without radial dispersion). For instance, the use of isothermal reactor models eliminates all thermo-kinetic multiplicities and allows for investigations on purely kinetic and/or isothermal multiplicities. On the contrary, the study of purely thermo-kinetic multiplicities is preferably done in the absence of kinetic and isothermal multiplicities.

Most studies dealing with thermo-kinetic multiplicity sources agree that axial dispersion of heat plays a vital role in the existence of multiple steady states in fixed-bed reactors. Eigenberger [Eig72b], in particular, argued that heat conduction through the solid phase (source B^{e}) must reduce an infinite multiplicity to a finite number of multiple steady states. The author also identified a maximum number of three or five multiple steady states, depending on the boundary conditions of the solid phase. It took about 20 years before this finding was revised. Therefore, Nibbelke et al. [NHM98] extended the model of Eigenberger [Eig72b] and considered a reaction kinetic with multiplicities at the active site (source C_2^m). The authors could prove that an infinite number of steady states is maintained even if axial heat dispersion through the solid phase is incorporated. Unfortunately, this research direction is still very narrow, which is certainly because the required heterogeneous model is a rather sophisticated numerical tool for such analyses [SW91]. The use of pseudo-homogeneous models provides a possible remedy. Although pseudo-homogeneous models are not able to distinguish between energy transport in source A and B, their results point in the same direction. By making use of dimensionless model formulations and bifurcation techniques Jensen and Ray [JR82] and Heinemann and Poore [HP81; HP82] classified several aspects that also contribute to the existence of multiplicity. Both stated that a nonadiabatic reactor with unequal Bodenstein numbers for heat and mass dispersion shows a unique solution, either for sufficiently high values of the Bodenstein numbers, for large heat transfer coefficients, or small values of the Damköhler number. These conditions also hold for industrial fixed-bed reactors; such that multiplicity was found to be relevant even for technical configurations [PBL89; Pus+81]. This is reflected in Tab. 3.1 by the broad range of Bodenstein numbers in which multiple steady states are observed. In most investigations, the number of three multiple steady states is confirmed. Beyond that, some studies report up to eleven multiple steady states. However, experimental evidence above four multiple steady states was not found. For instance, Wedel and Luss [WL84] validated their results with an experimental setup for CO and CO_2 methanation in a fixed-bed of 25 cm in length and 2.5 cm in diameter. The authors could reproduce predicted model solutions of one ignited and one extinguished state with identical feed concentration. Therefore, a one-dimensional axial dispersion model, which accounts for the diffusion-reaction interactions within the pellets, was found to be well suited for multiplicity analysis. Since their experimental setup has a low bed length and, thus, a low Bodenstein number ($\mathrm{Bo}^e = 8$), conclusions for industrial reactors are rather limited. Nevertheless, the good agreement between model and experiment verified and proved that state-space multiplicity is of significance within fixed-bed reactors. More recently, Agrawal et al. [AWB07] pointed out that the often reported high number of multiple solutions originates from the assumption of constant transport coefficients, which leads to many fragile solutions that emerge from unstable branches. Accounting for the variation of heat and mass transfer coefficients with local flow and reaction properties eliminates these nonphysical solutions. For this reason, recent works are often motivated to add more physical meaning to their models. This allows to additionally focus on effects of secondary order (e.g., flow maldistributions, localized hot-spots, spatial and spatiotemporal patterns) [She97; TR97; Jar+01; PEB01; ML03; AWB07; VSL08; NS12], which is, however, not subject of this work. Similarly, stable oscillatory solutions are also disregarded in this work, since they are unlikely to occur in fixed-bed reactors on an industrial scale due to their high thermal inertia [JR82].

In order to identify the full operating range of fixed-bed reactors, this work considers state-space multiplicity as a crucial feature. Therefore, thermo-kinetic sources are of major interest, since purely kinetic and isothermal multiplicities are found to be very fragile. The literature survey from above reveals that axial dispersion, as well as the diffusion-reaction interaction, are essential model components to obtain consistent results. However, for specific applications, these studies rather provide trends than generally valid correlations and criteria. The impact of several characteristic features simultaneously is certainly the main reason for this obstacle. Furthermore, the operation at unstable states (as OP_2 in Fig. 3.2) is also underrepresented in the literature and needs further elaboration. Therefore, the following sections intend to provide more insights and propose general criteria that unify the aspects uniqueness, multiplicity, and stability.

In the following, a single pseudo-homogeneous CSTR model is used to represent fully mixed reactive conditions and to illustrate its implications on uniqueness, multiplicity, and stability. Afterwards, the single CSTR is extended to a series of CSTRs (cell model) in order to approach conditions as they prevail in real fixed-bed reactors. All investigations are exemplified for methanation under realistic reactive conditions.

3.1.2 CSTR Analogy

As indicated by the previous section, back-mixing is an essential feature that determines multiplicity. In order to show how this applies to real reactors, the following derivations shall serve as a guideline for multiplicity analysis, exemplified for catalytic methanation. Beginning with the well-known limiting case of a fully mixed reactive volume illustrates the fundamental parameters that characterize the range and intensity of multiplicity. The technical relevance of this limiting case can be found, for instance, with Berty reactors, which are widely used for catalyst characterization. Although the relationships presented here are already state of knowledge, they are crucial for later excursions towards industrial-scale fixed-bed reactors.

Further on a CSTR model as illustrated in Fig. 3.4 and mathematically derived in Appendix A.1 on Page 119. The required mass and energy balances read accordingly:

$$\text{mass balance:} \qquad X_{\mathrm{CO_2}} = \frac{\tau}{\varepsilon}\,\frac{\mathrm{R_{meth}}(T,p,w_\alpha)}{c_{\mathrm{CO_2,in}}} \quad \text{with} \quad \tau = \frac{\varepsilon\, V}{\dot{V}_{\mathrm{in}}} = \frac{\varepsilon\, V\, \rho_{\mathrm{in}}}{\dot{m}_{\mathrm{in}}}, \tag{3.6}$$

$$\text{energy balance:} \qquad X_{\mathrm{CO_2}} = \frac{(1+\mathrm{St})}{\Delta T_{\mathrm{ad}}}\,(T - T_{\mathrm{op}}). \tag{3.7}$$

Consequently, steady-state operation of a single CSTR is governed by the equality of Eq. (3.6) and Eq. (3.7). In order to evaluate unique and non-unique operating points, Tab. A.1 on Page 123 provides reference parameters that correspond to carbon dioxide methanation in a fixed-bed reactor under realistic conditions.

The six key parameters in Tab. A.1 on Page 123 are highlighted in bold and result in Fig. 3.5 for variations of the operating temperature and Fig. 3.6 for variations of the Stanton number. The operating temperature is given in Eq. (A.13) on Page 122 and reflects changes in coolant and inlet temperature, whereas the Stanton number mainly results from changes in the coolant heat transfer. The left side of both figures shows that under realistic conditions, multiple equilibrium (or operating) points are indeed

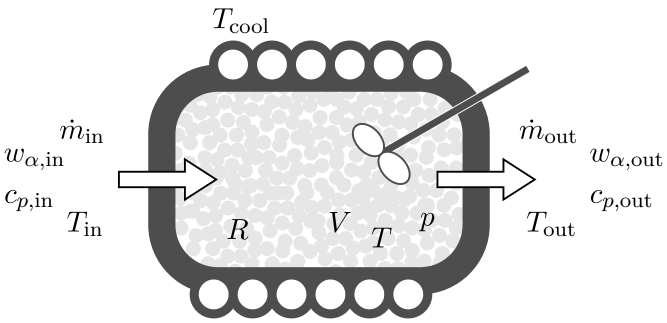

Fig. 3.4.: Illustration of the single CSTR model with heterogeneously catalyzed reaction.

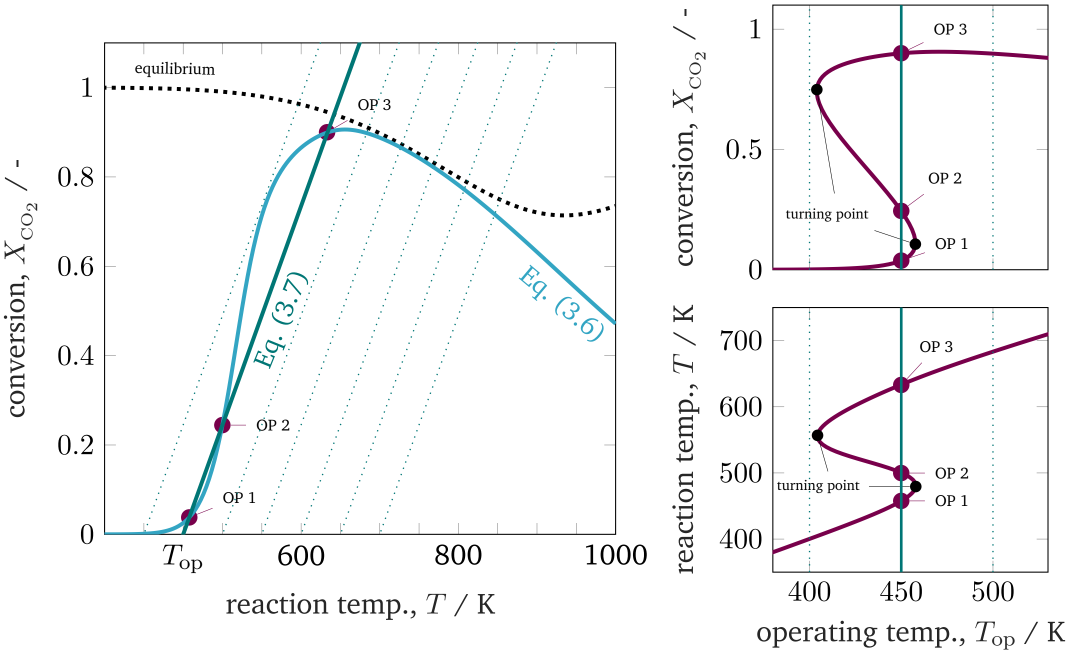

Fig. 3.5.: State-space diagram for mass and energy balance (left) and for all equilibrium points (right) under variation of the operating temperature, reference setting taken from Tab. A.1 on Page 123.

attainable, similar to the theoretical discussions in Section 3.1.1. The right side in both figures illustrates how hysteresis emerges when the operating parameter varies within realistic ranges. Apart from variations in operating temperature and Stanton

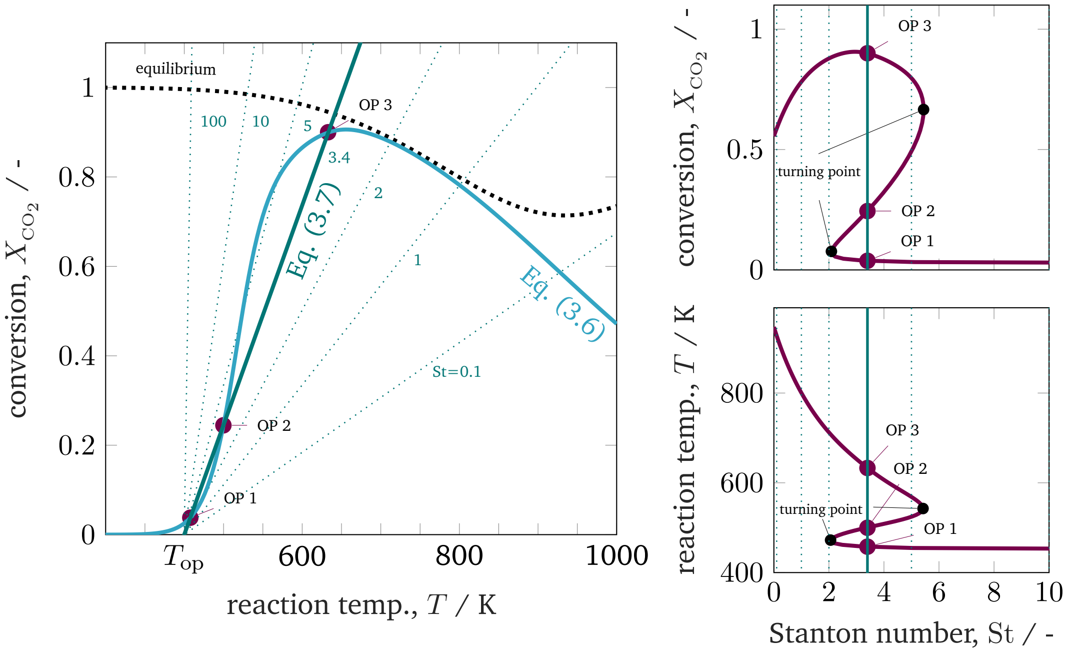

Fig. 3.6.: State-space diagram for mass and energy balance (left) and for all equilibrium points (right) under variation of the Stanton number, reference setting taken from Tab. A.1 on Page 123.

number, one might also consider variations of the residence time τ. Higher residence times correspond to higher Damköhler numbers and increase the curvature of the mass balance operating curve Eq. (3.6) and, thus, increase the hysteresis.

These results explicitly show that under perfect back-mixing at most three operating points are attainable, whereas two are stable (OP 1 and OP 3) and one is unstable (OP 2). As seen in the upper right figures, the unstable operating points are always surrounded by stable ones and cover a significant part of the attainable conversion range. If these unstable states are ignored for reactor design and operation, a significant potential might get lost. This clearly demonstrates the close connection between multiplicity and stability. Here, the generalized criterion for stability of a CSTR at a certain operating point is known to result from mass and energy-based sensitivities according to

$$\left.\frac{\mathrm{d}X}{\mathrm{d}T}\right|_{\mathrm{OP}} = \frac{\tau}{\varepsilon c_{\mathrm{in}}} \left.\frac{\mathrm{d}\mathrm{R}}{\mathrm{d}T}\right|_{\mathrm{OP}} < \frac{1+\mathrm{St}}{\Delta T_{\mathrm{ad}}}, \tag{3.8}$$

which is equivalent to the criteria proposed by svan Heerden [sva53], and Gilles and Hofmann [GH61]. Note that sensitivities might also be considered with respect to other parameters than temperature. However, this work focuses primarily on thermo-kinetic multiplicities, for which temperature sensitivities are the most relevant. The mass-based sensitivity may be further evaluated by resolving the total differential at constant τ and c_{in}, such that

$$0 = \frac{\mathrm{d}X}{\mathrm{d}T} - \frac{\tau}{\varepsilon c_{\mathrm{in}}}\frac{\mathrm{d}\mathrm{R}}{\mathrm{d}T} = \frac{\mathrm{d}X}{\mathrm{d}T} - \frac{\tau}{\varepsilon c_{\mathrm{in}}}\left(\frac{\partial \mathrm{R}}{\partial T} + \frac{\partial \mathrm{R}}{\partial X}\frac{\mathrm{d}X}{\mathrm{d}T}\right) \implies \frac{\mathrm{d}X}{\mathrm{d}T} = \frac{\frac{\tau}{\varepsilon c_{\mathrm{in}}}\frac{\partial \mathrm{R}}{\partial T}}{1-\frac{\tau}{\varepsilon c_{\mathrm{in}}}\frac{\partial \mathrm{R}}{\partial X}}.$$

Plugging this into Eq. (3.8) leads to the rate-based CSTR stability criterion

$$\text{CSTR stability:} \qquad \frac{\frac{\tau}{\varepsilon c_{\mathrm{in}}}\frac{\partial \mathrm{R}}{\partial T}}{1-\frac{\tau}{\varepsilon c_{\mathrm{in}}}\frac{\partial \mathrm{R}}{\partial X}} < \frac{1+\mathrm{St}}{\Delta T_{\mathrm{ad}}}. \tag{3.9}$$

In comparision, Szeifert et al. [Sze+07] comprehensibly reviewed available criteria for reactor stability, runaway, and parametric sensitivity. Among those, the authors recommend using the Ljapunov stability criterion for a PFTR in space (or for a batch reactor in time), which is very similar to the upper CSTR stability criterion. In case of an equimolar reaction the PFTR stability criterion reads

$$\text{PFTR stability:} \qquad \frac{\frac{\tau}{\varepsilon c_{\mathrm{in}}}\frac{\partial \mathrm{R}}{\partial T}}{\mathrm{St}-\frac{\tau}{\varepsilon c_{\mathrm{in}}}\frac{\partial \mathrm{R}}{\partial X}} < \frac{1}{\Delta T_{\mathrm{ad}}}.$$

Both criteria reveal that reactor stability is supported under intensive cooling conditions ($\mathrm{St} \to \infty$) and suppressed under reduced cooling conditions ($\mathrm{St} \to 0$). As explained in Section 3.1.1, the PFTR is primarily considered to have a unique solution for fixed parameters. Hence, the features stability, runaway, and parametric sensitivity need to be separated from multiplictiy, which was already highlighted by [BA56]. Until today, this separation is often considered to be generally valid. However, in the CSTR case a strong coupling of these features is clearly given. From the above explanations, generalized criteria for uniqueness and multiplicity within the operating range $\mathcal{O}$ derive very similar to the stability criterion and read

$$\text{CSTR uniqueness:} \qquad \max_{T\in\mathcal{O}} \frac{\mathrm{d}\,X}{\mathrm{d}\,T} = \left.\frac{\mathrm{d}\,X}{\mathrm{d}\,T}\right|_{T^*} \leq \frac{1+\mathrm{St}}{\Delta\,T_{\mathrm{ad}}}, \tag{3.10}$$

$$\text{CSTR multiplicity:} \qquad \max_{T\in\mathcal{O}} \frac{\mathrm{d}\,X}{\mathrm{d}\,T} = \left.\frac{\mathrm{d}\,X}{\mathrm{d}\,T}\right|_{T^*} > \frac{1+\mathrm{St}}{\Delta\,T_{\mathrm{ad}}}. \tag{3.11}$$

On the left hand, the mass-based sensitivity corresponds to the steepest conversion gradient at the inflection point $T = T^*$ of Eq. (3.6). On the right hand, the energy-based sensitivity corresponds to the constant conversion gradient of Eq. (3.7). Although the uniqueness criterion applies to all operating points in $\mathcal{O}$ (sufficient condition for uniqueness), the multiplicity criterion only indicates the existence of some operating points with multiple steady states in $\mathcal{O}$ (necessary condition for multiplicity). Thus, even if the multiplicity criterion holds, unique solutions in $\mathcal{O}$ might still exist. Furthermore, discontinuous jumps at the *turning points* (see Figs. 3.5 and 3.6) from a stable extinguished to a stable ignited branch - and vice versa - is also solely induced by the existence of multiplicity. These jumps coincide with what is generally denoted as *parametric sensitivity* and *reactor runaway* [MV82]. Moreover, the equivalence strikingly demonstrates the close connection between stability, runaway, parametric sensitivity, and multiplicity when back-mixing is present. However, commonly accepted criteria for reactor runaway and stability do not consider back-mixing at all [Sze+07; KV19]. To close this gap, the next section applies the upper correlations for mass and energy to a series of CSTRs, where a finite number of stages corresponds to finite back-mixing.

3.1.3 CSTR Cascade Analogy

In order to approach a more realistic description of industrial-scale fixed-bed reactors, this section extends the previous relations to a CSTR cascade with multiple stages. Note that such cascades also mimic finite volume schemes, which are widely used to solve dispersion models numerically. Appendix A.2 on Page 124 provides the entire cascade model notation, mass and energy balances, as well as the solution strategy. The resulting equations of each CSTR stage are

$$\text{mass balance:} \qquad X_{\mathrm{CO_2}}^{\{i\}} = \frac{1}{n}\,\frac{\tau}{\varepsilon\,c_{\mathrm{CO_2,in}}}\,\mathrm{R}_{\mathrm{meth}}^{\{i\}} = C_n\,\mathrm{R}_{\mathrm{meth}}^{\{i\}}, \tag{3.12}$$

$$\text{energy balance:} \qquad X_{\mathrm{CO_2}}^{\{i\}} = \frac{(1+\mathrm{St}_n)}{\Delta\,T_{\mathrm{ad}}^{\{i\}}}\,(T^{\{i\}} - T_{\mathrm{op}}^{\{i\}}). \tag{3.13}$$

In order to separate different multiplicity sources, isothermal and non-isothermal cascades are discussed in the following.

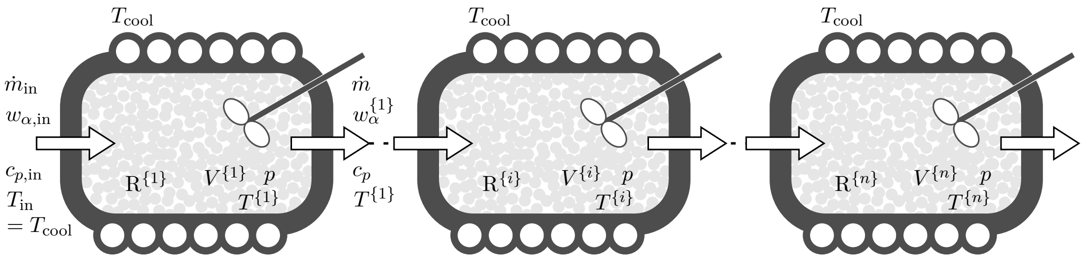
T_{cool}
T_{cool}
T_{cool}
$\dot{m}_{\mathrm{in}}$
$w_{\alpha,\mathrm{in}}$
$c_{p,\mathrm{in}}$
T_{in}
$= T_{\mathrm{cool}}$
$\mathrm{R}^{\{1\}}$
$V^{\{1\}}$
p
$T^{\{1\}}$
$\dot{m}$
$w_\alpha^{\{1\}}$
c_p
$T^{\{1\}}$
$\mathrm{R}^{\{i\}}$
$V^{\{i\}}$
p
$T^{\{i\}}$
$\mathrm{R}^{\{n\}}$
$V^{\{n\}}$
p
$T^{\{n\}}$

Fig. 3.7.: Illustration of the CSTR cascade model of n stages with heterogeneously catalyzed reaction.

Two isothermal CSTRs

Under intensive cooling conditions ($\mathrm{St} \to \infty$) or negligible heat release ($\Delta T_{\mathrm{ad}}^{\{i\}} \to 0$) the CSTR cascade becomes isothermal, meaning that $T_{\mathrm{in}} = T_{\mathrm{cool}} = T^{\{i\}}$. The corresponding implicit nonlinear equation system results from Eq. (3.12) and reads

$$\begin{aligned} 0 &= X_{\mathrm{CO_2}}^{\{1\}} - C_2\,\mathrm{R}_{\mathrm{meth}}^{\{1\}}, \\ 0 &= X_{\mathrm{CO_2}}^{\{2\}} - C_2\,\mathrm{R}_{\mathrm{meth}}^{\{2\}}, \end{aligned} \tag{3.14}$$

which can be solved consecutively (stage-wise) or simultaneously for $X_{\mathrm{CO_2}}^{\{1\}}$ and $X_{\mathrm{CO_2}}^{\{2\}}$ by root-finding algorithms (e.g., Newton-Raphson method). The solution of system (3.14) is illustrated in Fig. 3.8.

As seen on the left side of Fig. 3.8, the operating point (depicted by bullets) of each CSTR lies on a straight line in the R-X diagram. The unique intersection at any temperature proves, that no purely kinetic multiplicity ($\mathrm{C}_2^{\mathrm{m}}$ in Fig. 3.1) exists for the rate expressions used in this work. Since intraparticle and interfacial transport resistances are neglected

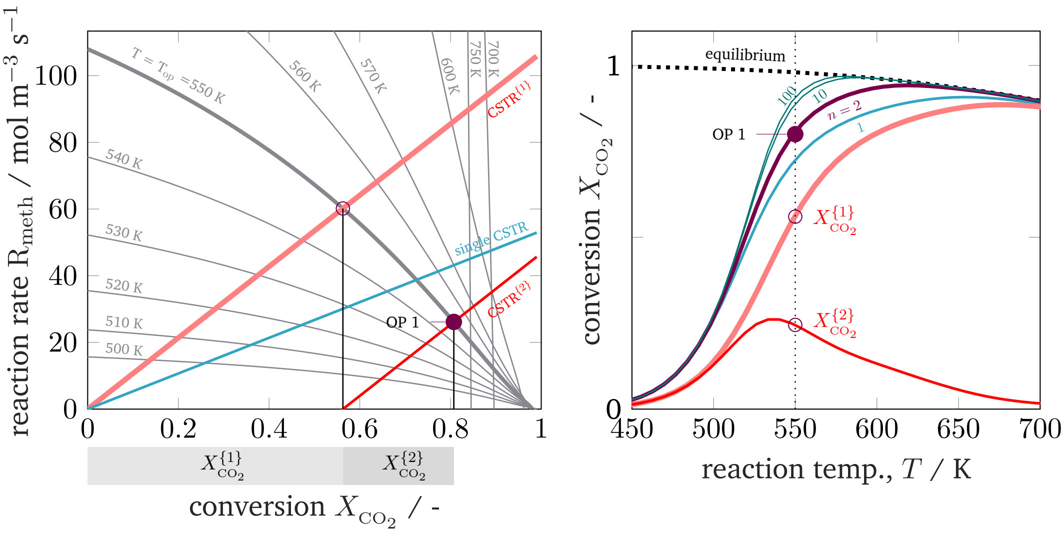

Fig. 3.8.: State-space diagram for a cascade of two isothermal CSTRs in the R-X (left) and X-T (right) plane, reference setting taken from Tab. A.1 on Page 123 but $T_{\mathrm{op}} = 550\,\mathrm{K}$.

($\eta_{\text{meth}} = 1$), the multiplicity sources $\mathrm{C}_1^{\mathrm{m}}$ and $\mathrm{C}_1^{\mathrm{e}}$ are also absent. This graphical analysis is also applicable to other reactions in order to check for these multiplicity sources. The right side of Fig. 3.8 depicts the stage operating range as well as the overall operating range for two CSTRs in series and compares it to scenarios with one, ten, and one hundred stages. The comparison shows the well-known tendency that the higher the stage number, the higher the conversion.

Two non-isothermal CSTRs

The operating points for a series of non-isothermal CSTRs are additionally determined by individual stage temperatures deviating from inlet and cooling temperature $T_{\text{in}} = T_{\text{cool}} \neq T^{\{i\}}$. Thus, the nonlinear equation system (3.14) needs to be extended by the stage energy balances in Eq. (3.13) such that

$$\begin{aligned}
0 &= X_{\mathrm{CO_2}}^{\{1\}} && - C_2\,\mathrm{R}_{\text{meth}}^{\{1\}},\\
0 &= X_{\mathrm{CO_2}}^{\{1\}}\,\Delta T_{\text{ad}}^{\{1\}} && + (1+\mathrm{St}_2)\,(T_{\text{op}}^{\{1\}} - T^{\{1\}}),\\
0 &= X_{\mathrm{CO_2}}^{\{2\}} && - C_2\,\mathrm{R}_{\text{meth}}^{\{2\}},\\
0 &= X_{\mathrm{CO_2}}^{\{2\}}\,\Delta T_{\text{ad}}^{\{2\}} && + (1+\mathrm{St}_2)\,(T_{\text{op}}^{\{2\}} - T^{\{2\}}).
\end{aligned} \tag{3.15}$$

This system can be solved again stage-wise or simultaneously for $X_{\mathrm{CO_2}}^{\{1\}}$, $X_{\mathrm{CO_2}}^{\{2\}}$,$T^{\{1\}}$, and $T^{\{2\}}$ by root-finding algorithms. The previous section showed that one single stage allows for up to three multiple solutions, which indicates that the CSTR cascade in (3.15) also generates multiple steady states. In theory, if each stage exhibits up to three multiple steady states (OP 1, 2, and 3), a total number of 3^n state combinations arise for the entire cascade. Standard root-finding algorithms, however, converge only to

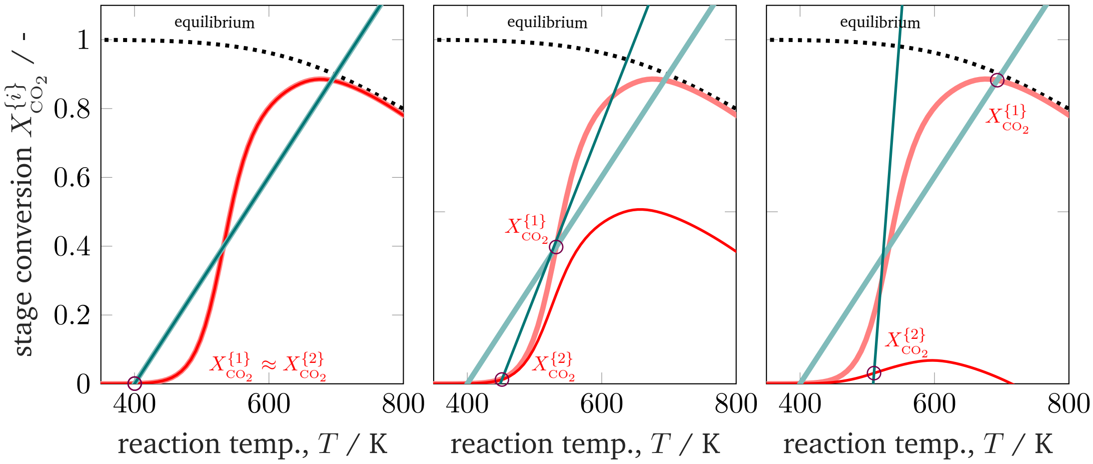

Fig. 3.9.: Graphical solution of a two-stage CSTR series with state combination [1-1], [2-1] and [3-1] (from left to right), reference setting taken from Tab. A.1 on Page 123 but $T_{\text{op}}^{\{1\}} = 400\,\mathrm{K}$ and $T_{\text{in}} = T_{\text{cool}}$.

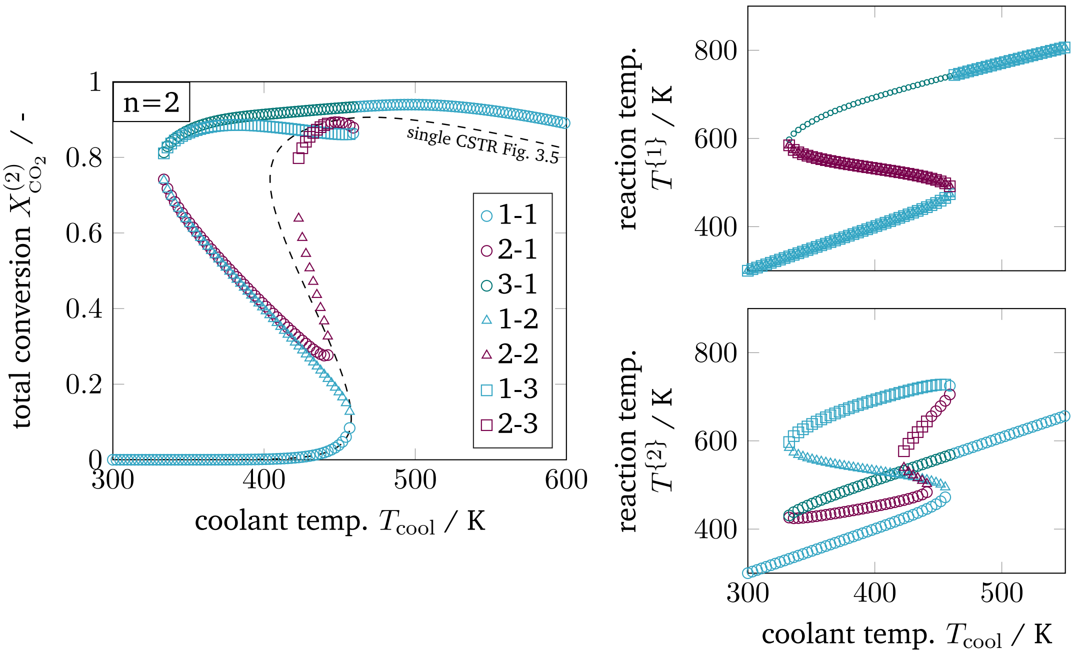

Fig. 3.10.: Enumerative solution of significant operating points in a two-stage CSTR series, reference setting taken from Tab. A.1 on Page 123 but $T_{\mathrm{in}} = T_{\mathrm{cool}}$. Note: T_{cool} is constant over the entire cascade, whereas T_{op} changes in each CSTR stage.

one local solution of system (3.15). Thus, finding all solutions requires further efforts, which is part of the following discussions.

The graphical solution of equation system (3.15) is shown in Fig. 3.9 considering three of nine possible combinations ([1-1], [2-1], [3-1]). This figure comprehensively shows how the first operating point influences its downstream stage. The more conversion is achieved within the first stage, the less remains within the next stage. Furthermore, the energy-based operating line (green) of the second stage becomes steeper due to the reduced ATR. Both effects simultaneously reduce the occurrence for multiplicities within the second stage, if the first stage operates at an ignited state (OP 2 or 3). Later, this will be an essential aspect to interpret solutions of multi-stage CSTRs. Enumerating all possible solutions within the relevant coolant temperature range leads to the results in Fig. 3.10.

Compared to the single CSTR, the hysteresis is more pronounced, and intermediate solutions emerge. Although combinatorics allows nine multiple steady states, only

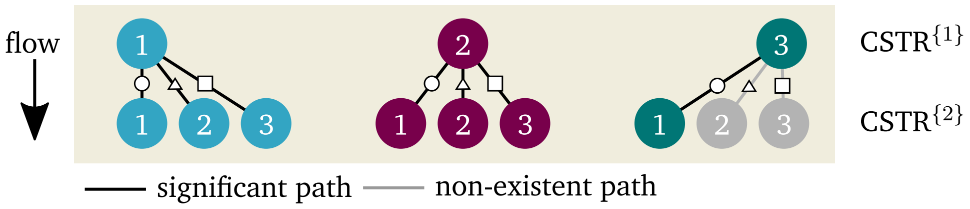

Fig. 3.11.: Possible state combinations for a two-stage CSTR cascade.

seven remain significant after enumeration. The combinations [3-2] and [3-3] cancel out, due to the previous discussions on Fig. 3.9. In addition, combinations [2-2] and [2-3] are rather seen as fragile because they exist in a very narrow operating range. In consequence, multiplicity driven by combinatorics is divided into significant and non-existing paths, as illustrated in Fig. 3.11.

These findings indicate that multiplicity in a CSTR cascade attributes only to a few stages. In order to confirm this hypothesis, a multi-stage cascade is analyzed in the following.

Multi-stage CSTR cascade

The enumeration effort of a multi-stage CSTR cascade increases exponentially with the number of stages if all possible combinations are taken into account. With six stages, there exist already $3^6{=}729$ state combinations for all coolant temperature increments (here 300), leading to over 200'000 solver runs. Although a brute force enumeration would provide all solutions, many of them will be insignificant, due to missing physical constraints. Thus, a more elegant way is the use of bifurcation theory and numerical continuation techniques, which track solution branches according to slight parameter changes (e.g., coolant temperature) within a predefined range. During these changes, the eigenvalues of the linearized system equations may change such that the system becomes unstable. The shift to instability occurs if some eigenvalues cross the imaginary axis. At this point, bifurcation can take place from which new branches spread. However, this method also suffers from extensive computational efforts due to the eigenvalue calculation and possible inaccuracies of the systems Jacobian close to the bifurcation point. Furthermore, there is no guarantee that this method obtains all solutions. More details on bifurcation theory and numerical continuation techniques can be found in [HP81; JR82; KM83; WE95].

In this work, the enumeration of all solutions was found to be the more convenient and illustrative approach. It is shown that the non-existent solutions can be excluded already in advance. Together with efficient nonlinear computation techniques (here provided by CasADi [And+18]) the enumeration of all solutions with reasonable computational effort becomes feasible. Accordingly, the results for three to six CSTRs in series are illustrated in Fig. 3.12.

Most importantly, the solutions in Fig. 3.12 aggregate in three main clusters forming - similar to a single CSTR - a stable ignition and extinction branch (IB and EB), as well as an unstable intermediate branch. The number of multiple steady states increases with increasing stage number n, but most solutions persistently converge to the three main clusters. Once again, each relevant solution has not more than two stages exhibiting multiplicity. Cascades with more stages as represented by Fig. 3.14 confirm that two stages are sufficient to map the dominating state clusters. These two stages are further

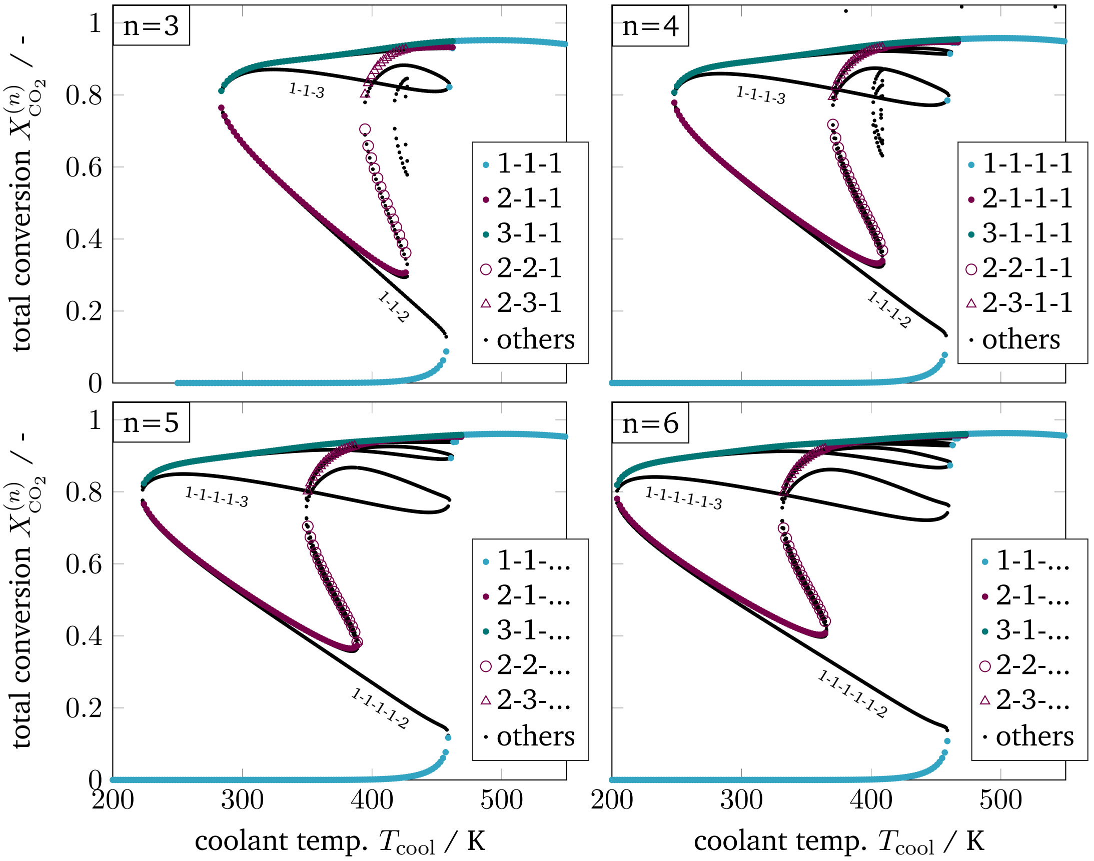

Fig. 3.12.: Enumerative solution of operating points (OP) in a multi-stage CSTR cascade, color - OPs of two key stages at the inlet, black - OPs of subordinate branches, reference setting taken from Tab. A.1 on Page 123 but $T_{\mathrm{in}} = T_{\mathrm{cool}}$.

on denoted as *key stages*, which may exist at any position within the cascade. The key stage solutions directly at the inlet are colored in Fig. 3.12. Solutions with the same key stage combination but different locations along the cascade aggregate within the same cluster. For instance, the upper IB is covered by n [...1-3-1...] combinations, the middle unstable branch is covered by n [...1-2-1...] combinations, and the lower EB is covered by n [...1-1-1...] combinations. Again $n-1$ [...1-2-2-1...] and $n-1$ [...1-2-3-1...] fragile

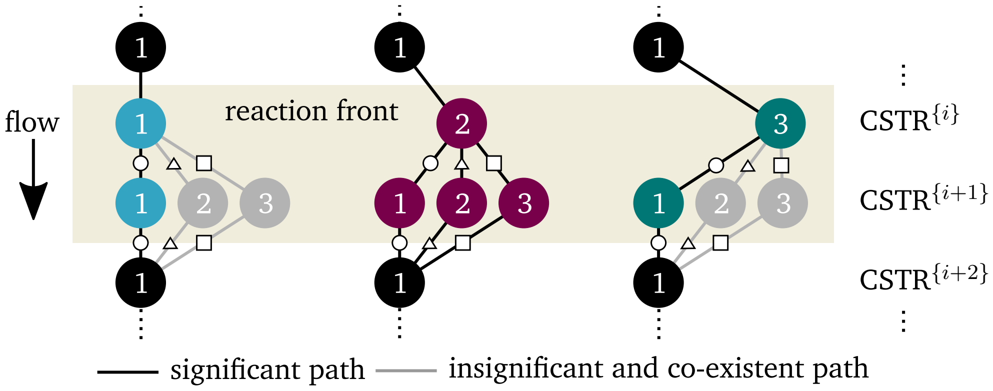
flow
reaction front
1
2
3
$\mathrm{CSTR}^{\{i\}}$
$\mathrm{CSTR}^{\{i+1\}}$
$\mathrm{CSTR}^{\{i+2\}}$
significant path
insignificant and co-existent path

Fig. 3.13.: Possible state combinations of a multi-stage CSTR cascade with two key stages.

combinations exist but appear only in a narrow operating range. This clustering can be explained by the insignificance of previous stages at the extinguished state [···1···]. The insignificance partly eliminates if the inlet and coolant temperature of the cascade differ, which is, however, not considered here. Beyond that, subordinate branches (in black) develop from the last stage ([···1-2], [···1-3]). These observations are summarized in the pathway structure of Fig. 3.13, showing the relevant state combinations of a multi-stage CSTR cascade.

As illustrated in Fig. 3.14, the clustering of all key stage solutions still remains for higher stage numbers. It was found that the hysteresis loop widens significantly with increasing stage number. However, after reaching a certain stage number, the hysteresis loop degenerates again until it finally disappears. Furthermore, different shapes of the unstable intermediate branch emerge, depending on the parameter setting. The unstable branch evolves more or less pronounced, as indicated by variations of the residence time in Fig. 3.14. This is in particular relevant if an operation at these unstable branches is aspired [BS19].

Technically, key stages are the analogy of narrow reaction fronts in real fixed-bed reactors. Those fronts often develop within a very short reactor segment, preferably close to the reactor inlet. Considering this, the key stages become less likely if they are located further downstream, which curtails the relevance of the black subordinate branches associated with the last stage. In real reactors, the actual reaction front position is typically determined by second-order effects (e.g., preheating, dispersion, flow maldistribution, heat conduction within the reactor jacket).

From all this, the following three-level hierarchy of thermo-kinetic multiplicity in fixed-bed reactors can be drawn:

assumption	multiplicity in all stages		two key stages (reaction front)		cluster formation
max # MSS	3^n	$\Longrightarrow$	$4\,n - 1$	$\Longrightarrow$	3 to 5

Moving from left to right considers more physical details and approaches the situation in real fixed-bed reactors. This three-level hierarchy compromises many different and controversial opinions found in the literature (see Section 3.1.1). For instance, the findings of Eigenberger [Eig72a; Eig72b] reporting only 3-5 multiple steady states are mainly associated with cluster formation, whereas studies that report an infinite number of multiple steady states (for $n \to \infty$) neglect clustering and count each state separately.

So far, state clustering and its connection to reaction fronts and multiplicity in real reactors is rather disregarded in literature. One reason might be the missing availability for efficient numerical tools, which have only been accessible in recent years. Since

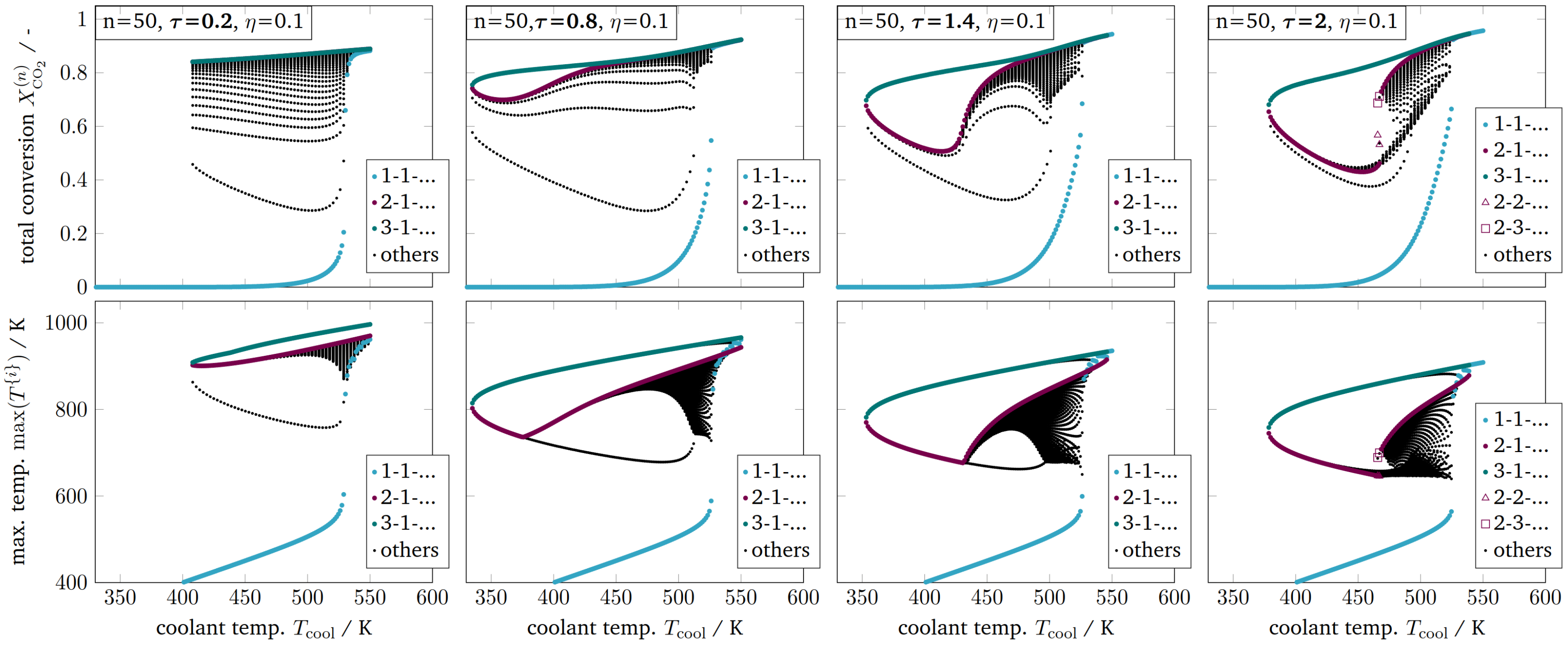

Fig. 3.14.: Enumerative solution of operating points (OP) in a multi-stage CSTR cascade with varying residence time, color - OPs of two key stages at the inlet, black - OPs of subordinate branches, reference setting taken from Tab. A.1 on Page 123 but $T_{in} = T_{cool}$.

the previous considerations mainly address multiplicity trends, it remains to be shown under which conditions uniqueness applies.

Until today, an exact uniqueness criterion for non-isothermal fixed-bed reactors largely remains an open question [Doc18]. The axial dispersion model has been a favorite target for extensive mathematical analyses but often limited to first-order reactions under isothermal conditions [Sch75; Var80; AR91]. However, numerous studies provide qualitative trends pointing in similar directions. For instance, Jensen and Ray [JR82] summarized, that the solution will be unique for sufficiently high Bodenstein numbers, large heat transfer coefficients, or small Damköhler numbers. The previous results are very much in line with these qualitative trends, but moreover, they reveal novel, generalized criteria for stability, uniqueness, and multiplicity of non-isothermal fixed-bed reactors. These criteria are derived in the following.

3.1.4 Novel Stability, Uniqueness, and Multiplicity Criteria

The observations from above show that the thermo-kinetic multiplicity feature of the first stage is entirely capable of representing the three main state clusters. Consequently, if the first stage is free of multiplicity, then all following stages are also free of multiplicity. This key feature enables the criteria of the first CSTR stage (see Eqs. (3.9) to (3.11)) to be assigned to the entire CSTR cascade (cell model) according to

$$\begin{aligned}
&\text{stability (CM):} & & & \frac{\mathrm{d}\,X^{\{1\}}}{\mathrm{d}\,T} &< \frac{1+\frac{\mathrm{St}}{n}}{\Delta T_{\mathrm{ad}}^{\{1\}}},\\
&\text{uniqueness (CM):} & \max_{T\in\mathcal{O}} \frac{\mathrm{d}\,X^{\{1\}}}{\mathrm{d}\,T} &= & \left.\frac{\mathrm{d}\,X^{\{1\}}}{\mathrm{d}\,T}\right|_{T=T^*} &\leq \frac{1+\frac{\mathrm{St}}{n}}{\Delta T_{\mathrm{ad}}^{\{1\}}},\\
&\text{multiplicity (CM):} & \max_{T\in\mathcal{O}} \frac{\mathrm{d}\,X^{\{1\}}}{\mathrm{d}\,T} &= & \left.\frac{\mathrm{d}\,X^{\{1\}}}{\mathrm{d}\,T}\right|_{T=T^*} &> \frac{1+\frac{\mathrm{St}}{n}}{\Delta T_{\mathrm{ad}}^{\{1\}}},
\end{aligned}$$

with $T = T^*$ as inflection point of Eq. (3.12) corresponding to the steepest conversion gradient. For simplicity, the index CO_2 is omitted here and in the following.

Consequently, in the absence of purely kinetic and isothermal multiplicity, uniqueness in non-isothermal CSTR cascades boils down to very few key parameters, lumped together as mass- and energy-based thermal sensitivity. Both sensitivities are evaluated in Fig. 3.15 with respect to the methanation reference setting of Tab. A.1 on Page 123.

According to the reference setting in Fig. 3.15, uniqueness can only be guaranteed for cascades with several thousand stages. This fact still applies to a wide range of heat transfer and catalyst activity, as indicated by variations of the Stanton number and effectiveness factor. Intensified heat transfer mainly affects cascades with higher back-mixing and leads to reduced multiplicity regions. In some scenarios, uniqueness is guaranteed for low and high back-mixing conditions, but not for the intermediates (e.g.,

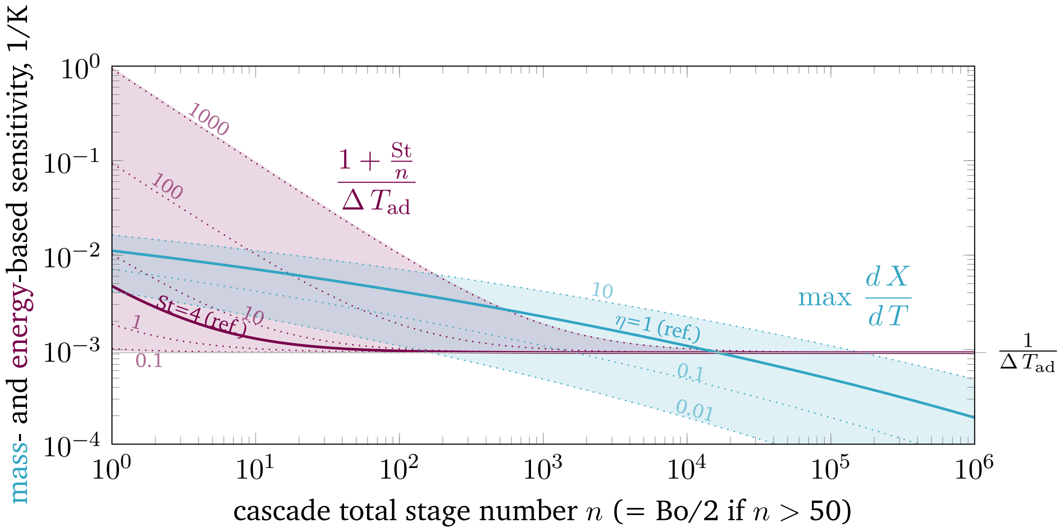

Fig. 3.15.: First stage mass and energy-based sensitivity for non-isothermal CSTR cascades with various stage number, effectiveness factor and Stanton number, reference setting taken from Tab. A.1 on Page 123.

for St=100 and η=1). In contrast, reducing the ATR (e.g., via product gas recycling, or dilution) always leads to diminished multiplicity regions. At adiabatic conditions ($\mathrm{St} \to 0$), back-mixing does not influence the energy-based thermal sensitivity, and uniqueness becomes solely determined by the mass-based thermal sensitivity and the ATR. Not shown is the influence of the remaining key parameters, pressure and residence time. However, both are indirectly incorporated into the Stanton number and effectiveness factor.

The equivalence of stage and Bodenstein number in Eq. (3.5) at low back-mixing ($\mathrm{Bo} > 100$) allows for transition from cell to dispersion models[1]. Therefore, the *surrogate conversion* $\tilde{X}$ is introduced which allows for applying the first stage mass balance from Eq. (3.12) to dispersion models according to

$$\tilde{X} = \frac{2}{\mathrm{Bo}} \frac{\tau}{\varepsilon\, c_{\mathrm{in}}} \mathrm{R} = C_{\mathrm{Bo}}\, \mathrm{R}, \tag{3.16}$$

which is then used to calculate the mass-based thermal sensitivity of a fixed-bed reactor. Together with the adapted energy-based thermal sensitivity from Eq. (3.13) at elevated Bodenstein numbers ($\mathrm{Bo} > 100$) the previous criteria read as

---

[1] This equivalence is exploited when finite volume schemes are used to solve dispersion models numerically. The corresponding number of finite volumes in flow direction inherently contains a certain degree of back-mixing. If the number of finite volumes is too low, an artificial dispersion (so-called numerical diffusion) will superimpose other dispersion components included in the model.

$$\text{stability (DM):} \qquad \frac{\mathrm{d}\,\tilde{X}}{\mathrm{d}\,T} < \frac{1+\frac{2\,\mathrm{St}}{\mathrm{Bo}}}{\Delta\,T_{\mathrm{ad,in}}}, \tag{3.17}$$

$$\text{uniqueness (DM):} \qquad \max_{T\in\mathcal{O}} \frac{\mathrm{d}\,\tilde{X}}{\mathrm{d}\,T} = \left.\frac{\mathrm{d}\,\tilde{X}}{\mathrm{d}\,T}\right|_{T=T^*} \leq \frac{1+\frac{2\,\mathrm{St}}{\mathrm{Bo}}}{\Delta\,T_{\mathrm{ad,in}}}, \tag{3.18}$$

$$\text{multiplicity (DM):} \qquad \max_{T\in\mathcal{O}} \frac{\mathrm{d}\,\tilde{X}}{\mathrm{d}\,T} = \left.\frac{\mathrm{d}\,\tilde{X}}{\mathrm{d}\,T}\right|_{T=T^*} > \frac{1+\frac{2\,\mathrm{St}}{\mathrm{Bo}}}{\Delta\,T_{\mathrm{ad,in}}}, \tag{3.19}$$

with $T = T^*$ as inflection point of Eq. (3.16) corresponding to the steepest conversion gradient. The evaluation of the reference setting from Tab. A.1 on Page 123 leads to the same results as in Fig. 3.15 with $n = \mathrm{Bo}/2$.

The generalized Criteria 3.17, 3.18, and 3.19 have not been found in literature yet. They can be used as an a priori estimate for any exothermic reaction and reactors at any scale, only requiring apparent rate expression, coolant heat transfer coefficient, inlet condition, and back-mixing intensity. Note that no expensive computation of the entire dispersion model is required, which makes it easy to use for reactor design, operation, and safety analysis. The criteria, however, demand for a representative Bodenstein number either mass or energy-based. As illustrated in Section 3.1.1, the energy feedback is of major interest for thermo-kinetic multiplicity, which indicates that the three to ten times smaller energy-based Bodenstein number is the most reasonable choice. Further discussions on the magnitude of these numbers will continue below in Section 3.2.2. Furthermore, the here proposed criteria recommend considering axial dispersion even for high Bodenstein numbers beyond 400. This is contrary to commonly accepted criteria of Hlaváček and Marek [HM66], Mears [Mea76], Young and Finlayson [YF73], and others [MAC09], which did neither consider multiplicity nor reactor stability and runaway.

In order to access the mass-based sensitivity on the left, the total differential applied to the implicit Eq. (3.16) is determined:

$$0 = \frac{\mathrm{d}\,\tilde{X}}{\mathrm{d}\,T} - C_{\mathrm{Bo}} \frac{\mathrm{d}\,\mathrm{R}}{\mathrm{d}\,T} = \frac{\mathrm{d}\,\tilde{X}}{\mathrm{d}\,T} - C_{\mathrm{Bo}} \left(\frac{\partial\,\mathrm{R}}{\partial\,T} + \frac{\partial\,\mathrm{R}}{\partial\,\tilde{X}} \frac{\mathrm{d}\,\tilde{X}}{\mathrm{d}\,T} \right).$$

Consequently, the sensitivity is represented by

$$\frac{\mathrm{d}\,\tilde{X}}{\mathrm{d}\,T} = \frac{C_{\mathrm{Bo}}\,\frac{\partial\,\mathrm{R}}{\partial\,T}}{1 - C_{\mathrm{Bo}}\,\frac{\partial\,\mathrm{R}}{\partial\,\tilde{X}}}. \tag{3.20}$$

Thus, the mass-based sensitivity only requires valid reaction rates, their partial derivatives and the main reactor parameters used in Eq. (3.16).

For first-order, equimolar reactions, the Damköhler number from Eq. (A.5) on Page 120 can be used to further simplify Eq. (3.20) via

$$\begin{aligned} \tilde{X} &= \frac{2}{\mathrm{Bo}}\,\mathrm{Da_I}\,(1-\tilde{X}) && = \frac{\frac{2}{\mathrm{Bo}}\,\mathrm{Da_I}}{1+\frac{2}{\mathrm{Bo}}\,\mathrm{Da_I}}, \\ \frac{\mathrm{d}\,\tilde{X}}{\mathrm{d}\,T} &= \frac{\frac{2}{\mathrm{Bo}}\,\mathrm{Da_I}}{1+\frac{2}{\mathrm{Bo}}\,\mathrm{Da_I}}\,(1-\tilde{X})\,\frac{E_\mathrm{A}}{\mathcal{R}T^2} && = \frac{\frac{2}{\mathrm{Bo}}\,\mathrm{Da_I}}{(1+\frac{2}{\mathrm{Bo}}\,\mathrm{Da_I})^2}\,\frac{E_\mathrm{A}}{\mathcal{R}T^2}. \end{aligned} \tag{3.21}$$

With Eq. (3.21), the mass-based sensitivity can be evaluated within the relevant temperature range to identify the maximum gradient at T^* and $\mathrm{Da_I^*}$. Thus, there is no further need to solve the implicit Eq. (3.16). Note that the here used Damköhler number remains as a function of temperature such that the above criteria condense to

$$\text{stability (1}^{\text{st}}\text{-order, equimolar):} \qquad \frac{\frac{2}{\mathrm{Bo}}\,\mathrm{Da_I}}{(1+\frac{2}{\mathrm{Bo}}\,\mathrm{Da_I})^2}\,\frac{E_\mathrm{A}}{\mathcal{R}T^2} < \frac{1+\frac{2\,\mathrm{St}}{\mathrm{Bo}}}{\Delta\,T_\mathrm{ad,in}}, \tag{3.22}$$

$$\text{uniqueness (1}^{\text{st}}\text{-order, equimolar):} \qquad \frac{\frac{2}{\mathrm{Bo}}\,\mathrm{Da_I^*}}{(1+\frac{2}{\mathrm{Bo}}\,\mathrm{Da_I^*})^2}\,\frac{E_\mathrm{A}}{\mathcal{R}T^{*2}} \leq \frac{1+\frac{2\,\mathrm{St}}{\mathrm{Bo}}}{\Delta\,T_\mathrm{ad,in}}, \tag{3.23}$$

$$\text{multiplicity (1}^{\text{st}}\text{-order, equimolar):} \qquad \frac{\frac{2}{\mathrm{Bo}}\,\mathrm{Da_I^*}}{(1+\frac{2}{\mathrm{Bo}}\,\mathrm{Da_I^*})^2}\,\frac{E_\mathrm{A}}{\mathcal{R}T^{*2}} > \frac{1+\frac{2\,\mathrm{St}}{\mathrm{Bo}}}{\Delta\,T_\mathrm{ad,in}}, \tag{3.24}$$

with T^* and $\mathrm{Da_I^*}$ as arguments of the maximum gradient of Eq. (3.21). Although these simplified criteria are not adequately applicable for methanation due to the strong influence of the thermodynamic equilibrium, they comprehensively show how the key parameters affect multiplicity. At the beginning of this section, the current state in the literature was highlighted to be rather qualitative. The statement of Jensen and Ray [JR82] saying that the solution will be unique for sufficiently high Bodenstein numbers ($\mathrm{Bo} \to \infty$), large heat transfer coefficients ($\mathrm{St} \to \infty$), or small Damköhler numbers ($\mathrm{Da} \to 0$) is perfectly represented by the Criteria 3.23 and 3.24. Furthermore, the limiting case of an adiabatic CSTR ($\mathrm{St} \to 0$, $\mathrm{Bo}/2 \to 1$) applied to (3.22) is equivalent to the stability criterion presented by Kimura and Levenspiel [KL77].

In extension to the infinite back-mixing case in Section 3.1.2, it can be confirmed that stability and uniqueness are closely related even for finite back-mixing. However, the finite back-mixing case ($1 < \mathrm{Bo}/2 < \infty$) is typically not considered in the literature [Sze+07; KV19], or was even found to be insignificant [BKN95] for stability analysis. In contrast, this work shows a distinct relevance of multiplicity for real reactors, so that back-mixing must also be highly relevant for stability, runaway, and parametric sensitivity. In this regard, the quantitative description of all features results in the novel Criteria proposed in this chapter.

In summary to this section, the multiplicity of non-isothermal fixed-bed reactors has proven to be a decisive phenomenon. Ignoring multiplicity would disregard a broad operating range and thus a substantial potential for flexible operation. Due to the close connection between multiplicity, stability, and parametric sensitivity, the here derived criteria are highly relevant and applicable to any exothermic reaction and reactors at any scale. To further demonstrate the relevance of multiplicity, a rigorous dynamic reactor model for catalytic methanation is presented in the next section.

3.2 Detailed Dynamic Fixed-Bed Reactor Model

To enable a detailed analysis of the entire reactor interior under steady and dynamic conditions, a multi-level, two-dimensional, pseudo-homogeneous reactor model with axial dispersion is derived. Therefore, mass and energy balances according to Eqs. (3.2) and (3.3) are applied to a cylindrical reactor geometry as illustrated in Fig. 3.16. Due to the symmetry any variations in φ-direction are neglected. Considering these assumptions, the following partial differential equation (PDE) system remains:

$$\begin{aligned} \varepsilon\, \rho_{\text{gas}} \frac{\partial w_\alpha}{\partial t} = -\rho_{\text{gas}}\, v_z \frac{\partial w_\alpha}{\partial z} - \frac{\partial (j_{z,\alpha})}{\partial z} - \frac{1}{r}\frac{\partial (j_{r,\alpha}\, r)}{\partial r} \\ + (1-\varepsilon)\ \eta_{\text{meth}}\, M_\alpha \sum_\beta \nu_{\alpha,\beta}\, \tilde{\mathrm{r}}_\beta, \end{aligned} \tag{3.25}$$

$$\begin{aligned} (\rho c_p)^{\text{eff}} \frac{\partial T}{\partial t} = -\sum_\alpha \rho_\alpha c_{p,\alpha} v_z \frac{\partial T}{\partial z} - \frac{\partial (\dot{q}_z)}{\partial z} - \frac{1}{r}\frac{\partial (\dot{q}_r\, r)}{\partial r} \\ + (1-\varepsilon)\ \eta_{\text{meth}} \sum_\beta \left(-\Delta_R \tilde{H}_\beta\right) \tilde{\mathrm{r}}_\beta. \end{aligned} \tag{3.26}$$

All components $\alpha \in \{\mathrm{CH_4}, \mathrm{CO}, \mathrm{CO_2}, \mathrm{H_2O}, \mathrm{H_2}, \mathrm{N_2}\}$ and reactions β (carbon dioxide methanation 2.1, carbon monoxide methanation 2.2, RWGS 2.3) on the catalyst side are jointly considered in a pseudo-homogeneous phase. In accordance with the criterion $\frac{2R}{d_\mathrm{p}} \geq 10$ plug-flow behavior with negligible flow-induced wall effects is assumed for mass transport [Pér00]. The model considers gas velocity changes exclusively as a result of the mole reduction due to reaction. As the overall axial mass flow remains constant, the following equation holds:

$$v_z = v_{z,\text{in}} \frac{\rho_{\text{in}}}{\rho}. \tag{3.27}$$

The remaining physical properties and correlations are summarized in Appendix A.3.1 on Page 127.

To solve Eqs. (3.25) and (3.26) over the entire two-dimensional model domain illustrated in Fig. 3.16 (top), the following boundary conditions at $r = R$ and $z = 0$ hold:

$$\begin{aligned} \left.\frac{\partial \rho_\alpha}{\partial r}\right|_{r=R} &= 0\,, & \rho_\alpha|_{z=0} &= \rho_{\alpha,\text{in}}\,, \\ \left.\frac{\partial T}{\partial r}\right|_{r=R} &= \frac{\mathrm{k_W}}{R\ \lambda_r^{\text{eff}}|_{r=R}} \left(T_{\text{cool}} - T|_{r=R}\right), & T|_{z=0} &= T_{\text{in}}. \end{aligned} \tag{3.28}$$

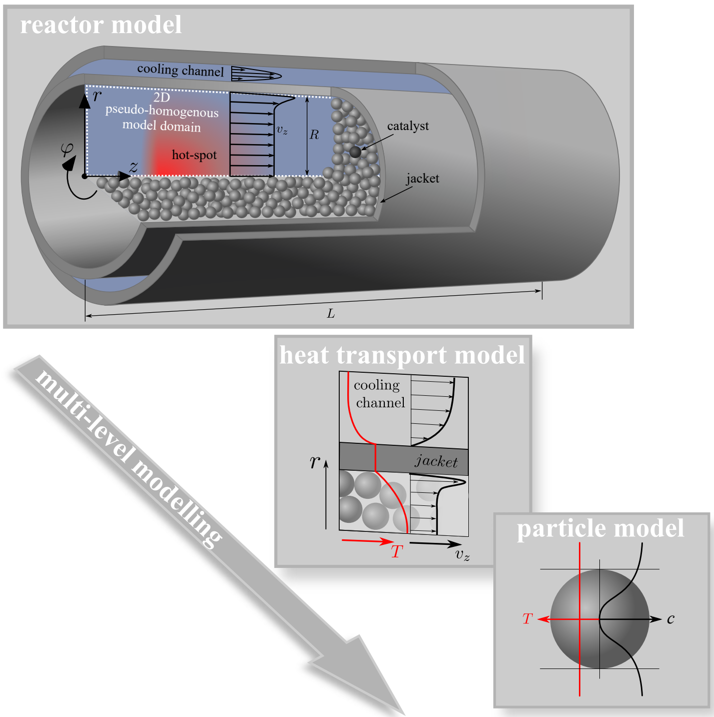
reactor model
cooling channel
r
2D
pseudo-homogenous
model domain
hot-spot
φ
z
v_z
R
catalyst
jacket
L
heat transport model
cooling
channel
jacket
r
T
v_z
particle model
T
c
multi-level modelling

Fig. 3.16.: Schematic illustration of the fixed-bed reactor model.

Furthermore, initial conditions at $t = 0$ are set according to the dynamic case (e.g., start-up, disturbance, step change), respectively.

The single reactor tube in Fig. 3.16 can be considered as part of a typical industrial-scale bundle configuration. The tube design as well as reference operating parameters are summarized in Tab. 3.2. Appendix A.4 on Page 133 illustrates the corresponding reference reactor state, including all its relevant characteristics. The major performance parameter used in this work are bed temperature and carbon dioxide conversion as stated in Eq. (A.2) on Page 120.

In the following, more details regarding reaction kinetics, mass and heat transport, catalyst diffusion limitation, as well as computational aspects are discussed.

3.2.1 Reaction Kinetics

In accordance with Section 2.1, the model deals with two different kinetic models for nickel-promoted carbon dioxide methanation: from Koschany et al. [KSH16] (very active, thermally sensitive) and Xu and Froment [XF89] (less active, thermally less sensitive). The consideration of both studies allows a better comparability and placement among other studies [SH14; KT15]. However, the reference kinetic model for most of the results presented in this work, are based on Koschany et al. [KSH16] due to the recent trend towards specialized methanation catalysts. In addition, the usage of two different kinetic approaches can be also seen as a variation of the catalyst activity,

Tab. 3.2.: Specifications and operating parameter for the reactor model reference case.

parameter	symbol	value	unit	source
inner reactor radius	R	0.01	m	
reactor length	L	2.5	m	
wall thickness	δ_{jac}	0.002	m	
wall thermal conductivity	λ_{jac}	20	W/(m K)	stainless steel
fixed-bed void fraction	ε	0.4		
cat. particle diameter	d_{p}	0.002	m	
cat. density (porous)	ρ_{cat}	2355.2	kg/m^3	[XF89]
cat. heat capacity (nonporous)	$c_{p,\mathrm{cat}}$	1107	J/(kg K)	[OGR10]
cat. emmisivity	ϵ_{cat}	0.9		
cat. thermal conductivity	λ_{cat}	3.6	W/(m K)	[FKD15; Kie17]
cat. tortuosity	τ_{p}	2		
cat. porosity	ε_{p}	0.6		
cat. pore diameter	d_{pore}	10	nm	
superficial velocity	v_z	1	m/s	
inlet pressure	p_{in}	5	bar	
inlet temperature	T_{in}	300	K	
inlet molar ratio	$H_2 : CO_2$	4:1	(undiluted)	
coolant heat transfer coefficient	α_{cool}	500	W/(m^2 K)	Appendix A.3.2
gas hourly space velocity	$\mathrm{GHSV}_{\mathrm{STP}}$	7200	1/h	
overall heat removal	$\dot{Q}_{\mathrm{cool}}^{\mathrm{tot}}$	1.7	kW	
intrinsic reaction kinetics				[KSH16]

which is closely related to possible catalyst degradation influences (e.g., at long-term operation).

The reference kinetic model (without particle transport limitations) from Koschany et al. [KSH16] relies on an LHHW-type rate equation, measured and parametrized for a broad range of conditions (453 - 613 K; 1 - 9 bar; stoichiometric and non-stoichiometric feed).

$$\mathrm{r}_{\mathrm{meth}} = k\, p_{\mathrm{CO_2}}^{0.5}\, p_{\mathrm{H_2}}^{0.5} \left(1 - \frac{p_{\mathrm{CH_4}}\, p_{\mathrm{H_2O}}^{2}}{K_{\mathrm{eq}}\, p_{\mathrm{CO_2}}\, p_{\mathrm{H_2}}^{4}}\right) \Big/ \mathrm{DEN}^2, \tag{3.29}$$

$$\mathrm{DEN} = 1 + K_{\mathrm{OH}} \frac{p_{\mathrm{H_2O}}}{p_{\mathrm{H_2}}^{0.5}} + K_{\mathrm{H_2}}\, p_{\mathrm{H_2}}^{0.5} + K_{\mathrm{mix}}\, p_{\mathrm{CO_2}}^{0.5}. \tag{3.30}$$

Although this rate equation was determined for a limited temperature range, extrapolation is possible. For higher temperatures, the reaction rates are limited by the chemical equilibrium (thermodynamically limited) and at lower temperatures the reaction rates approach zero (kinetically limited). The important temperature range is right between these two limiting cases and accordingly covered by Koschany et al. [KSH16]. Further details on all relevant correlations necessary to implement Eqs. (3.29) and (3.30) are outlined in Appendix A.3.3 on Page 130. There, more details on the rate equations according to Xu and Froment [XF89] are also given.

3.2.2 Mass and Heat Transport Assumptions

Throughout the entire pseudo-homogeneous phase, radial and axial heat and mass transfer is described by effective dispersion fluxes, such that

$$j_{r,\alpha} = -\rho_{\text{gas}}\, \mathcal{D}^{\text{eff}}_{r,\alpha} \frac{\partial w_\alpha}{\partial r}, \quad \dot{q}_r = -\lambda^{\text{eff}}_r \frac{\partial T}{\partial r}\,, \tag{3.31}$$

$$j_{z,\alpha} = -\rho_{\text{gas}}\, \mathcal{D}^{\text{eff}}_{z,\alpha} \frac{\partial w_\alpha}{\partial z}, \quad \dot{q}_z = -\lambda^{\text{eff}}_z \frac{\partial T}{\partial z}\,. \tag{3.32}$$

Details regarding the radial dispersion coefficients in Eq. (3.31) are given in Appendix A.3.1 on Page 127. As shown in the previous section, the axial transport in Eq. (3.32) is decisive for the operation of exothermic fixed-bed reactors and requires careful evaluation.

The introduced mass and energy-based Bodenstein numbers from Eq. (3.4) account for the effective transport coefficients and read

$$\text{Bo}^{\text{m}} = \frac{v_z\, L}{\mathcal{D}^{\text{eff}}_{z,\alpha}}, \quad \text{Bo}^{\text{e}} = \frac{v_z\, \rho_{\text{gas}}\, c_{p,\text{gas}}\, L}{\lambda^{\text{eff}}_z}\,. \tag{3.33}$$

Correspondingly, the mass and energy-based Péclet number only differs in the characteristic length

$$\text{Pe}^{\text{m,e}}_z = \frac{\text{Bo}^{\text{m,e}}\, d_{\text{p}}}{L}\,. \tag{3.34}$$

For high particle Reynolds numbers ($\text{Re}_{\text{p}} > 10$ - typical for catalytic reactors of industrial-scale, this work: $\text{Re}_{\text{p}} = 100$-$300$) the axial mass Péclet number converges to a constant value: $\text{Pe}^{\text{m}}_z \rightarrow 2$ [ER68; Del06; Fre08]. Under industrial conditions, the ratio of bed length to particle diameter easily reaches values of 500 and more. Are these values applied to Eq. (3.34), a mass-based Bodenstein number results with magnitudes in the order of 1000 and higher. Conventional criteria would suggest neglecting mass dispersion under such conditions [Pér00; MAC09].

In order to account for axial heat dispersion, Dixon and Cresswell [DC79] proposed for large $\frac{2R}{d_{\text{p}}}$ ratios to rely on

$$\frac{1}{\text{Pe}^{\text{e}}_z} = \frac{1}{\text{Pe}^{\text{m}}_z} + \frac{\frac{\lambda_{\text{bed}}}{\lambda_{\text{gas}}}}{\text{Re}_{\text{p}}\,\text{Pr}} \quad \text{with} \quad \text{Re}_{\text{p}} = \frac{v_z\, d_{\text{p}}}{\nu_{\text{gas}}}\,, \quad \text{Pr} = \frac{\nu_{\text{gas}}\, \rho_{\text{gas}}\, c_{\text{p,gas}}}{\lambda_{\text{gas}}}. \tag{3.35}$$

This is in accordance with correlations described by Tsotsas [Tso10] if the previous assumption $\text{Pe}^{\text{m}}_z \rightarrow 2$ holds. The conductivities λ_{bed} and λ_{gas} are equivalent to $\lambda_{\text{cond,r}}$ and λ_{gas} in Eqs. (A.19) and (A.20) on Page 128 as part of the effective radial heat conduction according to Bauer and Schlünder [BS78a]. However, to what extent axial heat dispersion influences the reactor behavior is just rarely studied [Eig72a; Pus+81]. With the reference reactor configuration in Tab. 3.2, the components of Eqs. (3.33) and (3.34) are illustrated in Fig. A.7 on Page 135 and reveal energy-based Péclet numbers in the range of 1.65 to 1.85. Using the same ratio of bed length to particle diameter again leads to energy-based Bodenstein numbers from 825 to 925, which is slightly lower than the estimated mass-based Bodenstein number. Therefore, a three to ten times higher energy dispersion, as reported in the literature (see Section 3.1), cannot be confirmed for the conditions in this work.

The similarity of both numbers indicates that the conductive term in Eq. (3.35) is subordinate and energy back-mixing results primarily from back-mixing of mass. So if conventional criteria (see Mederos et al. [MAC09]) suggest to exclude axial mass dispersion, this also holds for axial energy dispersion. However, the theoretical elaborations in Section 3.1 clearly emphasize the relevance of dispersion even for Bodenstein numbers of the above considered magnitude. The required numerical treatment of the dispersion term within the model will be discussed in Section 3.2.3.

Reactor jacket cooling

This work considers thermal oil as heat transfer medium flowing through the cooling channel (see Fig. 3.16). Thereby, the respective heat transport assumptions (represented via $\mathrm{k_w}$) are of major importance. According to Eq. (3.28), the coolant temperature remains constant between inlet and outlet. Two facts justify this assumption: First, the high coolant velocities, which are required to minimize the thermal resistances within the cooling channel. Second, the high heat capacities of liquid coolants (e.g., thermal oil, molten salt). Nevertheless, the thermal resistance of the cooling channel needs to be considered along with the interface resistance at the inner side of the jacket due to wall effects of the gas flow. Therefore, this work makes use of the α_w-model as described in [TS90; Tso10]. Although the jacket itself is rather irrelevant for the overall heat transport resistance, this term is still considered for the sake of completeness. In summary, the following series of thermal resistances are considered in Eq. (3.28):

$$\frac{1}{\mathrm{k_w}} = \frac{1}{\alpha_\mathrm{w}\, R} + \frac{1}{\mathrm{k_{jac}}} + \frac{1}{\alpha_\mathrm{cool}\,(R + \delta_\mathrm{jac})}\,. \tag{3.36}$$

Details regarding α_w, $\mathrm{k_{jac}}$, and α_cool are outlined in Appendix A.3.2 on Page 129. The corresponding coolant Nusselt number range indicates that the heat transfer coefficient in Tab. 3.2 of $\alpha_\mathrm{cool} = 500\,\mathrm{W/(m^2\,K)}$ is reasonable, but approximately four times lower than reported in other studies [SH14; DBB17; MRG18]. Higher values are certainly attainable for higher coolant flow velocities or when steam is used as heat transfer medium. However, Section 4.2 shows that a limiting coolant heat transfer is, in fact, favorable to widen the reactor operating range via stabilizing control.

Catalyst diffusion limitation

Mass and energy transport at the catalyst scale are subject to several resistances and strongly influenced by temperature. Thereby, the most relevant resistance belongs to intraparticle transport limitation [SH14; Pér00]. In contrast, interfacial transport limitations between solid and gas phase are found to be negligible for reactor configurations similar to this study [KT15].

In order to account for temperature dependent intra-particle mass transport limitations in combination with the pseudo-homogeneous phase assumption, the effectiveness factor based on the Thiele modulus for spherical particles is used

$$\eta_{\mathrm{meth}} = \frac{3}{\Phi_{\mathrm{CO_2}}} \left[\frac{1}{\tanh(\Phi_{\mathrm{CO_2}})} - \frac{1}{\Phi_{\mathrm{CO_2}}} \right], \tag{3.37}$$

where the Thiele modulus Φ considers the key reaction for methanation 2.1 as a first-order reaction with carbon dioxide as key component, such that

$$\Phi_{\mathrm{CO_2}} = \frac{d_{\mathrm{p}}}{2} \sqrt{\frac{\nu_{\mathrm{CO_2}} \tilde{\mathrm{r}}_{\mathrm{meth}}}{\mathcal{D}_{\mathrm{p,CO_2}} \left(c_{\mathrm{CO_2,eq}} - c_{\mathrm{CO_2}}\right)}}. \tag{3.38}$$

The effective diffusivity inside the particle $\mathcal{D}_{\mathrm{p}}$ accounts for molecular $\mathcal{D}_{\mathrm{M}}$ and Knudsen diffusion $\mathcal{D}_{\mathrm{Kn}}$ via

$$\frac{1}{\mathcal{D}_{\mathrm{p,CO_2}}} = \frac{{\tau_{\mathrm{p}}}^2}{\varepsilon_{\mathrm{p}}} \left(\frac{1}{\mathcal{D}_{\mathrm{M,CO_2}}} + \frac{1}{\mathcal{D}_{\mathrm{Kn,CO_2}}} \right), \tag{3.39}$$

$$\mathcal{D}_{\mathrm{Kn,CO_2}} = \frac{d_{\mathrm{pore}}}{3} \sqrt{\frac{8\,\mathcal{R}\,T}{\pi\,M_{\mathrm{CO_2}}}}. \tag{3.40}$$

Eqs. (3.39) and (3.40) also account for structural properties of the catalyst by the particle porosity ε_{p} and tortuosity τ_{p}, as well as the average pore diameter d_{pore}. The molecular diffusion $\mathcal{D}_{\mathrm{M}}$ is calculated according to Eq. (A.17) on Page 127.

This approach is certainly restricted due to the selection of one key component (here carbon dioxide) and the application to an equilibrium limited reaction. Recently, Kiewidt [Kie17] presented an extended and more accurate approach for general reaction rate forms as initially proposed by Bischoff [Bis65]. Still, the strong exothermicity might also cause distinct temperature gradients inside the catalyst particle, which might result in an effectiveness factor above one. However, all case studies in this work indicate an effectiveness factor below one along the entire reactor axis. This can be confirmed, due to the good agreement with results presented by Schlereth and Hinrichsen [SH14] (heterogeneous model) and Kiewidt and Thöming [KT15] (pseudo-homogeneous model) (see Fig. 3.17).

3.2.3 Computational Aspects

In order to discretize and solve the reactor model as described by Eqs. (3.25) and (3.26) a finite volume (FV) scheme is used. Therefore a piecewise constant axial approximation following the upwind scheme and a piecewise linear radial approximation with central

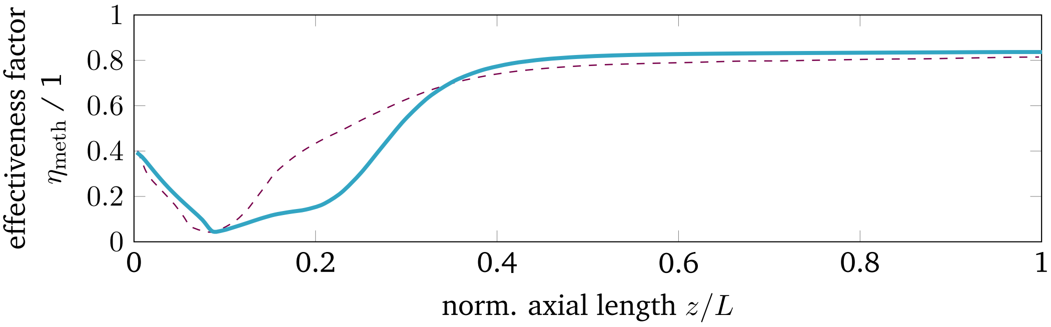

Fig. 3.17.: Reproduced axial dependency of effectiveness factor (——) according to Schlereth and Hinrichsen [SH14] (- - - -), adapted parameter: $T_{\mathrm{in}} = T_{\mathrm{cool}} = 593\,\mathrm{K}$, $\tau_{\mathrm{p}} = 4$, $d_{\mathrm{pore}} = 20\,\mathrm{nm}$, $d_{\mathrm{p}} = 5\,\mathrm{mm}$, $p_{\mathrm{in}} = 10\,\mathrm{bar}$, $L = 2.5\,\mathrm{m}$, $v_z = 1.7\,\mathrm{m/s}$, rate eqs. - Xu and Froment [XF89]

differences is used. One advantage of the finite volume method (FVM) is its conservative nature which forces each finite volume (FV) to obey the underlying conservation laws. This might be one reason for FVM to be very accurate even if other common methods (e.g., orthogonal collocation on finite elements) are possibly faster in terms of computation time [NK14].

Another reason for using the FVM in this work is its close connection to the CSTR cascade analogy of Section 3.1.3. Due to the applied upwind scheme in axial direction, each FV represents a perfectly mixed CSTR, such that the axial mesh resolution clearly determines the reactors overall back-mixing intensity according to Eq. (3.5) (where n represents the number of FVs). This effect is often called *numerical diffusion* and is considered to be a disadvantage for applying the FVM to PDEs without dispersive terms. A mathematical derivation of the numerical diffusion within the FVM is given in Appendix A.6 on Page 143. Since dispersion has proven to be an essential element in this work, numerical diffusion is rather seen as a useful feature. The key to making use of numerical diffusion is the correct number of axial FVs. This can be done according to the discussion on Péclet and Bodenstein number in Section 3.2.2. Since mass and energy-based Bodenstein numbers turned out to be of similar dimension with values ranging from 825 to 1000, an axial mesh resolution of 166 to 200 FVs per reactor meter reflects an accurate representation of the expected dispersion in this work. The consideration of additional dispersive fluxes according to Eq. (3.32) between each FV (see Fig. 3.18) as well as the use of flux limiters would distort the overall back-mixing intensity. Thus, this work considers the dispersive fluxes $j_{z,\alpha}$ and $\dot{q}_z$ to be zero and accounts dispersion solely by the amount of axial FVs. The validity of this approach is underpinned by the mathematical derivation in Appendix A.6 on Page 143.

Since this work considers computational tasks with different complexity, ranging from simulation to control and optimization, the full axial resolution was not always achievable. Thus, mesh resolutions of 8 to 12 FVs in radial and 150 to 400 FVs in axial direction were used to solve all seven PDEs (counting for six mass fractions and one

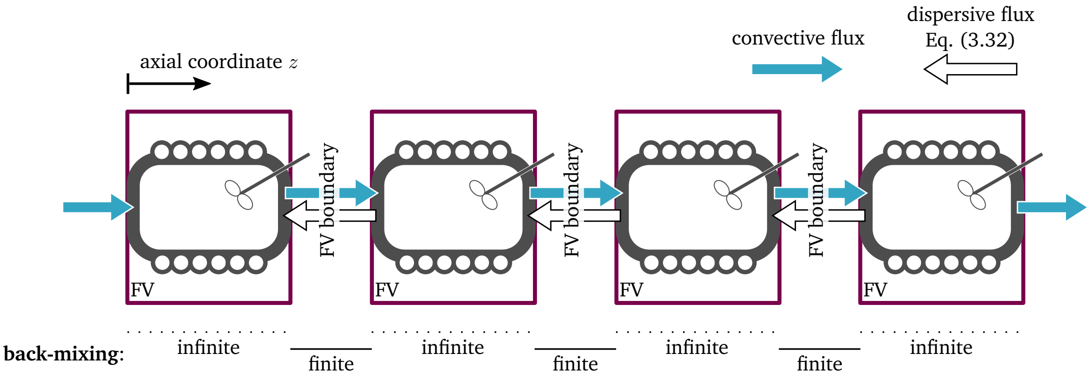

Fig. 3.18.: Axial back-mixing effects that can contribute to a reactor model based on the FVM scheme, FV - finite volume

temperature). An impression of the mesh resolution can be obtained from Appendix A.4 on Page 133. Consequently, the spatially discretized PDE system contains up to 12 × 400 × 7 = 33600 differential states, i.e. $\boldsymbol{x} \in \mathbb{R}^{33600}$. In addition, further algebraic states $\boldsymbol{z} \in \mathbb{R}^{400}$ are required to account for the pressure drop in axial direction, such that the entire reactor model is represented as the following nonlinear time-invariant system of differential algebraic equations (DAEs):

$$\begin{aligned} \frac{\mathrm{d}}{\mathrm{d}t}(\boldsymbol{x}) &= \boldsymbol{f}(\boldsymbol{x}(t), \boldsymbol{z}(t), u(t)), \quad \text{with} \;\; \boldsymbol{x}(t_0) = \boldsymbol{x}_0, \\ 0 &= \boldsymbol{g}(\boldsymbol{x}(t), \boldsymbol{z}(t)). \end{aligned} \tag{3.41}$$

The vector function $\boldsymbol{f} : \mathbb{R}^{33600} \rightarrow \mathbb{R}^{33600}$ contains all relations stated in the upper section. Most of the underlying physical correlations and properties from above are given explicitly and do not appear as additional algebraic equations. Only the reactor pressure, if calculated according to the extended Ergun equation (Eq. (A.16) on Page 127), is given implicitly via the velocity (Eq. (3.27)) and, thus, via the differential states. The scalar control $u \in \mathbb{R}^1$ solely refers to the temperature of the coolant T_{cool}. Based on this dynamic model, the transient reactor behavior can be simulated from each initial state $\boldsymbol{x}_0$ (e.g., for an ignited or non-ignited reactor). Thus, the broad operating range of such systems becomes accessible by state-of-the-art integrators. Therefore, CasADi v3.5.1 [And+18] allows for interfacing the DAE system (3.41) written in MATLAB to powerful SUNDAILS integrators [Hin+05]. With this setup, CPU times between 10 and 50 seconds for one dynamic simulation of 3000 seconds reactor operation is feasible, depending on how much the reactor condition is changing during the simulation. Such an effective computation is essential for the extensive dynamic studies presented in the next sections.

4 Reactor Operating Ranges

This chapter is divided into two sections. Initially, a computational study is conducted to gain new insights into typical static operating ranges of exothermic reactors using the example of carbon dioxide methanation. Therefore, different catalytic activities, as well as different reactor designs (conventional vs. intensified reactors and product recycle/feed dilution) are tested with respect to conversion and heat management performance. Finally, this chapter presents and thoroughly discusses the concept of stabilized coolant control and outline its relevance among conventional reactor concepts. Note that the content presented in this chapter is taken from [BS19] - published by The Royal Society of Chemistry.

4.1 Steady-State Operation

In order to characterize the reference reactor configuration from Tab. 3.2 with respect to the existence of steady-state multiplicity evoked by different cooling temperatures, several feed-forward simulation studies are performed. Furthermore, common strategies (intensification, product recycle/feed dilution) for improved heat management are compared and shown how they influence operating states and the overall reactor performance.

Starting with a cold reactor (gas compositions and temperatures similar to the feed condition), the control $u = T_{\mathrm{cool}}$ is increased step-wise until the thermodynamic equilibrium is reached. Each step is a dynamic simulation of 3000 seconds, which is long enough to reach the new steady-state. In this way, the *ignition branch* (IB) is screened. The complementary *extinction branch* (EB) is generated by stepwise reduction of the control u, starting from an already ignited reactor, which operates close to the equilibrium line. The result of this screening for the two different activity/kinetic cases, is illustrated in Fig. 4.1.

A significant influence of the different catalyst activities on the reactor performance is confirmed. Compared to the highly active catalyst (black), the IB and EB of the less active catalyst (blue) are shifted towards higher coolant temperatures. Nevertheless, the highest bed temperatures T_{max} are reduced due to lower CO_2 conversions caused by the chemical equilibrium. On the contrary, highly active methanation catalysts often suffer from a lower thermal resistance, such that during operation a critical catalyst temperature (typically $T_{\mathrm{crit}} = 775\,\mathrm{K}$) must not be exceeded [Aba+16; Rön+16a].

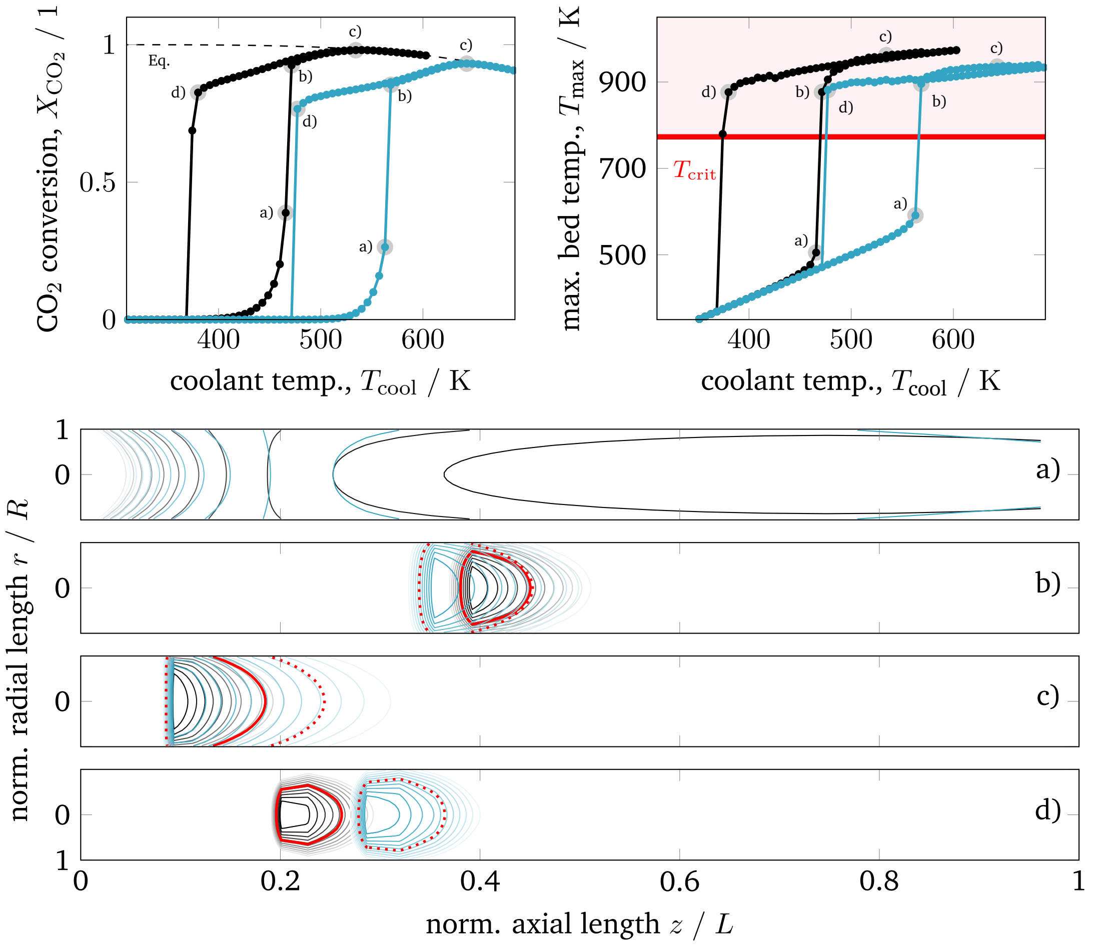

Fig. 4.1.: Ignition and extinction branches for different catalyst activities with respect to CO$_2$ conversion (top left), maximum bed temperature (top right), and spatial temperature field (bottom) - contours decrease in 2 %-increments of T_{max}; according to Koschany et al. [KSH16] (black); according to Xu and Froment [XF89] (blue), T_{crit} = 775 K.

Looking at the temperature field in Fig. 4.1 (bottom) reveals the stationary hot-spot position at different coolant temperatures. Following the IB by starting with low coolant temperatures, the non-ignited reactor behaves very similar to a heat exchanger. Towards the reactor outlet, the cold inlet gas is heated up until it reaches the coolant temperature (coolant acts as heater). A further increase of the coolant temperature leads to broad regions of elevated temperatures slightly above the coolant temperature, caused by a mild heat release of the exothermic reaction (state a). When the ignition temperature is reached, the heat release starts to exceed the heat removal and accumulates in the reactor center ($r = 0$). As a consequence, the temperature in the reactor center increases significantly (runaway) until the difference between reactor and coolant temperature is large enough to sufficiently remove the heat by the coolant. Thus, a distinct hot-spot is formed - for low inlet temperatures approximately in the middle of the reactor (state b). As long as the catalyst is able to tolerate these temperatures, kinetic limitations are reduced and yield higher conversions. When the coolant temperature is increased further, the hot-spot moves towards the reactor inlet and higher conversions are achieved until thermodynamic limitations become dominant and lower the CO_2conversion (state c).

To exploit the EB in Fig. 4.1, the coolant temperature is decreased starting from an already ignited reactor (state c). Until state b) is reached, there is almost no difference in conversion and highest bed temperature between EB and IB. Nevertheless, the hot-spot is not exactly restored in accordance to the IB. Instead, the high temperatures of the former steady-states are still "memorized" and lead to stretched hot-spot shapes, more closely located to the inlet. As a result, the ongoing heat release is able to keep the reaction running even for lower coolant temperatures and steeper radial temperature gradients as associated with state b) of the IB. However, as the heat removal becomes more dominant for lower coolant temperatures, the hot-spot extinction is induced approximately 100 K below the ignition temperature. Moreover, the hot-spot extinction occurs closer to the inlet than its former ignition. In addition, Fig. 4.1 illustrates that higher catalyst activities tend to sharper, more concentrated hot-spots with different locations, especially on the EB.

The operation close to a) - for non-ignited reactors - and d) - for ignited reactors - is very sensitive to changes in the cooling temperature. This phenomenon is well known as *parametric sensitivity* [MV82], and many authors suggest to avoid an operation close to or in between these states due to stability and safety restrictions. However, the operation on a distinct EB - not too close to d) - has a clear potential for stable operation when lower cooling temperatures and high conversions are required.

In order to validate the accuracy of the model, two key characteristics are of major importance: the highest bed temperature and the ignition temperature (runaway temperature). Although both characteristics can be found in various studies, a comparison is often rather limited due to the influence of the respective reactor design and operation case. Very close to this work's model set-up and considering the less active catalyst case, Schlereth and Hinrichsen [SH14] have shown detailed simulation studies in very good agreement to the IB results in Fig. 4.1 (blue), such that a bed temperatures above 900 K and an ignition temperature slightly below 570 K can be confirmed. As a third key characteristic, this work proposes to address the extinction temperature due to its pronounced dependence on the chosen heat transfer characteristics. Unfortunately, no reliable data to validate the results regarding this third key characteristic could be found in the literature so far.

Intensified Reactors

Intensified reactors used for methanation aim for a better heat removal due to higher cooling surface to reaction volume ratios (e.g., micro reactors, honeycomb reactors, monolithic reactors, plate reactors, catalytic wall reactors). In order to represent

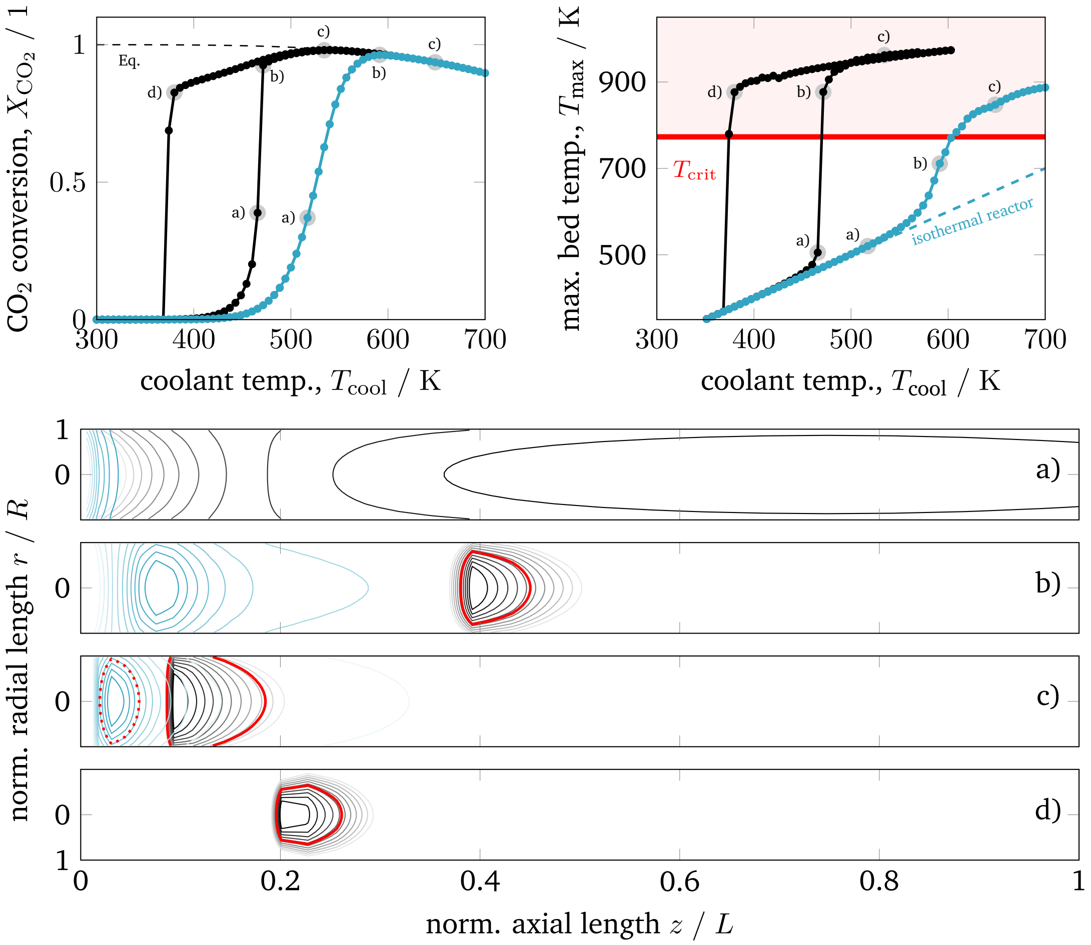

Fig. 4.2.: Ignition and extinction branches of reference case (black) in comparison to intensified reactors (blue - $L/10$, $R/10$, $d_{part}/10$) with respect to CO$_2$ conversion (top left), maximum bed temperature (top right), and spatial temperature field (bottom) - contours decrease in 2 %-increments of T_{max}, $T_{crit} = 775$ K.

this approach with the model presented here, the reactor dimension is reduced by one order of magnitude in length, radius and particle diameter. As the superficial velocity is sustained, the productivity of the reference case corresponds to a bundle of approximately 100 of these smaller tubes (neglecting differences in bed porosity). Furthermore, the same coolant mass flow was used to cool the bundled micro-channels, and results in an increased coolant heat transfer. The comparison to the reference configuration is shown in Fig. 4.2.

Obviously the improved heat removal eliminates the existence of multiple steady-states with respect to the coolant temperature. In contrast, a lower heat removal (e.g., due to larger reactor dimensions) can yield broader regions of multiple steady-states. Thus, the reactor dimension and coolant heat transfer are key parameters that influence steady-state multiplicity.

For the intensified case (blue) in Fig. 4.2, the IB and EB coincide and distinct ignitions are smoothed out (but still present compared to the limiting case of an isothermal reactor). In addition, at states of high conversion the bed temperature is relatively low and more equally distributed, even for the more active catalyst. Thus, intensified reactors are reasonable alternatives to improve heat management and to deal with possible temperature limitations of the catalytic system. Regarding dynamic considerations, Fig. 4.2 shows that intensified reactors are much less sensitive with respect to changes of the coolant temperature (reduced parametric sensitivity). Consequently, a possible reactor runaway due to load changes or disturbances is less likely. Furthermore, smaller reactor volumes with less thermal mass are favored to perform fast reactor start-up or load changes and, thus, allow for more flexible reactor operation. For this reason, intensified reactors are currently the topic of many research activities. [Sch15; Sud+10; Tro+04; Bro+07; BMP17; Bia+13] However, hot-spots might still appear in regimes of elevated coolant temperatures, where thermodynamic limitations are already pronounced. Disadvantages often include high pressure drop, high investment cost, and channel blockage. One further disadvantage is related to the enhanced coolant temperatures (approx. + 150 K for case b in Fig. 4.2), which can cause technical restrictions for the right coolant selection (see Section 4.2.2).

Product Recycle / Feed Dilution

Another common approach for improved heat management is associated to product recycle or feed dilution as illustrated in Fig. 4.3. In this way, the amount of reactive gas is reduced and less heat is generated. In addition, the non-reactive gas components are also acting as an internal coolant. At very high recycle ratio, the reactor behaves like a cooled CSTR (perfectly mixed), and the catalytic bed becomes isothermal. Consequently, higher coolant temperatures, similar to intensified reactors, are required to achieve sufficient conversions. Furthermore, the presence of product gas shifts the equilibrium towards the reactant side and leads to lower conversions. However, under high conversion conditions (e.g., at low temperature methanation) this shifting is rather insignificant.

Similar to intensified reactors, the mitigated heat generation eliminates the appearance of cooling related multiple-steady states. High conversion and tolerable bed temperatures are achieved, although the reactor dimensions correspond to the reference case. Another advantage compared to intensified reactors is given due to lower coolant temperatures (similar to the reference case) when operating in high conversion regimes. Consequently, dilution and product recycle are very promising strategies to improve heat management and often considered in methanation studies. [Mat+16; MKJ16; DBB17; Try+17]

Nevertheless, product recycle always requires additional auxiliary units (e.g., compressors, heat exchangers) and reduces the reactor space-time yield, whereas feed dilution increases the downstream separation load. In both cases, investment costs will certainly increase. In addition, the dynamic behavior of reactors with product recycle often

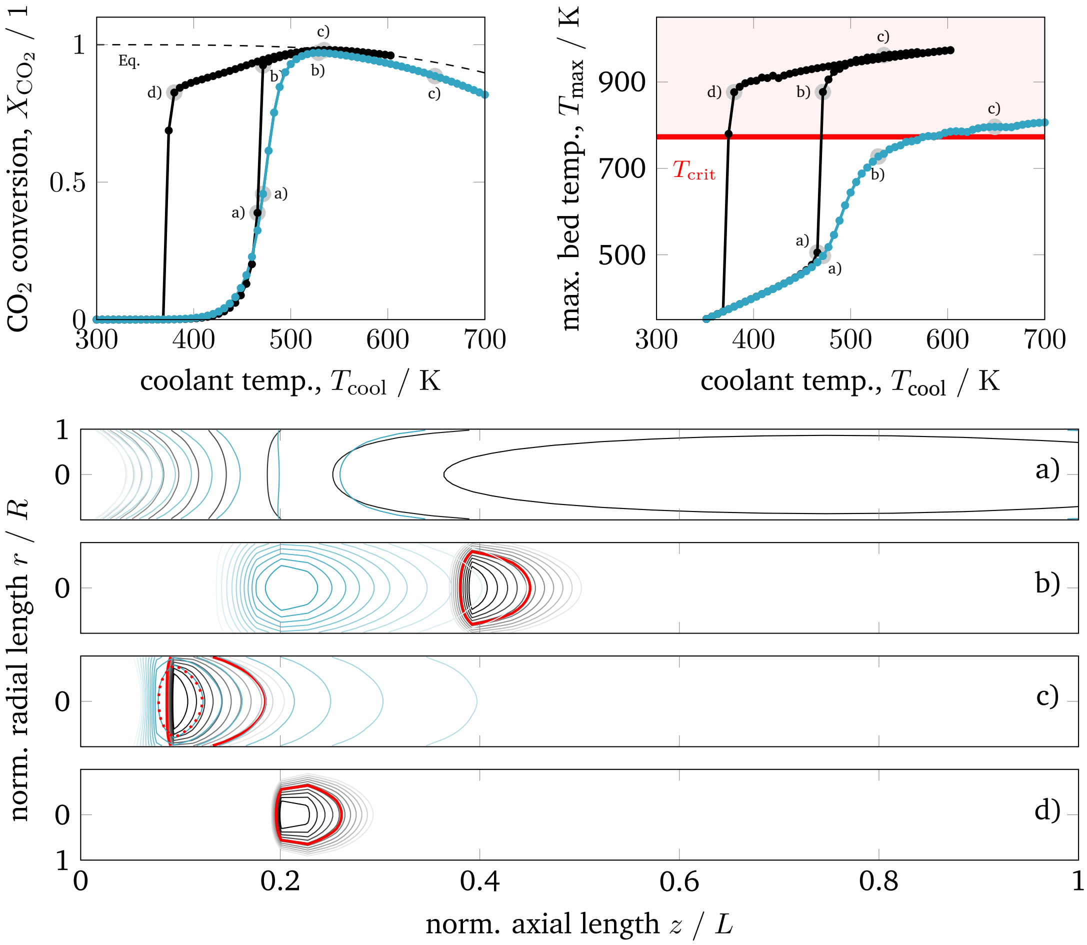

Fig. 4.3.: Ignition and extinction branches of reference case (black) in comparison to 40 % product recycle (blue) with respect to CO$_2$ conversion (top left), maximum bed temperature (top right), and spatial temperature field (bottom) - contours decrease in 2 %-increments of T_{max}, $T_{crit} = 775$ K.

suffers from transient oscillations during load changes and especially during start-up procedures. Apart from that, a permanent recycling can also lead to an accumulation of contaminants harming the catalyst (e.g., sulfur components). If theses reactor types are intended to be used very flexibly in a broad operating range, a deeper understanding of the respective dynamics is essential and subject of ongoing research activities (see e.g., [Mat+16]).

4.2 Stabilized Operation

In contrast to the open-loop simulations discussed above, this section deals with closed-loop reactor control via transient variations of the coolant temperature. The relevance of this approach to control the internal heat generation will also be demonstrated in the next chapter by means of rigorous optimization studies. This section, however, aims

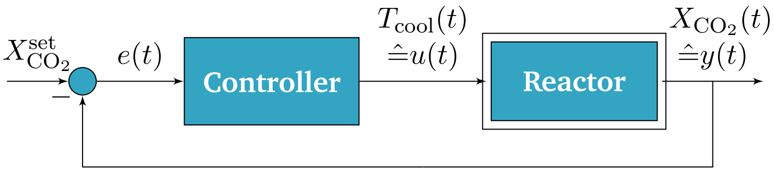

Fig. 4.4.: Closed-loop scheme for reactor control.

for more fundamental explanations and a better understanding of these optimization results with respect to a broader operating range and its technical relevance.

In order to allow for transient cooling temperature variations the reactor model is coupled with a PI-controller of the following structure

$$u(t) = \mathrm{K_P}\, e(t) + \mathrm{K_I} \int_0^t e(\tau)\, d\tau, \tag{4.1}$$

$$e(t) = X_{\mathrm{CO_2}}^{\mathrm{set}} - X_{\mathrm{CO_2}}(t), \tag{4.2}$$

where K_P and K_I are tuned to enable sufficiently fast transitions from one set-point to another, without pronounced oscillations and reasonable cooling temperature values. Therefore, $K_\mathrm{P} = 500\,\mathrm{K}$ and $K_\mathrm{I} = 50\,\mathrm{K/s}$ are found to perform well within the specifications of this work. Consequently, the corresponding closed-loop simulations are from now on performed for different conversion set-points $X_{\mathrm{CO_2}}^{\mathrm{set}}$ and not for different cooling temperatures. Furthermore, the simulation procedure in this section is initialized with a steady-state on the EB from which the conversion set-point is reduced stepwise always after reaching a new steady-state. The result of this procedure in comparison to the former open-loop simulations is illustrated in Fig. 4.5

The first closed-loop simulations with activated PI-controller (blue) are converging to the same EB steady-states as obtained with the open-loop simulations (black). The cooling temperature variations induced by the controller can be also interpreted as disturbances around the EB steady-states, which proves a certain stability of the EB. However, more important is the observed behavior after passing the state d) and approaching conversion set-points close to the former extinction point. Due to the activated controller, a further reduction of the conversion set-point does not lead to an extinction, as observed in the open-loop case. Instead, a new branch becomes attainable between the EB and the IB. Deactivating the controller in this domain after steady-state is reached leads the reactor back to a steady-state either on the EB or on the IB. The corresponding transition is characterized by slowly moving reaction fronts. Consequently, these new steady-states are open-loop unstable, but closed-loop stable. Although the existence of multiple unstable states within the hysteresis loop is already mentioned in various studies[Eig00; Gil77; KV80; Car87; WL84; RE13], this work shows that their stabilization at technical relevant conditions is indeed possible for controlled fixed-bed reactors.

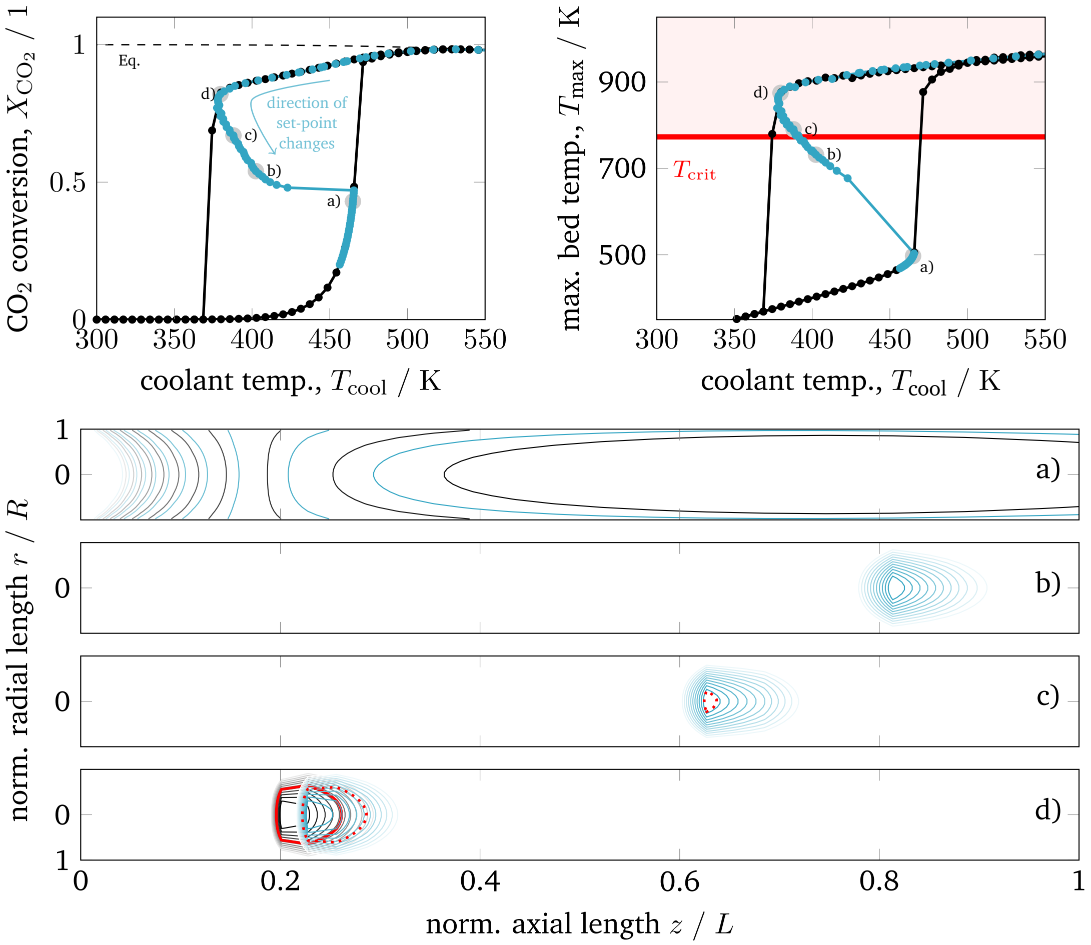

Fig. 4.5.: Ignition and extinction arcs of reference case (black) in comparison to stabilized operation via PI-control (blue) with respect to CO$_2$ conversion (top left), maximum bed temperature (top right), and spatial temperature field (bottom) - contours decrease in 2 %-increments of T_{max}, $T_{crit} = 775$ K.

In order to explain the stabilization effect, the thermal mass / inertia of the catalytic bed is of major importance. As a result of the distinct heat capacity and density of the solid particles, any bed temperature change (due to the chemical reaction or due to cooling changes) is delayed. This effect is incorporated within the model via the accumulation term in Eq. (3.26). As long as the change of the cooling temperature is faster than the thermal response of the reactor, a stabilization of the reaction zone becomes feasible. More details on open-loop and closed-loop stability and potential technical limitations are given in Sections 4.2.1 and 4.2.2.

From these observations, three major advantages of this control approach can be derived:

- Controlled exothermic fixed-bed reactors of common dimension can be operated in a much broader operating range.

- The new operating range involves reduced bed temperatures which can prevent catalysts from thermal degradation.
- Due to the proven controllability, a flexible reactor operation with regard to load or set-point changes is possible.

Looking at the temperature field in Fig. 4.5 shows that during closed-loop simulations the reactive zone moves towards the outlet. Similar to the explanations regarding the existence of the EB, the actual condition/position of the reaction zone is again strongly influenced by its former condition/position. Finally, the stabilized branch in Fig. 4.5 (blue) collapses once the reactive zone has reached the end of the reactor. A further reduction of the conversion set-point brings the reactor to the IB. Note that the observed stabilized branch agrees very well with the theoretical trends from Fig. 3.14.

Several parameter studies are performed to gain a better understanding of the stabilized states. Therefore, cooling intensity, the reactor pressure, as well as the particle diameter turned out to be of major importance. These parameter studies are also chosen to demonstrate that the stabilized states are not just result of a specific reactor configuration, but rather a characteristic feature of any exothermic fixed-bed reactor.

Since cooling intensity can be also manipulated via the coolant flow rate, which directly influences the cooling heat transfer coefficient α_{cool}, Fig. 4.6 illustrates this influence of higher and lower cooling rates.

Accordingly, under intensified heat transfer conditions, the hysteresis loop shrinks and all states on the stabilized branch are shifted towards higher cooling temperatures. This behavior is similar to the trends observed with intensified reactors. Thus, a further intensification of the heat transfer would eliminate the hysteresis loop and any corresponding stabilized branch. On the contrary, less intensive cooling features broader hysteresis loops and broader stabilized branches at lower cooling temperatures.

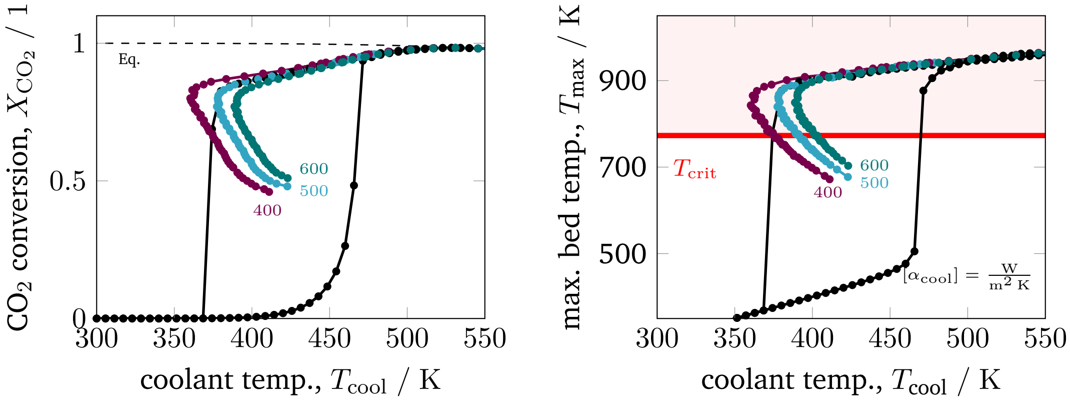

Fig. 4.6.: Stabilized operating range for varying coolant heat transfer, reference model set-up: controlled (colored) and uncontrolled (black), $T_{\mathrm{crit}} = 775\,\mathrm{K}$.

Compared to an operation at higher cooling temperatures or to reactor concepts without state-space multiplicity, the coolant mass flow reveals a larger impact on the reactor performance. This observation might also allow further control actions and a more flexible operation.

The inlet pressure influences the reactor performance in several ways. On the one hand, a higher pressure intensifies the reaction, so that more heat is generated. On the other hand, a higher pressure increases the effective radial heat conduction of the catalytic bed due to higher gas densities and intensified hydrodynamics/turbulences. Fig. 4.7 illustrates an inlet pressure variation.

In general, elevated pressures exhibit more pronounced hysteresis loops and broader stabilized branches. Looking at the EB for a constant cooling temperature reveals that higher pressure causes higher bed temperatures. The increased heat generation dominates the increased radial heat transfer. In contrast, the stabilized branch shows an inverse behavior. Apparently, for reduced reaction zones the increased radial heat transfer becomes dominant when the inlet pressure is increased. However, the reduced bed temperature also reduces the conversion. Nevertheless, the impact of the inlet pressure might offer further potential for additional control actions. For instance, a pressure variation in combination with the temperature control concept might be useful to allow for feed load changes (e.g., due to volatile production from renewable sources) under constant conversion.

The last parameter corresponds to the catalyst design. Currently, an increased interest on catalyst design under dynamic conditions can be observed in the literature. A comprehensive overview is provided by Kalz et al. [Kal+17] Since the model also accounts for mass transport limitations within the catalyst (see Section 3.2.2), the influence of diffusion limitations on the dynamic stabilization is also analyzed. Therefore, the particle diameter d_p is varied, which directly influences the diffusion limitation via the

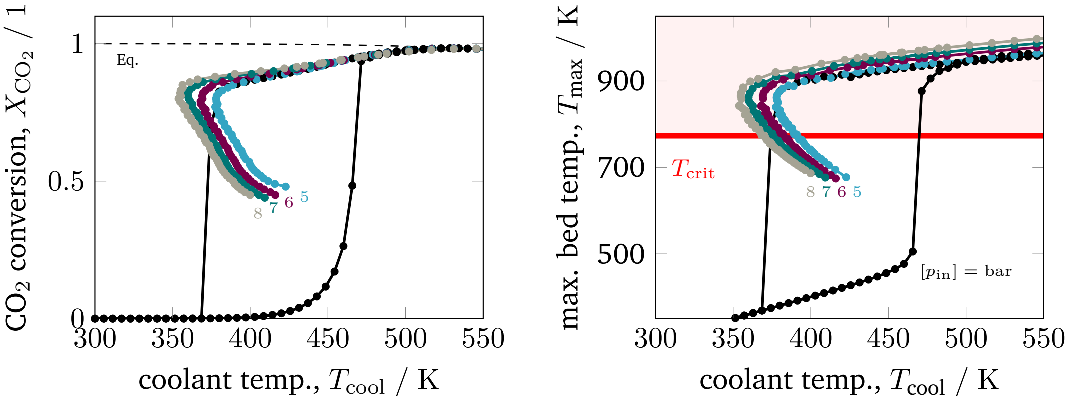

Fig. 4.7.: Stabilized operating range for varying inlet pressures, reference model set-up: controlled (colored) and uncontrolled (black), $T_\mathrm{crit} = 775\,\mathrm{K}$.

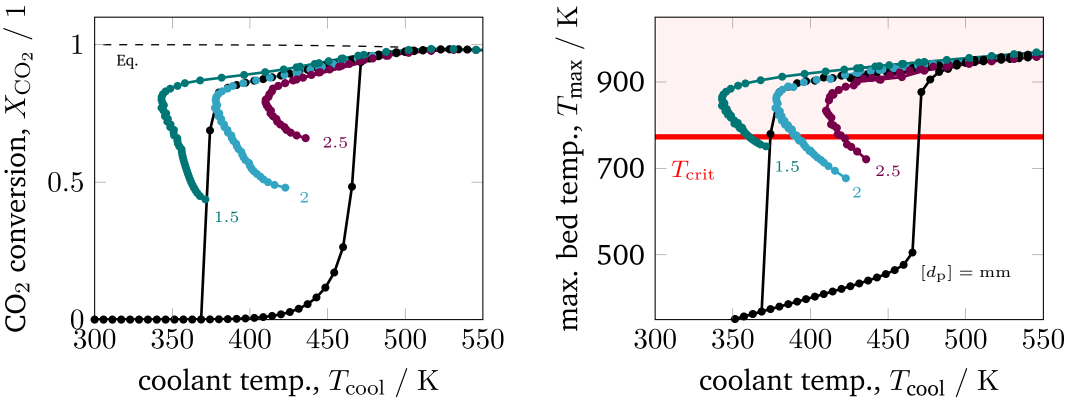

Fig. 4.8.: Stabilized operating range for varying particle diameter, reference model set-up: controlled (colored) and uncontrolled (black), $T_{crit} = 775\,K$.

effectiveness factor η_{meth} (see Eqs. (3.37) and (3.38)). Fig. 4.8 illustrates this influence in case of larger catalyst particles (increased diffusion limitation) and smaller particles (decreased diffusion limitation).

Compared to the other parameters, the particle diameter influence is even more pronounced. Larger particles and increased diffusion limitation lead to less reactive volume and less heat generation, which outweighs the influence on heat removal. Hence, the hysteresis loop shrinks, similar to the above illustrated reactor intensification. This weighting also remains for particle diameter reductions and lower diffusion limitations, so that heat generation dominates and leads to broader hysteresis loops. Consequently, diffusion limitation reveals an essential impact on the shape of the stabilization branch and, thus, also for any dynamic operation. Furthermore, the particle diameter influence is significantly less pronounced when an operation apart from the stabilization branch and close to chemical equilibrium is desired.

All trends presented in this section are very well reflected by the multiplicity criterion and, thus, support relevance and plausibility of the theoretical elaboration in Section 3.1.

4.2.1 Stability Analysis

To validate the observations regarding open-loop and closed-loop stability, an eigenvalue analysis based on a linearization of the strongly nonlinear System (3.41) is performed [JR82]. Certainly, an assignment of any stability measure coming from the linearized system to the respective nonlinear system is restricted to a narrow domain around the expansion point. However, a general measure allowing global statements on stability of such strongly nonlinear systems is not available or limited to weakly nonlinear systems.

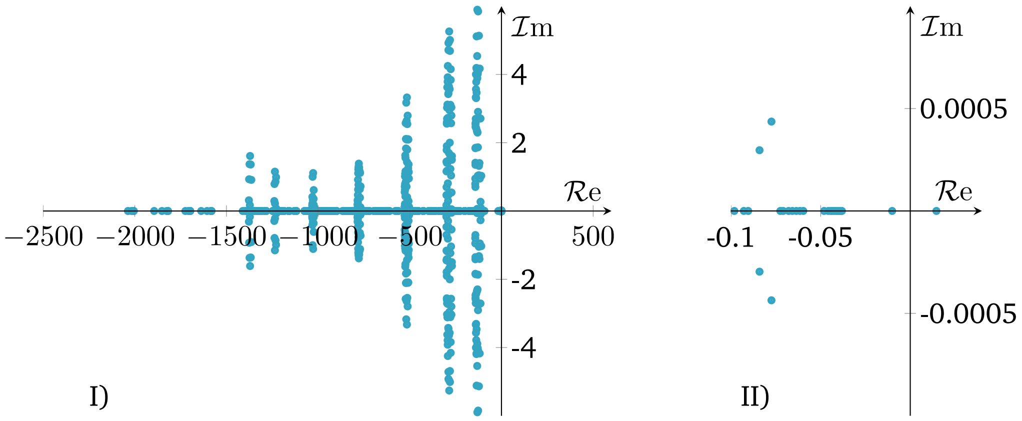

Fig. 4.9.: Open-loop eigenvalues of linearized state b) in Fig. 4.5; I) - full range , II) - largest eigenvalues.

Due to its minor influence, the pressure drop is assumed to be zero, so that the algebraic equations in Eq. (3.41) vanish. Consequently, for any steady operating point $(\tilde{\boldsymbol{x}}, \tilde{u})$ the remaining nonlinear ODE system holds

$$0 = f(\tilde{\boldsymbol{x}}, \tilde{u}).$$

The linearization around this operating point leads to the following state-space formulation of the dynamic system:

$$\begin{aligned}&\frac{\mathrm{d}}{\mathrm{d}t}(\boldsymbol{x}^*) = \mathbf{A}\,\boldsymbol{x}^*(t) + \mathbf{B}\,u^*(t),\\ &\text{with } \boldsymbol{x}(t) = \boldsymbol{x}^*(t) + \tilde{\boldsymbol{x}}\end{aligned}$$

where the state-transition matrix $\mathbf{A}$ and the input vector $\mathbf{B}$ correspond to the system's Jacobian at $(\tilde{\boldsymbol{x}}, \tilde{u})$ with respect to $\boldsymbol{x}$ and u, respectively. Furthermore, $\mathbf{A}$ is used to obtain the eigenvalues λ_i via

$$(\mathbf{A} - \lambda_i \mathbf{I})\,\boldsymbol{v}_i = 0,$$

where v_i is the corresponding eigenvector. Note that the $\mathbf{A}$ used to compute the eigenvalues in the open-loop case differs from the $\mathbf{A}$ in the closed-loop case due to the involved controller Eqs. (4.1) and (4.2). The respective eigenvalues for both cases can be found in Figs. 4.9 and 4.10, where state b) from Fig. 4.5 is used as expansion point.

The eigenvalue pattern confirms the observations from above. The open-loop system has a positive eigenvalue which leads to a divergent system behavior. However, there is only one positive eigenvalue very close to the origin pointing out that the instability is relatively weak/slow and potentially easy to stabilize. This was confirmed by applying a P-controller based on root locus analysis, showing that there is a broad range of different controller gains that shift positive eigenvalues/poles to the left-half plane. Nevertheless,

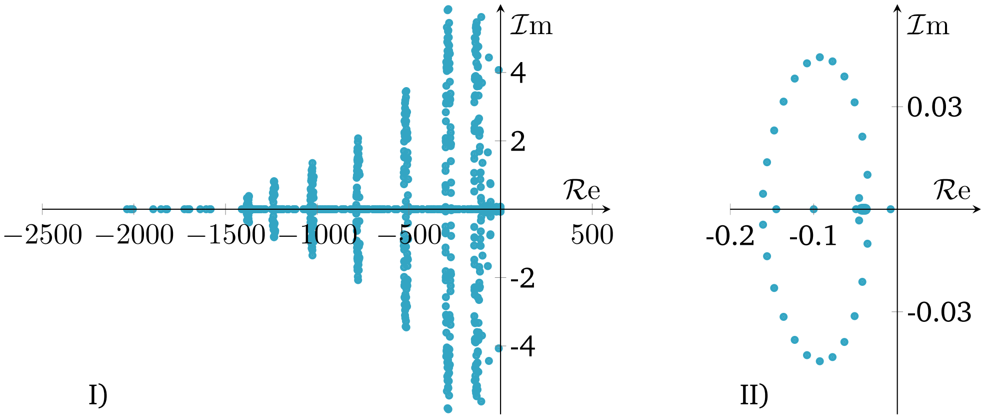

Fig. 4.10.: Closed-loop eigenvalues of linearized state b) in Fig. 4.5; I) - full range , II) - largest eigenvalues.

a P-controller leads to significant set-point deviations, so that an additional integral part becomes inevitable. Consequently, the selected PI-controller from above stabilizes the linearized system such that negative eigenvalues vanish (see Fig. 4.10).

A more detailed illustration of open-loop eigenvalues is provided in Fig. A.10 on Page 138, focusing on the stable state c) of the reference setting in Fig. 4.1.

Due to these results, the reactor stabilization can be locally proven with standard control theory. Furthermore, the observed unstable dynamics of the open-loop are rather slow and give rise to feasible controller implementations under real world scenarios with included measure and control delays, as well as uncertainties. Further discussions on technical aspects are part of the following section.

4.2.2 Technical Aspects

As seen from the results above, the relation between performance and cooling temperature of all presented reactor concepts differs significantly. Whereas intensified reactors require elevated cooling temperatures to ensure a high conversions, non-intensified reactors benefit from an internal heat accumulation. On the one hand, this allows for lower cooling temperatures. On the other hand, it needs to be controlled (via feed dilution or stabilizing coolant control) to comply with catalyst temperature limitations. In real world applications, finding the right coolant is one major process design decision. In Fig. 4.11, common coolants and their operating range are confronted with the performance of intensified and non-intensified reactors.

Looking at the observed stabilized arc and its corresponding low cooling temperatures in Fig. 4.11 clarifies that only thermal oil appears to be an appropriate coolant for operating under these dynamic conditions. Molten salt and steam do not cover the low temperatures required for this special operating strategy.

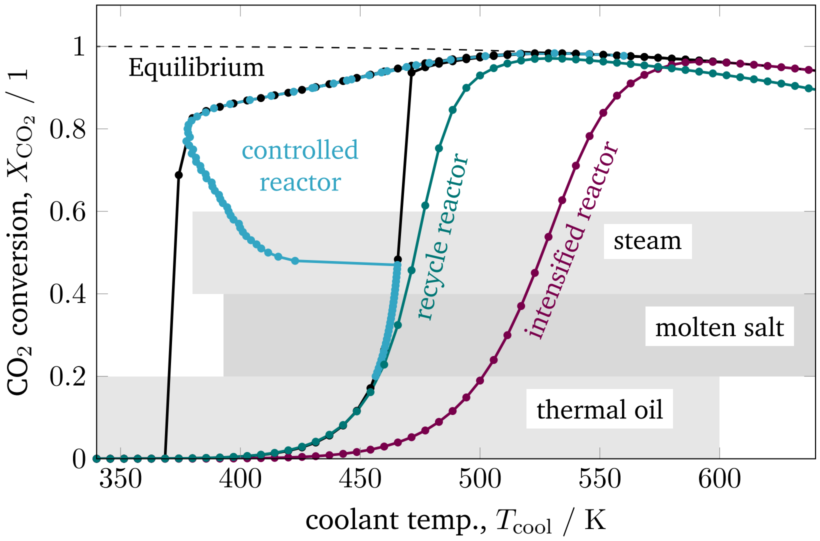

Fig. 4.11.: Coolant selection range related to prior case studies.

Despite explaining all technical details of each coolant option, this section focuses on their potentials for dynamic operation with regard to load changes and start-up time. Generally speaking, the more complex (e.g., due to many auxiliary units) a cooling system is, the more time it requires for start-up. Thermal oil cooling systems are known to be much simpler than steam and molten salt systems, which makes thermal oil a suitable candidate to ensure short start-up times. Choosing steam as coolant allows for very fast coolant temperature changes to facilitate load changes by simply manipulating the coolant pressure. Nevertheless, this advantage comes with increased pressures and large mechanical stress. Changing the coolant temperature with a molten salt or a thermal oil cooling system requires potentially more time compared to a steam cooled system. However, general statements in this context need to be considered carefully since detailed response times of these systems in the context of control applications are scarcely available in the literature and often a matter of the specific design.

In particular, advanced control strategies as those proposed in this work require not only sufficiently fast changes in the manipulated variable T_{cool}, but also in the controlled variable X_{CO_2}. In reality, both variables are certainly affected by response/reply delays, as well as uncertainties, depending on the involved actuators and sensors. Since measuring the conversion as done in this study is rather slow (e.g., when gas chromatography is used), one could also measure the bed temperature instead. Typically, these sensors and actuators are always required, also for steady process operation, which highlights the practicability of the proposed dynamic operating concept. However, further investigations with regard to response times and robustness are necessary and will be covered in Chapter 6.

4.3 Chapter Summary

This chapter pays special attention to possible stabilization concepts for unstable operating regimes of catalytic reactors. To identify unstable regimes, an initial screening of stable steady-states is used for different catalytic reactor concepts. Such a screening reveals multiplicity regimes that also contain unstable states. The proposed reactor control concept turned out to be capable of approaching and stabilizing these states. This way, the reactor can be operated within a broader performance range and with increased flexibility.

CO_2 methanation offers a distinct potential for dynamic operation and flexibility enhancement. Due to its strong exothermicity, multiple stable and unstable states can easily arise from thermal feedback and hot-spot formation if industrial scale fixed-bed reactors are used. The application of stabilized control is nothing more than controlling the expansion and positioning of the reaction zone, so that a broader operating range becomes feasible. This range is very attractive when thermal restrictions arise (e.g., due to the catalyst durability). In case of CO_2 methanation with very active catalytic materials, temperature limitations are very likely but not always possible to satisfy under conventional steady-state conditions. In regions of multiple steady states, unstable arcs featuring high CO_2 conversion and feasible catalyst temperatures exist and can be successfully approached by PI control. Without stabilizing control, similar achievements are possible when other reactor designs are considered (e.g., intensified reactors or product recycle / feed dilution). However, these designs still suffer from many technological obstacles, whereas the concept of stabilizing control can be applied to state-of-the-art reactor configurations that are widely used for large scale production units.

Catalytic properties have shown a tremendous impact on the dynamic behavior, suggesting that future investigations need to be aligned in this direction. Thereby, detailed dynamic models for the catalyst particle are required to be incorporated into the current reactor model. Features like diffusion limitation or heat capacity are certainly the right choice for optimized dynamic reactor designs and might offer possibilities that allow an easier and more robust stabilization and lead to lower technical requirements for the entire control loop.

These model-based results still need to be underpinned by experimental validation in order to provide the final prove of concept. Therefore, Chapter 6 introduces a pilot plant concept that has been developed specifically for the conditions presented in this chapter.

5

Optimal Reactor Start-Up

The preceding chapters revealed unconventional operating states that are of great interest in carbon dioxide methanation. From the perspective of an operator, however, it remains to be shown how these reactor states can be reached fast enough and without potential runaways. The most challenging control task in this regard is certainly the consideration of an entire reactor start-up. This scenario requires the reactor to go through a large proportion of the respective state-space until the final set-point is reached (starting from a cold extinguished state to a hot ignited state). Standard PI-controllers, as used in Section 4.2, often fail when the system's state is getting too far away from the targeted set-point, especially when the system behaves strongly nonlinear. The realization of such control tasks requires more advanced control concepts, which were already examined 50 years ago by Hahn et al. [HFH71]. The authors presented a start-up policy for a similar task, as described in this work. Therefore, a distributed maximum principle with path constraints on bed-temperature has been applied to a one-dimensional, tubular reactor with first-order exothermic, reversible reaction ($A \rightleftarrows B$). Although reaching a stabilized reactor state was not the authors objective, the results indicate that the dynamic interaction with reactors during start-up is a feasible approach to reach desired set-points quickly and safely. The authors also stated that such optimizations represent "formidable" computational problems. Until today, however, the literature pays little attention to such problems (see, e.g., [VvW92; HÅH09]).

This section takes up a similar dynamic optimization approach using the realistic example of carbon dioxide methanation. Powerful, state-of-the-art numerical routines are used for solving the resulting optimal control problem (OCP). The corresponding problem statement is explained in the following. Note that the content presented in this chapter has been published previously in [BRS17] and is reproduced with permission of John Wiley and Sons.

5.1 Dynamic Optimization

The start-up scenario is characterized by an operational setting similar to Tab. 3.2. However, some modifications and additions are required and highlighted in Tab. 5.1.

The considered stoichiometric inlet ratio of 4:1 between hydrogen and carbon dioxide ensures that the catalytic reaction leads to the highest possible temperature increase inside the reactor (worst-case scenario in terms of temperature control). Since the elevated inlet pressure is considered to be a result of an upstream compression unit, the inlet is here chosen to be above ambient temperature. Bounding the reactor temperature over the entire interior is of major importance to guarantee long-term stable operation according to the discussions in Section 2.1. Taking an additional margin of safety into consideration, the selected upper reactor temperature bound is 750 K. Due to the exothermic reaction, the lower reactor temperature bound is not relevant, but stated for consistency. The coolant temperature bounds are result of the discussions from Section 4.2.2.

The reactor start-up is initiated by a step change in the coolant temperature chosen by the optimizer while the initial reactor bulk gas phase is assumed to be equal to the inlet gas condition:

$$T_{\text{init}}(r,z) = T_{\text{in}}, \qquad p_{\text{init}}(r,z) = p_{\text{in}}, \qquad x_{\alpha,\text{init}}(r,z) = x_{\alpha,\text{in}}.$$

Based on these specifications, the following optimal control problem (OCP) is defined:

$$\begin{aligned} \max_{\boldsymbol{u}(t)} \quad & \int_0^{t_f} X_{\text{CO}_2}(\boldsymbol{x}(t), \boldsymbol{u}(t))\, dt \;-\; \Omega(\boldsymbol{u}(t)), \\ \text{s.t.} \quad & \dot{\boldsymbol{x}}(t) = \boldsymbol{f}(\boldsymbol{x}(t), \boldsymbol{u}(t)), \quad \forall t \in [0\ t_f], \\ & \boldsymbol{x}(0) = \boldsymbol{x}_0, \\ & X_{\text{CO}_2}(t) = \mathbf{L}^{\text{T}}\, \boldsymbol{x}(t), \\ & \boldsymbol{x}_{\text{ub}} \geq \boldsymbol{x} \geq \boldsymbol{x}_{\text{lb}}, \quad \boldsymbol{u}_{\text{ub}} \geq \boldsymbol{u} \geq \boldsymbol{u}_{\text{lb}}, \end{aligned} \tag{5.1}$$

where the ODE formulation of System (3.41) (excluding algebraic states) is embedded into a task for maximizing carbon dioxide conversion over the entire start-up time horizon. In contrast to System (3.41), the control $\boldsymbol{u}(t) \in \mathbb{R}^2$ consists of independently adjustable inlet and outlet coolant temperatures, which are used to approximate a linear temperature profile within the coolant channel. The Lagrange representation of the objective in Problem (5.1) is considered to be equivalent to a time minimal start-up objective. The conversion of carbon dioxide results from Eq. (A.2) on Page 120 with outlet mass fractions originating from the solution of the ODE system. During

Tab. 5.1.: Start-up operating parameters.

parameter	symbol	value	unit
inlet gas temperature	T_{in}	400	K
upper cooling temperature bound	$T_{\text{cool,ub}}$	650	K
lower cooling temperature bound	$T_{\text{cool,lb}}$	300	K
upper reactor temperature bound	T_{ub}	750	K
lower reactor temperature bound	T_{lb}	300	K
start-up time horizon	t_f	1000	s

reactor start-up, the fixed-bed is expected to run through a wide temperature range, so carbon dioxide methanation may not be the only relevant reaction (see Section 2.1). Consequently, this section also considers carbon monoxide methanation (2.2) and RWGS reaction (2.3) by making use of a kinetic model, valid for a less active catalyst, proposed by Xu and Froment [XF89]. The corresponding rate equations are provided in Appendix A.3.3 on Page 130. In the presence of multiple reactions, the outlet methane selectivity according to

$$S_{\mathrm{CH_4}}(t) = \frac{M_{\mathrm{CO_2}}}{M_{\mathrm{CH_4}}} \frac{w_{\mathrm{CH_4,out}}(t) - w_{\mathrm{CH_4,in}}(t)}{w_{\mathrm{CO_2,in}}(t) - w_{\mathrm{CO_2,out}}(t)}.$$

becomes an additional performance criterion, as values below one indicate undesirable CO formation.

The optimization objective is highly sensitive to the chosen control which can lead to severe fluctuations in the optimal control trajectories. This computational challenge is directly connected to the physical properties of the exothermic reaction system and its fast kinetics. To face this challenge and to achieve solutions relevant for technical applications, a penalty term Ω is added to the objective which regularizes the control fluctuations in the following manner:

$$\Omega(\boldsymbol{u}(t)) = \boldsymbol{\omega}^T \sum_{i=1}^{n_\mathrm{c}-1} \left(\boldsymbol{u}(t_{i+1}) - \boldsymbol{u}(t_i)\right)^2, \quad t_0 \leq \dots \leq t_{i-1} \leq t_i \leq t_{i+1} \leq \dots \leq t_f$$

where $\boldsymbol{\omega} \in \mathbb{R}^2$ is a constant penalty factor and n_c relates to the number of available time points. After reformulating Problem (5.1) to a fully discretized NLP, these time points correspond to the chosen collocation points, as described below. However, the penalty term affects the objective function and thus also the optimal solution. To prevent the penalty term from superimposing the actual objective, a sensitivity study relating to the optimization setup yields an appropriate factor of $\boldsymbol{\omega}^T = [0.001\ 0.001]$. The bounds on controls and on differential states in Problem (5.1) are selected according to Tab. 5.1.

5.1.1 Solution Strategy

Solving Problem (5.1) refers again to the described FVM in Section 3.2.3, considering the lowest spatial resolution. For integration and dynamic optimization, a simultaneous approach realized by orthogonal collocation of the remaining time coordinate is used. Therefore, states and controls are discretized into 40 equidistant finite elements within the entire start-up time horizon. Inside one finite element Lagrange polynomials approximate the state trajectories with three collocation points. Control trajectories are considered to be piecewise constant from one collocation point to another. Thus, differential states vanish and the remaining large-scale nonlinear NLP consists only of algebraic equality and inequality constrains. More details on this methodology are elaborated in a comprehensive overview by Biegler [Bie07].

Due to the discretization of two spatial dimensions and one temporal dimension, one single solver run would lead to at least one million variables. This high dimensionality typically exceeds common computational capacities, in particular due to memory limitations. This issue was addressed by making use of a moving horizon strategy which initially considers an optimization run with reduced time horizon (here four finite elements covering the first 100 seconds). After successfully solving the first time period, the time horizon is shifted forward by one finite time element. Thus, the next optimization run benefits from the previous solution as initial guess for the first three time elements of the new horizon. This procedure is repeated until the final time t_f is reached. All in all, the computational effort is just distributed to several sequential optimization runs, but limited memory capacities, in fact, demand for such treatments. All optimization subproblems are implemented using MATLAB and CasADi v3.5.1 [And+18] coding structures, which allow for solving all NLPs via the primal-dual interior point method provided by IPOPT v3.12 [WB06] with the HSL MA97 as underlaying linear solver [HSL07]. The large computation times can be improved by using environments other than MATLAB (e.g., AMPL, GAMS) due to a more efficient allocation of computational resources. Nevertheless, debugging, a more convenient access to all model components, as well as more flexibilities to initialize the problem (e.i, by using powerful SUNDIALS integrators [Hin+05]) makes MATLAB very powerful to deal with sensitive NLPs.

5.2 Results

To evaluate the dynamic optimization results a comparison of three cases is performed:

(a) the NLP solution,

(b) an unconstrained start-up simulation with fixed cooling temperatures of 650 K,

(c) an unconstrained start-up simulation with fixed cooling temperatures equal to the steady state solution of case (a) ($T_{\text{cool,in}} = 517\,\text{K}\,;\, T_{\text{cool,out}} = 650\,\text{K}$).

The unconstrained simulations represent limiting scenarios without control actions coming from the optimizer (open-loop). All scenarios are highlighted in Fig. 5.1 with respect to carbon dioxide conversion, methane selectivity and optimal control trajectories during the entire start-up horizon.

First of all, Fig. 5.1 illustrates that outlet methane selectivity is very close to one, which is plausible due to low outlet gas temperatures (< 650 K) coming from the cooling. In comparison, carbon monoxide formation mostly occurs above 800 K at elevated pressures (see Section 2.1). Nevertheless, the reaction rates for carbon monoxide formation dominate at lower temperatures, which is reflected by the lower methane selectivity within the first 100 s. Once the hot spot is developed, the temperature is high

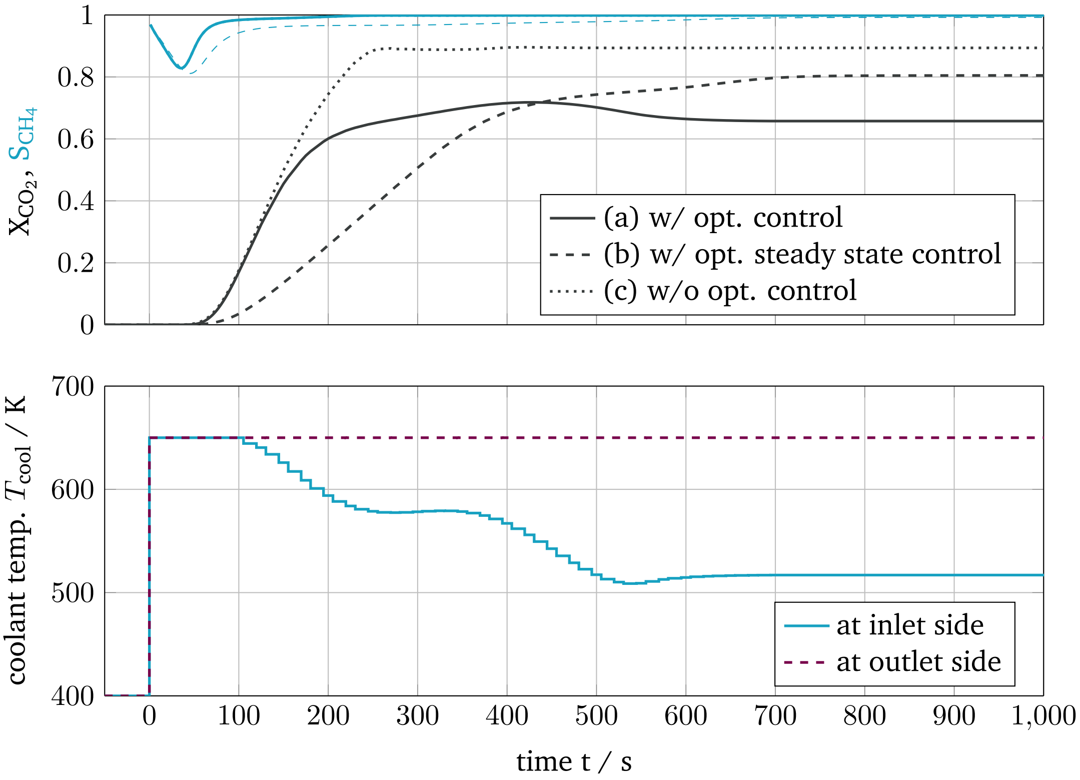

Fig. 5.1.: Top: carbon dioxide conversion and methane selectivity for optimally controlled (a) and uncontrolled (b,c) hot spot formation; bottom: control trajectories for (a).

enough such that the equilibrium superimposes kinetic limitations. Thus, conversion appears to be a more reasonable objective due to its higher sensitivity regarding the optimal cooling temperature. Furthermore, it can be seen that after approximately 100 s the optimal solution features a reduction in carbon dioxide conversion which is realized by a decrease of the inlet-side cooling temperature. This decision becomes reasonable by looking at the transient development of the fixed-bed temperature. Therefore, Fig. 5.2 illustrates the spatial temperature distribution at four different time points.

Initially, the optimizer chooses a step change to the highest cooling temperature. At this stage the cooling rather acts as a heating to initiate the catalytic reaction. At 180 s a clear elevation of the reactor temperature due to an advanced conversion is observed. Although, until that time in scenario (a) no bounds of the inner temperature are active, the optimizer already reduces the inlet cooling temperature to counteract the later exothermic heat release. At 550 s the highest inner temperature reaches the bound of 750 K and stays at that temperature until a steady state appears. From this time on, there is a distinct radial dependency that proves the importance of a two-dimensional model setup. In addition, the highest temperature occurs right at the central reactor axis which is due to the enhanced heat transport resistance in the center of the packed-bed. As a result of the thermal inertia of the reactor, the first control action is observed approx. 450 s before the maximal reactor temperature is reached. Considering the gas velocity in Tab. 5.1, the gas residence time of 2.5 s is significantly smaller than

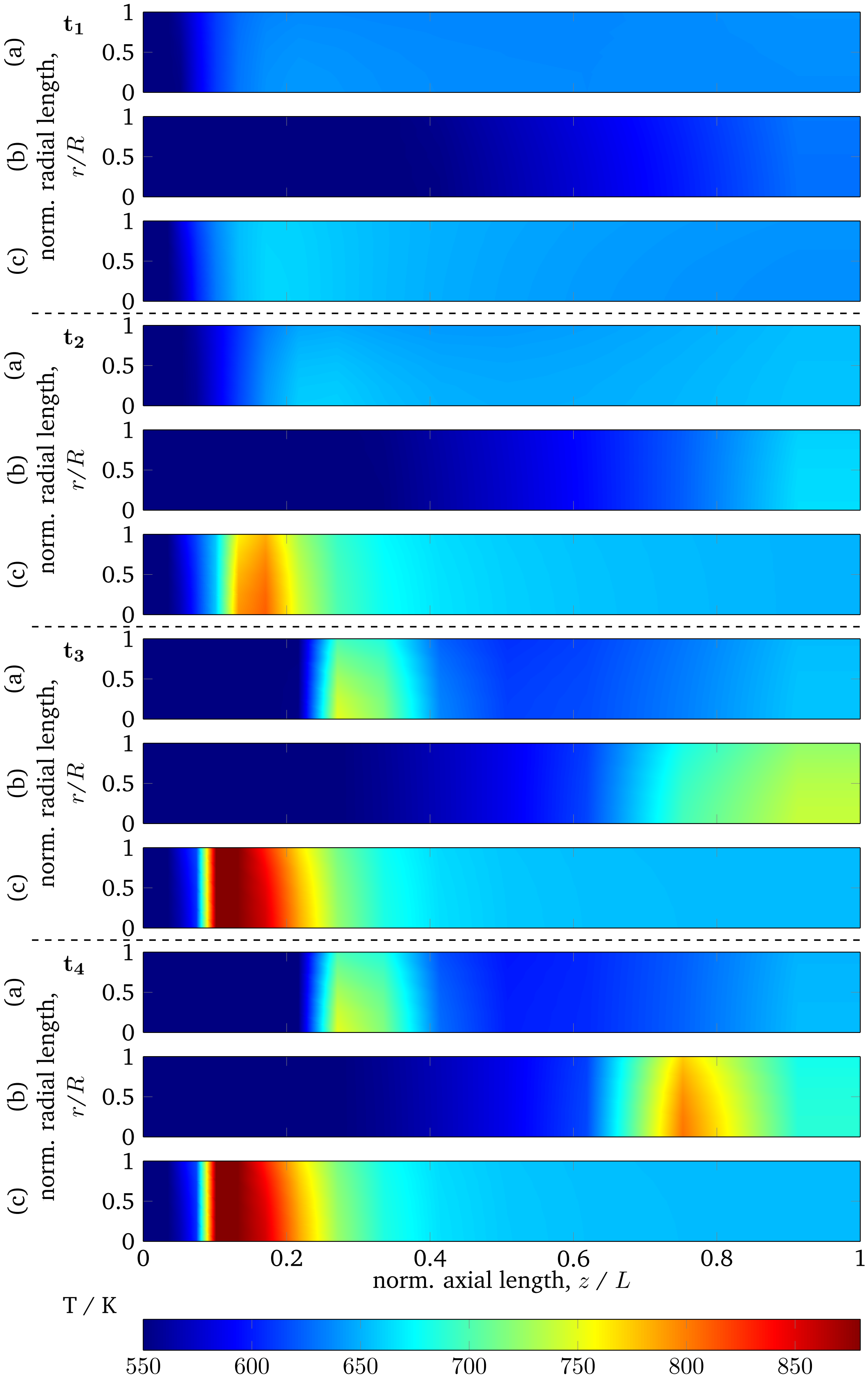

Fig. 5.2.: Controlled (a) and uncontrolled (b,c) reactor temperature distribution; for (b) with $T_{\text{cool,in}} = 517\,\text{K}$, $T_{\text{cool,out}} = 650\,\text{K}$ and for (c) with $T_{\text{cool,in}} = T_{\text{cool,out}} = T_{\text{cool,ub}}$; $t_1 = 180\,\text{s}$, $t_2 = 250\,\text{s}$, $t_3 = 550\,\text{s}$, t_4 - steady state.

the observed time delay which proves that the thermal inertia is much more relevant for optimal dynamic reactor operation. In the uncontrolled start-up scenario (b) with a cooling temperature of 650 K, a significant increase of the reactor temperature is visible and leads to temperatures of approx. 950 K. This drastically exceeds the defined bounds and proves the importance of the proposed methodology for optimal start-up operation.

An additional approach might be a steady state control optimization and subsequently using the resulting cooling temperature for reactor start-up. However, the steady state cooling temperatures taken from the dynamic optimization (scenario a) also lead to a violation of the defined bounds (scenario c). The reason for this behavior lies in a slower reactor start-up with an associated slower temperature increase of the fixed-bed, such that the hot-spot moves towards the warmer reactor outlet. In case of the dynamic optimization the hot spot ignition occurs already close to the reactor inlet due to the high cooling temperatures in the first 100 s. This also shows that the reactor steady state can be approached by different control trajectories leading to different start-up times.In this context, further start-up scenarios beside step changes (e.g., ramping) might be also possible for future investigations to control hot-spots within the fixed-bed.

Moreover, the final steady-state of scenario (a) features characteristics equivalent to the unstable operating branch in Section 4.2. The achieved conversion of 0.65 is neither attainable via the ignition branch nor via the extinction branch. The OCP formulation thus functions similar to a PI-controller and stabilizes the reactor at this favorable operating branch. In addition to the previous findings, this section provides a reliable methodology for finding suitable control trajectories that allow for fast and safe reactor start-up.

5.3 Chapter Summary

An optimal reactor start-up control has proven to be feasible and provides useful information about the dynamics of a carbon dioxide methanation reactor. Furthermore, the detailed dynamic reactor model turned out to be applicable to rigorous dynamic optimization studies. The obtained start-up policy revealed a fast and save transition from a reactor off-state to an unconventional operating state according to the findings in Section 4.2. This supports the relevance of operating at an open-loop unstable branch, as initially suggested from theory.

Nevertheless, the optimal control trajectory strongly relates to the underlying model assumptions. In this regard, it might be difficult to change the cooling fluid temperature fast enough to follow the proposed wall temperatures. Therefore, the penalty term could be used to account for possible control inertia. In addition, the thermal inertia of the reactor jacket, which is not considered here, certainly delays the heat removal depending on the wall thickness. At this point, an experiential model validation under steady and dynamic conditions becomes indispensable. This crucial aspect is addressed in the following Chapter 6.

Since the dynamic optimization approach works for the entire reactor start-up, future work with the focus on less complex set-point tracking scenarios under process disturbances (e.g., via load changes) also appears very promising. Such scenarios are, in particular, valuable for utilizing renewable energy by dynamic methanation. Next to optimal control trajectories, optimal reactor design is another highly relevant objective for future work. In addition, it needs to be underlined that the proposed model can also be used for other applications with heterogeneous catalytic gas-phase reactions. The major difference is often just given by the underlying rate equations, which are very easy to substitute. For instance, the proposed reactor model can be directly used for steam methane reforming due to equivalent reaction kinetics.

Experimental Validation

6

This chapter describes the design and operation of a pilot plant specifically designed to validate the theoretical results of this work. Thus, the pilot plant serves as an experimental assembly capable of operating an industrial-scale fixed-bed reactor under steady and dynamic conditions within a broad operating range. Measuring and controlling, in particular, the dynamic behavior at that scale and in real-time, was found be a challenge that has not yet received much attention in the literature. As outlined in this work, the temperature profile within the fixed-bed represents a unique fingerprint of the reactor state. In consequence, detailed transient temperature measurements along the reactor axis are one of the unique features of the developed pilot plant. Beyond that, a tailor-made heat transfer unit reliably provides well-conditioned thermal oil as a coolant and thus allows for fast and precise interactions with the reactor. Once experimental data are available, a calibration of the proposed two-dimensional dynamic reactor model is performed. The ultimate goal is to provide experimental proof of the validity of the model, the developed criteria, and the predicted reactor behavior under dynamic conditions. From now on, the unit for temperature is changed to degrees Celsius (°C), which is more common for many experimental applications.

6.1 The FOReCAST Pilot Plant

FOReCAST stands for **F**lexible **O**pe**R**ation for **CA**talytic **S**yn**T**heses and metaphorically highlights the importance of reliable state predictions if chemical reactors are operated in a flexible manner. Similar to weather forecasts, decisions must be made in advance to be able to react in time to changing conditions. Thereby, the prediction quality is crucial in order to be able to act to the right extent. The pilot plant aims at gathering sufficient information to enable such predictions to be made based on the model and the criteria introduced previously.

Fig. 6.1 illustrates the conceptual pilot plant piping and instrumentation scheme from gas supply to the exhaust. Five process sections are relevant: the *gas mixing line*, the *feed preheater*, the *reactor unit*, the *thermal oil heat transfer unit*, and the *condenser* with subsequent *gas analysis*.

The *gas mixing line* consists of five mass flow controllers (EL-FLOW® Select by Bronkhorst Deutschland Nord GmbH, Kamen, Germany) each dosing independently defined gas quantities (hydrogen 5.0, carbon dioxide 3.0, nitrogen 3.0, methane 2.5, and helium 5.0

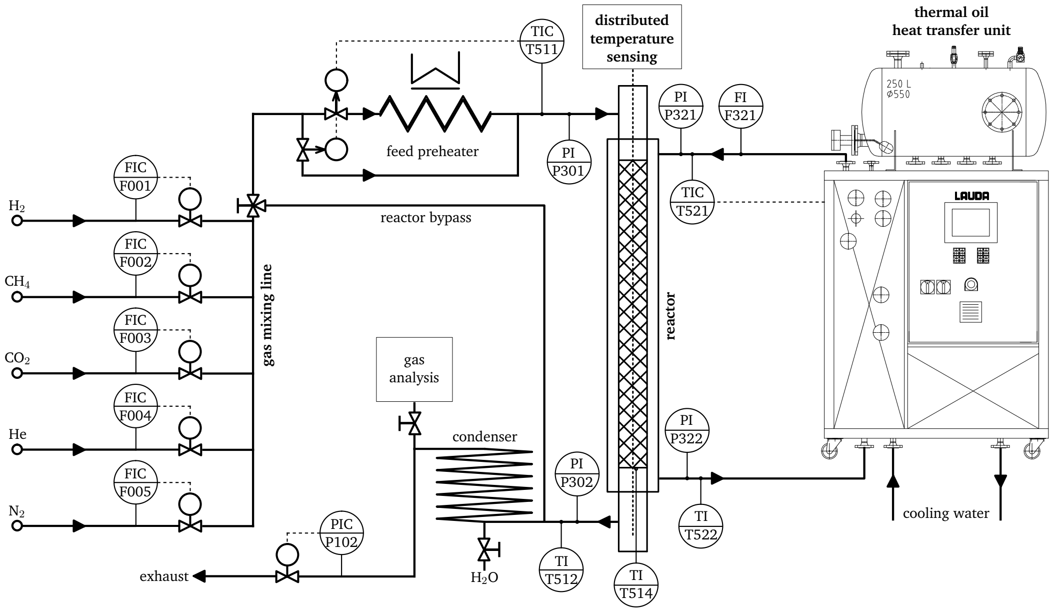
thermal oil
heat transfer unit
distributed temperature sensing
TIC T511
250 L
Φ550
PI P321
FI F321
feed preheater
PI P301
FIC F001
H₂
reactor bypass
TIC T521
LAUDA
FIC F002
CH₄
gas mixing line
FIC F003
CO₂
reactor
gas analysis
FIC F004
He
PI P322
condenser
PI P302
FIC F005
N₂
PIC P102
TI T522
cooling water
exhaust
H₂O
TI T512
TI T514

Fig. 6.1.: Simplified pilot plant piping and instrumentation scheme (not to scale), adapted from P&ID in Fig. A.11 on Page 140.

by Westfalen AG, Münster, Germany) to the central feed supply line. With slight modifications, which are not shown here, a supply with carbon monoxide is also possible. The central supply line then enters the *feed preheater*. Two coupled pneumatic valves are acting as mixing tab by forcing one part of the supply gas to flow into a heat exchanger while the remaining gas bypasses the heat exchanger. After establishing a PID controller circuit and performing step response experiments for parameter identification, the feed gas temperature at the reactor inlet (T511) is properly adjustable within a wide temperature range. The temperature-controlled feed gas enters the *reactor* and reacts according to the other operating conditions. Thereby, the *heat transfer unit* provides the desired thermal oil temperature within the cooling channel and the distributed temperature sensing (DTS) system records the temperature profile within the fixed-bed. The product gas leaves the reactor outlet and enters the water-cooled *condenser* unit in which the produced water is separated at an ambient temperature of 5 °C. Afterwards, a small amount of dry product gas enters the *gas analysis*, while the remaining gas is disposed of via the exhaust. For process control and automation, the Siemens Simatic S7 is used as programmable logic controller (PLC) arranging the communication between operator, sensors, and actuators.

The reactor unit in Fig. 6.1 represents the core of the whole pilot plant. Its design and dimension originate entirely from the computational results of the previous chapters. Accordingly, Fig. 6.2 provides the operating map, including relevant reactor characteristics at different flow rates of an undiluted, stoichiometric feed. At its design point (80 NL/min hydrogen, 20 NL/min carbon dioxide), a gas hourly space velocity (GHSV) of about 10’000 1/h is achieved. At full conversion 2.3 kW heat and 1.8 kg/h water are produced.

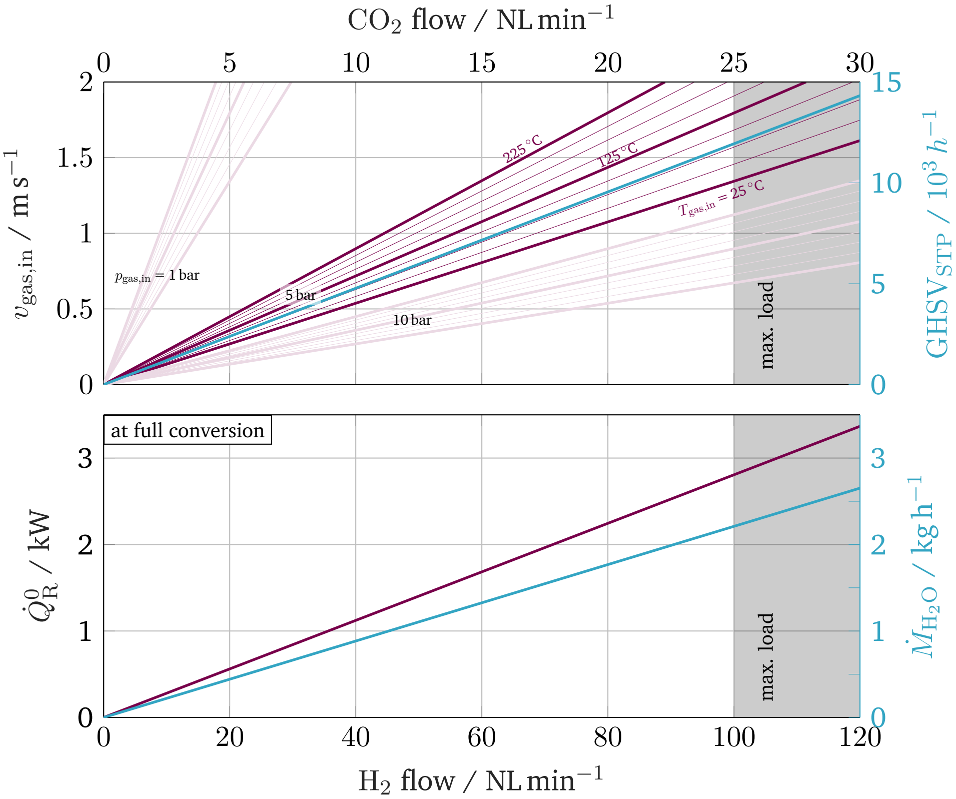

Fig. 6.2.: Reactor operating map for superficial velocity, GHSV, maximum heat and water production.

Since this work only relies on experiments from the first four days of operation, some functionalities could not have been established yet. For example, the gas analysis section was not fully installed, so that all following results are based entirely on the temperature field. Nonetheless, the temperature field alone is sufficient in case of high methane selectivities as expected for CO_2 methanation. Furthermore, the reactor gas load is limited to 20 NL/min hydrogen (design point is 80 NL/min), due to safety restrictions on the exhaust gas disposal. However, these restrictions were resolved after finishing the results for this work. More details on reactor, catalyst, DTS system and heat transfer unit are given in the following sections.

6.1.1 Reactor

The single-tube reactor design is completely driven by the numerical results of the previous chapters. Accordingly, the fixed-bed radius is small enough to allow for sufficient heat transfer and high gas flows simultaneously. Furthermore, the reactor is long enough to study moving reaction fronts and reactor states with hot-spots localized at the end of the fixed-bed. The cooling channel is tight enough to ensure a turbulent coolant flow with intensive heat transfer but no excessive pressure losses. This is particularly important during start-up when the thermal oil is cold and highly viscous. Additionally, the final design of the single-tube reactor is made to be directly transferable to a bundle of several tubes, as usually build for industrial applications.

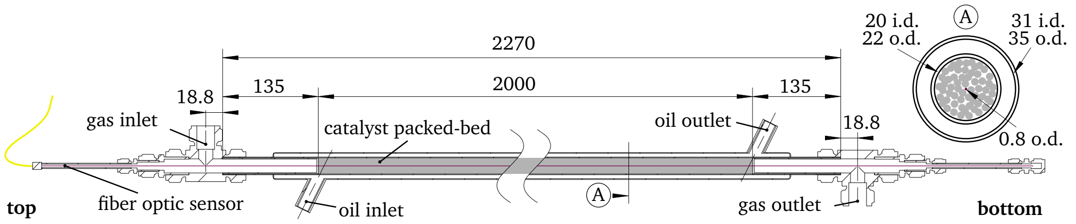

Fig. 6.3.: Constructional drawing of the FOReCAST single-tube reactor unit, measures in mm (not to scale).

The most important design specifications are stated in Fig. 6.3 and Tab. 6.1. The reactor consists of two telescoped and centered tubes of stainless steel. The inner tube contains the catalyst filling and the outer tube serves as a coolant channel. The catalyst bed is fixed from both sides by stainless steel meshes fixed on 135 mm bushings. A 0.8 mm o.d. fiber optic sensor is placed and centered through the inner reactor tube. This small diameter allows for minimally invasive distributed temperature sensing (DTS), which is later explained in greater detail.

6.1.2 Catalyst

Obtaining enough catalyst to fill the entire reactor was certainly one of the most tedious tasks in this work. Too much effort would have been necessary for in-house synthesizing and using a commercial catalyst is usually limited by intellectual properties and property rights that restrict an independent analysis of the delivered materials. Fortunately, an industrial partner was found, who supported this work with a catalyst free of any of those restrictions. In return, the industrial partner claims to remain unmentioned. Thus, the catalyst is further on merely named as Industrial Methanation Reference Catalyst (IMRC).

The IMRC is of spherical shape, as illustrated in Fig. 6.4, and contains nickel as the active component and alumina as support. Nickel was found to be equally dispersed within the entire sphere. A detailed summary of the most important characteristics and the applied analytical methods is given in Tab. 6.2. Besides, the measured values are compared to those used in the previous chapters. Large deviations can be found for density and thermal conductivity. All values are updated with the simulation results presented in this chapter.

Tab. 6.1.: Specifications of the reactor in comparison to previous model assumptions.

specification	symbol	model Tab. 3.2	experiment	unit
inner reactor radius	R	0.01	0.01	m
reactor length	L	2.5	2.0	m
wall thickness	δ_{jac}	2	1	mm
fixed-bed void fraction	ε	0.4	0.39	-
fixed-bed catalyst mass	m_{cat}	-	395.2	g

Tab. 6.2.: Specifications of the IMRC in comparison to previous model assumptions.

specification	symbol	model Tab. 3.2	experiment	unit	method
particle diameter	d_p	2	2.5	mm	particle sizer
density (porous)	ρ_cat	2355.2	1032	$\mathrm{kg/m^3}$	Hg porosimetry
density (nonporous)	ρ^*_cat	-	3451.4	$\mathrm{kg/m^3}$	He pycnometry
therm. conductivity (porous)	λ_cat	3.6	0.19	W/(m K)	heat flow meter
porosity	ε_p	0.6	0.687		Hg porosimetry
mean pore diameter	d_pore	10	9.9	nm	Hg porosimetry
spec. pore volume	$\hat{V}_\mathrm{pore}$	-	0.666	$\mathrm{cm^3/g}$	Hg porosimetry
spec. surface area	$\hat{A}_\mathrm{pore}$	-	146.2	$\mathrm{m^2/g}$	BET
nickel mass fraction	w_Ni	-	9	wt%	ICP-OES

In addition to material analysis, catalyst activity tests at lab-scale are also performed. Although these tests did not lead to a new kinetic model tailor-made for the IMRC, they validate the applicability of the kinetics used so far (see Koschany et al. [KSH16]).

Activity Tests

Catalyst activity tests are conducted using a separate computer-controlled lab-scale reactor. The reactor consists of an 8 mm diameter glass tube loaded with a mixture of one of two finely ground (106 - 150 μm particle diameter) methanation catalysts and a diluent (SiC, 9:1 mass ratio) in an oven. Glass wool is used to fix the catalyst bed in the glass tube. The reactor inlet is connected to preheated gas lines providing H_2, CO_2, and He for the experiments. Sensors are used to monitor the reactor pressures, and thermocouples measured the temperature of the oven heating element, the oven interior, and the catalyst bed. The product gas is analyzed with a micro gas chromatograph (Agilent Technologies 490 Micro GC). Additionally, the samples are collected in gas bags for manual analysis of CO concentration with an offline gas chromatograph (Agilent Technologies 6890 GC). The oven temperature, gas flow rates, and activation of the micro gas chromatograph are controlled by in-house software. The micro gas

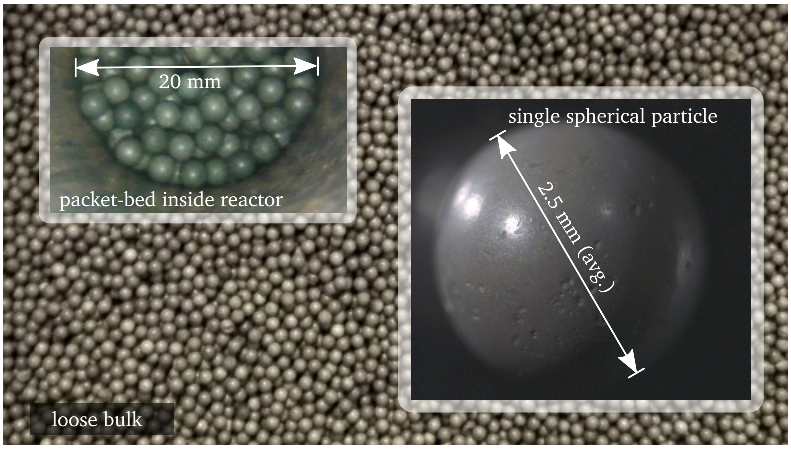

Fig. 6.4.: The Industrial Methanation Reference Catalyst (IMRC).

chromatograph itself is controlled by equipment-specific software (Agilent OpenLAB Chromatography Data System). Before running a methanation experiment, each catalyst sample is reduced by being heated to 350 °C and exposed to a gas stream (5 vol% H_2 in He) of 120 NmL/min for four hours.

Experiments on the IMRC samples are conducted at single oven temperatures (300 °C, 350 °C, or 400 °C), a total gas flow rate of 180 NmL/min, and a series of stoichiometric feed compositions ranging from 3.33 vol% to 13.33 vol% of CO_2 (0.033 bar CO_2 – 0.133 bar CO_2). Due to the strong exothermicity of the methanation reaction, the bed temperature strongly deviates from the oven temperature. The initial and final trials on each sample are conducted using identical parameters to assess for possible deactivation. The experiments on IMRC-4, 5, and 6 are preceded by a four hour conditioning period at a feed composition of 3.33 vol% CO_2 and the experimental temperature, respectively. The CO_2 conversion and CH_4 yield are calculated according to Eq. (A.2) on Page 120. The results are illustrated in Fig. 6.5 and compared to the kinetic model applied in this work. A complete compilation of experimental parameters and results by sample is given in Tab. A.4 of the Appendix on Page 139.

As seen in Fig. 6.5, the IMRC shows a lower activity compared to the kinetic model from Koschany et al. [KSH16]. One reason is certainly related to the lower catalyst loading of the IMRC (9 wt% vs. 19 wt%). Scaling the rate coefficient in Eq. (A.25) down to 20 % shows better agreement with the IMRC experiments. However, there are still significant deviations that are not reflected by the scaled kinetic model, in particular for the conditioned samples 4, 5, and 6. In consequence, it remains unclear to what extent the kinetic model is applicable to the IMRC. The performed tests are subject to many equipment-specific but also catalytic uncertainties, which can easily sum up to inaccuracies of $\pm$ 10 percent points. Thus, the presented data allow for a general estimation rather than a precise description of the catalytic activity.

One of the most significant error sources relates to the exothermicity of the reaction, which causes temperature increases up to 60 °C within the catalyst sample even at high catalyst and gas dilutions. Furthermore, the used micro gas chromatograph suffers from sensible calibration procedures and a required up-stream water separation unit. Depending on the reaction conditions, different amounts of water have to be separated, which leads to flow rates in the gas analysis section that may not fit the calibration. In order to validate the gas analysis, high-temperature tests have been performed, ensuring the reaction to run into the thermodynamic equilibrium without any kinetic limitation (sample 7-8 in Fig. 6.5). These tests show very good agreement with thermodynamic data and give rise to an acceptable quality of the gas analysis.

Besides these technical aspects, the catalyst activity is also found to depend on its prior operating conditions. Despite the complete reduction, the catalyst showed higher activities if it has once been exposed to higher conversion conditions. This trend is

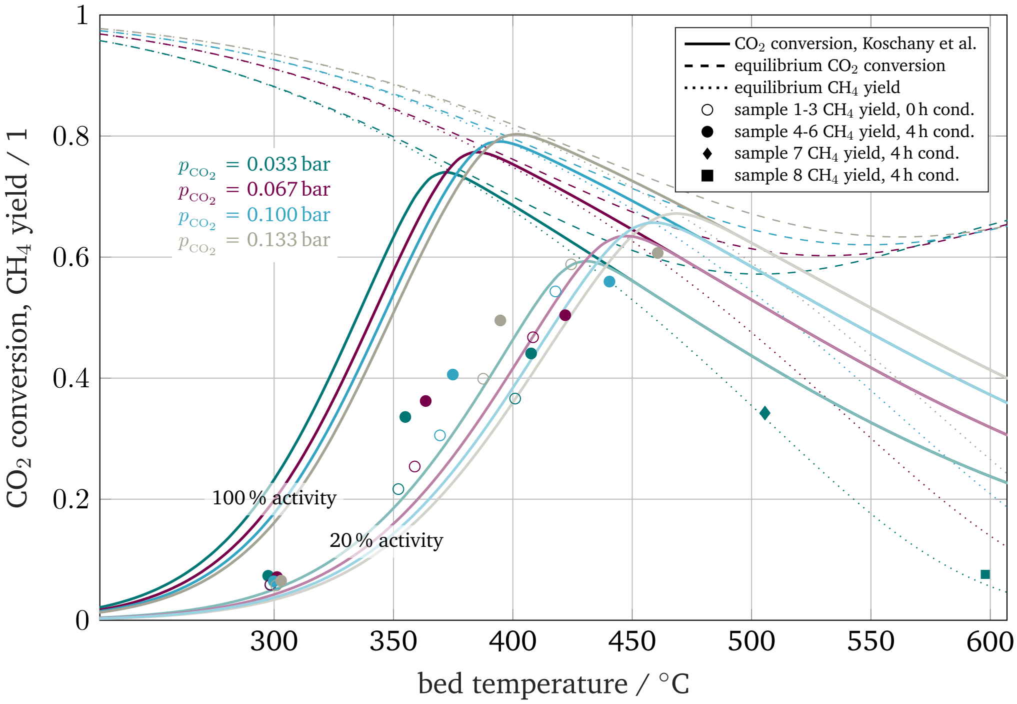

Fig. 6.5.: Activity tests of the IMRC in comparison with the reference kinetic model from Koschany et al. [KSH16], $p_{\mathrm{gas,in}}$=1 bar, $\mathrm{F_{in}}$=216 $\mathrm{NL\,h^{-1}\,g_{cat}^{-1}}$, cat. mass=50 mg, $\dot{V}_{\mathrm{gas,in}}$=180 $\mathrm{NmL\,min^{-1}}$, molar ratio H_2/CO_2=4, diluent: He, experiments conducted by Lisa Yvonne Downen, data and parameter available in Tab. A.4 on Page 139.

shown in Fig. 6.5 by comparing samples with and without a four-hour conditioning phase and indicates possible restructuring mechanisms of the catalyst at a micro-scale. A detailed analysis of this behavior is, however, not performed and open to future investigations.

6.1.3 Distributed Temperature Sensing (DTS)

Conventional temperature measurements for industrial or R&D applications are typically performed via thermocouples (TCs) or resistance temperature detectors (RTDs). However, these sensors only provide local point measurements. As this work aims for temperature distributions in the narrow fixed-bed geometry, these conventional measurements are insufficient. Fiber optics are lightweight, minimally invasive, and applicable as sensors to gather temporally and spatially resolved temperature data in various environments. Possible applications of this technology range from monitoring large nuclear infrastructures to automotive testing facilities. Commercially available systems operate with spatial resolutions in the order of millimeters and temporal resolutions of up to 50 Hz. In this work, the LUNA ODiSI-6100 and a custom-made fiber optic sensor are used to equip the given reactor with this novel distributed temperature sensing (DTS) technology.

The LUNA ODiSI-6100 utilizes swept-wavelength interferometry to interrogate the fiber optic sensor. Laser light is sent into the fiber and backscattered (Rayleigh scatter) differently depending on an external stimulus (e.g., strain, temperature). As a result, local spectral shifts are measured and compared to a second baseline measurement, revealing precise information about the fiber condition along its entire length. In theory, this so-called optical frequency domain reflectometry (OFDR) reaches a spatial resolution of approximately 10 μm that is determined by the spectral width of the tunable laser source. However, the software is limited to a resolution window of 0.6 - 2.5 mm to guarantee fast data processing. This resolution translates to 800 - 3333 simultaneous measurements along the two-meter fixed-bed in Fig. 6.3. Small changes of the measured spectral (or frequency) shifts are directly proportional to local temperature and strain changes [Kre+06]. For larger shifts, this dependency becomes nonlinear and fiber specific. Thus, covering large temperature ranges requires the fiber optic sensor to be calibrated at specific, well-known temperatures prior to any measurement task (see, e.g., [Woo+14]). A complete description of the sensing mechanism and its limitations can be found in the work conducted by Froggatt and Moore [FM98] and Kreger et al. [Kre+06].

In this work, the DTS calibration is performed against a reference Pt-100 1/10 DIN RTD (T514) placed directly at the outlet of the fixed-bed (see Fig. 6.1). Initially, the entire fixed-bed is conditioned by gas and thermal oil flow until inlet and outlet temperatures have equalized. At this temperature T_{tare}, the DTS is tared to zero. Afterwards, the injected thermal oil is used for conditioning the outlet gas temperatures between T_{tare} and 300 °C. In this range, the reference RTD itself showed an accuracy of 0.5 °C. Comparing DTS and RTD steady-state temperatures at the end of the fixed-bed results in the calibration curve of Fig. 6.6. Accordingly, the DTS accuracy was found to be in the order of 1 °C.

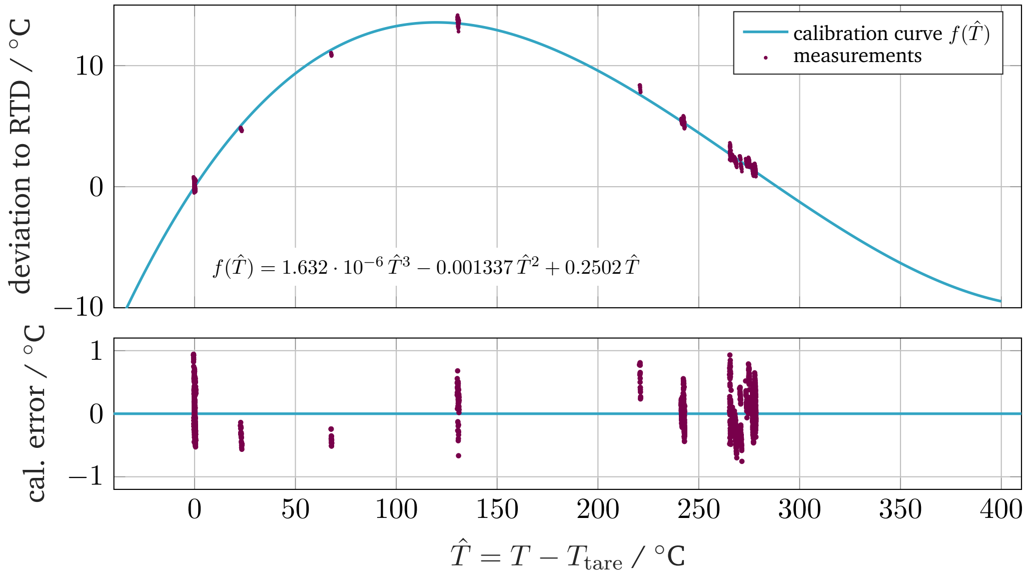

Fig. 6.6.: Calibration result of the DTS with RTD T514 placed directly at the end of the fixed-bed.

A calibration at temperatures beyond 300 °C would exceed the thermal oil operating limits. However, the calibration curve remains valid even at higher temperatures, if the tare temperature is adjusted accordingly. This is particularly necessary to keep track of the high-temperature hot-spots that have been predicted by the previous chapters.

6.1.4 Thermal Oil Heat Transfer Unit

As shown by the model-based control studies, the high thermal sensitivity of the reactor requires a cooling system that is capable of fast and accurate tempering of the cooling channel. Among the three most relevant reactor cooling concepts (see Section 4.2.2), a thermal oil-based cooling system was identified to fulfill all requirements with reasonable realization effort considering infrastructure and space of the available lab facilities. A critical aspect is the upper temperature limit of 330 °C of the chosen thermal oil (Marlotherm SH). At first glance, this limit appears to be violated when the model predicts hot-spot temperatures above 700 °C. However, the two-dimensional modeling approach in this work also predicts strong radial temperature gradients within the fixed-bed. Together with specifically designed cooling channel dimensions and thermal oil flow rates, a violation of the upper oil temperature limit is avoided.

The heat transfer unit, as illustrated in Fig. 6.1, is specifically designed for the unique requirements of this work. It is based on a LAUDA ITH 350 industrial heat transfer system.

The heat transfer unit primarily consists of two separate circuits; one low-temperature circuit and one high-temperature circuit. The low-temperature circuit is used to temper a buffer tank filled with approximately 200 L thermal oil up to 150 °C. The high-temperature circuit supplies the reactor cooling channel with oil at the desired temperature (up to 330 °C). In order to realize fast temperature changes as proposed in the previous chapters, cold thermal oil from the buffer tank can be injected into the high-temperature circuit. To achieve accurate temperature steps and ramps, a PID-controller is used to adjust the injection with respect to the supply temperature at the reactor inlet. With this setup it was proven that temperature steps of up to 150 °C/min are possible. Besides the fast interaction, temperature accuracy is also one design aspect. Therefore, Pt-100 1/10 DIN RTDs with an accuracy of 0.5 °C are installed at the inlet (T521) and outlet (T522) of the cooling channel (see Fig. 6.1). In addition to temperature and

Tab. 6.3.: Specifications of the thermal oil heat transfer unit.

cooling fluid	Marlotherm SH	
supply flow rate	5 - 60	L/min
supply temperature	20 - 330	°C
supply pressure	1 - 10	bar(a)
heating capacity (electric)	2 x 12	kW
cooling capacity (cooling water)	50	kW

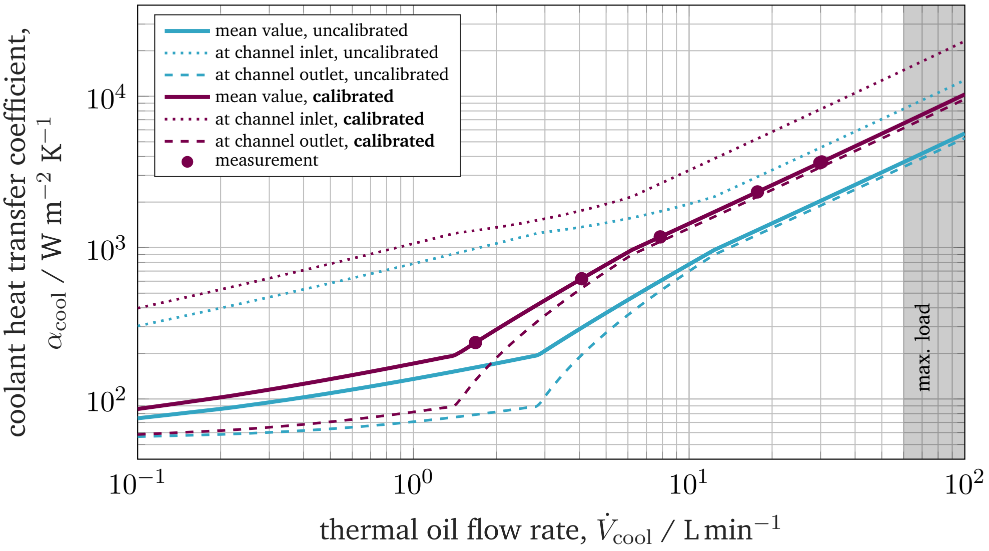

Fig. 6.7.: Coolant heat transfer coefficient according to the reactor dimensions in Fig. 6.3, based on correlations depicted in Fig. A.4 on Page 129.

pressure sensors, a Coriolis mass flow meter (F321) is also installed, which is essential to identify the heat transfer coefficient within the reactor cooling channel. Accordingly, Fig. 6.7 illustrates the uncalibrated and calibrated coolant heat transfer coefficients over the thermal oil flow rate that can be expected with the given experimental setup. Details regarding the calibration are described in the next section. Further specifications of the thermal oil heat transfer unit are given in Tab. 6.3.

6.2 Model Calibration

With the experimental setup from above, a reliable set of data can be obtained and compared to the detailed dynamic reactor model (from Section 3.2). Thereby the primary focus is attached to the temperature profile at the central reactor axis. Due to the model complexity, including a high number of uncertain parameters, good agreement with the experiments is expected to be only possible after adjusting the underlying correlations for mass and energy transport. For that purpose, however, no correlations for mass and energy transport are developed from scratch. Instead, the already implemented correlations are calibrated (reverse engineering approach) by identifying and adjusting the most relevant model parameters. Precisely this non-trivial task is the focus of this section.

Throughout the entire work, three model components have proven to be the most significant for calibration: *radial heat transfer*, *reaction kinetics* and *catalyst mass transport limitations*. The radial heat transfer is mainly determined by energy transport within the fixed-bed (convective and conductive), at the inner wall, and within the cooling channel. The reaction kinetics are adjusted by scaling the rate coefficient as well as the activation energy. The catalyst mass transport limitation is adjusted by

Tab. 6.4.: Parameters used for model calibration.

model component	target parameter	scaling factor	scaling interval	enters in	test used to identify
radial heat transfer	$\dot{V}_{\mathrm{cool}}$	$S_{\dot{V}_{\mathrm{cool}}}$	[0, 5]	Eq. (A.21)	nonreactive
	α_{w}	$S_{\alpha_{\mathrm{w}}}$	[0, 5]	Eq. (3.36)	nonreactive
	$\lambda_{\mathrm{cond},r}$	$S_{\lambda_{\mathrm{cond},r}}$	[0, 5]	Eq. (A.18)	nonreactive
	λ_{conv}	$S_{\lambda_{\mathrm{conv}}}$	[0, 5]	Eq. (A.18)	nonreactive
reaction kinetics	k_0	S_{k_0}	[0, 5]	Eq. (A.25)	reactive
	E_A	S_{E_A}	[0, 5]	Eq. (A.25)	reactive
catalyst mass transport limitations	Φ_{α}	$S_{\Phi_{\alpha}}$	0 or 1	Eq. (3.37)	reactive

switching the key component ($\alpha \in$ [CH_4, CO_2, H_2O, or H_2]) within the Thiele modulus calculation in Eq. (3.38). The corresponding scaling factors and the model equations in which they enter are listed in Tab. 6.4. Note that a scaling factor of one with CO_2 as Thiele modulus key component means that the model is evaluated at its reference setting. Furthermore, the parameters listed in Tabs. 6.1 and 6.2 are also updated within the model, respectively.

In addition to the parameters in Tab. 6.4, the model sensitivity with respect to the intraparticle diffusion coefficients in Eq. (3.39) has also been investigated. However, no significant contribution of these coefficients was found within reasonable surroundings from their reference setting. Another important aspect of a successful model calibration belongs to the spatial resolution of the FVM scheme. Most importantly, without radial discretization, the replication of the measured temperature profile at the central axis largely fails due to significant radial temperature gradients. This underlines the imperative nature of the two-dimensional modeling approach used in this work. A resolution of 200 FVs per meter in axial and 8 FVs per centimeter in radial direction shows the best trade-off between accuracy and numerical effort.

6.2.1 Plant Operation and Testing Procedure

Prior to the testings used for model calibration, several tests were conducted for pilot plant commissioning. During these tests, aspects such as controller design, sensor accuracy, gas and oil pressure drops and flow rates, catalyst reduction, and safety are examined. After successful pilot plant commissioning, a test plan for model calibration is designed such that mutual interference between the seven parameters in Tab. 6.4 is avoided as far as possible. Therefore the test plan consists of two parts: a *non-reactive* and a *reactive* test set.

The *non-reactive* test set contains experiments with inert gas flows mainly consisting of nitrogen, in which the reactor solely functions as a heat exchanger having cold inlet gas and hot inlet oil flowing in cocurrent direction. The corresponding measured conditions are listed in Tab. 6.5. These experimental conditions are set in such a way that the temperature profile is selectively responsive to the parameters for radial heat transfer. At high cooling loads (experiments 3 to 6), the radial energy transport is mainly determined by the fixed-bed, such that varying gas loads allow for selective identification of $\lambda_{\mathrm{cond},r}$ and λ_{conv}. In contrast, at low cooling loads (experiments 1,2,7,8) the radial energy transport is mainly determined by the remaining parameters ($\dot{V}_{\mathrm{cool}}$, α_{w}).

Prior to the *reactive* tests, the catalyst was reduced by adding hydrogen (1 NL/min) to an inert nitrogen gas flow (20 NL/min). Seconds after the hydrogen injection, the temperature at the inlet increases by about 20 °C and forms a reaction wave that travels through the entire reactor. Once the bed temperature is equalized, the hydrogen ratio is increased stepwise until the catalyst is exposed to a 100 % hydrogen atmosphere (flow rate remains at 20 NL/min). During this procedure, no further traveling reaction waves are observed. After 10 min pure hydrogen flow without any detectable temperature increase, the catalyst counts as fully reduced and ready for reactive experiments.

The *reactive* test set contains experiments with stoichiometric mixtures of hydrogen and carbon dioxide differently diluted with nitrogen. Initially, a high dilution is selected in order to avoid unexpected reactor runaways. Afterwards, experiments with lower dilution and/or higher pressures are performed in order to collect enough data for calibrating the parameters related to reaction kinetics and catalyst mass transport. The corresponding measured conditions are listed in Tab. 6.6.

6.2.2 The Uncalibrated Model

Before model calibration, the raw version of the model and its deviation from the experiments is examined. This version matches the model used in the previous chapters, but considers the parameter updates from Tabs. 6.1 and 6.2. It is further referred to as *Case 0* and contains the respective scaling factors from Tab. 6.7.

Comparing the nonreactive temperature profiles in Fig. 6.8, reveals moderate deviations of less than 20 °C. More significant deviations are observed by looking at the reactive experiments in Fig. 6.9. This mismatch is mainly caused by wrong hot-spot positions and wrong peak temperatures. Nonetheless, trends and relations between the individual experiments are well reflected, which verifies the general applicability of the proposed two-dimensional model approach. Consequently, further improvements are expected by an appropriate model calibration as demonstrated in the next section.

Tab. 6.5.: Nonreactive test set and corresponding experimental conditions at steady state.

exp	date & time	$p_{\mathrm{gas}}^{\mathrm{in}}$ bar(g)	$p_{\mathrm{gas}}^{\mathrm{out}}$ bar(g)	$T_{\mathrm{gas}}^{\mathrm{in}}$ °C	$T_{\mathrm{gas}}^{\mathrm{out}}$ °C	$v_{\mathrm{gas}}^{\mathrm{in}}$ m/s	$p_{\mathrm{cool}}^{\mathrm{in}}$ bar(g)	$p_{\mathrm{cool}}^{\mathrm{out}}$ bar(g)	$T_{\mathrm{cool}}^{\mathrm{in}}$ °C	$T_{\mathrm{cool}}^{\mathrm{out}}$ °C	$T_{\mathrm{cool}}^{\mathrm{mod}}$ °C	$\dot{V}_{\mathrm{cool}}$ L/min	$\dot{V}_{\mathrm{gas}}^{\mathrm{in}}$ NL/min	$x_{\mathrm{CH_4}}^{\mathrm{in}}$ %	$x_{\mathrm{CO_2}}^{\mathrm{in}}$ %	$x_{\mathrm{H_2O}}^{\mathrm{in}}$ %	$x_{\mathrm{H_2}}^{\mathrm{in}}$ %	$x_{\mathrm{N_2}}^{\mathrm{in}}$ %
1	29.11.2019 11:14:16	0.23	0.17	60.9	302.2	0.529	1.21	1.06	300.6	300.5	302.2	29.8	10.0	0	0	0	0	100
2	29.11.2019 11:51:11	6.60	5.49	30.2	301.8	0.775	1.17	1.07	300.2	299.7	301.8	30.3	100.0	0	0	0	0	100
3	04.03.2020 15:41:24	8.36	7.48	82.4	298.2	0.732	0.69	0.69	300.8	298.1	297.9	7.9	99.2	0	0	0	0	100
4	04.03.2020 15:49:31	8.36	7.50	82.9	299.8	0.745	0.84	0.79	301.0	299.6	299.5	17.7	100.9	0	0	0	0	100
5	05.03.2020 11:25:51	0.49	0.15	165.5	299.2	1.145	0.78	0.80	301.0	299.4	301.0	13.8	20.0	0	0	0	0	100
6	05.03.2020 13:49:13	0.15	0.11	227.4	299.3	0.846	0.74	0.71	300.9	300.1	300.9	12.0	10.0	0	0	0	0	100
7	05.03.2020 14:13:27	0.39	0.13	218.5	300.3	1.308	1.10	0.96	301.0	300.5	301.0	28.3	19.0	0	0	0	21.0	79.0
8	05.03.2020 14:26:55	0.34	0.13	196.9	250.3	1.299	1.13	0.99	250.8	250.4	250.8	28.1	19.0	0	0	0	21.0	79.0

Tab. 6.6.: Reactive test set and corresponding experimental conditions at steady state.

exp	date & time	$p_{\mathrm{gas}}^{\mathrm{in}}$ bar(g)	$p_{\mathrm{gas}}^{\mathrm{out}}$ bar(g)	$T_{\mathrm{gas}}^{\mathrm{in}}$ °C	$T_{\mathrm{gas}}^{\mathrm{out}}$ °C	$v_{\mathrm{gas}}^{\mathrm{in}}$ m/s	$p_{\mathrm{cool}}^{\mathrm{in}}$ bar(g)	$p_{\mathrm{cool}}^{\mathrm{out}}$ bar(g)	$T_{\mathrm{cool}}^{\mathrm{in}}$ °C	$T_{\mathrm{cool}}^{\mathrm{out}}$ °C	$T_{\mathrm{cool}}^{\mathrm{mod}}$ °C	$\dot{V}_{\mathrm{cool}}$ L/min	$\dot{V}_{\mathrm{gas}}^{\mathrm{in}}$ NL/min	$x_{\mathrm{CH_4}}^{\mathrm{in}}$ %	$x_{\mathrm{CO_2}}^{\mathrm{in}}$ %	$x_{\mathrm{H_2O}}^{\mathrm{in}}$ %	$x_{\mathrm{H_2}}^{\mathrm{in}}$ %	$x_{\mathrm{N_2}}^{\mathrm{in}}$ %	$\mathrm{H_2/CO_2}^{\mathrm{in}}$ -
9	05.03.2020 14:36:49	0.27	0.11	197.9	253.9	1.223	1.14	1.00	251.0	250.7	250.8	28.0	17.0	0	5.9	0	23.5	70.6	3.99
10	05.03.2020 14:47:14	0.29	0.11	199.6	267.5	1.210	1.11	1.00	266.2	265.9	266.1	28.0	17.0	0	5.9	0	23.5	70.5	4.00
11	05.03.2020 14:53:52	0.45	0.13	195.8	268.3	1.478	1.14	0.98	265.9	265.7	265.8	28.0	23.5	0	7.4	0	28.9	63.7	3.92
12	05.03.2020 15:24:43	0.59	0.16	192.6	269.0	1.709	1.13	1.01	266.0	265.9	265.9	28.1	30.0	0	9.9	0	40.2	49.9	4.06
13	05.03.2020 15:35:27	1.03	0.76	192.6	268.5	1.335	1.14	0.98	266.0	265.9	265.9	28.1	30.0	0	10.0	0	40.0	50.0	4.02
14	05.03.2020 15:44:10	1.13	0.77	191.8	269.0	1.484	1.12	1.00	266.0	266.0	266.0	28.1	35.0	0	11.4	0	45.8	42.8	4.02
15	05.03.2020 16:48:45	0.14	0.17	193.6	267.8	1.185	1.13	0.97	265.9	265.9	265.9	28.0	15.0	0	19.9	0	80.1	0	4.02
16	05.03.2020 17:05:50	0.44	0.39	186.2	268.0	1.118	1.16	1.01	265.9	265.9	265.9	28.0	18.0	0	16.7	0	66.7	16.6	3.99

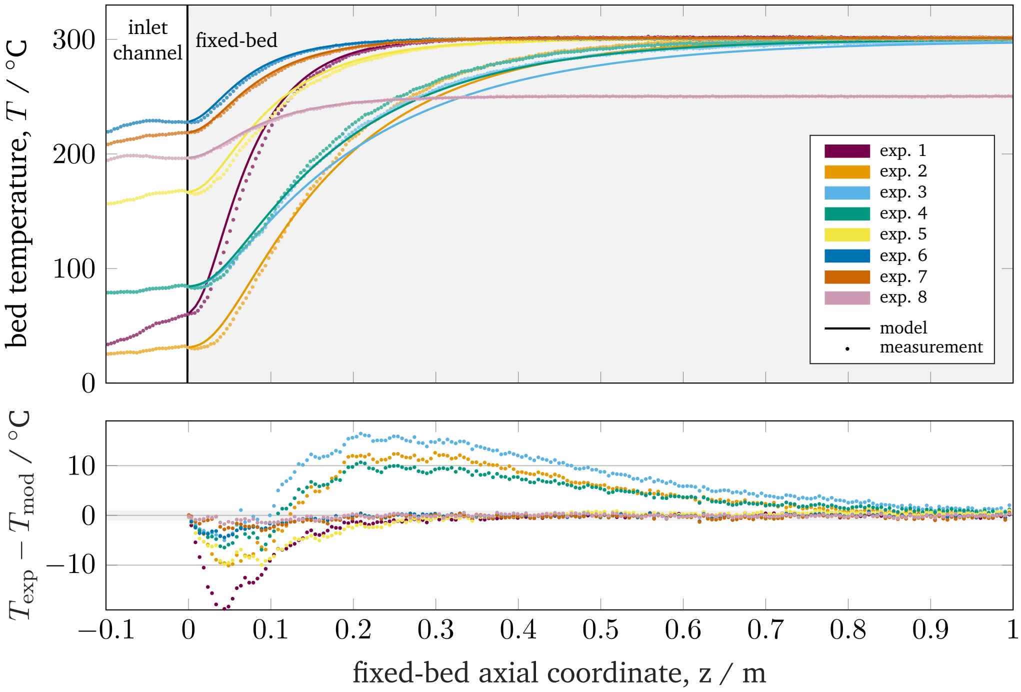

Fig. 6.8.: Nonreactive experiments in comparison to the uncalibrated model (Case 0).

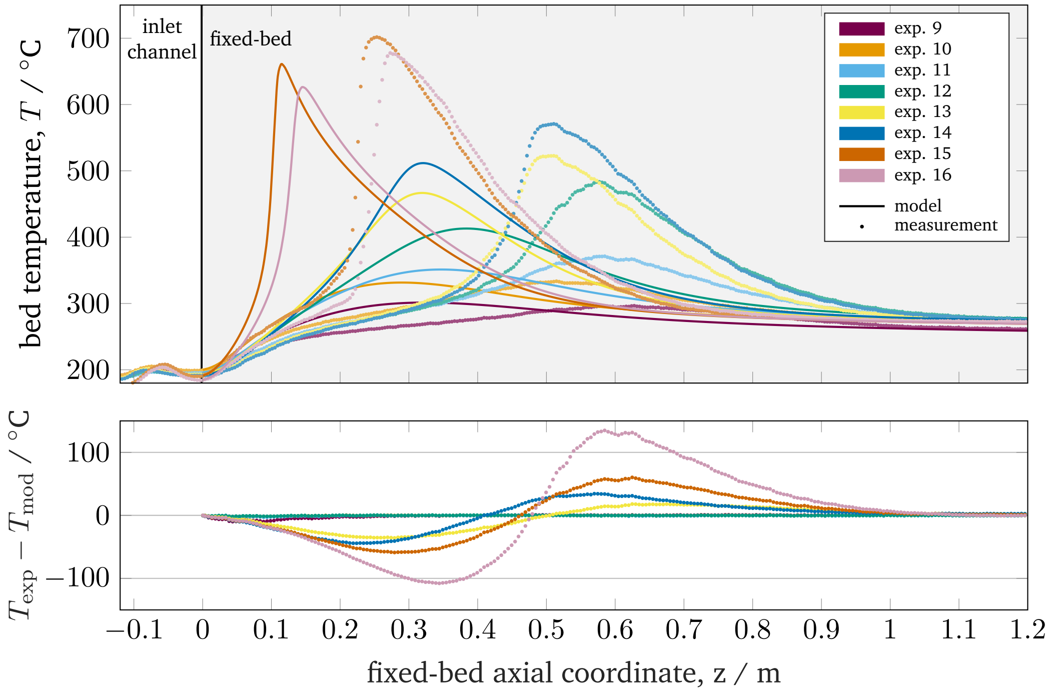

Fig. 6.9.: Reactive experiments in comparison to the uncalibrated model (Case 0).

6.2.3 Model Calibration and Parameter Identification

As indicated by Figs. 6.8 and 6.9 temperature changes are mainly located within the first meter of the fixed-bed. Thus, the model calibration is exclusively performed on this segment which includes 770 equally distributed temperature measurements for each experiment. In order to use this information for model calibration, all data sets need to be scaled down and interpolated to match the 200 axial grid points of the model.Consequently, the model calibration is performed on 16 experiments with 200 temperature measurements each, located along the central reactor axis.

Based on the computed and measured temperature profiles a least squares minimization strategy is used to calibrate the model. Therefore, the following nonlinear optimization problem is formulated:

$$\begin{aligned} \min_{\boldsymbol{p}} \quad & \sum_{i=1}\sum_{j=1} \frac{(T_{i,j}^{\text{mod}} - T_{i,j}^{\text{exp}})^2}{n^T \, n^{\text{meas}}}, \\ \text{s.t.} \quad & 0 = \boldsymbol{f}_j(\boldsymbol{x}_j, \boldsymbol{u}_j, \boldsymbol{p}), \\ & T_{:,j}^{\text{mod}} = \mathbf{M}\, \boldsymbol{x}_j, \\ & 0 \leq \boldsymbol{x}_j \leq \inf, \quad \boldsymbol{p}_{\text{lb}} \leq \boldsymbol{p} \leq \boldsymbol{p}_{\text{ub}}, \\ & i \in 1, ..., n^T, \quad j \in 1, ..., n^{\text{exp}}. \end{aligned} \tag{6.1}$$

The objective function considers the difference between modeled and measured temperatures expressed by their normalized residual sum of squares. The nonlinear function $\boldsymbol{f}_j$ represents a stationary reactor model similar to the representation in Eq. (3.41) and corresponds to the respective experiment j. Thus, the more experiments are considered, the more nonlinear functions constrain the optimization problem. Accordingly, each experiment is characterized by individual differential states $\boldsymbol{x}_j \in \mathbb{R}^{11200}$, experimental settings $\boldsymbol{u}_j \in \mathbb{R}^{10}$, and calibration parameters $\boldsymbol{p}_j \in \mathbb{R}^{10}$. Here, $\boldsymbol{u}$ and $\boldsymbol{p}$ are arranged as

$$\begin{aligned} \boldsymbol{p} &= \left[S_{\dot{V}_{\text{cool}}} \; S_{\lambda_{\text{cond},r}} \; S_{\alpha_{\text{w}}} \; S_{\lambda_{\text{conv}}} \; S_{k_0} \; S_{E_A} \; S_{\Phi_{\text{CH4}}} \; S_{\Phi_{\text{CO2}}} \; S_{\Phi_{\text{H2O}}} \; S_{\Phi_{\text{H2}}} \right], \\ \boldsymbol{u} &= \left[p_{\text{gas}}^{\text{in}} \; T_{\text{gas}}^{\text{in}} \; \dot{V}_{\text{gas}}^{\text{in}} \; T_{\text{cool}}^{\text{mod}} \; \dot{V}_{\text{cool}} \; x_{\text{CH}_4}^{\text{in}} \; x_{\text{CO}_2}^{\text{in}} \; x_{\text{H}_2\text{O}}^{\text{in}} \; x_{\text{H}_2}^{\text{in}} \; x_{\text{N}_2}^{\text{in}} \right], \end{aligned}$$

and correspond to the values of each experiment in Tabs. 6.5 and 6.6. The selection matrix $\boldsymbol{M} \in \mathbb{R}^{200 \times 11200}$ simply picks those states of $\boldsymbol{x}$ that correspond to the temperature values at the central axis. In order to guarantee physically plausible results, all states and parameters are properly bounded. Thereby, the parameter bounds $\boldsymbol{p}_{\text{lb}}$ and $\boldsymbol{p}_{\text{ub}}$ correspond to the scaling interval in Tab. 6.4. Due to low pressure drops of the reactive experiments, the model is considered with constant pressure equal to the respective inlet pressure. With this assumption algebraic states $\boldsymbol{z}$ as used in Eq. (3.41) are omitted within the optimization.

Since each experiment considered in Problem (6.1) demands for an additional set of model equations, the problem size can easily reach 200’000 states, if all experiments are used simultaneously. However, the previously proposed separate consideration of non-reactive and reactive experiments splits the calibration into two problems of about 100’000 states each and, thus, leads to less computational effort for solving. These large-scale nonlinear optimization problems are implemented using MATLAB and CasADi v3.5.1 [And+18] coding structures, which allow for solving all NLPs via the primal-dual interior point method provided by IPOPT v3.12 [WB06] with the HSL MA97 as underlying linear solver [HSL07]. The initial guesses required for the optimization match the uncalibrated model solutions (Case 0) in Figs. 6.8 and 6.9.

First, the calibration with nonreactive experiments is discussed. Then, the obtained heat transport parameters are fixed and used for the calibration with reactive experiments to identify the remaining reaction parameters.

Heat Transport Calibration

The optimization problem for heat transport calibration is further on denoted as *Case A* and considers experiment 1 to 8 of Tab. 6.5. Hence, only heat transport parameters are calibrated such that

$$\boldsymbol{p} = \left[S_{\dot{V}_{\text{cool}}}\ S_{\lambda_{\text{cond},r}}\ S_{\alpha_{\text{w}}}\ S_{\lambda_{\text{conv}}}\ 1\ 1\ 0\ 1\ 0\ 0\right].$$

The optimization results are illustrated in Fig. 6.10 and indicate a significant model improvement with deviations below 5 °C, which is far better than without calibration (compare to Fig. 6.8). However, the remaining model deviation is still larger than the uncertainty of the temperature sensor, which indicates further unknown systematic uncertainties either on the modeling or on the experimental side. Possible sources for uncertainty are part of the discussions later on.

The corresponding optimal scaling factors are listed under Case A in Tab. 6.7. Despite the moderate impact on the temperature profiles, scaling factors between 0.6 and 3.2 emphasize the significance of the model calibration. Besides the here presented results, some optimization runs are also performed with fixed parameter subsets in order to analyze the sensitivity of the final solution. As a result, the radial transport parameters within the fixed-bed $S_{\lambda_{\text{cond},r}}$ and $S_{\lambda_{\text{conv}}}$ turned out to be very consistent between different optimization runs, whereas $S_{\dot{V}_{\text{cool}}}$ and $S_{\alpha_{\text{w}}}$ appear to be rather variant. This is certainly a result of the dominating radial heat transport resistance within the fixed-bed. A detailed model-based sensitivity analysis can help to identify more suitable experiential settings, but is recommended for future studies.

Reaction Calibration

The optimization problem for reaction calibration is conducted in two ways: *Case B* allows for different (locally valid) reaction parameters for each experiment, whereas

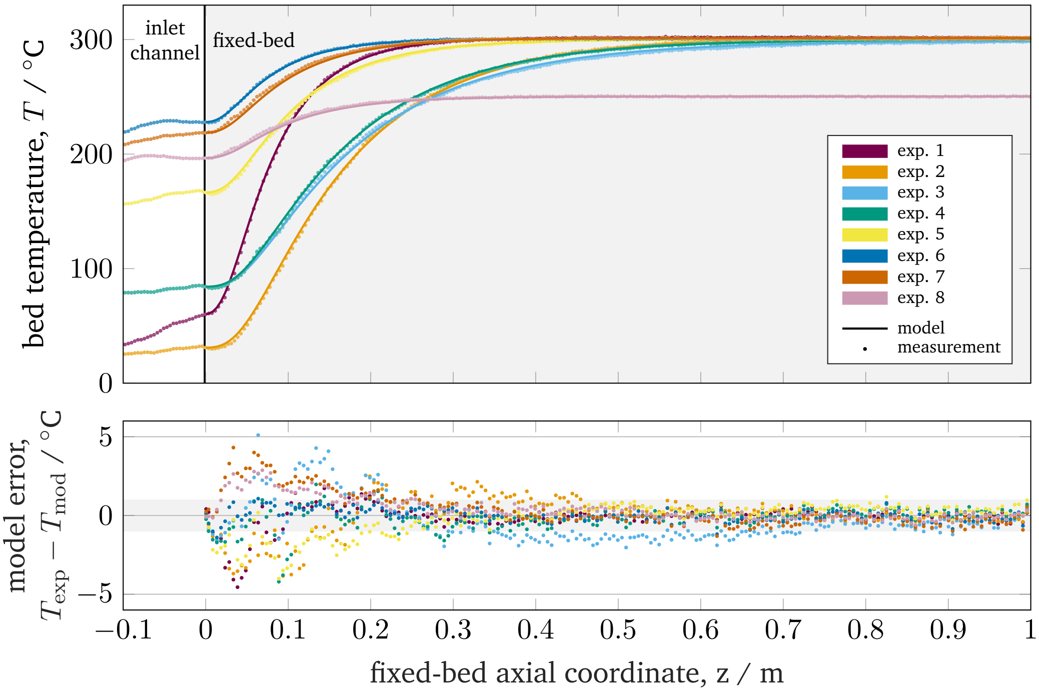

Fig. 6.10.: Nonreactive experiments in comparison to the calibrated model (Case A) at steady state, bottom figure with temperature sensor uncertainty of 1 °C shaded in gray.

Case C demands each reaction parameter to be the same (globally valid) through all experiments. This distinction provides more insight about quality and sensitivity of the selected reaction parameter. Case B considers experiment 9 to 16, whereas Case C only considers experiment 11 to 14 of Tab. 6.6 with fixed heat transport parameters as obtained from Case A. Hence, only reaction parameters are calibrated such that a local parameter set for each experiment j

$$\boldsymbol{p} = [p_1 \dots p_8], \quad \text{with}$$
$$\boldsymbol{p}_j = [1.9960\ 0.8094\ 3.2060\ 0.6384\ S_{k_0,j}\ S_{E_A,j}\ 0\ 0\ 0\ 1]\,,$$

accounts for Case B and a global parameter set for all experiments

$$\boldsymbol{p} = [1.9960\ 0.8094\ 3.2060\ 0.6384\ S_{k_0}\ S_{E_A}\ 0\ 0\ 0\ 1]\,, \tag{6.2}$$

accounts for Case C; exemplified with hydrogen as key component for Thiele modulus calculation. In fact, after careful evaluation of several optimization runs, hydrogen as Thiele modulus key component always provides the best match between experimental and computational hot-spot shapes.

The result for Case B is illustrated in Fig. 6.11 and shows a significant improvement of the model quality under reactive conditions. The model well reproduces all hot-spot shapes and positions. Apart from experiment 15 an 16, deviations are reduced below 20 °C. Looking at the corresponding optimal local scaling factors under Case B in Tab. 6.7 shows activities of around 20 %. This is very much in line with the lab-scale activity tests from Fig. 6.5 and proves the general validity of the here presented calibration strategy. However, marked differences of the optimal local scaling factors between each experiment (especially experiment 9, 10, 15, and 16) indicate that uncertainties coming form the model and/or the measurements are still present. For instance, under mild reaction conditions as represented by experiment 9, and 10, the mass flow controllers for feed gas supply suffer from large uncertainties since they operate far below their actual design point (< 10 % of max. flow rate). Moreover, the DTS measures within intense reaction zones (experiment 15 and 16) are partly out of the sensor calibration range from Fig. 6.6.

An exemplary use case of the calibrated model is illustrated in Fig. 6.13. Here, the calibrated model uncovers the entire two-dimensional temperature field and, thus, provides profound information about the radial temperature decrease towards the cooling channel. This result provides evidence for correct design and dimensioning of the reactor unit, as it ensures fixed-bed boundary temperatures that are tolerable for the cooling fluid (see thermal oil specifications in Section 6.1.4). To further support the predicted radial temperature gradients, additional measurements near the wall are recommended for future elaborations.

The final optimization Case C only considers the most reliable experiments 11 to 14 as training set and the two global scaling factors from Eq. (6.2). The remaining reactive experiments are solely used for testing and do not enter the optimization. Case C is seen to be the most reasonable for further use of the calibrated model, but requires a

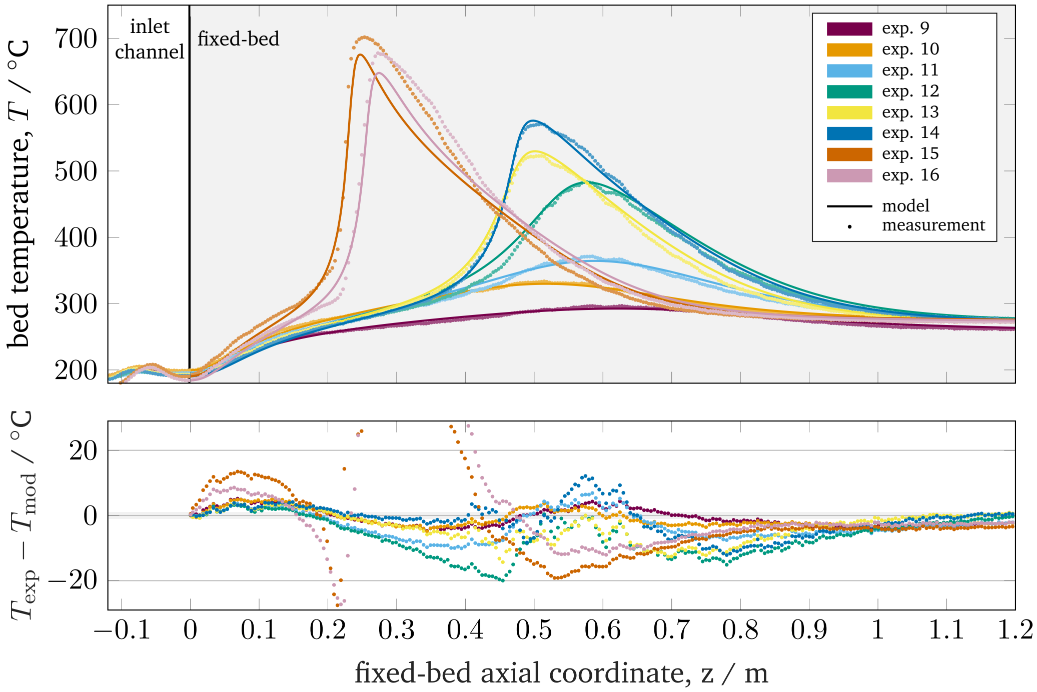

Fig. 6.11.: Reactive experiments in comparison to the calibrated model (Case B) with hydrogen as key component for Thiele modulus calculation at steady state, bottom figure with temperature sensor uncertainty of 1 °C shaded in gray.

Tab. 6.7.: Scaling factors and considered experiments of all calibration cases, free decision variables of each case are highlighted in bold.

Case	exp.	$S_{\dot{V}_{\mathrm{cool}}}$	$S_{\lambda_{\mathrm{cond},r}}$	$S_{\alpha_{\mathrm{w}}}$	$S_{\lambda_{\mathrm{conv}}}$	S_{k_0}	S_{E_A}	$S_{\Phi_{\mathrm{CH_4}}}$	$S_{\Phi_{\mathrm{CO_2}}}$	$S_{\Phi_{\mathrm{H_2O}}}$	$S_{\Phi_{\mathrm{H_2}}}$
		-	-	-	-	-	-	-	-	-	-
0	1-16	1	1	1	1	1	1	0	1	0	0
A	1-8	**1.9960**	**0.8094**	**3.2060**	**0.6384**	1	1	0	1	0	0
B	9	1.9960	0.8094	3.2060	0.6384	**0.3282**	**1.4912**	0	0	0	1
	10	1.9960	0.8094	3.2060	0.6384	**0.2037**	**1.3279**	0	0	0	1
	11	1.9960	0.8094	3.2060	0.6384	**0.2204**	**1.2186**	0	0	0	1
	12	1.9960	0.8094	3.2060	0.6384	**0.2169**	**1.1581**	0	0	0	1
	13	1.9960	0.8094	3.2060	0.6384	**0.1888**	**1.2278**	0	0	0	1
	14	1.9960	0.8094	3.2060	0.6384	**0.1885**	**1.2617**	0	0	0	1
	15	1.9960	0.8094	3.2060	0.6384	**0.1741**	**0.9897**	0	0	0	1
	16	1.9960	0.8094	3.2060	0.6384	**0.1871**	**1.0412**	0	0	0	1
C	11-14	1.9960	0.8094	3.2060	0.6384	**0.2017**	**1.1705**	0	0	0	1

high reliability of the underlying kinetic model. As seen from the results in Fig. 6.12 the reduced degree of freedom leads to higher model deviations with respect to both training and testing data. Nevertheless, the results of Case C still outperform the uncalibrated model in terms of hot-spot position, shape, and intensity.

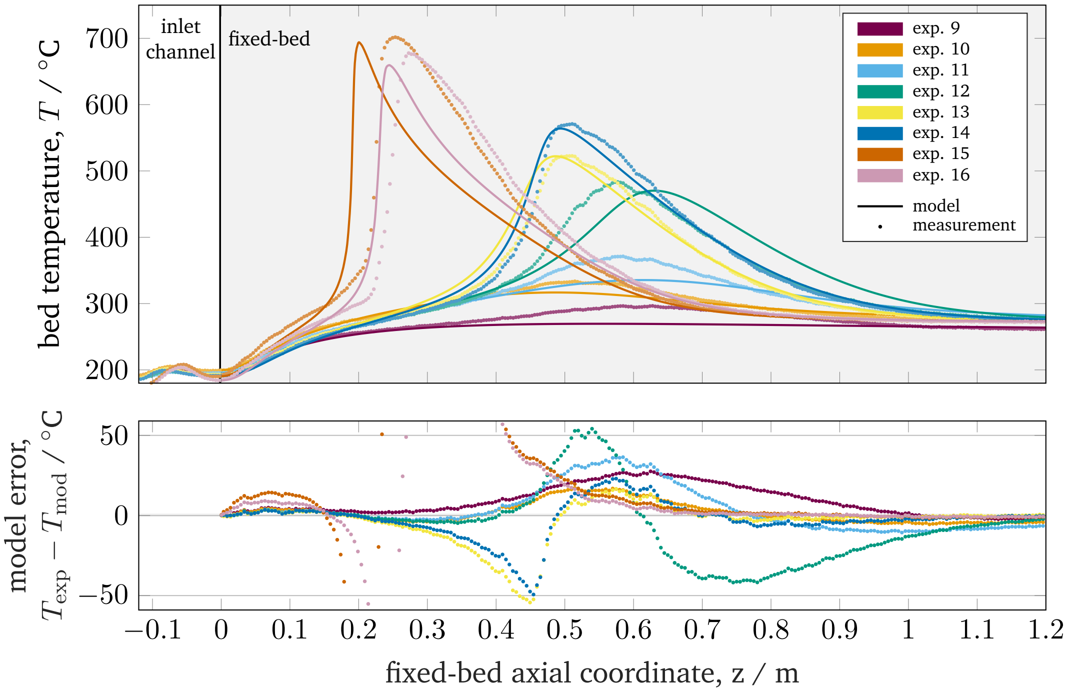

Fig. 6.12.: Reactive experiments in comparison to the calibrated model (Case C) with hydrogen as key component for Thiele modulus calculation at steady state, bottom figure with temperature sensor uncertainty of 1 °C shaded in gray.

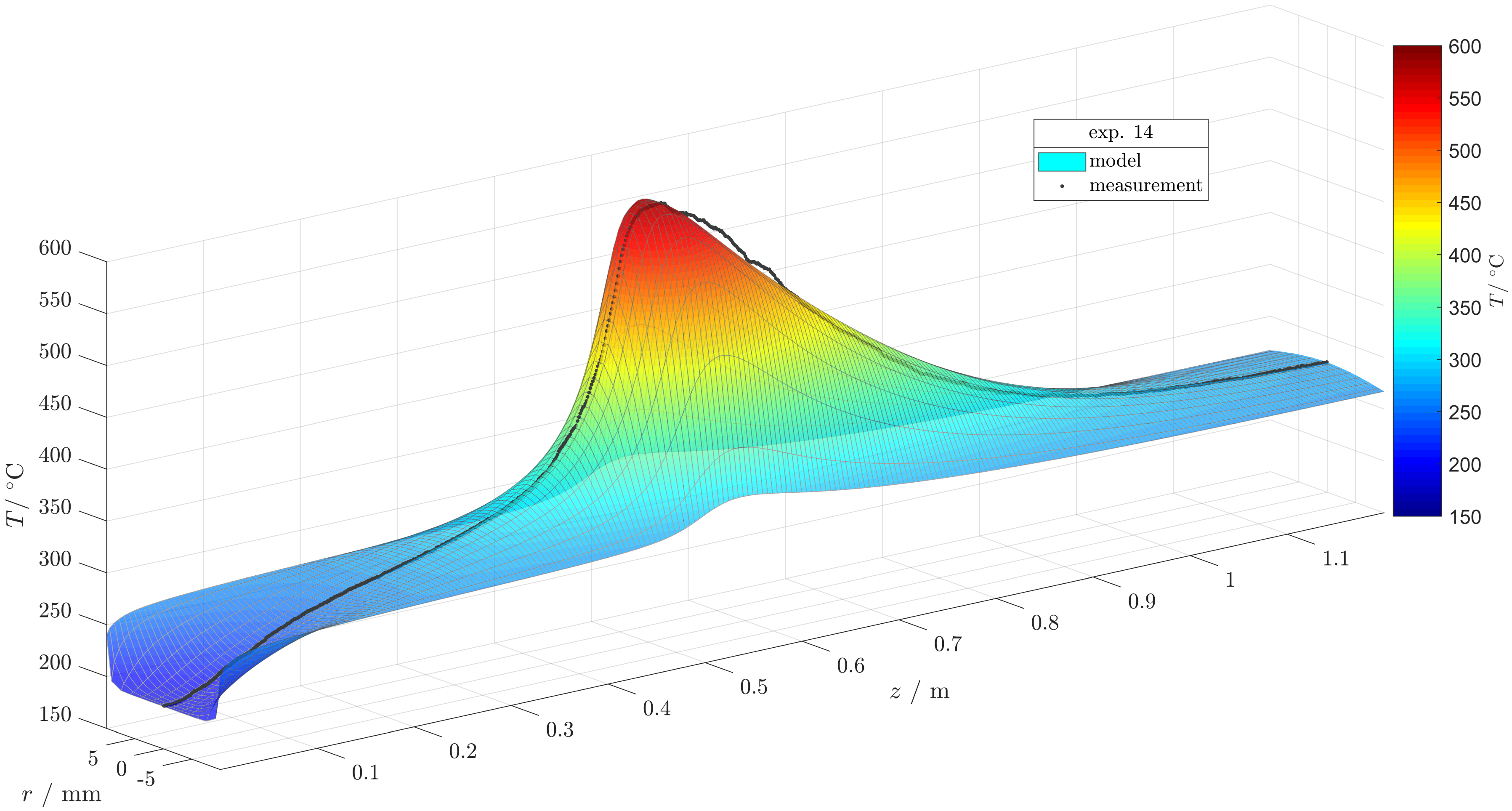

Fig. 6.13.: Two-dimensional fixed-bed temperature field after model calibration (Case B) considering experiment 14 and hydrogen as key component for Thiele modulus calculation at steady state.

Comparing the optimal scaling factors of Case B and C in Tab. 6.7 reveals that variations of 5 to 10 % significantly influence the predicted hot-spot position and shape. However, the high-resolution DTS detects these variations accurately and uncovers existing inconsistencies between model and experiment. Despite the already improved model quality reflected by Case B and C, remaining inconsistencies may be eliminated by detailed uncertainty and sensitivity analyses. Considering that standard investigations on intrinsic catalyst kinetics with differential reactors are also ranging from 5 to 10 % [KSH16], the here proposed methodology might offer new opportunities for future kinetic investigations with lower uncertainty and increased applicability.

The last section of this chapter takes up the calibrated model according to Case B and examines its quality under dynamic scenarios. In addition, the criteria from Section 3.1 are applied and validated based on the experimental observations.

6.3 Dynamic Experiments and Criteria Validation

This section analyses the reactor behavior under dynamic conditions. In accordance with the previous chapters, the coolant temperature is considered as the key control variable. In order to capture essential dynamic characteristics and to identify possible multiplicity features, cool-down perturbation experiments are performed starting from an ignited reactor steady-state. During the perturbation all operating conditions remain fixed except for the inlet coolant temperature. Two initial states according to experiment 11 and 16 from Tab. 6.6 are selected to cover cases with mild and intensive reaction conditions.

The first cool-down perturbation with respect to experiment 11 is illustrated in Fig. 6.14. Since the feed is highly diluted with nitrogen, hot-spot temperatures are limited to values below 400 °C. The heat transfer unit reduces the inlet coolant temperature (T521) within the first minute by about 100 °C. This fast interaction shows that the heat transfer unit successfully operates within the required specifications from Section 6.1.4. After two minutes the coolant temperature settles to the new setpoint and with slight delay the bed temperature follows accordingly. Fig. 6.14 also shows the associated prediction by the calibrated model. Apart from a slightly faster depletion of the axial temperature profile, the general trend is well reflected by the model. Moreover, the model result also includes the change in carbon dioxide conversion over time, confirming that the entire reaction extinguishes. Due to missing gas analysis an experimental validation of the conversion has to be postponed to future investigations.

A similar cool-down perturbation is performed under intensive reaction conditions. The results are highlighted in Fig. 6.15 and indicate a very different, nonintuitive dynamic behavior. Instead of extinguishing, the hot-spot temperature develops in opposite direction increasing by almost 90 °C (wrong-way behavior). Additionally a sharper reaction front is formed and moves towards the reactor outlet with almost constant velocity. Unfortunately, a malfunction of the carbon dioxide mass flow controller interrupted the experiment after 14 minutes and led to an extinction of the reaction front before reaching the end of the fixed-bed. However, the experiment can be reproduced with the calibrated model at least for the first 12 minutes. During this period, model and experiment agree well, considering that the model was solely calibrated with respect to the initial steady state and only includes steady-state catalyst rate expressions. The traveling speed of the reaction front is determined experimentally to 5.7 cm/min, whereas the model predicts a slightly higher velocity. Moreover, the calculated conversion drops from 0.93 down to 0.66. Although such traveling reaction fronts and wrong-way behaviors are a well-known dynamic phenomena in adiabatic fixed-bed reactors (see literature review in Chapter 1), several novel aspects are evident here:

- the precise transient measurement,
- the industrially relevant scale,
- the occurrence in a cooled fixed-bed reactor,
- the excellent model agreement.

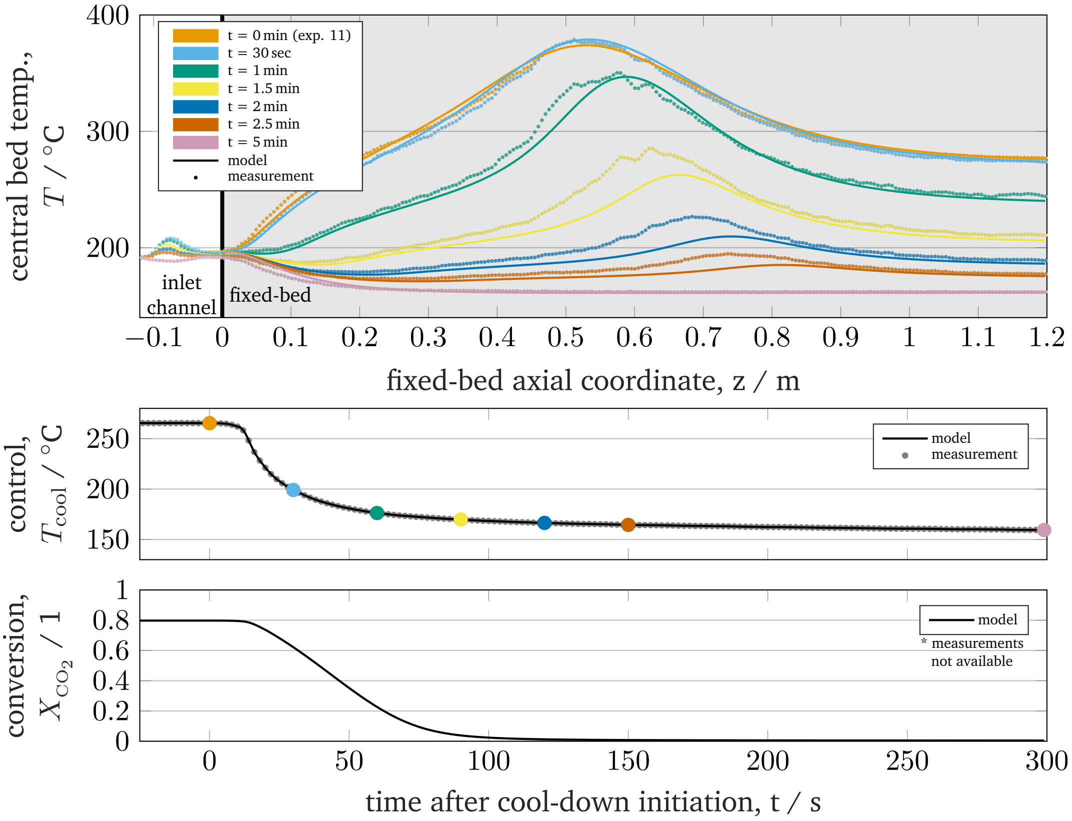

Fig. 6.14.: Dynamic reactor behavior under mild reaction conditions after cool-down perturbation in comparison with the calibrated model (Case B), initial state corresponds to experiment 11 in Tab. 6.6.

In order to explain the good agreement between model and experiment, the model is further analyzed by variation of the axial dispersion. This approach is mainly motivated by the pioneering work of Eigenberger [Eig72a], who found dispersion to be decisive for the velocity of moving reaction fronts. Thus, the model results in Fig. 6.15 are replicated with doubled and halved dispersion (by doubling and halving the amount of FVs in axial direction) according to Figs. A.12 and A.13 on Page 142. Both figures clearly demonstrate that on the one hand axial dispersion is indeed decisive for the traveling speed, and that on the other hand the axial resolution/dispersion calibrated under steady-state conditions is very well applicable also to dynamic conditions.

In contrast to the mild reaction conditions of experiment 11, the reaction front in experiment 16 remains ignited during cool-down perturbation but eventually extinguishes after reaching the reactor outlet. The observed behavior is therefore a purely dynamic behavior, which is not covered by the steady-state criteria developed in Section 3.1. However, the fact that the reactor extinguishes indicates that there is no state-space multiplicity available for both experiments. To support this observation all required parameters to calculate mass- and energy-based sensitivities (e.g., effectiveness factor, Stanton number, residence time, ATR, Bodenstein number) are determined according to the conditions in Tab. 6.6 and summarized in Tab. A.5 on Page 141, respectively.

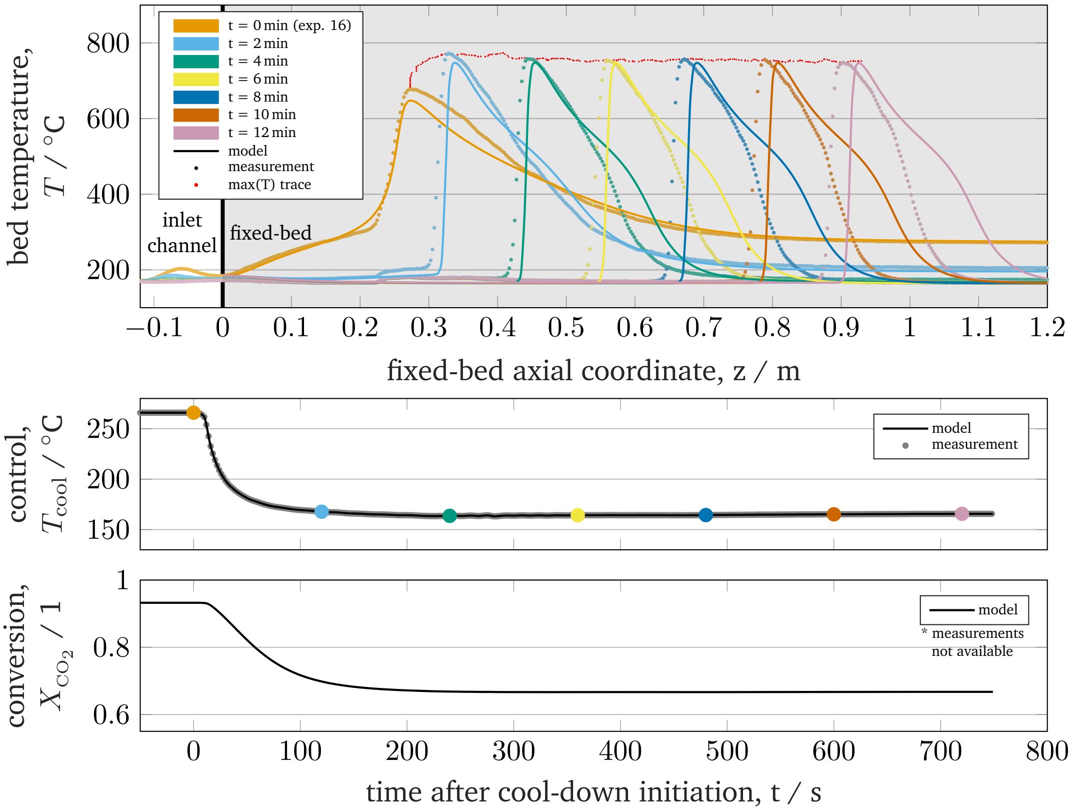

Fig. 6.15.: Dynmaic reactor behavior under intensive reaction conditions after cool-down perturbation in comparison with the calibrated model (Case B), initial state corresponds to experiment 16 in Tab. 6.6.

Afterwards, the mass- and energy-based sensitivities in Eqs. (3.18) and (3.19) are evaluated within a wide Bodenstein number range.

Both sensitivities are contrasted in Fig. 6.16. For experiment 11, the mass-based sensitivity (blue) is usually lower or just slightly higher than the energy-based sensitivity (red). Considering the axial dispersion (n = Bo/2 $\approx$ 400) and the reduced catalyst activity (here S_{k_0}=η=0.2) obtained from the model calibration, both sensitivities are almost equal. Keeping also in mind that the activity is further reduced due to catalyst mass transport limitations, the energy-based sensitivity rather outweighs the mass-based sensitivity. Thus, the criterion for uniqueness is fulfilled and excludes any state-space multiplicity. This result is very much in line with the experimental behavior in Fig. 6.14.

For experiment 16, the mass-based sensitivity in Fig. 6.16 (bottom) outweighs the energy-based sensitivity if S_{k_0}=η=0.2. However, the model predicts catalyst mass transport limitations, which can reduce η to 0.004 - 0.01 for temperatures in the range of 600 - 800 °C. In consequence, the uniqueness criterion is seen as fulfilled rather than the multiplicity criterion. The derived criteria, however, allow for identifying conditions that provoke multiplicity. Higher catalyst activities (as reported by Koschany

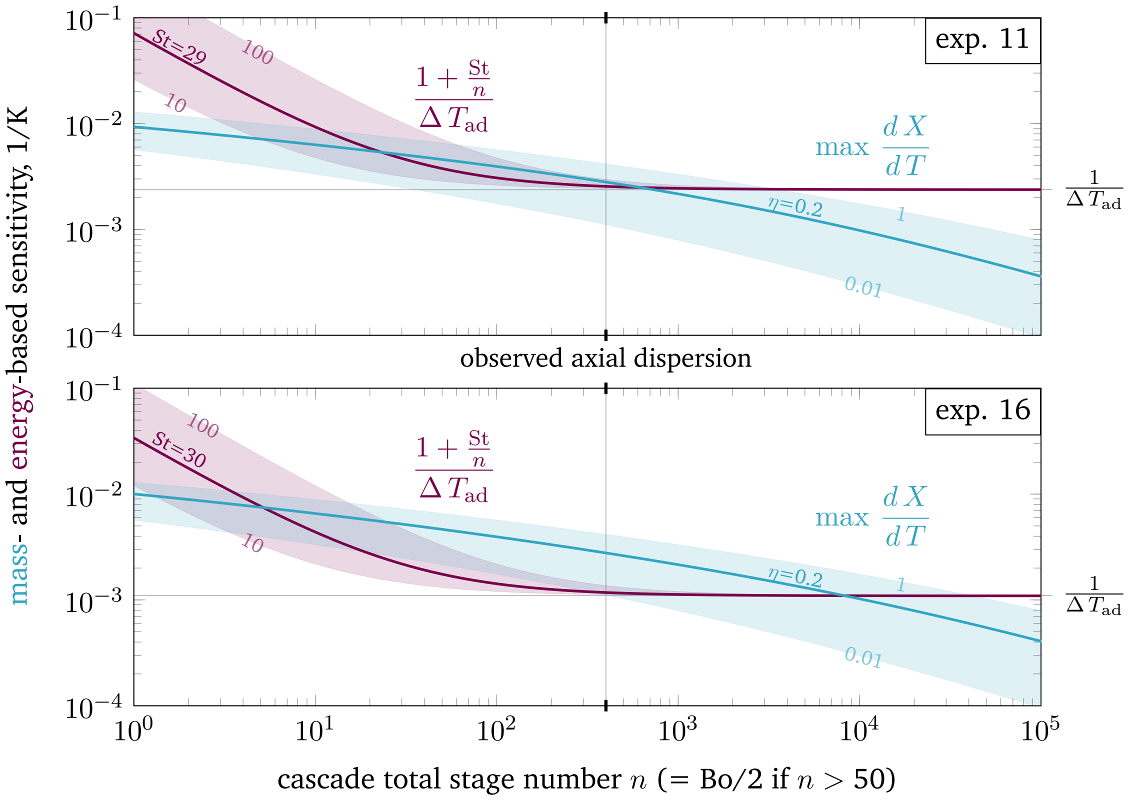

Fig. 6.16.: Mass- and energy-based sensitivity for uniqueness and multiplicity criteria on a broad axial dispersion range and for the conditions of experiment 11 (top) and 16 (bottom), all required parameters are available in Tab. A.5 on Page 141 and correspond to the Case B model calibration.

et al. [KSH16]) and lower intra-particle mass transport limitations (for instance with catalyst mean pore diameters of 50 nm instead of 10 nm) would increase the mass-based sensitivity and lead to multiplicity domains larger than 100 °C. This scenario is reflected in Fig. 6.16 (bottom) by η values above 0.2 and fits state-of-the-art high-performance industrial catalysts. It should also be noted that the criteria consider ideal mixing in radial direction, which obviously not applies to the conducted low-load experiments (compare Fig. 6.13). Hence, lower active reaction volumes are necessary to compensate for this divergence from reality. It is recommended to address these aspects in future investigations, which then allows for uncovering possible multiplicity domains, including unstable and stable states. The required technical equipment is available and ready for use.

6.4 Chapter Summary

In summary, the experimental setup has proven to be reliable and well-suited to investigate the steady and dynamic behavior of an industrial scale fixed-bed reactor. At its present state, the setup offers novel opportunities to study in particular thermal conditions and temperature excursions within the fixed-bed. The DTS successfully delivered accurate temperature profiles highly resolved in spatial and temporal directions. With them, unique fingerprints of several test conditions turned out to be precious for calibrating the detailed dynamic reactor model. The proposed least-squares minimization strategy has proven to be suitable for model calibration but requires the careful use of powerful numerical tools. After calibration, the model achieved a remarkably high accuracy even under dynamic conditions, which substantiates the underlying model assumptions (e.g., pseudo-homogeneous phase, radial gradients). Axial dispersion turned out to be the decisive feature for an accurate numerical description of dynamic scenarios. Note that the calibration disregarded any gas composition measurement, but still provides reasonable estimates for intrinsic kinetic properties like activity and activation energy. Furthermore, cool-down perturbation experiments revealed the development of moving reaction fronts underlining the relevance of non-intuitive dynamic reactor behavior and state-space multiplicity. The predictions resulting from uniqueness and multiplicity criteria also reliably match the experimental observations. Overall, the close connection between theory and reality impressively underlines the importance and reliability of the models and findings presented in this work.

Considering that all data originate from the first four days of testing, the experimental setup could only show its basic capabilities yet. Further milestones will relate to the operation at higher loads, with load changes, with online control, and over longer time horizons. Additionally, a detailed analysis of measurement uncertainties and systematic sensitivities is recommended to provide the next experimental plans and to improve the model quality even further.

Conclusions and Outlook

7

For many years there was little practical relevance to the advanced operation of fixed-bed reactors. Until the early 1990s, reaction engineering suffered from a lack of use cases due to the permanent availability of fossil-based raw materials. Furthermore, well-elaborated concepts for advanced operations were mainly applied to niche products or fine chemicals due to their limited scale-up potential. The current trend towards a more sustainable operation of chemical processes, which notably includes fixed-bed reactors, motivates new incentives supporting the need for advanced reactor operation even at mid- and large-scale.

7.1 Concluding Remarks

While focusing on carbon dioxide methanation in the context of PtX, this work provides an example process that has been shown to benefit from advanced reactor operation when processing volatile renewable energy. Transient scenarios (e.g., start-up, shut-down, load changes) during operation appear more frequently and demand a better understanding of the reactor's operating range (flexibility), as well as its transition from one operating point to another (resiliency). Therefore, this work covers a range of different engineering disciplines from bottom up and contains basic theory, simulation, numerical optimization, control, as well as experimental validation.

The foundations for flexibility are addressed in Chapter 3 by revising the current perspective on the operating range of non-isothermal fixed-bed reactors. State-space multiplicity and stability were found to be determining the reactor's flexibility. Before this work, however, the literature reported conflicting views on multiplicity and stability due to the quantitatively unknown contribution of back-mixing within real reactors. Therefore, this work proposes a novel approach to assess this contribution in a general way and derives criteria that can be used for any fixed-bed reactor configuration. The approach also rates generally accepted criteria for the relevance of dispersion in fixed-bed reactors (e.g., the Mear's criterion [Mea76]) to be unsatisfactory, as they do not account for state-space multiplicity. Besides, unstable states are observed to appear in regimes that are beneficial for the catalyst durability. Present criteria for reactor instability have been found to disregard back-mixing and are therefore too conservative for realistic applications. The analysis of reactor instability motivates this work to reconsider the pervasive opinion that unstable reactor operating points must be avoided in practical applications. As prove of concept, Chapter 4 and 5 apply strategies for stabilizing control and confirm that such unstable states are attainable under realistic conditions.

Besides the developed criteria, the second pillar of this work is a detailed reactor model. In the course of this work the modeling results were repeatedly questioned by several scientists. There were justified doubts about the quality of the temperature profiles and the dynamic operating strategies derived from them. The experimental validation in Chapter 6 confirms these doubts at least quantitatively due to some uncertain initial settings and assumptions. Therefore, a novel experimental setup, the FOReCAST pilot plant, delivered necessary data from static, as well as dynamic experiments. However, qualitatively the model replicates similar trends as seen in the experiments. Many settings and assumptions could have been reevaluated based on various experimental tests. With these experiments, the plant allowed for studying the flexibility and dynamics of fixed-bed reactors at an industrial scale and provides unprecedented accuracy in capturing the rector's temperature profile in real-time. In its calibrated form, the model is able to reproduce steady and dynamic operating scenarios more accurately. The model also proves that the theoretical derivations on multiplicity are indeed transferable to realistic reactor configurations, as they are currently found in the industry.

The literature reports very diversely on the minimal requirements of a mathematical reactor model for dynamic investigations. Many authors recommend to favor heterogeneous models over pseudo-homogeneous, or emphasize the need for dynamic rate equations (as represented, for instance, by microkinetic models). However, the good model agreement in this work shows that such improvements may not provide worthwhile insights at the reactor level. Instead, the bottleneck for advanced reactor operation is still related to computational efforts. Thus, this work recommends to further elaborate on reducing the model's complexity by intelligent numerical routines (e.g., model order reduction) or smarter modeling assumptions. Such reactor models and advanced numerical tools have been identified as crucial elements to further support the paradigm shift towards a more flexible and sustainable operation of chemical reactors.

In summary, this work expands the current state of knowledge due to the following key aspects:

1. The **operating range of real, non-isothermal FBRs** is fundamentally analyzed to uncover the reactor's full potential for flexible operation.
2. **Novel criteria for the existence and stability of multiple steady states** are developed in order to estimate the reactor's flexibility potential.
3. **State clustering in a CSTR cascade model** was found to be the key to compromise conflicting views on state-space multiplicity.

4. A **novel reactor heat management approach** via stabilizing control has been developed and tested under realistic conditions exemplified for carbon dioxide methanation.
5. A **comprehensive literature survey** confirms the relevance of stabilizing control among other reactor concepts.
6. A **detailed dynamic reactor model** has been developed that is suitable for extensive simulation, optimization, and control, while simultaneously allowing an accurate representation of experimental data.
7. A dynamic optimization methodology has been presented that delivers **optimal policies for fast and safe transition** between different operating points.
8. A **novel pilot plant concept**, fully based on modeling results, has been designed and build to validate preceding theoretical observations.
9. The pilot plant showed an unprecedented level of detail in **real-time monitoring of the reactor's temperature profile** (state fingerprint).

7.2 Outlook

This work hopefully convinces the reader that even a traditional and broadly explored research field, offers many opportunities for further progress, especially when new incentives are coming to the fore. These incentives currently come from three different directions. On the one hand, there is the trend towards transient operation of chemical reactors to enable sustainable production. Secondly, the increasing performance of numerical methods allow for detailed analyses of the complex physiochemical interactions simultaneously on several reactor scales. And thirdly, improved experimental methods are opening up many new possibilities for the phenomenological description of catalyst and reactor behavior under dynamic conditions. This work only reflects sub-aspects of each of the three directions, yet it raises a number of new questions.

As seen in this work, the mass transport limitation within the catalyst has a decisive influence on the operating range and dynamic behavior of the reactor. Accordingly, the question about the right reactor and catalyst design under dynamic conditions is seen as one important future research direction. Special attention also goes to the catalyst activity. Too much activity can quickly lead to higher efforts in reactor design. This conflict must be resolved by bringing together researchers from catalysis and reaction engineering. Furthermore, it remains to show how the theoretical discourse applies to other exothermic reactions, endothermic reactions, and reactions with selectivity issues. Prominent examples, therefore, are steam methane reforming, Fischer-Tropsch synthesis, and ammonia synthesis.

The advanced operation strategies presented in this work still suffer from high computational costs. In consequence, the proposed optimal control methodology is not yet ready for real-time application, since reactor dynamics are several times faster than the computation of the control trajectory. More intelligent numerical routines (e.g., via model order reduction) and smarter modeling assumptions are seen as possible remedies. To be more specific, this work extensively used modern algorithms for solving and optimizing large-scale nonlinear problems. The foundation of these algorithms usually goes back to the solution of a linear equation system, which, however, can quickly reach dimensions of several million variables. Considering that modern engineering tools often use direct linear solvers, which date back to the 1980s, they indeed represent a hidden bottleneck for speeding up computations. State-of-the-art indirect linear solvers are known to be much faster but found yet only little attention in engineering science.

However, fast computation shall not be seen as the ultimate solution. In fact, much computational effort may be saved by simple engineering thinking, e.g., supported by the use of well-known correlations and dimensionless numbers that have been developed by several engineering generations. True to the leitmotif "With great power comes great responsibility", modern engineering tools must be used carefully and checked for plausibility. Very often the answer to a scientific question a priori appears impossible, but turns out to be trivial after successful computation. Nevertheless, triviality must be understood as a vital companion on the path to knowledge as it always excludes unrewarding search directions. Due to this fact, many efforts also contributed to the outcome of this work, which ultimately remained undiscussed.

With regard to advancements in future experimental methods, this work particularly emphasizes a novel temperature measurement technique. The used carbon dioxide conversion as state-measure in control applications typically relies on slow devices for gas analysis (e.g., GC). The temperature profile measured by DTS turned out to be very accurate and fast, and thus well-suited for reactor control. However, dealing with such high performance sensors also generates a large amount of data, which needs to be processed again in real-time. Even offline data processing and evaluation can become a problem if it is not done carefully. This aspect is currently emphasized in many research and development areas with the buzzword "big data". In research, the growing amount of data may no longer be processed by a single research group and therefore increasingly demands for teaming up with other groups around the world. In this sense, it is to be hoped that in the future another buzzword, which is rather a statement, will come to the fore: "share data!"

Finally, this work recalls the big picture from Chapter 1. Regardless that the production of methane might be rather seen as transition technology until hydrogen becomes the dominating energy carrier, chemical reactors will certainly continue to be indispensable for future societies. Within recent years, there is one area that receives increasing attention: space exploration. In particular, crewed missions to Mars are largely seen as the next frontier in human space exploration, but also engineering. According to the concepts of leading private companies, methane will be the dominating solution to refuel space transportation systems for their return to Earth. Conceptually they present similar solutions as currently discussed for PtM on Earth. Carbon dioxide from Mars' atmosphere and hydrogen generated from solar energy and water are converted into methane, which is then liquefied and used as fuel. For this reason, methanation and advanced reactor operation could also be far more important in the distant future than it currently appears.

Appendix

A

A.1 CSTR Analogy

The following assumptions for the CSTR model hold:

- single non-equimolar reaction:
  $CO_2 + 4\,H_2 \rightleftharpoons CH_4 + 2\,H_2O, \quad \Delta_R\tilde{H}^0 = -164.9$ kJ/mol
- constant effectiveness factor η for catalyst mass transport limitations
- constant pressure p
- constant gas heat capacity: $c_{p,\text{in}} = c_{p,\text{out}}$
- constant heat of reaction $\Delta_R\tilde{H}$
- no phase distinction (pseudo-homogeneous)

A.1.1 Mass balance

The component mass balances for a single CSTR, as illustrated in Fig. A.1, considers the entire reactor to be one single and perfectly mixed control volume at steady-state. This leads to

$$\begin{aligned} 0 &= \dot{m}_\text{in}\, w_{\alpha,\text{in}} - \dot{m}_\text{out}\, w_{\alpha,\text{out}} + V\, M_\alpha\, \nu_\alpha\, \mathrm{R}_\text{meth}, \\ 0 &= w_{\alpha,\text{in}} - w_{\alpha,\text{out}} + \frac{V}{\dot{m}_\text{in}} M_\alpha\, \nu_\alpha\, \mathrm{R}_\text{meth}, \end{aligned} \tag{A.1}$$

and compromises the equality of inlet and outlet mass flow ($\dot{m}_\text{in} = \dot{m}_\text{out}$) as well as the reactive source for $\alpha \in \{CH_4, CO_2, H_2O, H_2\}$. In order to represent the heterogeneously catalyzed methanation reaction, the void fraction ε, stoichiometric

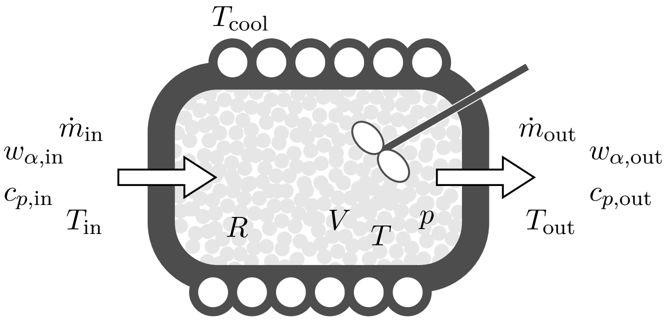

Fig. A.1.: Illustration of the single CSTR model with heterogeneously catalyzed reaction.

coefficients ν_α, and the effectiveness factor η_{meth} are incorporated within the effective reaction rate via

$$\mathrm{R}_{\mathrm{meth}} = (1-\varepsilon)\,\eta_{\mathrm{meth}}\,\tilde{\mathrm{r}}_{\mathrm{meth}} \quad \text{with} \quad [\mathrm{R}_{\mathrm{meth}}] = \mathrm{mol}/(\mathrm{m}^3\,\mathrm{s}).$$

Further, the conversion of each component is considered as

$$X_\alpha = \frac{\dot{m}_{\alpha,\mathrm{in}} - \dot{m}_{\alpha,\mathrm{out}}}{\dot{m}_{\alpha,\mathrm{in}}} = \frac{w_{\alpha,\mathrm{in}} - w_{\alpha,\mathrm{out}}}{w_{\alpha,\mathrm{in}}}. \tag{A.2}$$

With carbon dioxide methanation as single reaction, Eq. (A.1) simplifies to

$$0 = X_\alpha\, w_{\alpha,\mathrm{in}} + \frac{V}{\dot{m}_{\mathrm{in}}} M_\alpha\, \nu_\alpha\, \mathrm{R}_{\mathrm{meth}}, \tag{A.3}$$

$$0 = X_{\mathrm{CO_2}}\, w_{\mathrm{CO_2,in}} + \frac{\tau}{\varepsilon\,\rho_{\mathrm{in}}} M_{\mathrm{CO_2}}\,(-\mathrm{R}_{\mathrm{meth}}) \quad \text{with} \quad \tau = \frac{\varepsilon\,V}{\dot{V}_{\mathrm{in}}} = \frac{\varepsilon\,V\,\rho_{\mathrm{in}}}{\dot{m}_{\mathrm{in}}}, \tag{A.4}$$

This equation represents the mass-based operating range as a function of internal (temperature, pressure, composition) and external (inlet) operating conditions. If first-order equimolar reaction conditions are assumed, Eq. (A.4) may be rearranged to solve for the carbon dioxide conversion

$$\boxed{X_{\mathrm{CO_2}} = \frac{\tau}{\varepsilon}\,\frac{\mathrm{R}_{\mathrm{meth}}(T,p,w_\alpha)}{c_{\mathrm{CO_2,in}}} = \mathrm{Da_I}\,(1 - X_{\mathrm{CO_2}}),} \tag{A.5}$$

which reveals the well-known dimensionless first Damköhler number $\mathrm{Da_I}$. Note that the Damköhler number is considered here to be temperature-dependent. However, this work refers to realistic reaction rates with pronounced equilibrium limitations and, thus, excludes the first-order assumption in Eq. (A.5).

In order to calculate the remaining components of the methanation reaction, the extent of reaction yields

$$w_\alpha = -X_{\mathrm{CO_2}}\,\frac{\nu_\alpha}{\nu_{\mathrm{CO_2}}}\,\frac{M_\alpha}{M_{\mathrm{CO_2}}}\,w_{\mathrm{CO_2,in}} + w_{\alpha,\mathrm{in}},$$

such that

$$\tilde{\mathrm{r}}_{\mathrm{meth}}(T,p,w_\alpha) = \tilde{\mathrm{r}}_{\mathrm{meth}}(T,p,w_{\mathrm{CO_2,in}},X_{\mathrm{CO_2}}). \tag{A.6}$$

Hence, at constant operating parameters, Eq. (A.4) can be expressed as an implicit nonlinear equation

$$0 = X_{\mathrm{CO_2}} - f(X_{\mathrm{CO_2}}), \tag{A.7}$$

that is solved with respect to $X_{\mathrm{CO_2}}$ by standard root-finding algorithms (e.g., the Newton-Raphson method). It is important to mention that the here considered nonlinear reaction rate in $f(X_{\mathrm{CO_2}})$ has a unique solution with respect to $X_{\mathrm{CO_2}}$, which is shown in

Fig. 3.8 on Page 44. In consequence, the solution of Eq. (A.7) must be unique as well.

A.1.2 Energy balance

Similar to the mass balance, the energy balance applied to the CSTR reads

$$\begin{aligned} 0 = \dot{m}_{\text{in}}\, c_{p,\text{in}}\, T_{\text{in}} - \dot{m}_{\text{out}}\, c_{p,\text{out}}\, T_{\text{out}} + \text{k}\, A\, (T_{\text{cool}} - T) \\ + V\, (1-\varepsilon)\, \eta_{\text{meth}}\, \tilde{\text{r}}_{\text{meth}}\, (-\Delta_R \tilde{H}). \end{aligned} \tag{A.8}$$

The conversion from Eq. (A.3) may be plugged into Eq. (A.8) via

$$X_\alpha = \frac{-V\, M_\alpha\, \nu_\alpha\, \text{R}_{\text{meth}}}{\dot{m}_{\text{in}}\, w_{\alpha,\text{in}}} = \frac{-V\, M_\alpha\, \nu_\alpha\, \text{R}_{\text{meth}}}{\dot{V}_{\text{in}}\, \rho_{\alpha,\text{in}}} = \frac{-V\, (1-\varepsilon)\, \eta_{\text{meth}}\, \nu_\alpha\, \tilde{\text{r}}_{\text{meth}}}{\dot{V}_{\text{in}}\, c_{\alpha,\text{in}}},$$

which leads to

$$\begin{aligned} 0 = \dot{m}_{\text{in}}\, c_{p,\text{in}}\, T_{\text{in}} - \dot{m}_{\text{out}}\, c_{p,\text{out}}\, T + \text{k}\, A\, (T_{\text{cool}} - T) \\ - X_\alpha\, \dot{V}_{\text{in}}\, \frac{c_{\alpha,\text{in}}}{\nu_\alpha}\, (-\Delta_R \tilde{H}). \end{aligned} \tag{A.9}$$

With constant gas heat capacity $c_{p,\text{in}} = c_{p,\text{out}}$ and constant reaction enthalpy $\Delta_R \tilde{H}$, Eq. (A.9) is evaluated for carbon dioxide and divided by $\dot{m}_{\text{in}}\, c_{p,\text{in}} = \dot{V}_{\text{in}}\, \rho_{\text{in}}\, c_{p,\text{in}}$ such that

$$0 = (T_{\text{in}} - T) + \frac{\text{k}\, A}{\dot{m}_{\text{in}}\, c_{p,\text{in}}}\, (T_{\text{cool}} - T) + X_{\text{CO}_2}\, \frac{c_{\text{CO}_2,\text{in}}\, (-\Delta_R \tilde{H})}{\rho_{\text{in}}\, c_{p,\text{in}}}. \tag{A.10}$$

Introducing the dimensionless Stanton number St as the relation between coolant heat transfer and convective heat transport

$$\text{St} = \frac{\text{k}\, A}{\dot{m}_{\text{in}}\, c_{p,\text{in}}},$$

as well as the adiabatic temperature rise (ATR)

$$\Delta\, T_{\text{ad}} = \frac{c_{\text{CO}_2}\, (-\Delta_R \tilde{H})}{\rho_{\text{gas}}\, c_{p,\text{gas}}} = \frac{w_{\text{CO}_2}\, (-\Delta_R \tilde{H})}{M_{\text{CO}_2}\, c_{p,\text{gas}}},$$

allows for rewriting Eq. (A.10)

$$0 = (T_{\text{in}} - T) + \text{St}\, (T_{\text{cool}} - T) + X_{\text{CO}_2}\, \Delta\, T_{\text{ad}}, \tag{A.11}$$

which is equivalent to

$$X_{\text{CO}_2} = \frac{(T - T_{\text{in}}) + \text{St}\, (T - T_{\text{cool}})}{\Delta\, T_{\text{ad}}} = \frac{(1+\text{St})T - T_{\text{in}} - \text{St}\, T_{\text{cool}}}{\Delta\, T_{\text{ad}}}. \tag{A.12}$$

A more compact form can be achieved, if coolant temperature T_{cool} and inlet temperature T_{in} are lumped together. This lumped temperature is further on denoted as operating temperature

$$T_{\mathrm{op}} = \frac{T_{\mathrm{in}} + \mathrm{St}\, T_{\mathrm{cool}}}{1 + \mathrm{St}}, \tag{A.13}$$

which represents the CSTR outlet temperature without reaction or with $\Delta_R \tilde{H} = 0$. Thus, the remaining compact form of Eq. (A.12) is

$$\boxed{X_{\mathrm{CO_2}} = \frac{(1 + \mathrm{St})}{\Delta T_{\mathrm{ad}}} (T - T_{\mathrm{op}}),} \tag{A.14}$$

and defines the energy-based operating range. As the conversion $X_{\mathrm{CO_2}}$ is also determined by the mass balance in Eq. (A.4), reordering provides the corresponding operating temperature

$$T_{\mathrm{op}} = T - X_{\mathrm{CO_2}} \frac{\Delta T_{\mathrm{ad}}}{(1 + \mathrm{St})},$$

which may lead to multiple solutions due to the nonlinear relation between reaction temperature T and conversion $X_{\mathrm{CO_2}}$. The evaluation of the here presented mass and energy balance in Sections 3.1.2 and 3.1.3 is based on the reference parameter setting of Tab. A.1. This table also provides realistic ranges for each parameter suitable for carbon dioxide methanation in a tubular fixed-bed reactor of industrial scale.

Tab. A.1.: Realistic parameter ranges of carbon dioxide methanation in a fixed-bed reactor, key parameters for sensitivity evaluation highlighted in bold.

parameter	symbol	ref. value	range		unit
inlet temperature	T_in	300	[300	500]	K
operating temperature	T_op	450	[400	700]	K
reaction temperature	T	various	[400	1000]	K
inlet pressure	p_in	5	[1	15]	bar
inlet molar ratio	$\mathrm{H_2 : CO_2}$	4:1		-	
inlet superficial velocity	v_in	1	[0.5	2]	m/s
tubular geometry	L/R	21	[10	100]	-
catalyst density (porous material)	ρ_cat	2355.2		-	$\mathrm{kg/m^3}$
bed void fraction	ε	0.4		-	-
effectiveness factor	η_meth	1	[0.05	1]	-
residence time	τ	0.2	[0.04	1.6]	s
heat transfer coeff.	k	500	[100	2000]	$\mathrm{W/(m^2\,K)}$
inlet gas heat capacity	$c_{p,\mathrm{in}}$	2946	[2947	3086]	J/(kg K)
inlet gas density	ρ_in	2	[0.25	6.26]	$\mathrm{kg/m^3}$
inlet $\mathrm{CO_2}$ concentration	$c_{\mathrm{CO_2},\mathrm{in}}$	40	[4.8	120]	$\mathrm{mol/m^3}$
inlet $\mathrm{CO_2}$ density	$\rho_{\mathrm{CO_2},\mathrm{in}}$	1.76	[0.2	5.3]	$\mathrm{kg/m^3}$
surface/flow-rate ratio	$\frac{A}{\dot{V}_\mathrm{in}} = \frac{2\,L}{v_\mathrm{in}\,R}$	42	[10	400]	s/m
Stanton number	St	3.4	[0.05	1035]	-
adiabatic temperature rise	$\Delta\,T_\mathrm{ad}$	1074	[1074	1085]	K

A.2 CSTR Cascade Analogy

Fig. A.2 illustrates the respective model concept of a CSTR cascade, which is based on the following additional assumptions:

- variables with $^{\{i\}}$ account for the i-th stage
- variables without $^{\{i\}}$ are constant within the entire CSTRs cascade
- mass and energy in each stage are perfectly mixed
- no mass and energy back-mixing from stage to stage
- constant cascade volume V evenly distributed over all stages: $V^{\{i\}} = \frac{1}{n} V$
- constant mass flow: $\dot{m}_{\text{in}} = \dot{m}^{\{i\}} = \dot{m}$
- constant pressure: $p = p^{\{i\}}$
- constant gas heat capacities: $c_{p,\text{in}} = c_p^{\{i\}} = c_p$
- constant and equal coolant and inlet temperature: $T_{\text{in}} = T_{\text{cool}}$
- temperature change due to reaction: $T^i \neq T^{\{i-1\}}$
- reference parameter setting taken from Tab. A.1

Consequently, the total conversion $X_\alpha^{(n)}$ is represented by the sum of all stage conversions $X_\alpha^{\{i\}}$ according to

$$X_\alpha^{(n)} = \frac{w_{\alpha,\text{in}} - w_{\alpha,\text{out}}^{\{n\}}}{w_{\alpha,\text{in}}} = \sum_{i=1}^{n} \frac{w_{\alpha,\text{in}}^{\{i\}} - w_{\alpha,\text{out}}^{\{i\}}}{w_{\alpha,\text{in}}} = \sum_{i=1}^{n} \frac{w_{\alpha,\text{in}}^{\{i\}} - w_{\alpha,\text{in}}^{\{i+1\}}}{w_{\alpha,\text{in}}} = \sum_{i=1}^{n} X_\alpha^{\{i\}}.$$

Although, the cascade residence time τ still matches Eq. (A.4), the density change entails different stage residence times

$$\tau^{\{i\}} = \frac{\varepsilon\, V\, \rho_{\text{in}}^{\{i\}}}{n\, \dot{m}_{\text{in}}}.$$

Hence, proceeding with constant volume to mass-flow ratio was found to be more convenient

$$\frac{V^{\{i\}}}{\dot{m}_{\text{in}}} = \frac{1}{n}\,\frac{V}{\dot{m}_{\text{in}}} = \frac{1}{n}\,\frac{\tau}{\varepsilon\, \rho_{\text{in}}},$$

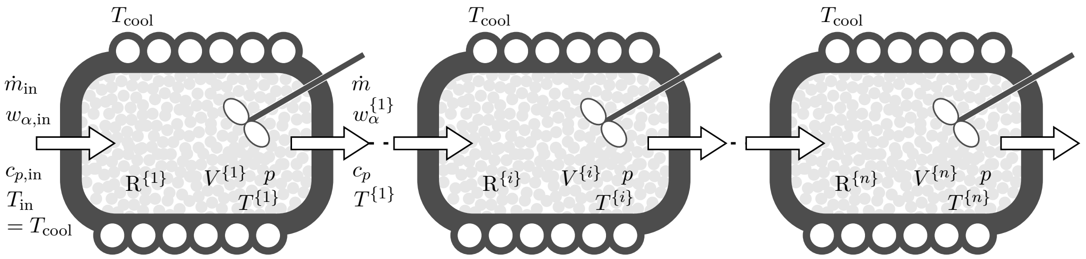

Fig. A.2.: Illustration of the CSTR cascade model of n stages with heterogeneously catalyzed reaction.

which is implemented in Eq. (A.3) to describe the i-th stage with respect to carbon dioxide. As result, the mass-based stage operating range meets

$$0 = X_\alpha^{\{i\}}\, w_{\alpha,\mathrm{in}} + \frac{1}{n}\, \frac{\tau}{\varepsilon\, \rho_\mathrm{in}}\, M_\alpha\, \nu_\alpha\, \mathrm{R}_\mathrm{meth}^{\{i\}},$$

$$\boxed{0 = X_{\mathrm{CO}_2}^{\{i\}} + \frac{1}{n}\, \frac{\tau}{\varepsilon\, c_{\mathrm{CO}_2,\mathrm{in}}}\, (-\mathrm{R}_\mathrm{meth}^{\{i\}}) = X_{\mathrm{CO}_2}^{\{i\}} + C_n\, (-\mathrm{R}_\mathrm{meth}^{\{i\}}),} \tag{A.15}$$

where C_n is constant for all stages. Furthermore, Eq. (A.6) as well as the distinction between isothermal and non-isothermal also holds for the cascade, such that

$$\begin{aligned} &\text{isothermal:} && \mathrm{R}_\mathrm{meth}^{\{i\}}(T, p, w_{\mathrm{CO}_2}^{\{i\}}) && = \mathrm{R}_\mathrm{meth}^{\{i\}}(T, p, w_{\mathrm{CO}_2,\mathrm{in}}, X_\alpha^{(i)}), \\ &\text{non-isothermal:} && \mathrm{R}_\mathrm{meth}^{\{i\}}(T^{\{i\}}, p, w_{\mathrm{CO}_2}^{\{i\}}) && = \mathrm{R}_\mathrm{meth}^{\{i\}}(T^{\{i\}}, p, w_{\mathrm{CO}_2,\mathrm{in}}, X_\alpha^{(i)}). \end{aligned}$$

Under isothermal conditions, Eq. (A.15) is solved implicitly solely with respect to all stage conversions. Under non-isothermal conditions, the temperature in the i-th stage depends on its previous stage. Thus, Eq. (A.15) needs to be solved implicitly with respect to both stage conversion and temperature, which requires the incorporation of the respective stage heat balance - adapted from Eq. (A.11)

$$0 = (T^{\{i-1\}} - T^{\{i\}}) + \mathrm{St}_n\, (T_\mathrm{cool} - T^{\{i\}}) + X_{\mathrm{CO}_2}^{\{i\}}\, \Delta\, T_\mathrm{ad}^{\{i\}}.$$

Here, the cascade Stanton number St_n and stage ATR $\Delta\, T_\mathrm{ad}^{\{i\}}$ comply with

$$\begin{aligned} \mathrm{St}_n &= \frac{\mathrm{k}_\mathrm{ov}\, A_n}{\dot{m}_\mathrm{in}\, c_p} = \frac{1}{n}\, \mathrm{St}, \\ \Delta\, T_\mathrm{ad}^{\{i\}} &= \frac{c_{\mathrm{CO}_2,\mathrm{in}}^{\{i\}}\, (-\Delta_R \tilde{H})}{\rho_\mathrm{in}\, c_p} = \frac{w_{\mathrm{CO}_2}^{\{i-1\}}\, (-\Delta_R \tilde{H})}{M_{\mathrm{CO}_2}\, c_p} = \left(1 - X_{\mathrm{CO}_2}^{(i-1)}\right)\, \Delta\, T_\mathrm{ad,in}. \end{aligned}$$

Similar to Eq. (A.14), the energy-based stage operating range, thus, satisfies

$$\boxed{X_{\mathrm{CO}_2}^{\{i\}} = \frac{(1 + \mathrm{St}_n)}{\Delta\, T_\mathrm{ad}^{\{i\}}}\, (T^{\{i\}} - T_\mathrm{op}^{\{i\}}).}$$

For simplicity, the first stage is considered with equal inlet and coolant temperature $T_\mathrm{in} = T_\mathrm{cool} = T_\mathrm{op}^{\{1\}}$. Similar to the single CSTR, all remaining parameters are taken from Tab. A.1.

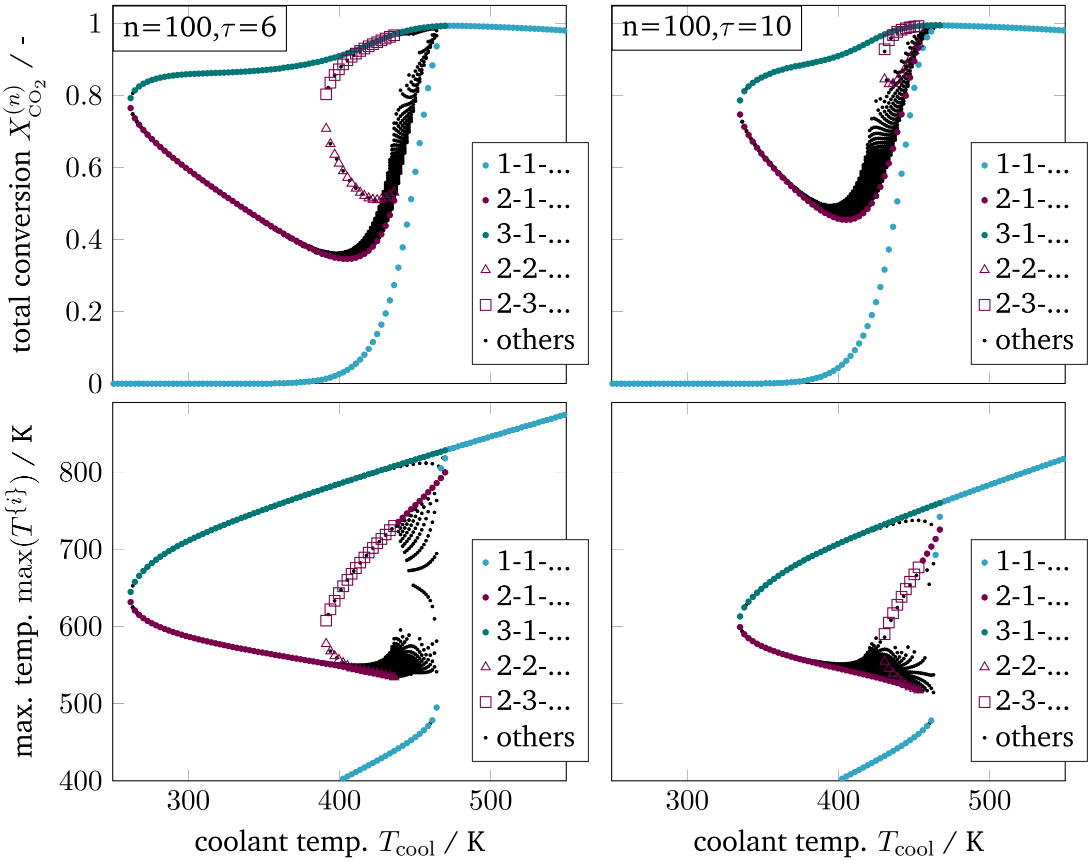

Fig. A.3.: Enumerative solution of operating points (OP) in a multi-stage CSTR cascade with varying residence time, color - OPs of two key stages at the inlet, black - OPs of subordinate branches, reference setting taken from Tab. A.1 but $T_{\mathrm{in}} = T_{\mathrm{cool}}$.

A.3 Components of Detailed Reactor Model

Most of the physical parameters in Eqs. (3.25) and (3.26) are significantly influenced by temperature, pressure, and composition. Considering this, the presence of strong nonlinear dependencies leads to an increase in model complexity. However, fixed-bed reactor models require this level of complexity to sufficiently depict their real behavior.

A.3.1 Fixed-Bed Transport Correlations

With regard to pressure changes, it is assumed that the dynamic momentum balance of a fixed-bed is typically dominated by friction, allowing us to rely on the extended Ergun equation from Eisfeld and Schnitzlein [ES01] to compute the corresponding pressure drop

$$\frac{\partial p}{\partial z} = v_z \frac{(1-\varepsilon)}{\varepsilon^3} \left(\frac{\mathrm{c}_1\,(1-\varepsilon)\,\mu_{\mathrm{gas}}}{d_{\mathrm{p}}{}^2} + \frac{\mathrm{c}_2\,\rho_{gas}}{d_{\mathrm{p}}} v_z \right) \tag{A.16}$$

Another transport coefficient which needs to be considered in Eq. (3.25) is the effective radial dispersion coefficient $\mathcal{D}_{r,\alpha}^{\mathrm{eff}}$. To incorporate the influence of the axial convection on the radial diffusion Tsotsas and Schlünder [TS88] established the following correlation:

$$\mathcal{D}_{r,\alpha}^{\mathrm{eff}} = \left(1 - \sqrt{1-\bar{\varepsilon}}\right) \mathcal{D}_{r,\alpha} + \frac{v_z\, d_p}{8},$$

where the first term accounts for a weighted molecular diffusion and the second term results from cross-mixing effects within the fixed-bed. As part of our assumptions the averaged porosity $\bar{\varepsilon}$ equals to the constant ε in Tab. 3.2. The molecular diffusion coefficient $\mathcal{D}_{\mathrm{M},\alpha}$ is calculated according to Kee et al. [KCG03]. Therefore, mixture averaged diffusion coefficients are required, which account for a single species α diffusing into a mixture of other gases.

$$\mathcal{D}_{\mathrm{M},\alpha}(T,p,\rho_\alpha) = \frac{\frac{\rho}{M} - \frac{\rho_\alpha}{M_\alpha}}{\sum\limits_{\substack{j=1 \\ j\neq\alpha}} \frac{\rho_j}{M_j} \frac{1}{\mathcal{D}_{\alpha,j}(T,p)}} \qquad \text{with} \qquad \frac{\rho}{M} = \sum_{\alpha} \frac{\rho_\alpha}{M_\alpha}. \tag{A.17}$$

The binary diffusion coefficients are obtained from Fuller et al. [FSG66] considering special diffusion volumes υ_α

$$\mathcal{D}_{\alpha_1,\alpha_2}(T,p) = \frac{10^{-7}\, T^{1.75}\, \sqrt{10^3\,(1/M_{\alpha_1} + 1/M_{\alpha_2})}}{(p/1.01325)\, \left[\sqrt[3]{\upsilon_{\alpha_1}} + \sqrt[3]{\upsilon_{\alpha_2}}\right]^2}.$$

Further correlations in Eq. (3.26) are dedicated to the effective volumetric heat capacity

$$\begin{aligned}(\rho c_p)^{\text{eff}} &= (1-\varepsilon)\,\rho_{\text{cat}}\,c_{p,\text{cat}} + \varepsilon\,\rho_{\text{gas}}\,c_{p,\text{gas}},\\ c_{p,\text{gas}} &= \sum_{\alpha} w_\alpha\,c_{p,\alpha}\ ,\end{aligned}$$

which consists of constant parameters (e.g., ε, ρ_{cat}, $c_{p,\text{cat}}$ as stated in Tab. 3.2) and temperature dependent mixed gas heat capacity $c_{p,\text{gas}}(T,\rho_\alpha)$. The necessary component heat capacities $c_{p,\alpha}$ relate to polynomial correlations with coefficients taken from VDI [VDI10].

The gas density is described by the ideal gas law

$$\rho_{\text{gas}} = \frac{p\,M_{\text{gas}}}{\mathcal{R}\,T}\ .$$

Since this work considers only one pseudo-homogeneous phase to represent the fixed-bed, heat conduction in radial direction is based on the effective heat conductivity. Bauer and Schlünder [BS78b] combined the influence of the axial convective transport, radiation, and the actual conduction by the following relation:

$$\lambda_{\text{eff},r} = \lambda_{\text{conv}} + \lambda_{\text{cond},r}, \tag{A.18}$$

$$\lambda_{\text{conv}} = \frac{1.15\,\rho\,v_z\,c_{p,\text{gas}}\,d_p}{8\left[2-(1-d_p/R)^2\right]},$$

$$\lambda_{\text{cond},r} = \left(1-\sqrt{1-\varepsilon}\right)(\lambda_{\text{gas}}+\varepsilon\,\lambda_r) + \sqrt{1-\varepsilon}\,\lambda_{rs}, \tag{A.19}$$

$$\lambda_r = 2.27\cdot 10^{-7}\,\frac{\epsilon_{\text{cat}}}{2-\epsilon_{\text{cat}}}\,T^3\cdot d_p.$$

Further details on the parameter λ_{rs} can be found in Bauer and Schlünder [BS78b]. The thermal gas conductivity λ_{gas} is taken from Poling et al. [PPO01]

$$\lambda_{\text{gas}}(T,\rho_\alpha) = \sum_{\alpha_1} \frac{\frac{\rho_{\alpha_1}}{M_{\alpha_1}}\,\lambda_{\alpha_1}(T)}{\sum\limits_{\alpha_2}\frac{\rho_{\alpha_2}}{M_{\alpha_2}}\,\phi_{\alpha_1,\alpha_2}(T)}, \tag{A.20}$$

which is determined by thermal component conductivities λ_α and a dynamic viscosity mixing rule

$$\phi_{\alpha_1,\alpha_2}(T) = \frac{\left[1+(\eta_{\alpha_1}(T)/\eta_{\alpha_2}(T))^{0.5}(M_{\alpha_2}/M_{\alpha_1})^{0.25}\right]^2}{\sqrt{8\,(1+M_{\alpha_1}/M_{\alpha_2})}}.$$

The dynamic viscosities η_α and the thermal component conductivities λ_α are again extracted from VDI [VDI10].

A.3.2 Coolant Transport Correlations

Jacket

The heat transport coefficient for the reactor jacket $\mathrm{k_{jac}}$ in Eq. (3.36) is obtained from

$$\mathrm{k_{jac}} = \left(\frac{1}{\lambda_{\mathrm{jac}}} \ln((\mathrm{R} + \delta_{\mathrm{jac}})/\mathrm{R}) \right)^{-1},$$

to compensate radial mismatch between inner and outer jacket surface. Its impact on the overall heat transport is illustrated in Fig. A.9.

Cooling channel

The heat transport inside the cooling channel (considered as an annular gap) is calculated via the correlations from Gnielinski [Gni10]. As heat transfer medium the synthetic oil *Marlotherm SH* is selected and the corresponding thermo-physical properties are taken from [Pre+10]. Fig. A.4 illustrates the results for the coolant Nusselt number over a broad coolant Reynolds number range and for different technically relevant coolant temperatures. With these correlations and fixed cooling channel dimensions, the coolant heat transfer coefficient α_{cool} remains to be a nonlinear function of flow rate (or velocity), temperature, and axial position

$$\alpha_{\mathrm{cool}} = f(\dot{V}_{\mathrm{cool}}, T_{\mathrm{cool}}, z). \tag{A.21}$$

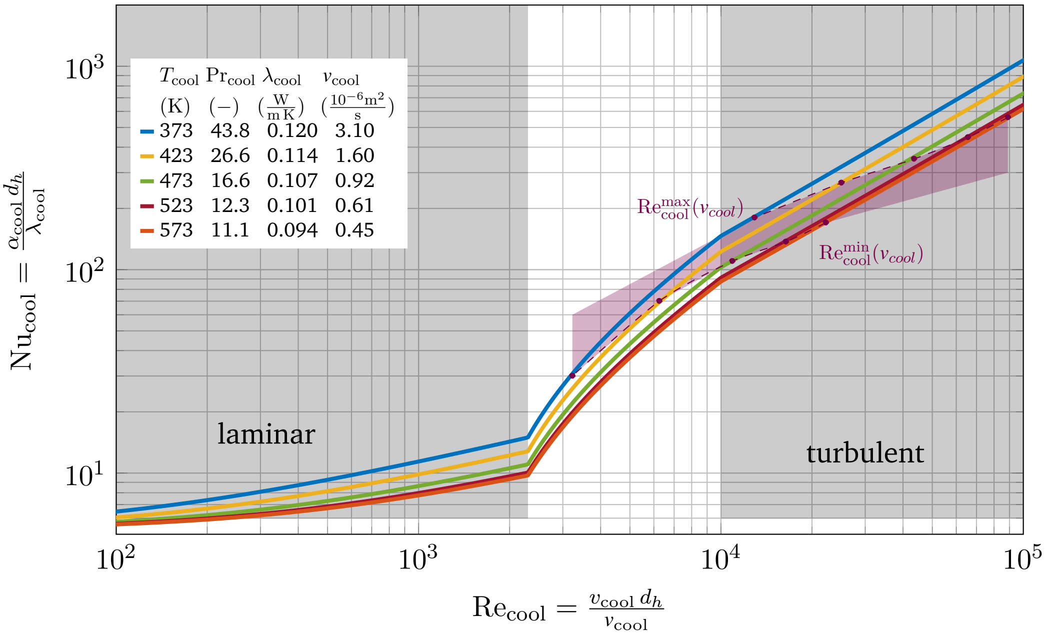

Fig. A.4.: Nu-Re-dependency for the heat transfer medium *Marlotherm SH*; $d_{\mathrm{h}} = 0.01\,\mathrm{m}$ and $L = 2.5\,\mathrm{m}$; thermo-physical data from [Pre+10].

Technically relevant values for coolant velocity and hydraulic cooling channel diameter are

$$v_{\mathrm{cool}} = 1 - 2\,\frac{\mathrm{m}}{\mathrm{s}} \quad \text{and} \quad d_h = 0.01 - 0.02\,\mathrm{m}.$$

The resulting cooling regime in Fig. A.4 that is relevant for this work is shaded in red. Consequently, two limiting cases can be identified to estimate a reasonable range for the coolant heat transfer coefficient α_{cool} averaged over the reactor length:

Max. case:

$T_{\mathrm{cool}} =$	573	K	$\Delta p_{\mathrm{cool}} =$	0.3	bar
$d_h =$	0.02	m	$\dot{V}_{\mathrm{cool}} =$	2.1	l/s
$v_{\mathrm{cool}} =$	2	m/s			

$$\begin{aligned} &\mathrm{Re}_{\mathrm{cool}} = 8.9 \times 10^4 \Rightarrow \mathrm{Nu}_{\mathrm{cool}} = 560 \\ \Rightarrow\ &\alpha_{\mathrm{cool}} = 2632\,\frac{\mathrm{W}}{\mathrm{m}^2\,\mathrm{K}}, \end{aligned}$$

Min. case:

$T_{\mathrm{cool}} =$	373	K	$\Delta p_{\mathrm{cool}} =$	0.04	bar
$d_h =$	0.01	m	$\dot{V}_{\mathrm{cool}} =$	0.45	l/s
$v_{\mathrm{cool}} =$	1	m/s			

$$\begin{aligned} &\mathrm{Re}_{\mathrm{cool}} = 3.2 \times 10^3 \Rightarrow \mathrm{Nu}_{\mathrm{cool}} = 30 \\ \Rightarrow\ &\alpha_{\mathrm{cool}} = 360\,\frac{\mathrm{W}}{\mathrm{m}^2\,\mathrm{K}}. \end{aligned}$$

Thus, the reference heat transfer coefficient α_{cool} of 500 W/(m^2 K) used in Tab. 3.2 is relatively moderate. A more detailed description of α_{cool} with respect to the reactor design used for the experimental validation in Chapter 6 is provided in Fig. 6.7.

A.3.3 Reaction Rate Expressions

The rate expressions used in our model are adapted from Xu and Froment [XF89] and Koschany et al. [KSH16], which have been implemented via the following correlations.

Rate expressions of Xu and Froment

Xu and Froment [XF89] considered three rate equations including the water-gas-shift (WGS) reaction:

$$\mathrm{r}_1 = \frac{k_1}{p_{H_2}^{2.5}} \left(p_{CH_4} p_{H_2O} - \frac{p_{H_2}^3 p_{CO}}{K_1} \right) \Big/ \mathrm{DEN}^2, \tag{A.22}$$

$$\mathrm{r}_2 = \frac{k_2}{p_{H_2}} \left(p_{CO} p_{H_2O} - \frac{p_{H_2} p_{CO_2}}{K_2} \right) \Big/ \mathrm{DEN}^2, \tag{A.23}$$

$$\mathrm{r}_3 = \frac{k_3}{p_{H_2}^{3.5}} \left(p_{CH_4} p_{H_2O}^2 - \frac{p_{H_2}^4 p_{CO_2}}{K_3} \right) \Big/ \mathrm{DEN}^2, \tag{A.24}$$

where p_α is the partial pressure of the respective component in bar and DEN is a dimensionless parameter defined as

$$\begin{aligned} \mathrm{DEN} = {} & 1 + K_{CO}\, p_{CO} + K_{H_2}\, p_{H_2} \\ & + K_{CH_4}\, p_{CH_4} + \frac{K_{H_2O}\, p_{H_2O}}{p_{H_2}}. \end{aligned}$$

K_α is the respective adsorption constant for CH_4, CO, H_2O and H_2 and b_β are rate coefficients exponentially depending on temperature via:

$$\begin{aligned} K_\alpha &= \mathcal{A}_\alpha \exp\left(-\frac{\Delta H_\alpha}{\mathcal{R}T} \right), \\ k_\beta &= \mathcal{A}_\beta \exp\left(-\frac{E_\beta}{\mathcal{R}T} \right). \end{aligned}$$

$\mathcal{A}_\beta$, E_β, $\mathcal{A}_\alpha$, ΔH_α are constant kinetic parameters stated in Tab. A.2.

Tab. A.2.: Kinetic parameters for Eqs. (A.22) to (A.24); each pre-exponential factor contains a multiplier of 1.225 (see Xu and Froment [XF89])

α	Formula	$\mathcal{A}_\alpha$	$[\mathcal{A}_\alpha]$	ΔH_α	$[\Delta H_\alpha]$	β	$\mathcal{A}_\beta$	$[\mathcal{A}_\beta]$	E_β	$[E_\beta]$
1	CH_4	8.15×10^{-4}	bar^{-1}	-38.28	$\frac{\mathrm{kJ}}{\mathrm{mol}}$	1	5.176×10^{15}	$\frac{\mathrm{kmol\,bar}^{0.5}}{\mathrm{kg_{cat}\,h}}$	240.10	$\frac{\mathrm{kJ}}{\mathrm{mol}}$
2	CO	10.08×10^{-5}	bar^{-1}	-70.65	$\frac{\mathrm{kJ}}{\mathrm{mol}}$	2	2.395×10^{6}	$\frac{\mathrm{kmol}}{\mathrm{kg_{cat}\,h\,bar}}$	67.13	$\frac{\mathrm{kJ}}{\mathrm{mol}}$
4	H_2O	2.17×10^{5}		88.68	$\frac{\mathrm{kJ}}{\mathrm{mol}}$	3	1.250×10^{15}	$\frac{\mathrm{kmol\,bar}^{0.5}}{\mathrm{kg_{cat}\,h}}$	243.90	$\frac{\mathrm{kJ}}{\mathrm{mol}}$
5	H_2	7.50×10^{-9}	bar^{-1}	-82.90	$\frac{\mathrm{kJ}}{\mathrm{mol}}$					

The temperature dependent equilibrium constants K_1, K_2 and K_3 are based on the Gibbs reaction energy (STP) as shown in Poling et al. [PPO01].

Finally, a unit conversion is required to adequately implement these rate equations to Eqs. (3.25) and (3.26):

$$\tilde{\mathrm{r}}_\beta = \mathrm{r}_\beta\, \rho_{\mathrm{cat}}\, 1000/3600.$$

Rate expressions of Koschany et al.

Koschany et al. [KSH16] exclusively considered carbon dioxide methanation to describe they experimental kinetic data. The corresponding rate equation is:

$$\mathrm{r}_{\mathrm{meth}} = k\, p_{\mathrm{CO_2}}^{0.5}\, p_{\mathrm{H_2}}^{0.5} \left(1 - \frac{p_{\mathrm{CH_4}}\, p_{\mathrm{H_2O}}^{2}}{K_{\mathrm{eq}}\, p_{\mathrm{CO_2}}\, p_{\mathrm{H_2}}^{4}}\right) \Big/ \mathrm{DEN}^2,$$

$$\mathrm{DEN} = 1 + K_{\mathrm{OH}} \frac{p_{\mathrm{H_2O}}}{p_{\mathrm{H_2}}^{0.5}} + K_{\mathrm{H_2}}\, p_{\mathrm{H_2}}^{0.5} + K_{\mathrm{mix}}\, p_{\mathrm{CO_2}}^{0.5},$$

which is determined by the following correlations for rate coefficient k, adsorption constant K_x and equilibrium constant K_{eq}:

$$k = k_{0,\mathrm{ref}} \exp\left(\frac{E_{\mathrm{A}}}{\mathcal{R}}\left(\frac{1}{T_{\mathrm{ref}}} - \frac{1}{T}\right)\right), \tag{A.25}$$

$$K_x = K_{x,0,\mathrm{ref}} \exp\left(\frac{\Delta H_x}{\mathcal{R}}\left(\frac{1}{T_{\mathrm{ref}}} - \frac{1}{T}\right)\right), \tag{A.26}$$

$$K_{\mathrm{eq}} = 137\, T^{-3.998} \exp\left(\frac{158.7\,\mathrm{kJ/mol}}{\mathcal{R}\, T}\right). \tag{A.27}$$

Tab. A.3.: Kinetic parameters for Eqs. (A.25) to (A.27); (see Koschany et al. [KSH16])

T_{ref}	550	K
$k_{0,\mathrm{ref}}$	3.46e-4	mol/(bar s g_{cat})
E_{A}	77.5	kJ/mol
$K_{\mathrm{OH,0,ref}}$	0.5	bar$^{-0.5}$
ΔH_{OH}	22.4	kJ/mol
$K_{\mathrm{H2,0,ref}}$	0.44	bar$^{-0.5}$
ΔH_{H2}	-6.2	kJ/mol
$K_{\mathrm{mix,0,ref}}$	0.88	bar$^{-0.5}$
ΔH_{mix}	-10	kJ/mol

Again, a unit conversion is required to adequately implement this rate equation to Eqs. (3.25) and (3.26):

$$\tilde{\mathrm{r}}_\beta = \mathrm{r}_\beta\, \rho_{\mathrm{cat}}\, 1000.$$

A.4 Reference Case of Detailed Reactor Model

In this section, the reference reactor setting in Tab. 3.2 and the corresponding steady state is presented in order to enable a simple replication of the results in this work. Surface plots illustrate the finite volume mesh density and provide a clearer visualization of our chosen PDE discretization.

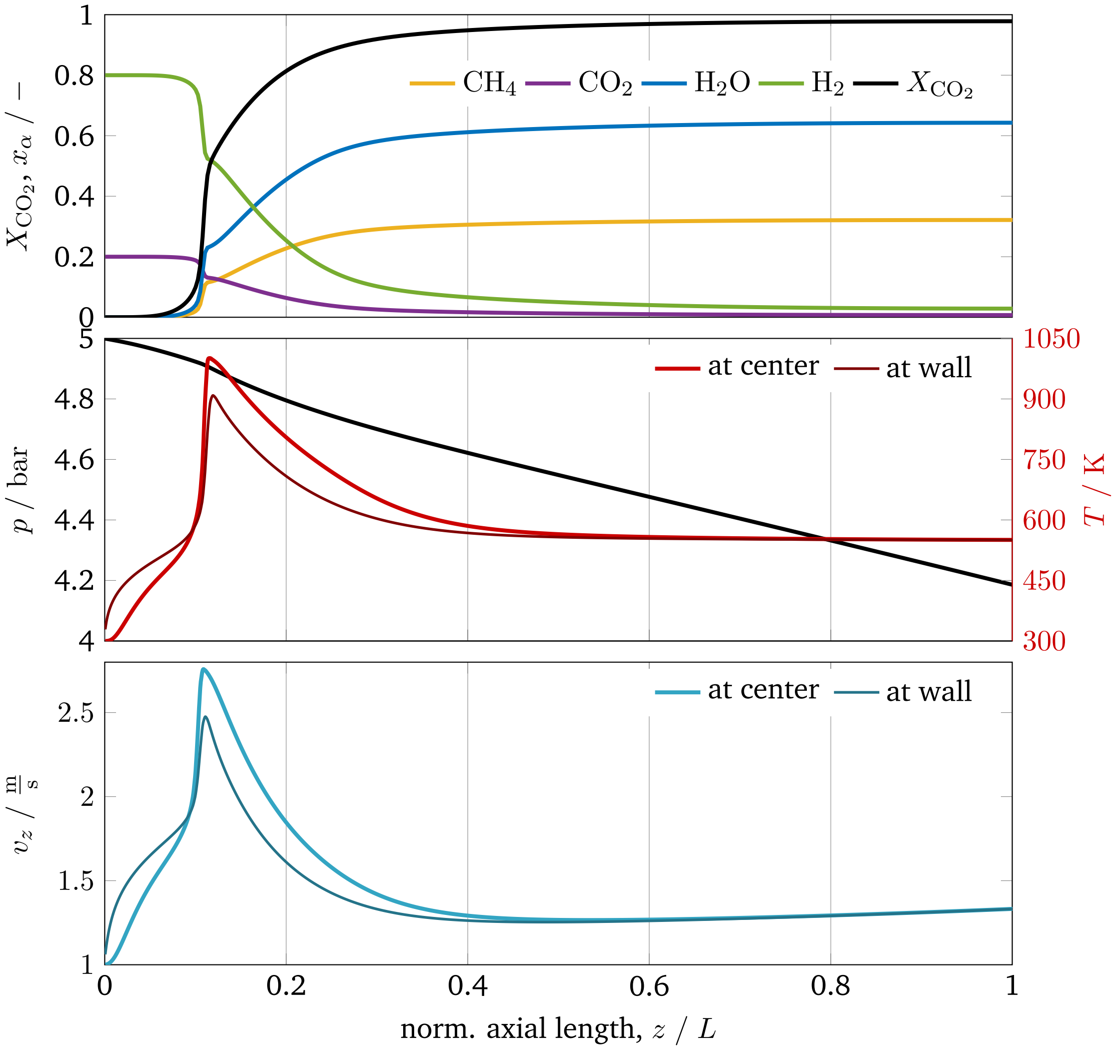

Fig. A.5.: Conversion, composition, temperature, pressure and velocity changes along the entire reactor length; reactor setting according to Tab. 3.2 and at $T_{\text{cool}} = 550\,\text{K}$

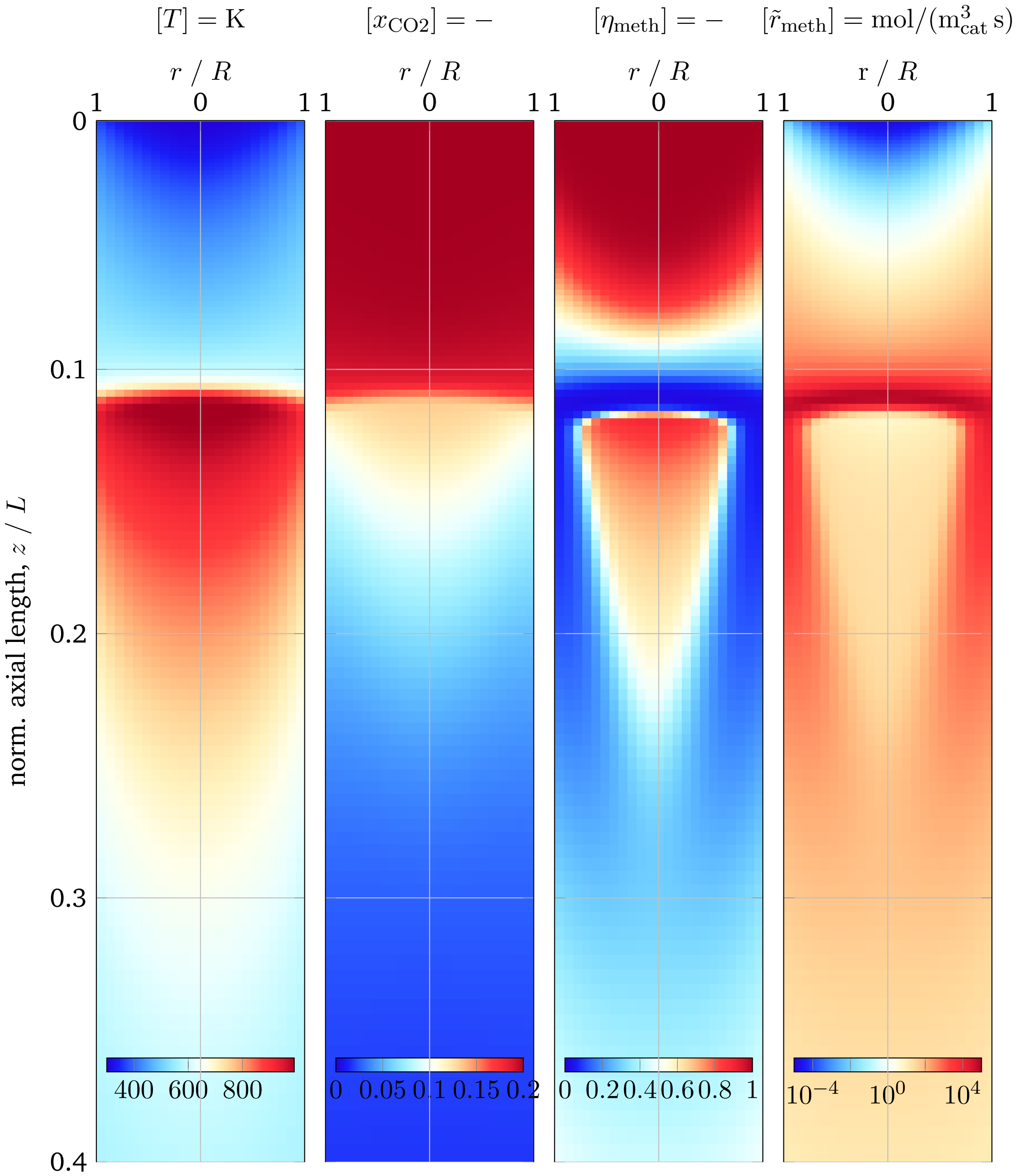

Fig. A.6.: Temperature, CO_2-composition, effectiveness factor and reaction rate changes around the reactive zone; reactor setting according to Tab. 3.2 and at $T_{\mathrm{cool}} = 550\,\mathrm{K}$

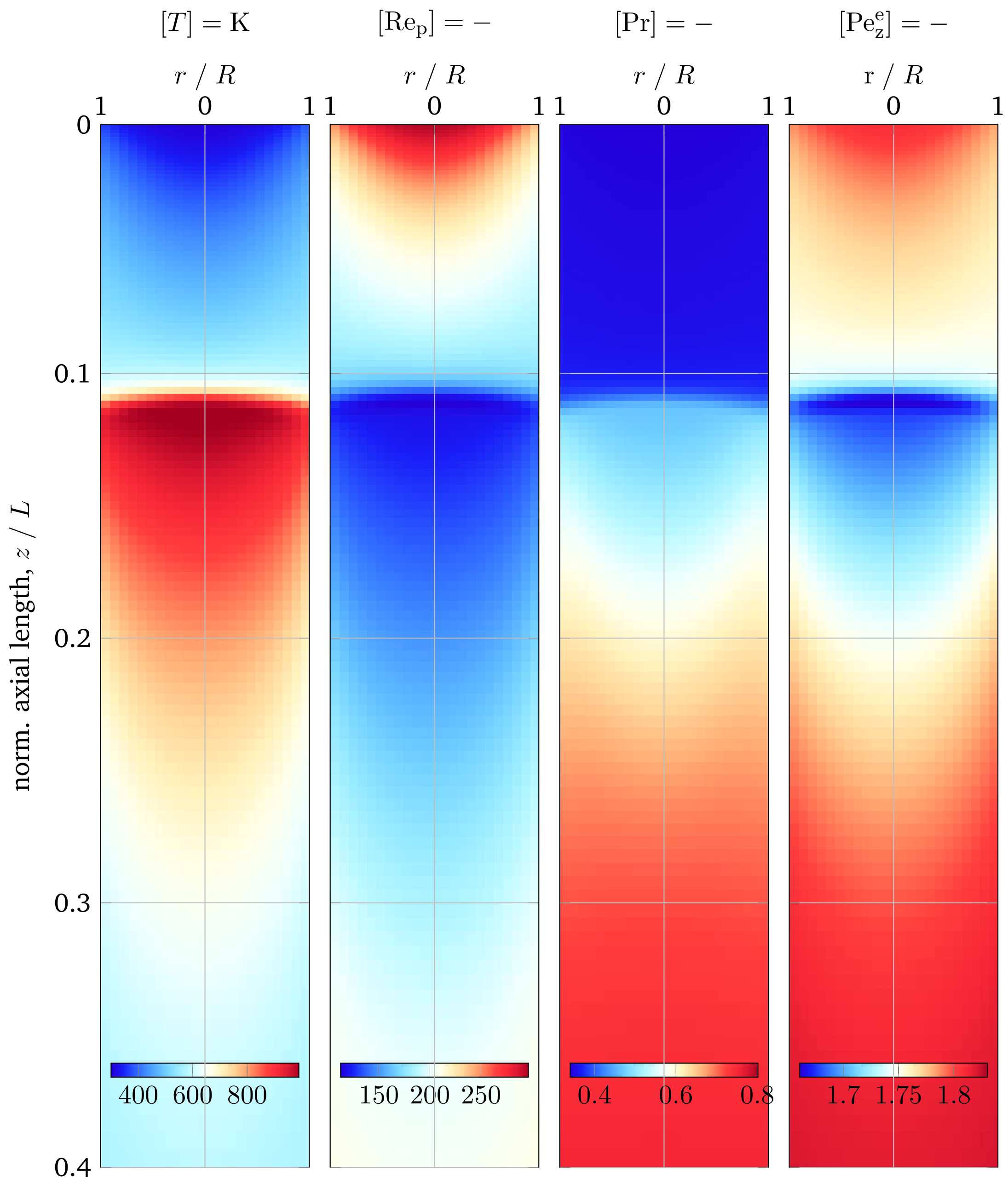

Fig. A.7.: Temperature, Reynolds number, Prandtl number and effective axial Péclet number around the reactive zone; reactor setting according to Tab. 3.2 and at $T_{\mathrm{cool}} = 550\,\mathrm{K}$

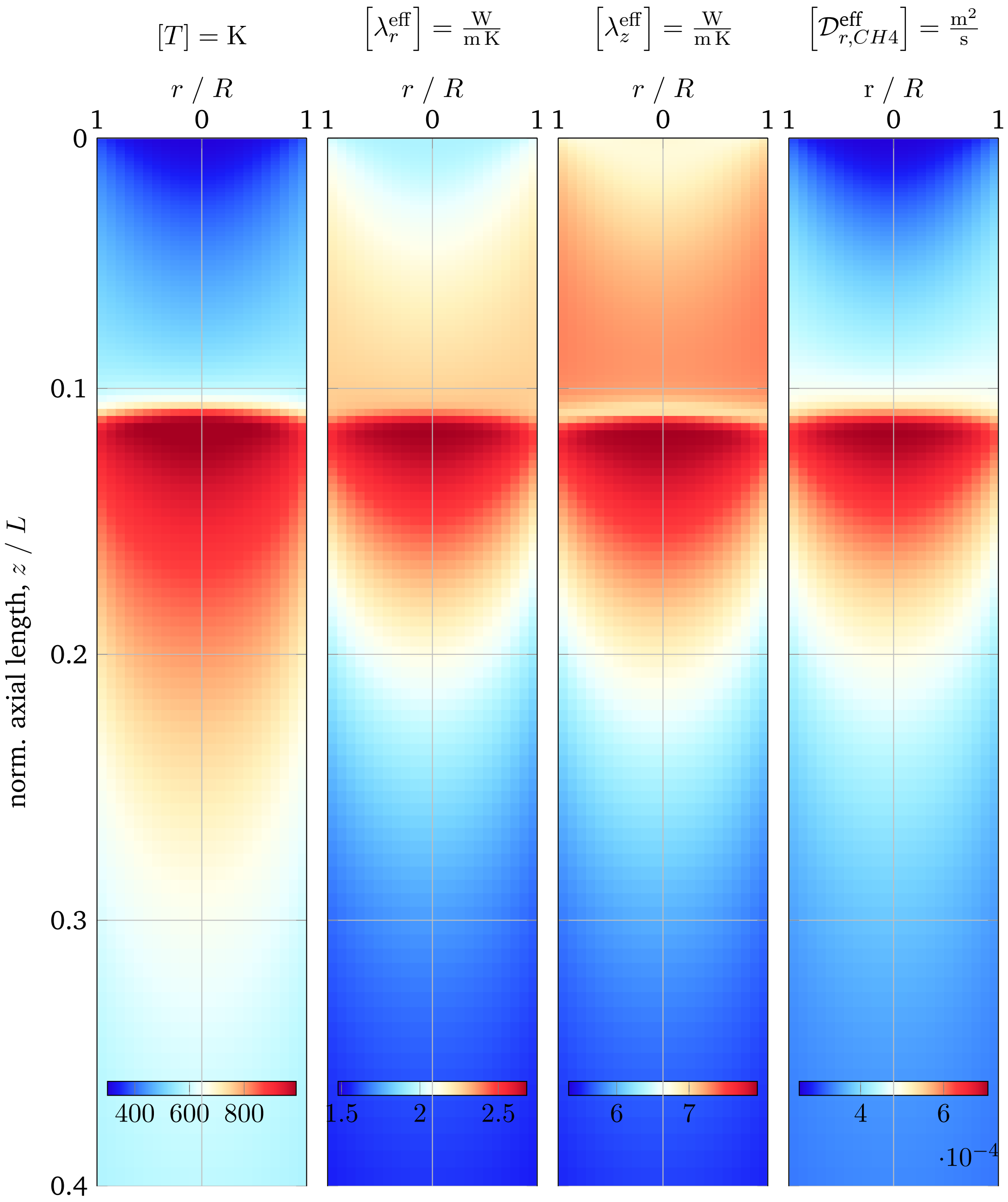

Fig. A.8.: Temperature, effective radial conductivity, effective axial conductivity and effective CH_4 diffusion coefficient around the reactive zone; reactor setting according to Tab. 3.2 and at $T_{\mathrm{cool}} = 550\,\mathrm{K}$

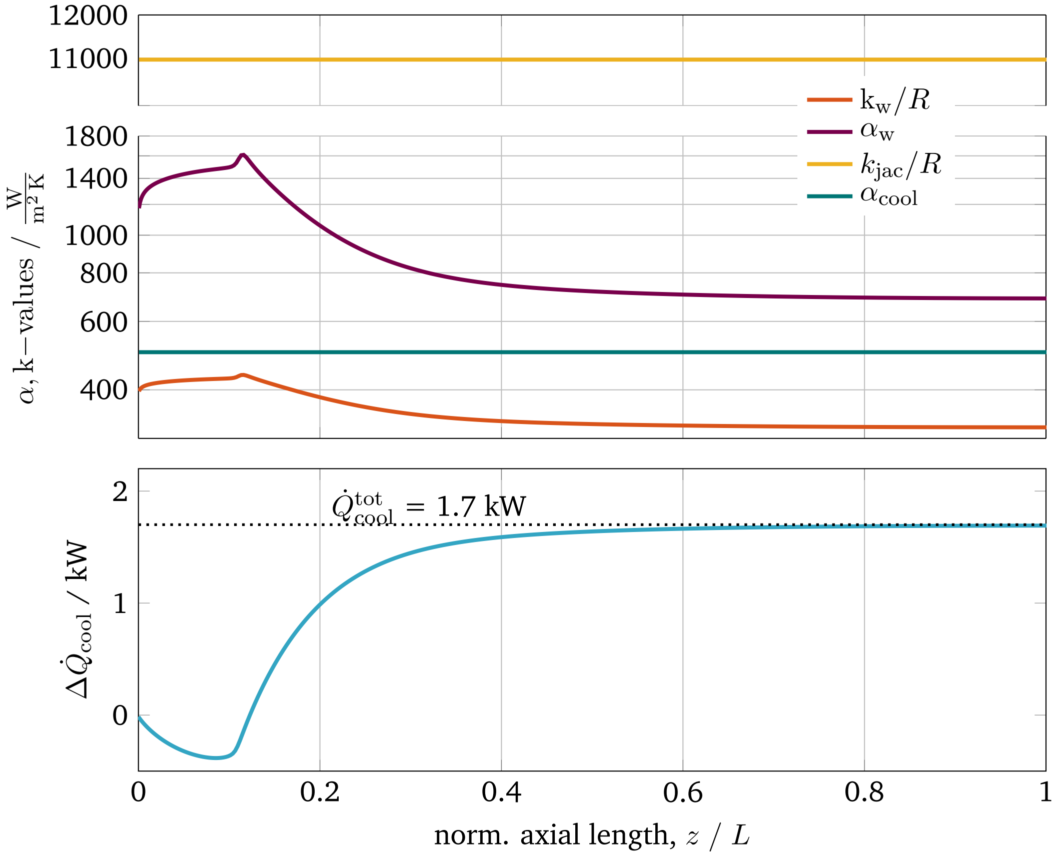

Fig. A.9.: Heat transport coefficients and cumulative heat transfer from reactor to coolant along the entire reactor length; reactor setting according to Tab. 3.2 and at $T_\mathrm{cool} = 550\,\mathrm{K}$

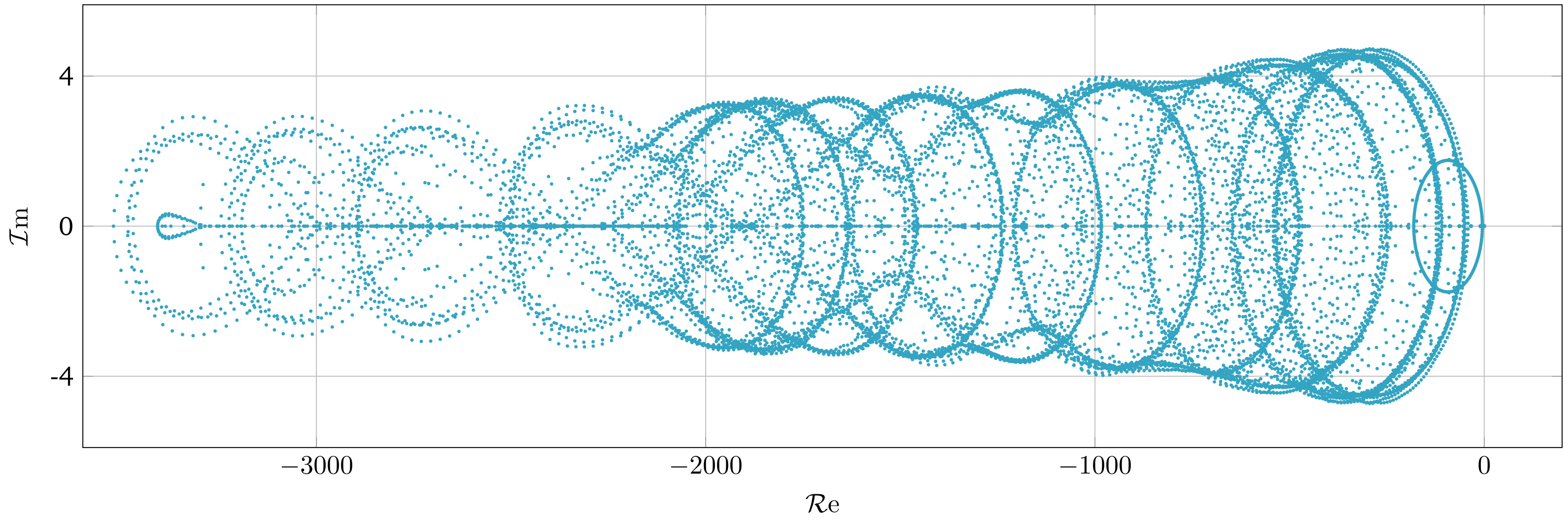

Fig. A.10.: Open-loop eigenvalues of linearized state c) of the reference setting in Fig. 4.1.

A.5 Experiments

Tab. A.4.: Measured CH_4 and CO yields for the industrial methanation reference catalyst (IMRC) samples over two hours reaction time. Experiments conducted by Lisa Yvonne Downen.

sample ID	red.	cond.	$\dot{V}_{\alpha}$ (NmL/min)			T_{bed}	yield (%)		ppm CO
	(h)	(h)	H_2	CO_2	He	(°C)	CH_4	CO	
IMRC-1	2	0	24	6	150	351.9	21.67	–	–
			48	12	120	358.7	25.40	–	–
			72	18	90	369.3	30.55	–	–
			96	24	60	387.4	39.90	–	–
			24	6	150	355.4	34.35	–	–
IMRC-2	4	0	24	6	150	298.3	5.92	–	–
			48	12	120	298.3	5.85	–	–
			72	18	90	301.2	6.02	–	–
			96	24	60	300.7	5.76	0.89	1268
			24	6	150	299.6	9.00	1.55	529.0
IMRC-3	4	0	24	6	150	400.8	36.62	–	–
			48	12	120	408.3	46.76	–	–
			72	18	90	417.7	54.33	–	–
			96	24	60	424.3	58.81	1.20	1883
			24	6	150	403.6	49.26	2.22	767.6
IMRC-4	4	4	24	6	150	354.8	33.58	–	–
			48	12	120	363.4	36.22	–	–
			72	18	90	374.7	40.59	–	–
			96	24	60	394.6	49.53	1.37	2072
			24	6	150	354.3	38.85	2.06	710.6
IMRC-5	4	4	24	6	150	297.4	7.35	–	–
			48	12	120	301.1	7.13	–	–
			72	18	90	299.7	6.44	1.09	1103
			96	24	60	302.8	6.54	–	–
			24	6	150	298.6	9.55	–	–
IMRC-6	4	4	24	6	150	407.5	44.08	–	–
			48	12	120	421.8	50.40	–	–
			72	18	90	440.3	55.96	–	–
			96	24	60	460.5	60.68	1.34	2126
			24	6	150	409.6	48.49	2.91	1005
IMRC-7	4	4	24	6	150	505.5	34.23	16.18	–
IMRC-8	4	4	24	6	150	597.8	7.58	45.48	–

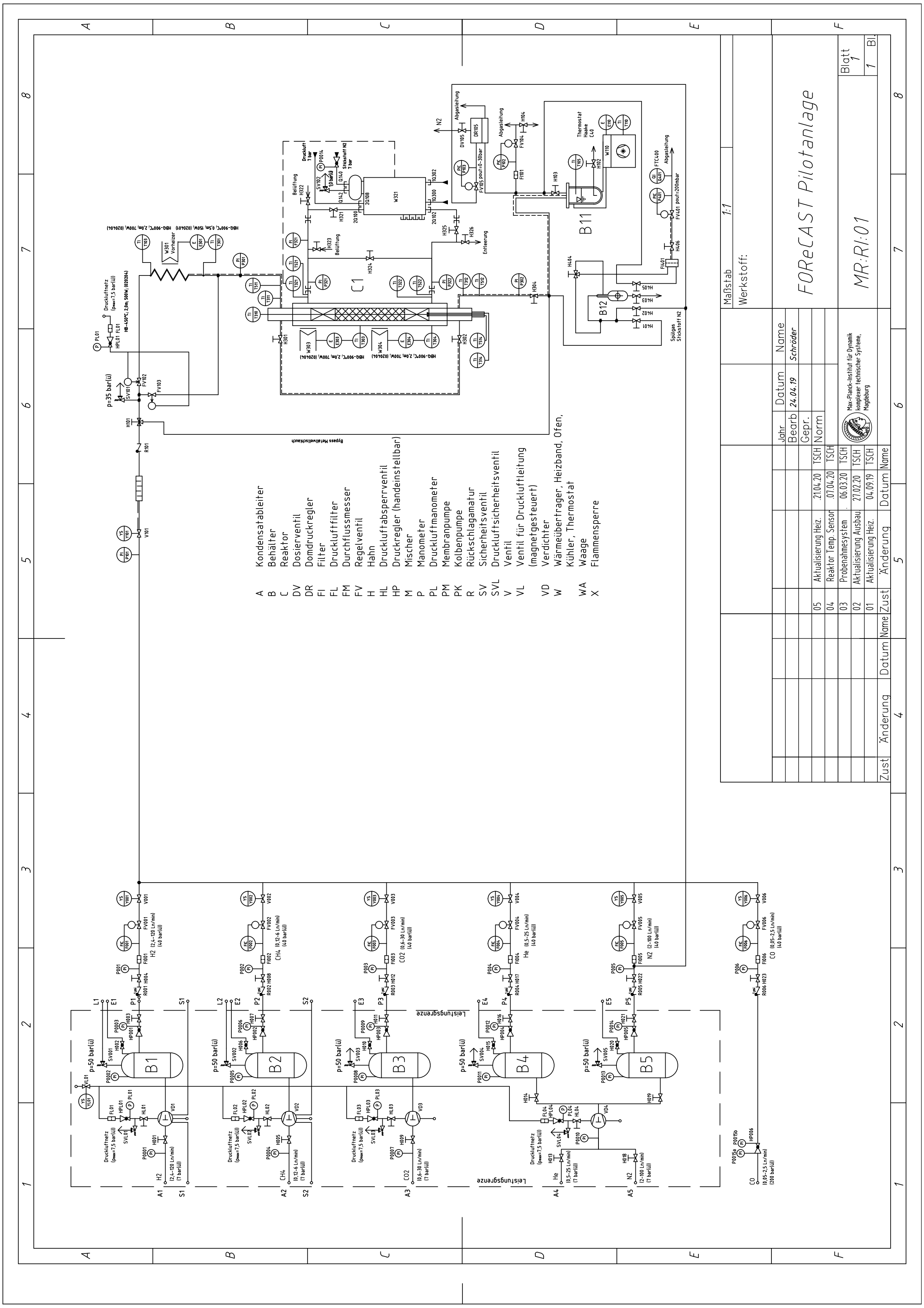
A Kondensatableiter
B Behälter
C Reaktor
DV Dosierventil
DR Domdruckregler
FI Filter
FL Druckluftfilter
FM Durchflussmesser
FV Regelventil
H Hahn
HL Druckluftabsperrventil
HP Druckregler (handeinstellbar)
M Mischer
P Manometer
PL Druckluftmanometer
PM Membranpumpe
PK Kolbenpumpe
R Rückschlagarmatur
SV Sicherheitsventil
SVL Druckluftsicherheitsventil
V Ventil
VL Ventil für Druckluftleitung (magnetgesteuert)
VD Verdichter
W Wärmeübertrager, Heizband, Ofen, Kühler, Thermostat
WA Waage
X Flammensperre
B1
B2
B3
B4
B5
B11
B12
C1
H2
CH4
CO2
He
N2
CO
p=50 bar(ü)
p=35 bar(ü)
Druckluftnetz
Leistungsgrenze
Bypass Metallwellschlauch
Spülgas Stickstoff N2
Abgasleitung
Entleerung
Belüftung
Thermostat Haake C40
W301 Vorheizer
Maßstab 1:1
Werkstoff:
FOReCAST Pilotanlage
MR:RI:01
Blatt 1
1 Bl.
Jahr Datum Name
Bearb. 24.04.19 Schröder
Gepr.
Norm
05 Aktualisierung Heiz. 21.04.20 TSCH
04 Reaktor Temp. Sensor 07.04.20 TSCH
03 Probenahmesystem 06.03.20 TSCH
02 Aktualisierung Ausbau 27.02.20 TSCH
01 Aktualisierung Heiz. 04.09.19 TSCH
Zust. Änderung Datum Name
Max-Planck-Institut für Dynamik komplexer technischer Systeme, Magdeburg

Fig. A.11.: Piping and instrumentation diagram of the FOReCAST pilot plant.

Tab. A.5.: Parameters for evaluating uniqueness and multiplicity criteria under experimental conditions, considering Case B as model calibration.

parameter	symbol	Tab. A.1	exp. 11	exp. 16	unit
inlet temperature	T_{in}	27	196	186	°C
inlet pressure	p_{in}	5	1.41	1.44	bar
inlet molar ratio	H_2:CO_2:N_2	4:1:0	4:1:8.6	4:1:1	-
inlet velocity	v_{in}	1	1.48	1.12	m/s
tubular geometry	L/R	21	200	200	-
catalyst density (w/ pores)	ρ_{cat}	2355	1032	1032	kg/m^3
void fraction	ε	0.4	0.39	0.39	-
effectiveness factor	η_{meth}	1	0.20	0.20	-
residence time	τ	0.2	0.52	0.70	s
heat transfer coeff.	k_{ov}	500	120	100	$\text{W/(m}^2\,\text{K)}$
inlet gas heat capacity	$c_{p,\text{in}}$	2946	1403	2359	J/(kg K)
inlet gas density	ρ_{in}	2	0.78	0.50	kg/m^3
inlet CO_2 concentration	$c_{\text{CO}_2,\text{in}}$	40	2.67	6.30	mol/m^3
inlet CO_2 density	$\rho_{\text{CO}_2,\text{in}}$	1.76	0.12	0.28	kg/m^3
surface/flow-rate ratio	$\frac{A}{\dot{V}_{\text{in}}} = \frac{2\,L}{v_{\text{in}}\,R}$	42	267	357	s/m
Stanton number	St	3.4	29.1	30.1	-
adiabatic temperature rise	$\Delta\,T_{\text{ad}}$	1074	420	915	K
axial Bodenstein number	Bo (from Eq. (3.33))	-	900	720	-
axial Bodenstein number	Bo (implied by FVM)	-	800	800	-
mass-based sensitivity	$\max\,\frac{d\,X}{d\,T}$	-	0.0027	0.0026	1/K
energy-based sensitivity	$\frac{1+\frac{2\,\mathrm{St}}{\mathrm{Bo}}}{\Delta\,T_{\text{ad}}}$	-	0.0025	0.0012	1/K

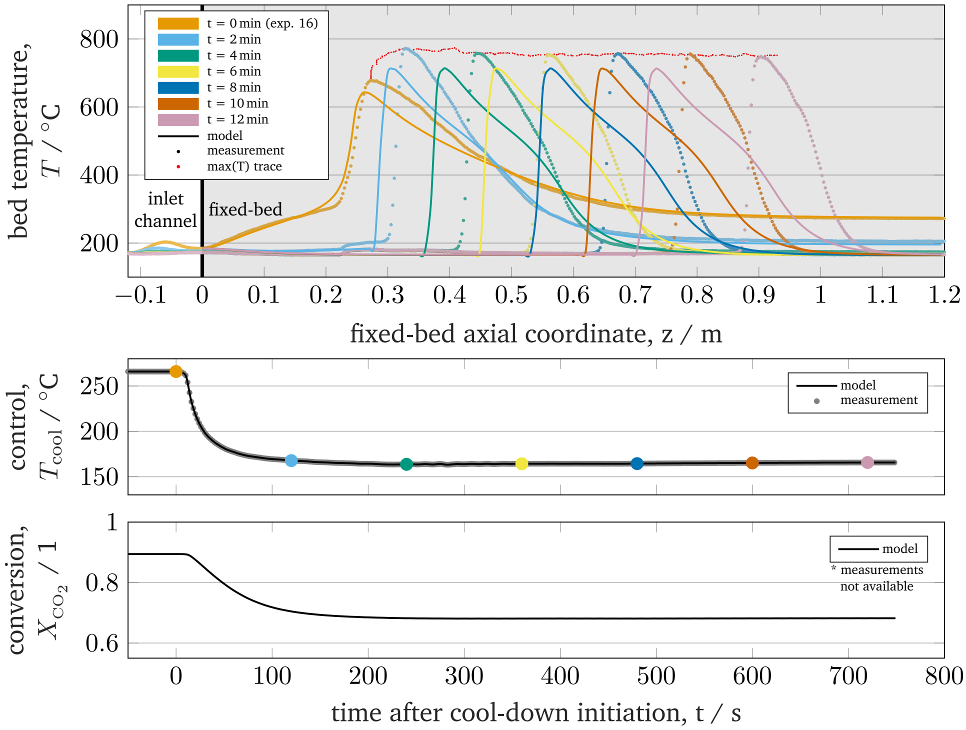

Fig. A.12.: Reactor behavior under intensive reaction conditions after cool-down perturbation in comparison with the calibrated model (Case B), initial state corresponds to experiment 16 in Tab. 6.6, replicates Fig. 6.15 but with 100 instead of 200 axial FVs.

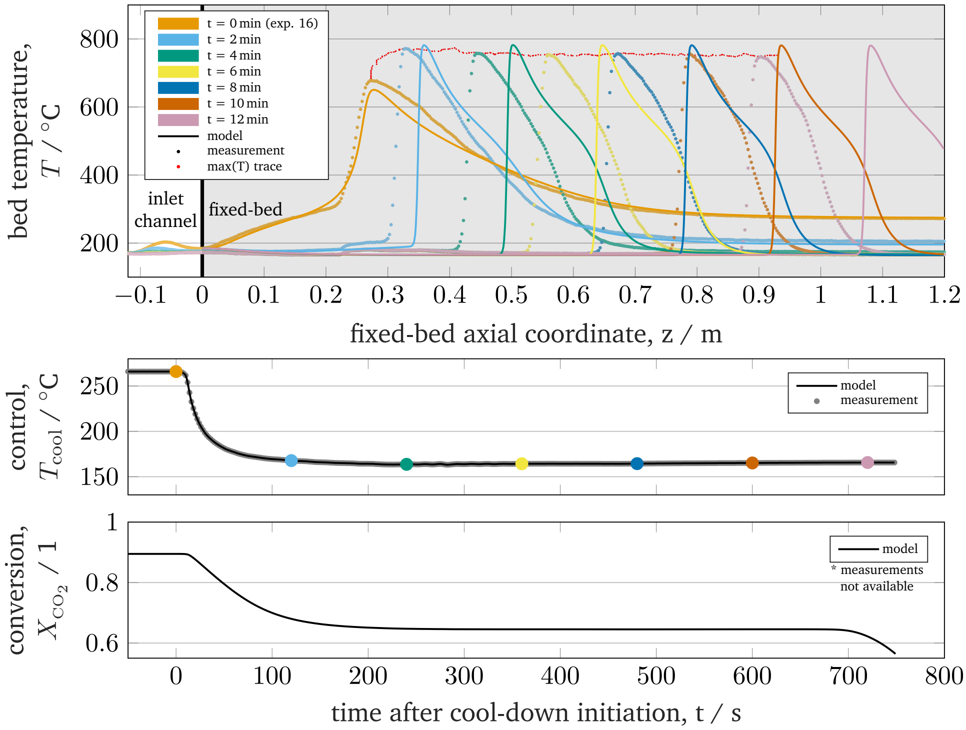

Fig. A.13.: Reactor behavior under intensive reaction conditions after cool-down perturbation in comparison with the calibrated model (Case B), initial state corresponds to experiment 16 in Tab. 6.6, replicates Fig. 6.15 but with 400 instead of 200 axial FVs.

A.6 Numerical Diffusion within the FVM

Considering the following simplified formulation of Eqs. (3.25) and (3.26):

$$\frac{\partial x}{\partial t} + v\frac{\partial x}{\partial z} - \mathcal{D}_{\text{phy}}\frac{\partial^2 x}{\partial z^2} + \sigma(x) = 0. \tag{*}$$

The function x may represent mass fraction or temperature that propagates at velocity $v{>}0$ and disperses in a fixed-bed with $\mathcal{D}_{\text{phy}}{>}0$, called physical dispersion coefficient. In addition a nonlinear source $\sigma(x)$ may or may not be considered. Since discretization is the main focus here, initial and boundary conditions are unnecessary.

The discretization of equation (*) (e.g., with a FV scheme) results in:

$$\begin{aligned}\frac{\partial x}{\partial z} &\approx \frac{x_i - x_{i-1}}{\Delta z},\\ \frac{\partial^2 x}{\partial z^2} &\approx \frac{x_{i-1} - 2x_i + x_{i+1}}{\Delta z^2}.\end{aligned}$$

The following numerical approximation of (*) remains:

$$\frac{\partial x}{\partial t} + v\frac{x_i - x_{i-1}}{\Delta z} - \mathcal{D}_{\text{phy}}\frac{x_{i-1} - 2x_i + x_{i+1}}{\Delta z^2} + \sigma(x_i) = 0 \tag{**}$$

To find the solution of equation (**), a transformation is carried out using the Taylor expansion:

$$x_{i\pm1} = x_i \pm \frac{\partial x}{\partial z}\Delta z + \frac{1}{2}\frac{\partial^2 x}{\partial z^2}\Delta z^2 \pm \frac{1}{6}\frac{\partial^3 x}{\partial z^3}\Delta z^3 + \mathcal{O}(\Delta z^4),$$

and finds:

$$\frac{\partial x}{\partial t} + v\left[\frac{\partial x}{\partial z} - \frac{1}{2}\frac{\partial^2 x}{\partial z^2}\Delta z + \mathcal{O}(\Delta z^2)\right] - \mathcal{D}_{\text{phy}}\left[\frac{\partial^2 x}{\partial z^2} + \mathcal{O}(\Delta z^2)\right] + \sigma(x) = 0$$

When using the scheme (**), the following equation is exactly approximated (up to an error $\mathcal{O}(\Delta z^2)$):

$$\frac{\partial x}{\partial t} + v\frac{\partial x}{\partial z} - \left(\mathcal{D}_{\text{phy}} + \frac{v\Delta z}{2}\right)\frac{\partial^2 x}{\partial z^2} + \sigma(x) = \mathcal{O}(\Delta z^2).$$

Hence, the discretization inherently leads to an apparent diffusion, with is simply the sum of physical ($\mathcal{D}_{\text{phy}}$) and numerical diffusion ($v\Delta z/2$). Considering the Bodenstein analogy from Eq. (3.5) for Bo > 100 in which the stage number n is equivalent to the number of discretization elements within the domain L, results in

$$n = \frac{\text{Bo}}{2} = \frac{vL}{2\,\mathcal{D}_{\text{num}}} = \frac{v\Delta z}{2\,\mathcal{D}_{\text{num}}}\frac{L}{\Delta z} = \frac{v\Delta z}{2\,\mathcal{D}_{\text{num}}}n \quad\Longleftrightarrow\quad \frac{v\Delta z}{2} = \mathcal{D}_{\text{num}}.$$

This proofs that physical diffusion can be replaced by numerical diffusion, if the number of discretization elements n are selected in such a way, that $\mathcal{D}_{\text{phy}} = \mathcal{D}_{\text{num}}$.

Bibliography

[AA06] J. Alvarez-Ramirez and J. Alvarez. „Linear PI control of batch exothermic reactors with temperature measurement“. In: *International Journal of Robust and Nonlinear Control* 16.3 (2006), pp. 113–131 (cit. on p. 30).

[AA58a] R. Aris and N. R. Amundson. „An analysis of chemical reactor stability and control—I“. In: *Chemical Engineering Science* 7.3 (1958), pp. 121–131 (cit. on p. 30).

[AA58b] R. Aris and N. R. Amundson. „An analysis of chemical reactor stability and control—II“. In: *Chemical Engineering Science* 7.3 (1958), pp. 132–147 (cit. on p. 4).

[AB09] T. A. Adams II and P. I. Barton. „A dynamic two-dimensional heterogeneous model for water gas shift reactors“. In: *International Journal of Hydrogen Energy* 34.21 (2009), pp. 8877–8891 (cit. on p. 10).

[Aba+16] S. Abate, C. Mebrahtu, E. Giglio, F. Deorsola, S. Bensaid, S. Perathoner, R. Pirone, and G. Centi. „Catalytic performance of γ-Al_2O_3-ZrO_2-TiO_2-CeO_2 composite oxide supported Ni-based catalysts for CO_2 methanation“. In: *Industrial & Engineering Chemistry Research* 55.16 (2016), pp. 4451–4460 (cit. on pp. 23, 63).

[And+18] J. A. E. Andersson, J. Gillis, G. Horn, J. B. Rawlings, and M. Diehl. „CasADi – A software framework for nonlinear optimization and optimal control“. In: *Mathematical Programming Computation* (2018) (cit. on pp. 47, 62, 82, 102).

[AR88] D. W. Agar and W. Ruppel. „Multifunktionale Reaktoren für die heterogene Katalyse“. In: *Chemie Ingenieur Technik - CIT* 60.10 (1988), pp. 731–741 (cit. on pp. 3, 4).

[AR91] P. Arce and D. Ramkrishna. „Pattern formation in catalytic reactors: The role of fluid mixing“. In: *AIChE Journal* 37.1 (1991), pp. 98–110 (cit. on pp. 36, 37, 51).

[Ari69] R. Aris. *Elementary chemical reactor analysis*. Prentice-Hall international series in the physical and chemical engineering sciences. Englewood Cliffs: Prentice-Hall, 1969 (cit. on p. 3).

[AS90] J. Adaje and M. Sheintuch. „Comparison of multiplicity patterns of a single catalytic pellet and a fixed catalytic bed for ethylene oxidation“. In: *Chemical Engineering Science* 45.5 (1990), pp. 1331–1342 (cit. on p. 37).

[AWB07] R. Agrawal, D. H. West, and V. Balakotaiah. „Modeling and analysis of local hot spot formation in down-flow adiabatic packed-bed reactors“. In: *Chemical Engineering Science* 62.18-20 (2007), pp. 4926–4943 (cit. on pp. 37, 39).

[BA56] O. Bilous and N. R. Amundson. „Chemical reactor stability and sensitivity: II. Effect of parameters on sensitivity of empty tubular reactors“. In: *AIChE Journal* 2.1 (1956), pp. 117–126 (cit. on pp. 6, 42).

[Bad+11] A. Bader, S. Bauersfeld, C. Brunhuber, R. Pardemann, and B. Meyer. „Modelling of a chemical reactor for simulation of a methanisation plant“. In: *The 8th International Modelica Conference, Technical Univeristy, Dresden, Germany*. Linköping Electronic Conference Proceedings. Linköping University Electronic Press, 2011, pp. 572–578 (cit. on p. 25).

[Bak+09] M. Bakošová, D. Puna, P. Dostál, and J. Závacká. „Robust stabilization of a chemical reactor“. In: *Chemical Papers* 63.5 (2009), p. 3042 (cit. on p. 30).

[Bak+12] M. Bakošová, A. Mészáros, J. J. Klemeš, and J. Oravec. „Robust and optimal control approach for exothermic reactor stabilization“. In: *Theoretical Foundations of Chemical Engineering* 46.6 (2012), pp. 740–746 (cit. on p. 30).

[Bar+18] J. Bard, S. Becker, M. von Bonin, T. Fischer, H. Ganal, I. Ganal, N. Gerhardt, C. Hoffmann, B. Krautkremer, S. Pogacar, M. Puchta, D. Schmidt, and R. Schröer. *Energy transition barometer 2018*. Ed. by Fraunhofer IEE. Kassel, 2018 (cit. on p. 1).

[Bar01] C. H. Bartholomew. „Mechanisms of catalyst deactivation“. In: *Applied Catalysis A: General* 212.1-2 (2001), pp. 17–60 (cit. on p. 23).

[Bia+13] E. Bianchi, T. Heidig, C. G. Visconti, G. Groppi, H. Freund, and E. Tronconi. „Heat transfer properties of metal foam supports for structured catalysts: Wall heat transfer coefficient“. In: *Catalysis Today* 216 (2013), pp. 121–134 (cit. on pp. 26, 67).

[Bie07] L. T. Biegler. „An overview of simultaneous strategies for dynamic optimization“. In: *Chemical Engineering and Processing: Process Intensification* 46.11 (2007), pp. 1043–1053 (cit. on p. 81).

[Bis65] K. B. Bischoff. „Effectiveness factors for general reaction rate forms“. In: *AIChE Journal* 11.2 (1965), pp. 351–355 (cit. on p. 60).

[BK19] A. Bazzanella and D. Krämer. *Technologies for sustainability and climate protection – Chemical processes and use of* CO_2. Frankfurt am Main: DECHEMA, Gesellschaft für Chemische Technik und Biotechnologie e.V, 2019 (cit. on p. 2).

[BKN95] V. Balakotaiah, D. Kodra, and D. Nguyen. „Runaway limits for homogeneous and catalytic reactors“. In: *Chemical Engineering Science* 50.7 (1995), pp. 1149–1171 (cit. on p. 54).

[BL83] V. Balakotaiah and D. Luss. „Multiplicity features of reacting systems“. In: *Chemical Engineering Science* 38.10 (1983), pp. 1709–1721 (cit. on p. 36).

[BMP17] M. Belimov, D. Metzger, and P. Pfeifer. „On the temperature control in a microstructured packed bed reactor for methanation of CO/CO_2 mixtures“. In: *AIChE Journal* 63.1 (2017), pp. 120–129 (cit. on pp. 26, 67).

[Bon+18] D. Bongartz, L. Doré, K. Eichler, T. Grube, B. Heuser, L. E. Hombach, M. Robinius, S. Pischinger, D. Stolten, G. Walther, and A. Mitsos. „Comparison of light-duty transportation fuels produced from renewable hydrogen and green carbon dioxide“. In: *Applied Energy* 231 (2018), pp. 757–767 (cit. on p. 1).

[Bre+17] J. Bremer, P. Goyal, L. Feng, P. Benner, and K. Sundmacher. „POD-DEIM for efficient reduction of a dynamic 2D catalytic reactor model“. In: *Computers & Chemical Engineering* 106 (2017), pp. 777–784 (cit. on pp. 13, 19).

[Bri+05] J. Brightling, P. Farnell, C. Foster, and F. Beyer. „Steam reforming - 50 years of development and the challenges for the next 50 years“. In: *Ammonia Plant Safety and Related Facilities* 46 (2005) (cit. on p. 23).

[Bro+07] K. P. Brooks, J. Hu, H. Zhu, and R. J. Kee. „Methanation of carbon dioxide by hydrogen reduction using the Sabatier process in microchannel reactors“. In: *Chemical Engineering Science* 62.4 (2007), pp. 1161–1170 (cit. on pp. 26, 67).

[Bro+18] T. W. Brown, T. Bischof-Niemz, K. Blok, C. Breyer, H. Lund, and B. V. Mathiesen. „Response to ‘Burden of proof: A comprehensive review of the feasibility of 100% renewable-electricity systems’“. In: *Renewable and Sustainable Energy Reviews* 92 (2018), pp. 834–847 (cit. on p. 1).

[BRS17] J. Bremer, K. H. G. Rätze, and K. Sundmacher. „CO_2 methanation: Optimal start-up control of a fixed-bed reactor for power-to-gas applications“. In: *AIChE Journal* 63.1 (2017), pp. 23–31 (cit. on pp. ix, 13, 19, 27, 79).

[Bru+20] B. Bruns, F. Herrmann, M. Polyakova, M. Grünewald, and J. Riese. „A systematic approach to define flexibility in chemical engineering“. In: *Journal of Advanced Manufacturing and Processing* (2020) (cit. on pp. 2, 29).

[BS10] S. A. Bostandzhiyan and K. G. Shkadinskii. „Multiple steady states and transitional regimes in a cylindrical fixed-bed catalytic reactor“. In: *Theoretical Foundations of Chemical Engineering* 44.2 (2010), pp. 119–125 (cit. on pp. 32, 37).

[BS16] S. M. Biollaz and T. J. Schildhauer, eds. *Synthetic natural gas from coal, dry biomass, and power-to-gas applications*. Hoboken, New Jersey: John Wiley & Sons Inc, 2016 (cit. on pp. 17, 25).

[BS19] J. Bremer and K. Sundmacher. „Operation range extension via hot-spot control for catalytic CO_2 methanation reactors“. In: *Reaction Chemistry & Engineering* 4 (2019), pp. 1019–1037 (cit. on pp. ix, 13, 49, 63).

[BS21] J. Bremer and K. Sundmacher. „Novel multiplicity and stability criteria for non-isothermal fixed-bed reactors“. In: *Frontiers in Energy Research* 8 (2021), p. 549298 (cit. on p. ix).

[BS78a] R. Bauer and E. U. Schlünder. „Effective radial thermal conductivity of packing in gas flow. Part I. Convective transport coefficient“. In: *International Chemical Engineering* 18.2 (1978), pp. 181–188 (cit. on p. 58).

[BS78b] R. Bauer and E. U. Schlünder. „Effective radial thermal conductivity of packing in gas flow. Part II. Thermal conductivity of the packing fraction without gas flow“. In: *International Chemical Engineering* 18.2 (1978), pp. 189–204 (cit. on p. 128).

[BSM08] G. A. Bunimovich, P. L. Silverston, and J. Š. Matros. „Unsteady-state reactor operation“. In: *Handbook of Heterogeneous Catalysis*. Ed. by G. Ertl, H. Knözinger, F. Schüth, and J. Weitkamp. Weinheim, Germany: Wiley-VCH Verlag GmbH & Co. KGaA, 2008 (cit. on pp. 3, 4, 30).

[BU14] A. Bansode and A. Urakawa. „Towards full one-pass conversion of carbon dioxide to methanol and methanol-derived products“. In: *Journal of Catalysis* 309 (2014), pp. 66–70 (cit. on p. 17).

[BW14] V. Balakotaiah and D. H. West. „Thermal effects and bifurcations in gas phase catalytic partial oxidations“. In: *Current Opinion in Chemical Engineering* 5 (2014), pp. 68–77 (cit. on p. 30).

[Car87] J. J. Carberry, ed. *Chemical reaction and reactor engineering*. Vol. 26. Chemical industries. New York: Dekker, 1987 (cit. on p. 69).

[CL89] Y. C. Chen and D. Luss. „Wrong-way behavior of packed-bed reactors: Influence of interphase transport“. In: *AIChE Journal* 35.7 (1989), pp. 1148–1156 (cit. on p. 6).

[DA20] C. Drechsler and D. W. Agar. „Intensified integrated direct air capture - power-to-gas process based on H_2O and CO_2 from ambient air“. In: *Applied Energy* 273 (2020), p. 115076 (cit. on p. 18).

[DBB17] J. Ducamp, A. Bengaouer, and P. Baurens. „Modelling and experimental validation of a CO_2 methanation annular cooled fixed-bed reactor exchanger“. In: *The Canadian Journal of Chemical Engineering* 95.2 (2017), pp. 241–252 (cit. on pp. 59, 67).

[DBW99] S. M. S. Dommeti, V. Balakotaiah, and D. H. West. „Analytical criteria for validity of pseudohomogeneous models of packed-bed catalytic reactors“. In: *Industrial & Engineering Chemistry Research* 38.3 (1999), pp. 767–777 (cit. on p. 37).

[DC79] A. G. Dixon and D. L. Cresswell. „Theoretical prediction of effective heat transfer parameters in packed beds“. In: *AIChE Journal* 25.4 (1979), pp. 663–676 (cit. on p. 58).

[Del06] J. M. P. Q. Delgado. „A critical review of dispersion in packed beds“. In: *Heat and Mass Transfer* 42.4 (2006), pp. 279–310 (cit. on p. 58).

[DJS80] G. R. Dissinger, S. H. Johnson, and F. P. Stein. „Dynamic simulation of methanation reactors, interstage heat exchangers, and controllers“. In: *Chemical Engineering Communications* 4.4-5 (1980), pp. 577–591 (cit. on p. 5).

[Doc18] D. Dochain. „Analysis of the multiplicity of steady-state profiles of two tubular reactor models“. In: *Computers & Chemical Engineering* 114 (2018), pp. 318–324 (cit. on pp. 37, 51).

[DPY92] D. Dochain, M. Perrier, and B. E. Ydstie. „Asymptotic observers for stirred tank reactors“. In: *Chemical Engineering Science* 47.15-16 (1992), pp. 4167–4177 (cit. on p. 30).

[Dra+08] A. K. Dramé, C. Lobry, J. Harmand, A. Rapaport, and F. Mazenc. „Multiple stable equilibrium profiles in tubular bioreactors“. In: *Mathematical and Computer Modelling* 48.11-12 (2008), pp. 1840–1853 (cit. on p. 37).

[EE93] S. Elnashaie and S. S. Elshishini. *Modelling, simulation and optimization of industrial fixed bed catalytic reactors*. Vol. 7. Topics in Chemical Engineering. Philadelphia, Pa.: Gordon and Breach, 1993 (cit. on p. 36).

[Eig00] G. Eigenberger. „Fixed-bed reactors“. In: *Ullmann's Encyclopedia of Industrial Chemistry*. Wiley-VCH Verlag GmbH & Co. KGaA, 2000 (cit. on p. 69).

[Eig08] G. Eigenberger. „Catalytic fixed-bed reactors“. In: *Handbook of Heterogeneous Catalysis*. Ed. by G. Ertl, H. Knözinger, F. Schüth, and J. Weitkamp. Weinheim, Germany: Wiley-VCH Verlag GmbH & Co. KGaA, 2008 (cit. on p. 3).

[Eig72a] G. Eigenberger. „On the dynamic behavior of the catalytic fixed-bed reactor in the region of multiple steady states—I. The influence of heat conduction in two phase models“. In: *Chemical Engineering Science* 27.11 (1972), pp. 1909–1915 (cit. on pp. 4, 36, 37, 49, 58, 109).

[Eig72b] G. Eigenberger. „On the dynamic behavior of the catalytic fixed-bed reactor in the region of multiple steady states—II. The influence of the boundary conditions in the catalyst phase“. In: *Chemical Engineering Science* 27.11 (1972), pp. 1917–1924 (cit. on pp. 37, 38, 49).

[Eig83] G. Eigenberger. „Dynamik und Stabilität verfahrenstechnischer Prozesse“. In: *Chemie Ingenieur Technik - CIT* 55.7 (1983), pp. 503–515 (cit. on pp. 33, 36).

[EN88] G. Eigenberger and U. Nieken. „Catalytic combustion with periodic flow reversal“. In: *Chemical Engineering Science* 43.8 (1988), pp. 2109–2115 (cit. on p. 4).

[ER00] G. Eigenberger and W. Ruppel. „Catalytic fixed-bed reactors“. In: *Ullmann's Encyclopedia of Industrial Chemistry*. Wiley-VCH Verlag GmbH & Co. KGaA, 2000 (cit. on p. 3).

[ER68] M. F. Edwards and J. F. Richardson. „Gas dispersion in packed beds“. In: *Chemical Engineering Science* 23.2 (1968), pp. 109–123 (cit. on p. 58).

[ER91] J. W. Eaton and J. B. Rawlings. „Model predictive control of chemical processes“. In: *1991 American Control Conference*. IEEE, 1991, pp. 1790–1795 (cit. on p. 10).

[ERS15] A. El-Sibai, L. Rihko-Struckmann, and K. Sundmacher. „Synthetic methane from CO_2: Dynamic optimization of the Sabatier process for power-to-gas applications“. In: *12th International Symposium on Process Systems Engineering (PSE) & 25th European Symposium on Computer Aided Process Engineering (ESCAPE)*. 2015, pp. 1157–1162 (cit. on p. 18).

[ERS17] A. El Sibai, L. K. Rihko Struckmann, and K. Sundmacher. „Model-based optimal sabatier reactor design for power-to-gas applications“. In: *Energy Technology* 5.6 (2017), pp. 911–921 (cit. on p. 27).

[Ert+08] G. Ertl, H. Knzinger, F. Schth, and J. Weitkamp, eds. *Handbook of heterogeneous catalysis*. Weinheim, Germany: Wiley-VCH Verlag GmbH & Co. KGaA, 2008 (cit. on p. 3).

[ES01] B. Eisfeld and K. Schnitzlein. „The influence of confining walls on the pressure drop in packed beds“. In: *Chemical Engineering Science* 56.14 (2001), pp. 4321–4329 (cit. on p. 127).

[ES89] G. Eigenberger and H. Schuler. „Reactor stability and safe reaction engineering“. In: *International Chemical Engineering* 29 (1989) (cit. on pp. 7, 29).

[Fac+18] A. Fache, F. Marias, V. Guerré, and S. Palmade. „Optimization of fixed-bed methanation reactors: Safe and efficient operation under transient and steady-state conditions“. In: *Chemical Engineering Science* 192 (2018), pp. 1124–1137 (cit. on p. 19).

[FF20] K. L. Fischer and H. Freund. „On the optimal design of load flexible fixed bed reactors: Integration of dynamics into the design problem“. In: *Chemical Engineering Journal* (2020), p. 124722 (cit. on p. 2).

[FKD15] T. Fischedick, M. Kind, and B. Dietrich. „High temperature two-phase thermal conductivity of ceramic sponges with stagnant fluid – Experimental results and correlation including thermal radiation“. In: *International Journal of Thermal Sciences* 96 (2015), pp. 1–11 (cit. on p. 57).

[FM98] M. Froggatt and J. Moore. „High-spatial-resolution distributed strain measurement in optical fiber with rayleigh scatter“. In: *Applied optics* 37.10 (1998), pp. 1735–1740 (cit. on p. 94).

[Fre08] H. Freund. *Ortsaufgelöste Simulation von Transportprozessen in durchströmten Festbetten: Zugl.: Erlangen-Nürnberg, Univ., Diss., 2007*. Berichte aus der Verfahrenstechnik. Aachen: Shaker, 2008 (cit. on p. 58).

[FSG66] E. N. Fuller, P. D. Schettler, and J. C. Giddins. „A new method for prediction of binary gas-phase diffusion coefficients“. In: *Industrial And Engineering Chemistry* 58.5 (1966), pp. 18–27 (cit. on p. 127).

[GA13] J. H. Ghouse and T. A. Adams. „A multi-scale dynamic two-dimensional heterogeneous model for catalytic steam methane reforming reactors“. In: *International Journal of Hydrogen Energy* 38.24 (2013), pp. 9984–9999 (cit. on p. 31).

[Gao+12] J. Gao, Y. Wang, Y. Ping, D. Hu, G. Xu, F. Gu, and F. Su. „A thermodynamic analysis of methanation reactions of carbon oxides for the production of synthetic natural gas“. In: *RSC Advances* 2.6 (2012), pp. 2358–2368 (cit. on p. 21).

[GCG14] I. E. Grossmann, B. A. Calfa, and P. Garcia-Herreros. „Evolution of concepts and models for quantifying resiliency and flexibility of chemical processes“. In: *Computers & Chemical Engineering* 70 (2014), pp. 22–34 (cit. on p. 29).

[GH61] E. D. Gilles and H. Hofmann. „Bemerkung zu der Arbeit: An analysis of chemical reactor stability and control“. In: *Chemical Engineering Science* 15.3-4 (1961), pp. 328–331 (cit. on p. 42).

[Gil68] E. D. Gilles. „Das dynamische Verhalten chemischer Reaktoren. Eine Übersicht“. In: *Chemie Ingenieur Technik - CIT* 40.9-10 (1968), pp. 469–477 (cit. on p. 3).

[Gil77] E. D. Gilles. „Dynamisches Verhalten von Festbettreaktoren“. In: *Chemie Ingenieur Technik - CIT* 49.2 (1977), pp. 142–149 (cit. on pp. 4, 5, 36, 69).

[GM83] I. E. Grossmann and M. Morari. *Operability, resiliency, and flexibility: Process design objectives for a changing world*. 1983 (cit. on p. 29).

[Gni10] V. Gnielinski. „G2 Heat transfer in concentric annular and parallel plate ducts“. In: *VDI Heat Atlas*. Berlin, Heidelberg: Springer Berlin Heidelberg, 2010, pp. 701–708 (cit. on p. 129).

[Goe+12] A. Goeppert, M. Czaun, G. K. Surya Prakash, and G. A. Olah. „Air as the renewable carbon source of the future: An overview of CO_2 capture from the atmosphere“. In: *Energy & Environmental Science* 5.7 (2012), p. 7833 (cit. on p. 18).

[Göt+16] M. Götz, J. Lefebvre, F. Mörs, A. McDaniel Koch, F. Graf, S. Bajohr, R. Reimert, and T. Kolb. „Renewable power-to-gas: A technological and economic review“. In: *Renewable Energy* 85 (2016), pp. 1371–1390 (cit. on pp. 17–19, 26).

[GR19] G. Glenk and S. Reichelstein. „Economics of converting renewable power to hydrogen“. In: *Nature Energy* 4.3 (2019), pp. 216–222 (cit. on p. 1).

[Gru+18] M. Gruber, P. Weinbrecht, L. Biffar, S. Harth, D. Trimis, J. Brabandt, O. Posdziech, and R. Blumentritt. „Power-to-gas through thermal integration of high-temperature steam electrolysis and carbon dioxide methanation - Experimental results“. In: *Fuel Processing Technology* 181 (2018), pp. 61–74 (cit. on pp. 25, 27).

[Güt13] R. Güttel. „Study of unsteady-state operation of methanation by modeling and simulation“. In: *Chemical Engineering & Technology* 36.10 (2013), pp. 1675–1682 (cit. on pp. 10, 19, 30).

[HÅH09] S. Haugwitz, J. Åkesson, and P. Hagander. „Dynamic start-up optimization of a plate reactor with uncertainties“. In: *Journal of Process Control* 19.4 (2009), pp. 686–700 (cit. on p. 79).

[Hay17] W. M. Haynes, ed. *CRC handbook of chemistry and physics: A ready-reference book of chemical and physical data*. 97th edition. Boca Raton, London, and New York: CRC Press, 2017 (cit. on p. 20).

[HFH71] D. R. Hahn, L. T. Fan, and C. L. Hwang. „Optimal startup control of a jacketed tubular reactor“. In: *AIChE Journal* 17.6 (1971), pp. 1394–1401 (cit. on p. 79).

[Hin+05] A. C. Hindmarsh, P. N. Brown, K. E. Grant, S. L. Lee, R. Serban, D. E. Shumaker, and C. S. Woodward. „SUNDIALS: Suite of nonlinear and differential/algebraic equation solvers“. In: *ACM Transactions on Mathematical Software (TOMS)* 31.3 (2005), pp. 363–396 (cit. on pp. 62, 82).

[HL67] F. J. M. Horn and R. C. Lin. „Periodic processes: A variational approach“. In: *Industrial & Engineering Chemistry Process Design and Development* 6.1 (1967), pp. 21–30 (cit. on pp. 3, 4, 30).

[HL85] M. P. Harold and D. Luss. „An experimental study of steady-state multiplicity features of two parallel catalytic reactions“. In: *Chemical Engineering Science* 40.1 (1985), pp. 39–52 (cit. on p. 37).

[HM66] V. Hlaváček and M. Marek. „Axialer Stoff- und Wärmetransport im adiabatischen Rohrreaktor - II. Numerische Untersuchung - Ablauf einer einfachen Reaktion bezw. einer Folgereaktion“. In: *Chemical Engineering Science* 21.6-7 (1966), pp. 501–513 (cit. on p. 53).

[HMR81] B. Höhlein, R. Menzer, and J. Range. „High temperature methanation in the long-distance nuclear energy transport system“. In: *Applied Catalysis* 1.3-4 (1981), pp. 125–139 (cit. on pp. 24, 25).

[Höh+85] B. Höhlein, R. Menzer, H. Schiebahn, M. Vorwerk, H. Kiilerich-Hansen, and A. Skov. *Zusammenfassender Bericht zum Projekt Nukleare Fernenergie (NFE): Projekt Nukleare Fernenergie Jül-Spez-303*. Ed. by R. C. Jülich. 1985 (cit. on pp. 25, 27).

[HP81] R. F. Heinemann and A. B. Poore. „Multiplicity, stability, and oscillatory dynamics of the tubular reactor“. In: *Chemical Engineering Science* 36.8 (1981), pp. 1411–1419 (cit. on pp. 5, 30, 37, 38, 47).

[HP82] R. F. Heinemann and A. B. Poore. „The effect of activation energy on tubular reactor multiplicity“. In: *Chemical Engineering Science* 37.1 (1982), pp. 128–131 (cit. on pp. 36–38).

[HS97] U. Hoffmann and K. Sundmacher. „Multifunktionale Reaktoren“. In: *Chemie Ingenieur Technik - CIT* 69.5 (1997), pp. 613–622 (cit. on p. 3).

[HSL07] HSL. *A collection of Fortran codes for large-scale scientific computation*. 2007 (cit. on pp. 82, 102).

[Hud+13] R. R. Hudgins, P. L. Silveston, A. Renken, and Y. S. Matros. „Introduction“. In: *Periodic operation of reactors*. Ed. by P. L. Silveston and R. R. Hudgins. IChemE Advancing chemical engineering worldwide. Amsterdam and Waltham, Mass.: Elsevier and Butterworth-Heinemann, 2013, pp. 1–22 (cit. on p. 30).

[Hwa+12] S. Hwang, J. Lee, U. G. Hong, J. C. Jung, D. J. Koh, H. Lim, C. Byun, and I. K. Song. „Hydrogenation of carbon monoxide to methane over mesoporous nickel-M-alumina (M=Fe, Ni, Co, Ce, and La) xerogel catalysts“. In: *Journal of Industrial and Engineering Chemistry* 18.1 (2012), pp. 243–248 (cit. on pp. 21, 23).

[IES16] M. Iglesias González, H. Eilers, and G. Schaub. „Flexible operation of fixed-bed reactors for a catalytic fuel synthesis-CO_2 hydrogenation as example reaction“. In: *Energy Technology* 4.1 (2016), pp. 90–103 (cit. on p. 12).

[Jar+01] A. Jaree, H. M. Budman, R. R. Hudgins, P. L. Silveston, V. Yakhnin, and M. Menzinger. „Temperature excursions in reactors packed with segregated layers of catalyst and inert solids“. In: *Chemical Engineering Science* 56.20 (2001), pp. 5719–5726 (cit. on pp. 7, 39).

[Jør86] S. B. Jørgensen. „Fixed bed reactor dynamics and control - A review“. In: *IFAC Proceedings Volumes* 19.15 (1986), pp. 11–24 (cit. on pp. 6, 7).

[JR82] K. F. Jensen and W. Ray. „The bifurcation behavior of tubular reactors“. In: *Chemical Engineering Science* 37.2 (1982), pp. 199–222 (cit. on pp. 30, 37–39, 47, 51, 54, 73).

[Jür+15] L. Jürgensen, E. A. Ehimen, J. Born, and J. B. Holm-Nielsen. „Dynamic biogas upgrading based on the Sabatier process: Thermodynamic and dynamic process simulation“. In: *Bioresource technology* 178 (2015), pp. 323–329 (cit. on pp. 11, 21, 23).

[Kal+17] K. F. Kalz, R. Kraehnert, M. Dvoyashkin, R. Dittmeyer, R. Gläser, U. Krewer, K. Reuter, and J.-D. Grunwaldt. „Future challenges in heterogeneous catalysis: Understanding catalysts under dynamic reaction conditions“. In: *ChemCatChem* 9.1 (2017), pp. 17–29 (cit. on pp. 3, 72).

[KCG03] R. J. Kee, M. E. Coltrin, and P. Glarborg. *Chemically reacting flow: Theory and practice*. Hoboken, NJ: Wiley-Interscience, 2003 (cit. on p. 127).

[Kei09] D. W. Keith. „Why capture CO_2 from the atmosphere?“ In: *Science (New York, N.Y.)* 325.5948 (2009), pp. 1654–1655 (cit. on p. 18).

[KFE00] G. Kolios, J. Frauhammer, and G. Eigenberger. „Autothermal fixed-bed reactor concepts“. In: *Chemical Engineering Science* 55.24 (2000), pp. 5945–5967 (cit. on p. 3).

[Kie17] L. Kiewidt. „Solid sponges as support for heterogeneous catalysts in gas-phase reactions“. PhD thesis. Bremen: Diss., Univ. Bremen, 2017 (cit. on pp. 21, 26, 57, 60).

[KK18] E. I. Koytsoumpa and S. Karellas. „Equilibrium and kinetic aspects for catalytic methanation focusing on CO_2 derived substitute natural gas (SNG)“. In: *Renewable and Sustainable Energy Reviews* 94 (2018), pp. 536–550 (cit. on p. 25).

[KL77] S. Kimura and O. Levenspiel. „Temperature excursions in adiabatic packed bed reactors“. In: *Industrial & Engineering Chemistry Process Design and Development* 16.1 (1977), pp. 145–148 (cit. on p. 54).

[KM83] M. Kubíček and M. Marek. *Computational methods in bifurcation theory and dissipative structures*. Springer Series Computational Physics. Berlin and Heidelberg: Springer, 1983 (cit. on p. 47).

[Kop10] J. Kopyscinski. „Production of synthetic natural gas in a fluidized bed reactor“. PhD thesis. ETH Zürich, 2010 (cit. on p. 25).

[Kre+06] S. T. Kreger, D. K. Gifford, M. E. Froggatt, B. J. Soller, and M. S. Wolfe. „High resolution distributed strain or temperature measurements in single- and multi-mode fiber using swept-wavelength interferometry“. In: *Optical Fiber Sensors*. Washington, D.C.: OSA, 2006, ThE42 (cit. on p. 94).

[Kre+19] B. Kreitz, J. Friedland, R. Güttel, G. D. Wehinger, and T. Turek. „Dynamic methanation of CO_2 – Effect of concentration forcing“. In: *Chemie Ingenieur Technik - CIT* 91.5 (2019), pp. 576–582 (cit. on p. 19).

[KSB10] J. Kopyscinski, T. J. Schildhauer, and S. M. Biollaz. „Production of synthetic natural gas (SNG) from coal and dry biomass – A technology review from 1950 to 2009“. In: *Fuel* 89.8 (2010), pp. 1763–1783 (cit. on pp. 18, 25).

[KSH16] F. Koschany, D. Schlereth, and O. Hinrichsen. „On the kinetics of the methanation of carbon dioxide on coprecipitated NiAl(O)x“. In: *Applied Catalysis B: Environmental* 181 (2016), pp. 504–516 (cit. on pp. 20, 21, 26, 56, 57, 64, 91–93, 107, 110, 130, 132).

[KT15] L. Kiewidt and J. Thöming. „Predicting optimal temperature profiles in single-stage fixed-bed reactors for CO_2-methanation“. In: *Chemical Engineering Science* 132 (2015), pp. 59–71 (cit. on pp. 27, 56, 60).

[KV19] A. Kummer and T. Varga. „Completion of thermal runaway criteria: Two new criteria to define runaway limits“. In: *Chemical Engineering Science* 196 (2019), pp. 277–290 (cit. on pp. 43, 54).

[KV80] O. Kalthoff and D. Vortmeyer. „Ignition/extinction phenomena in a wall cooled fixed bed reactor“. In: *Chemical Engineering Science* 35.7 (1980), pp. 1637–1643 (cit. on pp. 37, 69).

[KWT18] B. Kreitz, G. D. Wehinger, and T. Turek. „Dynamic simulation of the CO_2 methanation in a micro-structured fixed-bed reactor“. In: *Chemical Engineering Science* (2018) (cit. on pp. 19, 30).

[LA62] S.-L. Liu and N. R. Amundson. „Stability of adiabatic packed bed reactors. An elementary treatment“. In: *Industrial & Engineering Chemistry Fundamentals* 1.3 (1962), pp. 200–208 (cit. on pp. 36, 37).

[LA63] S.-L. Liu and N. R. Amundson. „Stability of adiabatic packed-bed reactors. Effect of axial mixing“. In: *Industrial & Engineering Chemistry Fundamentals* 2.3 (1963), pp. 183–189 (cit. on p. 37).

[Lef+15] J. Lefebvre, M. Götz, S. Bajohr, R. Reimert, and T. Kolb. „Improvement of three-phase methanation reactor performance for steady-state and transient operation“. In: *Fuel Processing Technology* 132 (2015), pp. 83–90 (cit. on p. 11).

[Leh+14] M. Lehner, R. Tichler, H. Steinmüller, and M. Koppe. *Power-to-gas: Technology and business models*. Cham: Springer International Publishing, 2014 (cit. on pp. 17, 19).

[Lev99] O. Levenspiel. *Chemical reaction engineering*. 3. ed. Hoboken, NJ: Wiley, 1999 (cit. on pp. 32, 38).

[LM97] P. Linstrom and W. G. Mallard. *NIST chemistry webBook, NIST standard reference database number 69*. 1997 (cit. on p. 20).

[LMV87] C. K. Lee, M. Morbidelli, and A. Varma. „Steady state multiplicity behavior of an isothermal axial dispersion fixed-bed reactor with nonuniformly active catalyst“. In: *Chemical Engineering Science* 42.7 (1987), pp. 1595–1608 (cit. on pp. 36, 37).

[LS05] D. Luss and M. Sheintuch. „Spatiotemporal patterns in catalytic systems“. In: *Catalysis Today* 105.2 (2005), pp. 254–274 (cit. on p. 9).

[Lun74] P. J. Lunde. „Modeling, simulation, and operation of a Sabatier reactor“. In: *Industrial & Engineering Chemistry Process Design and Development* 13.3 (1974), pp. 226–233 (cit. on p. 5).

[LYZ13] X. Li, B. Yang, and Y. Zhang. „Dynamics and control study on the low temperature methanation reactor with mass and heat recycle“. In: *Journal of Process Control* 23.10 (2013), pp. 1360–1370 (cit. on p. 11).

[MAC09] F. S. Mederos, J. Ancheyta, and J. Chen. „Review on criteria to ensure ideal behaviors in trickle-bed reactors“. In: *Applied Catalysis A: General* 355.1-2 (2009), pp. 1–19 (cit. on pp. 53, 58, 59).

[Mat+16] S. Matthischke, R. Krüger, S. Rönsch, and R. Güttel. „Unsteady-state methanation of carbon dioxide in a fixed-bed recycle reactor — Experimental results for transient flow rate ramps“. In: *Fuel Processing Technology* 153 (2016), pp. 87–93 (cit. on pp. 13, 19, 27, 67, 68).

[Mat89] J. Š. Matros. *Catalytic processes under unsteady-state conditions*. Vol. 43. Studies in surface science and catalysis. Amsterdam: Elsevier, 1989 (cit. on pp. 3, 4).

[MB96] J. Š. Matros and G. A. Bunimovich. „Reverse-flow operation in fixed bed catalytic reactors“. In: *Catalysis Reviews* 38.1 (1996), pp. 1–68 (cit. on p. 30).

[Mea76] D. E. Mears. „On criteria for axial dispersion in nonisothermal packed-bed catalytic reactors“. In: *Industrial & Engineering Chemistry Fundamentals* 15.1 (1976), pp. 20–23 (cit. on pp. 32, 53, 113).

[Mia+16] B. Miao, S. S. K. Ma, X. Wang, H. Su, and S. H. Chan. „Catalysis mechanisms of CO_2 and CO methanation“. In: *Catalysis Science & Technology* 6.12 (2016), pp. 4048–4058 (cit. on p. 24).

[MKJ16] M. Martinez Molina, C. Kern, and A. Jess. „Catalytic hydrogenation of carbon dioxide to methane in wall-cooled fixed-bed reactors“. In: *Chemical Engineering & Technology* 39.12 (2016), pp. 2404–2415 (cit. on p. 67).

[ML03] B. Marwaha and D. Luss. „Hot zones formation in packed bed reactors“. In: *Chemical Engineering Science* 58.3-6 (2003), pp. 733–738 (cit. on pp. 8, 39).

[MMP08] A. Marković, A.-S. Morgenstern, and M. Petkovska. „Evaluation of the potential of periodically operated reactors based on the second order frequency response function“. In: *Chemical Engineering Research and Design* 86.7 (2008), pp. 682–691 (cit. on pp. 4, 30).

[MMZ19] E. Moioli, R. Mutschler, and A. Züttel. „Renewable energy storage via CO_2 and H_2 conversion to methane and methanol: Assessment for small scale applications“. In: *Renewable and Sustainable Energy Reviews* 107 (2019), pp. 497–506 (cit. on pp. 1, 17).

[Moh+01] K. Mohl, A. Kienle, K. Sundmacher, and E. Gilles. „A theoretical study of kinetic instabilities in catalytic distillation processes: Influence of transport limitations inside the catalyst“. In: *Chemical Engineering Science* 56.18 (2001), pp. 5239–5254 (cit. on p. 36).

[Moh+12] F. Mohseni, M. Magnusson, M. Görling, and P. Alvfors. „Biogas from renewable electricity – Increasing a climate neutral fuel supply“. In: *Applied Energy* 90.1 (2012), pp. 11–16 (cit. on p. 21).

[Mor+10] J. A. Moreno, J. Alvarez, E. Rocha-Cózatl, and J. Diaz-Salgado. „Super-twisting observer-based output feedback control of a class of continuous exothermic chemical reactors“. In: *IFAC Proceedings Volumes* 43.5 (2010), pp. 727–732 (cit. on p. 30).

[MRG18] S. Matthischke, S. Roensch, and R. Güttel. „Start-up time and load range for the methanation of carbon dioxide in a fixed-bed recycle reactor“. In: *Industrial & Engineering Chemistry Research* (2018) (cit. on pp. 13, 19, 59).

[MSL81] P. S. Mehta, W. N. Sams, and D. Luss. „Wrong-way behavior of packed-bed reactors: 1. The pseudo-homogeneous model“. In: *AIChE Journal* 27.2 (1981), pp. 234–246 (cit. on p. 6).

[MSV86] M. Morbidelli, A. Servida, and A. Varma. „Optimal catalyst activity profiles in pellets. 4. Analytical evaluation of the isothermal fixed-bed reactor“. In: *Industrial & Engineering Chemistry Fundamentals* 25.3 (1986), pp. 307–313 (cit. on pp. 36, 37).

[Muh+94] M. Muhler, E. Trnqvist, L. P. Nielsen, B. S. Clausen, and H. Topse. „On the role of adsorbed atomic oxygen and CO_2 in copper based methanol synthesis catalysts“. In: *Catalysis Letters* 25.1-2 (1994), pp. 1–10 (cit. on p. 17).

[MV82] M. Morbidelli and A. Varma. „Parametric sensitivity and runaway in tubular reactors“. In: *AIChE Journal* 28.5 (1982), pp. 705–713 (cit. on pp. 6, 43, 65).

[NHM98] R. H. Nibbelke, J. Hoebink, and G. B. Marin. „Kinetically induced multiplicity of steady states in integral catalytic reactors“. In: *Chemical Engineering Science* 53.12 (1998), pp. 2195–2210 (cit. on pp. 32, 36–38).

[NK14] P. S. Nashtaee and B. Khoshandam. „Noncatalytic gas-solid reactions in packed bed reactors: A comparison between numerical and approximate solution techniques“. In: *Chemical Engineering Communications* 201.1 (2014), pp. 120–152 (cit. on p. 61).

[NKE94a] U. Nieken, G. Kolios, and G. Eigenberger. „Control of the ignited steady state in autothermal fixed-bed reactors for catalytic combustion“. In: *Chemical Engineering Science* 49.24 (1994), pp. 5507–5518 (cit. on p. 30).

[NKE94b] U. Nieken, G. Kolios, and G. Eigenberger. „Fixed-bed reactors with periodic flow reversal: Experimental results for catalytic combustion“. In: *Catalysis Today* 20.3 (1994), pp. 335–350 (cit. on p. 4).

[NS12] O. Nekhamkina and M. Sheintuch. „Are 3-D models necessary to simulate packed bed reactors? Analysis and 3-D simulations of adiabatic and cooled reactors“. In: *AIChE Journal* 58.11 (2012), pp. 3494–3503 (cit. on pp. 9, 39).

[NWS13] T. Nguyen, L. Wissing, and M. S. Skjøth-Rasmussen. „High temperature methanation: Catalyst considerations“. In: *Catalysis Today* 215 (2013), pp. 233–238 (cit. on p. 23).

[OGR10] E. L. G. Oliveira, C. A. Grande, and A. E. Rodrigues. „Methane steam reforming in large pore catalyst“. In: *Chemical Engineering Science* 65.5 (2010), pp. 1539–1550 (cit. on p. 57).

[PBL89] J. Pita, V. Balakotaiah, and D. Luss. „Thermoflow multiplicity in a packed-bed reactor: Conduction and cooling effects“. In: *AIChE Journal* 35.3 (1989), pp. 373–384 (cit. on pp. 37, 39).

[PCL88] V. Pinjala, Y. C. Chen, and D. Luss. „Wrong-way behavior of packed-bed reactors: II. Impact of thermal dispersion“. In: *AIChE Journal* 34.10 (1988), pp. 1663–1672 (cit. on p. 6).

[PEB01] D. Papadias, L. Edsberg, and P. Björnbom. „Effect of eccentricity and interaction between kinetics and mass transfer on the behaviour of catalytic annular reactors: A comparison between lumped and distributed models“. In: *Chemical Engineering Science* 56.16 (2001), pp. 4863–4878 (cit. on p. 39).

[Pér00] J. Pérez-Ramírez. „The six-flow reactor technology: A review on fast catalyst screening and kinetic studies“. In: *Catalysis Today* 60.1-2 (2000), pp. 93–109 (cit. on pp. 32, 55, 58, 60).

[Pet01] M. Petkovska. „Nonlinear frequency response of nonisothermal adsorption systems“. In: *Nonlinear Dynamics* 26.4 (2001), pp. 351–370 (cit. on p. 4).

[PGC96] V. B. Pai, J. L. Gainer, and G. Carta. „Simulated moving bed chromatographic reactors“. In: *Fundamentals of Adsorption*. Ed. by M. D. LeVan. Vol. 356. The Kluwer International Series in Engineering and Computer Science. Boston, MA: Springer US, 1996, pp. 733–740 (cit. on p. 30).

[PH84] J. Puszyński and V. Hlavacek. „Experimental study of ignition and extinction waves and oscillatory behavior of a tubular nonadiabatic fixed bed reactor for the oxidation of carbon monoxide“. In: *Chemical Engineering Science* 39.4 (1984), pp. 681–692 (cit. on p. 37).

[PPO01] B. E. Poling, J. M. Prausnitz, and J. P. O’Connell. *The properties of gases and liquids*. McGraw-Hill, 2001 (cit. on pp. 128, 131).

[Pre+10] E. Preisegger, F. Flohr, G. Krakat, A. Glück, and D. Hunold. „D4 Properties of industrial heat transfer media“. In: *VDI Heat Atlas*. Berlin, Heidelberg: Springer Berlin Heidelberg, 2010, pp. 419–512 (cit. on p. 129).

[Pus+81] J. Puszyński, D. Šnita, V. Hlaváček, and H. Hofmann. „A Revision of multiplicity and parametric sensitivity concepts in nonisothermal nonadiabatic packed bed chemical reactors“. In: *Chemical Engineering Science* 36.10 (1981), pp. 1605–1609 (cit. on pp. 32, 37, 39, 58).

[PW67] G. Padberg and E. Wicke. „Stabiles und instabiles Verhalten eines adiabatischen Rohrreaktors am Beispiel der katalytischen CO-Oxydation“. In: *Chemical Engineering Science* 22.7 (1967), pp. 1035–1051 (cit. on pp. 4, 33, 37).

[RE13] J. B. Rawlings and J. G. Ekerdt. *Chemical reactor analysis and design fundamentals*. 2nd edition. Madison, Wisconsin: Nob Hill Publishing, 2013 (cit. on p. 69).

[ROD17] S. Rönsch, A. Ortwein, and S. Dietrich. „Start-and-stop operation of fixed-bed methanation reactors - Results from modeling and simulation“. In: *Chemical Engineering & Technology* 40.12 (2017), pp. 2314–2321 (cit. on p. 27).

[Rön+14] S. Rönsch, S. Matthischke, M. Müller, and P. Eichler. „Dynamische Simulation von Reaktoren zur Festbettmethanisierung“. In: *Chemie Ingenieur Technik - CIT* 86.8 (2014), pp. 1198–1204 (cit. on p. 11).

[Rön+16a] S. Rönsch, J. Köchermann, J. Schneider, and S. Matthischke. „Global reaction kinetics of CO and CO_2 methanation for dynamic process modeling“. In: *Chemical Engineering & Technology* 39.2 (2016), pp. 208–218 (cit. on pp. 26, 63).

[Rön+16b] S. Rönsch, J. Schneider, S. Matthischke, M. Schlüter, M. Götz, J. Lefebvre, P. Prabhakaran, and S. Bajohr. „Review on methanation - From fundamentals to current projects“. In: *Fuel* 166 (2016), pp. 276–296 (cit. on pp. 18, 21, 23, 24).

[SA63] R. A. Schmitz and N. R. Amundson. „An analysis of chemical reactor stability and control—VII“. In: *Chemical Engineering Science* 18.7 (1963), pp. 447–456 (cit. on p. 37).

[SB15] A. Sternberg and A. Bardow. „Power-to-what? – Environmental assessment of energy storage systems“. In: *Energy & Environmental Science* 8.2 (2015), pp. 389–400 (cit. on p. 1).

[SB80] D. Sinčić and J. E. Bailey. „Analytical optimization and sensitivity analysis of forced periodic chemical processes“. In: *Chemical Engineering Science* 35.5 (1980), pp. 1153–1161 (cit. on p. 4).

[Sch15] D. Schlereth. „Kinetic and reactor modeling for the methanation of carbon dioxide“. Dissertation. München: Technische Universität München, 2015 (cit. on pp. 26, 67).

[Sch75] R. A. Schmitz. „Multiplicity, stability, and sensitivity of states in chemically reacting systems - A review“. In: *Chemical Reaction Engineering Reviews*. Ed. by H. M. Hulburt. Vol. 148. Advances in Chemistry. Washington, D. C.: American Chemical Society, 1975, pp. 156–211 (cit. on p. 51).

[Sei+18] C. Seidel, A. Jörke, B. Vollbrecht, A. Seidel-Morgenstern, and A. Kienle. „Kinetic modeling of methanol synthesis from renewable resources“. In: *Chemical Engineering Science* 175 (2018), pp. 130–138 (cit. on p. 17).

[SH13] P. L. Silveston and R. R. Hudgins, eds. *Periodic operation of reactors*. 1. ed. IChemE Advancing chemical engineering worldwide. Amsterdam and Waltham, Mass.: Elsevier and Butterworth-Heinemann, 2013 (cit. on p. 4).

[SH14] D. Schlereth and O. Hinrichsen. „A fixed-bed reactor modeling study on the methanation of CO_2“. In: *Chemical Engineering Research and Design* 92.4 (2014), pp. 702–712 (cit. on pp. 56, 59–61, 65).

[She87] M. Sheintuch. „The determination of global solutions from local ones in catalytic systems showing steady-state multiplicity“. In: *Chemical Engineering Science* 42.9 (1987), pp. 2103–2114 (cit. on pp. 33, 35).

[She97] M. Sheintuch. „Dynamics of catalytic reactions and reactors“. In: *Catalysis Today* 36.4 (1997), pp. 461–476 (cit. on pp. 7, 39).

[SHV76] J. Sinkule, V. Hlaváček, and J. Votruba. „Modeling of chemical reactors—XXXI“. In: *Chemical Engineering Science* 31.1 (1976), pp. 31–36 (cit. on p. 37).

[Sil98] P. L. Silveston. *Composition modulation of catalytic reactors*. Vol. 11. Topics in chemical engineering. Amsterdam: Gordon & Breach, 1998 (cit. on pp. 4, 30).

[Sin+76] J. Sinkule, J. Votruba, V. Hlaváček, and H. Hofmann. „Modeling of chemical reactors - XXX Steady-state analysis of combined axial and gas-to-solid heat and mass transfer in a tubular adiabatic reactor“. In: *Chemical Engineering Science* 31.1 (1976), pp. 23–29 (cit. on p. 37).

[SK95] A. Stankiewicz and M. Kuczynski. „An industrial view on the dynamic operation of chemical converters“. In: *Chemical Engineering and Processing: Process Intensification* 34.4 (1995), pp. 367–377 (cit. on pp. 3, 4, 7, 30).

[SMW19] T. Salmi, J.-P. Mikkola, and J. P. Wärmå. *Chemical reaction engineering and reactor technology*. Second edition. Chemical industries. Boca Raton: CRC Press., 2019 (cit. on p. 32).

[SS02] P. Sabatier and J. B. Senderens. „New synthesis of methane“. In: *Comptes Rendus Hebdomadaires des seances de l'Academie des Sciences* 134 (1902), pp. 514–516 (cit. on p. 20).

[SS17] D. Sun and D. S. Simakov. „Thermal management of a Sabatier reactor for CO_2 conversion into CH_4: Simulation-based analysis“. In: *Journal of CO_2 Utilization* 21 (2017), pp. 368–382 (cit. on p. 13).

[Sto+13] D. Stolten, B. Emonts, T. Grube, and M. Weber. „Hydrogen as an enabler for renewable energies“. In: *Transition to Renewable Energy Systems*. Ed. by D. Stolten and V. Scherer. Vol. 28. Weinheim, Germany: Wiley-VCH Verlag GmbH & Co. KGaA, 2013, pp. 195–216 (cit. on p. 17).

[Sud+10] M. Sudiro, A. Bertucco, G. Groppi, and E. Tronconi. „Simulation of a structured catalytic reactor for exothermic methanation reactions producing synthetic natural gas“. In: *20th European Symposium on Computer Aided Process Engineering*. Vol. 28. Computer Aided Chemical Engineering. Elsevier, 2010, pp. 691–696 (cit. on pp. 26, 67).

[sva53] C. svan Heerden. „Autothermic processes“. In: *Industrial & Engineering Chemistry* 45.6 (1953), pp. 1242–1247 (cit. on pp. 35, 42).

[SW91] T. Salmi and J. P. Wärmå. „Modelling of catalytic packed-bed reactors—comparison of different diffusion models“. In: *Computers & Chemical Engineering* 15.10 (1991), pp. 715–727 (cit. on p. 38).

[SWH18] C. Schüler, M. Wolf, and O. Hinrichsen. „Contactless temperature measurements under static and dynamic reaction conditions in a single-pass fixed bed reactor for CO_2 methanation“. In: *Journal of CO_2 Utilization* 25 (2018), pp. 158–169 (cit. on pp. 13, 14).

[Sze+07] F. Szeifert, T. Chován, L. Nagy, J. Abonyi, and P. Árva. „Runaway of chemical reactors: Parametric sensitivity and stability“. In: *Hungarian Journal of Industry and Chemistry* 35.1 (2007) (cit. on pp. 42, 43, 54).

[TBS19] M. Thema, F. Bauer, and M. Sterner. „Power-to-gas: Electrolysis and methanation status review“. In: *Renewable and Sustainable Energy Reviews* 112 (2019), pp. 775–787 (cit. on p. 24).

[The19] S. Theurich. „Unsteady-state operation of a fixed-bed recycle reactor for the methanation of carbon dioxide“. Dissertation. Ulm: Universität Ulm, 2019 (cit. on p. 2).

[Tid+13] B. Tidona, C. Koppold, A. Bansode, A. Urakawa, and P. Rudolf von Rohr. „CO_2 hydrogenation to methanol at pressures up to 950bar“. In: *The Journal of Supercritical Fluids* 78 (2013), pp. 70–77 (cit. on p. 17).

[TR96] S. Trinh and D. Ramkrishna. „Pattern formation in fixed bed catalytic reactors—I“. In: *Chemical Engineering Science* 51.21 (1996), pp. 4887–4901 (cit. on p. 37).

[TR97] S. Trinh and D. Ramkrishna. „Pattern formation in fixed-bed catalytic reactors—II“. In: *Chemical Engineering Science* 52.20 (1997), pp. 3561–3578 (cit. on pp. 37, 39).

[Tre+15] A. Tremel, P. Wasserscheid, M. Baldauf, and T. Hammer. „Techno-economic analysis for the synthesis of liquid and gaseous fuels based on hydrogen production via electrolysis“. In: *International Journal of Hydrogen Energy* 40.35 (2015), pp. 11457–11464 (cit. on p. 1).

[Tro+04] E. Tronconi, G. Groppi, T. Boger, and A. Heibel. „Monolithic catalysts with 'high conductivity' honeycomb supports for gas/solid exothermic reactions: Characterization of the heat-transfer properties“. In: *Chemical Engineering Science* 59.22-23 (2004), pp. 4941–4949 (cit. on pp. 26, 67).

[Try+17] R. Try, A. Bengaouer, P. Baurens, and C. Jallut. „Dynamic modeling and simulations of the behavior of a fixed-bed reactor-exchanger used for CO_2 methanation“. In: *AIChE Journal* (2017) (cit. on pp. 13, 67).

[TS88] E. Tsotsas and E. U. Schlünder. „On axial dispersion in packed beds with fluid flow: Über die axiale Dispersion in durchströmten Festbetten“. In: *Chemical Engineering and Processing: Process Intensification* 24.1 (1988), pp. 15–31 (cit. on p. 127).

[TS90] E. Tsotsas and E.-U. Schlünder. „Heat transfer in packed beds with fluid flow: remarks on the meaning and the calculation of a heat transfer coefficient at the wall“. In: *Chemical Engineering Science* 45.4 (1990), pp. 819–837 (cit. on p. 59).

[Tso10] E. Tsotsas. „M7 Heat and mass transfer in packed beds with fluid flow“. In: *VDI Heat Atlas*. Berlin, Heidelberg: Springer Berlin Heidelberg, 2010, pp. 1327–1342 (cit. on pp. 58, 59).

[URS19] J. Uebbing, L. K. Rihko-Struckmann, and K. Sundmacher. „Exergetic assessment of CO_2 methanation processes for the chemical storage of renewable energies“. In: *Applied Energy* 233-234 (2019), pp. 271–282 (cit. on pp. 1, 17, 18).

[van17] R. A. van Santen. *Modern heterogeneous catalysis: An introduction*. Weinheim: Wiley-VCH Verlag GmbH & Co. KGaA, 2017 (cit. on p. 3).

[Var80] A. Varma. „On the number and stability of steady states of a sequence of continuous-flow stirred tank reactors“. In: *Industrial & Engineering Chemistry Fundamentals* 19.3 (1980), pp. 316–319 (cit. on pp. 37, 51).

[VDI10] VDI. *VDI Heat Atlas*. VDI-Buch. Springer Berlin Heidelberg, 2010 (cit. on p. 128).

[VDI19] VDI. „Brennstoff, Wärme, Kraft: Jahresausgabe 2019“. In: *Brennstoff, Wärme, Kraft* 71 (2019) (cit. on pp. 1, 18).

[vJ76a] H. van Doesburg and W. A. de Jong. „Transient behaviour of an adiabatic fixed-bed methanator—I“. In: *Chemical Engineering Science* 31.1 (1976), pp. 45–51 (cit. on p. 5).

[vJ76b] H. van Doesburg and W. A. de Jong. „Transient behaviour of an adiabatic fixed-bed methanator—II“. In: *Chemical Engineering Science* 31.1 (1976), pp. 53–58 (cit. on p. 5).

[VJB97] F. Viel, F. Jadot, and G. Bastin. „Global stabilization of exothermic chemical reactors under input constraints“. In: *Automatica* 33.8 (1997), pp. 1437–1448 (cit. on p. 30).

[VSL08] G. A. Viswanathan, M. Sheintuch, and D. Luss. „Transversal hot zones formation in catalytic packed-bed reactors“. In: *Industrial & Engineering Chemistry Research* 47.20 (2008), pp. 7509–7523 (cit. on pp. 9, 39).

[VvW92] J. W. Verwijs, H. van den Berg, and K. R. Westerterp. „Startup of an industrial adiabatic tubular reactor“. In: *AIChE Journal* 38.12 (1992), pp. 1871–1880 (cit. on p. 79).

[WA17] K. Wagemann and F. Ausfelder. *E-Fuels - mehr als eine Option White Paper*. Frankfurt am Main: DECHEMA, Gesellschaft für Chemische Technik und Biotechnologie e.V., 2017 (cit. on p. 2).

[WB06] A. Wächter and L. T. Biegler. „On the implementation of an interior-point filter line-search algorithm for large-scale nonlinear programming“. In: *Mathematical programming* 106.1 (2006), pp. 25–57 (cit. on pp. 82, 102).

[WE94] G. T. Wright and T. F. Edgar. „Nonlinear model predictive control of a fixed-bed water-gas shift reactor: An experimental study“. In: *Computers & Chemical Engineering* 18.2 (1994), pp. 83–102 (cit. on p. 10).

[WE95] K. M. Wagialla and S. Elnashaie. „Bifurcation and complex dynamics in fixed-bed catalytic reactors“. In: *Chemical Engineering Science* 50.17 (1995), pp. 2813–2832 (cit. on pp. 30, 36, 37, 47).

[WEB75] H. S. Weng, G. Eigenberger, and J. B. Butt. „Catalyst poisoning and fixed bed reactor dynamics“. In: *Chemical Engineering Science* 30.11 (1975), pp. 1341–1351 (cit. on p. 4).

[Wen18] M. Wenzel. „Reverse water-gas shift chemical looping for syngas production from CO_2“. PhD thesis. Magdeburg: Otto-von-Guericke-Universität Magdeburg, 2018 (cit. on p. 20).

[WL84] S. Wedel and D. Luss. „Steady-state multiplicity features of an adiabatic fixed-bed reactor with Langmuir-Hinshelwood kinetics; carbon monoxide or carbon dioxide methanation“. In: *Industrial & Engineering Chemistry Fundamentals* 23.3 (1984), pp. 280–288 (cit. on pp. 37, 39, 69).

[WNT12] D. A. Wood, C. Nwaoha, and B. F. Towler. „Gas-to-liquids (GTL): A review of an industry offering several routes for monetizing natural gas“. In: *Journal of Natural Gas Science and Engineering* 9 (2012), pp. 196–208 (cit. on p. 25).

[Woo+14] T. W. Wood, B. Blake, T. E. Blue, C. M. Petrie, and D. Hawn. „Evaluation of the performance of distributed temperature measurements with single-mode fiber using rayleigh backscatter up to 1000 °C“. In: *IEEE Sensors Journal* 14.1 (2014), pp. 124–128 (cit. on p. 94).

[XF89] J. Xu and G. F. Froment. „Methane steam reforming, methanation and water-gas shift: I. Intrinsic kinetics“. In: *AIChE Journal* 35.1 (1989), pp. 88–96 (cit. on pp. 20, 21, 56, 57, 61, 64, 81, 130, 131).

[YF73] L. C. Young and B. A. Finlayson. „Axial dispersion in nonisothermal packed bed chemical reactors“. In: *Industrial & Engineering Chemistry Fundamentals* 12.4 (1973), pp. 412–422 (cit. on p. 53).

[Zha+13] G. Zhang, T. Sun, J. Peng, S. Wang, and S. Wang. „A comparison of Ni/SiC and Ni/Al_2O_3 catalyzed total methanation for production of synthetic natural gas“. In: *Applied Catalysis A: General* 462 Ű 463 (2013), pp. 75–81 (cit. on p. 23).

List of Symbols

Latin

A	surface	m^2
Bo	Bodenstein number	–
C	constant	various
c	concentration	$\mathrm{mol\,m^{-3}}$
c_p	heat capacity	$\mathrm{J\,kg^{-1}\,K^{-1}}$
$\mathrm{Da_I}$	first Damköhler number	–
$\mathcal{D}$	diffusion / dispersion coefficient	$\mathrm{m^2\,s^{-1}}$
d	diameter	m
E_A	activation energy	$\mathrm{kJ\,mol^{-1}}$
F	specific gas flow	$\mathrm{Nl\,h^{-1}\,g_{cat}^{-1}}$
e	set-point deviation	–
HHV	higher heating value	$\mathrm{J\,kg^{-1}}$
j	mass flux	$\mathrm{kg\,m^{-2}\,s^{-1}}$
K	adsorption and equilibrium constant	various
K	controller parameter	various
k	heat transport coefficient	$\mathrm{W\,m^{-1}\,K^{-1}}$
k	reaction rate constant	various
L	reactor length	m
M	molar mass	$\mathrm{kg\,mol^{-1}}$
n	total number of CSTR stages	–
Pe	Péclet number	–
Pr	Prandtl number	–
p	pressure	bar
$\boldsymbol{p}$	parameter	–
$\dot{Q}$	heat flow	W
$\dot{q}$	heat flux density	$\mathrm{W\,m^{-2}}$
R	effective molar reaction rate	$\mathrm{mol\,m^{-3}\,s^{-1}}$
R	tube inner radius	m
$\mathcal{R}$	universal gas constant	$\mathrm{J\,mol^{-1}\,K^{-1}}$
Re	Reynolds number	–
r	mass-based reaction rate	$\mathrm{mol\,kg_{cat}^{-3}\,s^{-1}}$
$\tilde{\mathrm{r}}$	molar reaction rate	$\mathrm{mol\,m_{cat}^{-3}\,s^{-1}}$
r	radial coordinate	m
St	Stanton number	–
S	scaling factor	–
T	temperature	K
t	time	s
$\boldsymbol{u}$	control	–

V	volume	m^3
$\dot{V}$	volumetric flow rate	$\mathrm{m}^3\,\mathrm{s}^{-1}$
v	superficial velocity	$\mathrm{m\,s}^{-1}$
w	mass fraction	–
X	conversion	–
$\tilde{X}$	surrogate conversion	–
x	molar fraction	–
$\boldsymbol{x}$	differential state	–
Y	yield	–
z	axial coordinate	m
$\boldsymbol{z}$	algebraic state	–

Greek

α	heat transport coefficient	$\mathrm{W\,m}^{-2}\,\mathrm{K}^{-1}$
γ	inactive, adiabatic model zone	m
$\Delta_R\tilde{H}^0$	reaction enthalpy (STP)	$\mathrm{J\,mol}^{-1}$
$\Delta_R H^0$	reaction enthalpy (STP)	$\mathrm{J\,kg}^{-1}$
ΔT^0	temperature rise (STP)	K or °C
ΔT	temperature rise / difference	K or °C
δ	wall thickness	m
ε	void fraction	–
η	catalyst effectiveness factor	–
λ	thermal conductivity	$\mathrm{W\,m}^{-1}\,\mathrm{K}^{-1}$
μ	dynamic viscosity	$\mathrm{Pa\,s}$
v	kinematic viscosity	$\mathrm{m}^2\,\mathrm{s}$
ν	stoichiometric coefficient	–
ρ	density	$\mathrm{kg\,m}^{-3}$
τ	tortuosity	–
τ	residence time	s
Φ	Thiele modulus	–
φ	azimuthal coordinate	$^\circ$

Subscripts

ad	adiabatic
α	component $\mathrm{CH_4, CO, CO_2, H_2O, H_2, N_2}$
β	reaction
bed	catalyst bed
cat	catalyst phase
cond	conduction
cool	cooling
crit	critical
e	energy
eq	equilibrium
ext	extinction
feed	feed
gas	gas phase
h	hydraulic
I	integral term
ign	ignition

in	inlet
jac	jacket
Kn	Knudsen
M	molecular
m	mass
max	maximum
meth	methanation reaction
mix	mixture
n	total number of CSTR stages
OP	operation point
P	proportional term
p	particle
pore	pore
r	radial
rad	radiation
react	reaction
site	catalyst site
w	wall
z	axial

Acronyms and Abbreviations

ATR	adiabatic temperature rise
CM	cell model
CPU	central processing unit
CSTR	continuously stirred tank reactor
DEN	denominator
DM	dispersion model
DAE	differential algebraic system
DME	dimethyl ether
DTS	distributed temperature sensing
EB	extinction branch
FBR	fixed-bed reactor
FV	finite volume
FVM	finite volume method
GtL	gas to liquid
HICOM	high combined shift methanation
IB	ignition branch
ICP-OES	inductively coupled plasma optical emission spectrometry
IGCC	integrated gasification combined cycle
IR	infrared
LHHW	Langmuir-Hinshelwood Hougen-Watson
LMPC	linear model predictive control
NMPC	nonlinear model predictive control
NLP	nonlinear program
OP	operation point
PDE	partial differential equation
PFTR	plug flow tubular reactor
PtG	power to gas
PtL	power to liquid
PtM	power to methane
PtX	power to X

P&ID	piping and instrumentation diagram
RPM	Ralph M. Parsons
RWGS	reverse water gas shift
SMR	steam methane reforming
SNG	synthetic natural gas
STP	standard temperature and pressure
TIGAS	Topsøe improved gasoline synthesis
TOS	time on stream
TREMP	Topsøe recycle energy-efficient methanation process
WGS	water-gas-shift

List of Figures

1.1 Towards more flexible processes in chemical engineering. 2
1.2 Several motions of hot zones on catalyst particles. 8
1.3 Characteristic times for maximum and minimum reactor load at the catalyst bed calculated for exemplary reactor dimensions. 12

2.1 Methane-based PtX process routes with flexible and continuous processes and fluxes. 19
2.2 Mole fractions at chemical equilibrium and kinetic conversion over temperature for pure, stoichiometric feed at different pressures and flows. . . 20
2.3 Mole fractions at chemical equilibrium over temperature at different pressures. 22
2.4 Adiabatic temperature rise of CO_2 methanation for various temperatures and for stoichiometric feed diluted with different methane, water, and product gas fractions. 23
2.5 Commercial SNG TREMP^{TM} technology flow-sheet. 25
2.6 State-space diagram of exemplary reaction pathways in adiabatic and polytropic reactors. 26
2.7 Polytropic reactor concepts for improved heat management. 26

3.1 Flux network and sources A to E for multiplicity within fixed-bed reactors. 33
3.2 Qualitative energy flows under exothermic conditions without a) and with b) coolant transport resistance, OP - operating point. 35
3.3 Feedback scenarios according to Fig. 3.2. 36
3.4 Illustration of the single CSTR model with heterogeneously catalyzed reaction. 40
3.5 State-space diagram for mass and energy balance and all attainable operating points under variation of the operating temperature. 41
3.6 State-space diagram for mass and energy balance and all attainable operating points under variation of the Stanton number. 41
3.7 Illustration of the CSTR cascade model of n stages with heterogeneously catalyzed reaction. 44
3.8 State-space diagram for a cascade of two isothermal CSTRs in the R-X and X-T plane. 44

3.9 Graphical solution of a two-stage CSTR series. 45
3.10 Enumerative solution of significant operating points in a two-stage CSTR series. 46
3.11 Possible state combinations for a two-stage CSTR cascade. 46
3.12 Enumerative solution of operating points in a multi-stage CSTR cascade. . 48
3.13 Possible state combinations of a multi-stage CSTR cascade with two key stages. 48
3.14 Enumerative solution of operating points in a multi-stage CSTR cascade with varying residence time. 50
3.15 First stage mass and energy-based sensitivity for non-isothermal CSTR cascades with various stage number. 52
3.16 Schematic illustration of the fixed-bed reactor model. 56
3.17 Reproduced axial dependency of effectiveness factor. 61
3.18 Axial back-mixing effects that can contribute to a reactor model based on the FVM scheme. 62

4.1 Ignition and extinction branches for different catalyst activities. 64
4.2 Ignition and extinction branches of reference case in comparison to intensified reactors. 66
4.3 Ignition and extinction branches of reference case in comparison to 40 % product recycle. 68
4.4 Closed-loop scheme for reactor control. 69
4.5 Ignition and extinction arcs of reference case in comparison to stabilized operation via PI-control. 70
4.6 Stabilized operating range for varying coolant heat transfer. 71
4.7 Stabilized operating range for varying inlet pressures. 72
4.8 Stabilized operating range for varying particle diameter. 73
4.9 Open-loop eigenvalues of linearized state b). 74
4.10 Closed-loop eigenvalues of linearized state b). 75
4.11 Coolant selection range related to prior case studies. 76

5.1 Optimal and non-optimal carbon dioxide conversion, methane selectivity, and control trajectories. 83
5.2 Controlled and uncontrolled reactor temperature distribution. 84

6.1 Simplified pilot plant piping and instrumentation scheme. 88
6.2 Reactor operating map for superficial velocity. 89
6.3 Constructional drawing of the FOReCAST single-tube reactor unit. 90
6.4 The Industrial Methanation Reference Catalyst (IMRC). 91
6.5 Activity tests of the IMRC in comparison with the reference kinetic model. 93
6.6 Calibration result of the DTS with RTD T514 placed directly at the end of the fixed-bed. 94
6.7 Coolant heat transfer coefficient according to the reactor dimensions. . . . 96

6.8 Nonreactive experiments in comparison to the uncalibrated model (Case 0). 100
6.9 Reactive experiments in comparison to the uncalibrated model (Case 0). . 100
6.10 Nonreactive experiments in comparison to the calibrated model (Case A) at steady state. 103
6.11 Reactive experiments in comparison to the calibrated model (Case B). . . . 104
6.12 Reactive experiments in comparison to the calibrated model (Case C). . . 105
6.13 Two-dimensional fixed-bed temperature field after model calibration (Case B) considering experiment 14. 106
6.14 Dynamic reactor behavior under mild reaction conditions after cool-down perturbation in comparison with the calibrated model (Case B). 108
6.15 Dynmaic reactor behavior under intensive reaction conditions after cool-down perturbation in comparison with the calibrated model (Case B). . . 109
6.16 Mass- and energy-based sensitivity for uniqueness and multiplicity criteria on a broad axial dispersion range and for the conditions of experiment 11 and 16. 110

A.1 Illustration of the single CSTR model with heterogeneously catalyzed reaction. 119
A.2 Illustration of the CSTR cascade model of n stages with heterogeneously catalyzed reaction. 124
A.3 Enumerative solution of operating points in a multi-stage CSTR cascade with varying residence time. 126
A.4 Nu-Re-dependency for the heat transfer medium *Marlotherm SH*. 129
A.5 Conversion, composition, temperature, pressure and velocity changes along the entire reactor length. 133
A.6 Temperature, CO_2-composition, effectiveness factor and reaction rate changes around the reactive zone. 134
A.7 Temperature, Reynolds number, Prandtl number and effective axial Péclet number around the reactive zone. 135
A.8 Temperature, effective radial conductivity, effective axial conductivity and effective CH_4 diffusion coefficient around the reactive zone. 136
A.9 Heat transport coefficients and cumulative heat transfer from reactor to coolant along the entire reactor length. 137
A.10 Open-loop eigenvalues of linearized state c) of the reference setting. . . . 138
A.11 Piping and instrumentation diagram of the FOReCAST pilot plant. 140
A.12 Reactor behavior under intensive reaction conditions after cool-down perturbation in comparison with the calibrated model. 142
A.13 Reactor behavior under intensive reaction conditions after cool-down perturbation in comparison with the calibrated model. 142

List of Tables

3.1 Review on multiplicity sources within fixed-bed reactors. 37
3.2 Specifications and operating parameter for the reactor model reference case. 57

5.1 Start-up operating parameters. 80

6.1 Specifications of the reactor in comparison to previous model assumptions. 90
6.2 Specifications of the IMRC in comparison to previous model assumptions. 91
6.3 Specifications of the thermal oil heat transfer unit. 95
6.4 Parameters used for model calibration. 97
6.5 Nonreactive test set and corresponding experimental conditions. 99
6.6 Reactive test set and corresponding experimental conditions. 99
6.7 Scaling factors and considered experiments of all calibration cases. 105

A.1 Realistic parameter ranges of carbon dioxide methanation in a tubular fixed-bed reactor. 123
A.2 Kinetic parameters for Eqs. (A.22) to (A.24). 131
A.3 Kinetic parameters for Eqs. (A.25) to (A.27). 132
A.4 Measured CH_4 and CO yields for the industrial methanation reference catalyst (IMRC). 139
A.5 Parameters for evaluating uniqueness and multiplicity criteria under experimental conditions. 141

Colophon

This thesis was typeset with $\LaTeX\,2_\varepsilon$. It uses the *Clean Thesis* style developed by Ricardo Langner. The design of the *Clean Thesis* style is inspired by user guide documents from Apple Inc.

Download the *Clean Thesis* style at `http://cleanthesis.der-ric.de/`.